SIMON ERKER

Theoretical Modeling of Charge Transfer Effects at Semiconductor/Organic Interfaces

DOCTORAL THESIS

to achieve the university degree of

Doktor der technischen Wissenschaften

submitted to

Graz University of Technology

Supervisor:
Ao.Univ.-Prof. Dr. Egbert Zojer
Co-Supervisor:
Dr. Oliver T. Hofmann
Institute of Solid State Physics

Graz, January 2019

Statutory Declaration

I, Simon Erker, declare that I have authored this thesis independently, that I have not used other than the declared sources/resources, and that I have explicitly indicated all material which has been quoted either literally or by content from the sources used. The text document uploaded to TUGRAZonline is identical to the present doctoral thesis.

Abstract

**Theoretical Modeling of Charge Transfer Effects at
Semiconductor/Organic Interfaces**

by Simon Erker

In hybrid inorganic/organic electronics the hetero-interface between inorganic semiconductors and organic molecules decisively determines the functionality and efficiency of devices. In this dissertation, charge transfer processes at such interfaces are investigated by means of first-principle calculations at the level of density functional theory (DFT). Developing methods and gaining insight into how such processes can be reliably modeled, constitute an important part of this thesis.

The charge transfer at semiconductor/organic interfaces and, therefore, also many device properties depend heavily on the exact surface structure of the substrate material. However, in particular for materials such as ZnO, which is the inorganic semiconductor investigated in this work, the surface composition is often not well understood. We used first principle methods and collaborated with experimentalists to investigate the surface structure of this transparent conductive oxide. To study the effect of bulk doping on the phase stability of O-terminated ZnO surfaces, a novel formalism is presented to incorporate the long-ranged band-bending effects directly into DFT calculations. The collaboration with experimentalists included the exploration of the surface structure of Zn-terminated ZnO by using organic molecules as a probe for the surface structure.

The charge transfer mechanism is then thoroughly investigated for a F4TCNQ monolayer adsorbed on the mixed-terminated ZnO surface through hybrid DFT. At inorganic/organic interfaces, charge transfer occurs in different types, usually depending on the nature of the substrate. Either the transferred charge is equally distributed over all molecules (fractional charge transfer), or localized on individual molecules (integer charge transfer). Interestingly for the F4TCNQ/ZnO system, we find that both mechanisms appear simultaneously. To verify the charge transfer in real systems we collaborated with experimentalists. We probed the charge state of F6TCNNQ molecules adsorbed on mixed-terminated ZnO by IR-spectroscopy and conducted a theoretical analysis of the vibrational modes. We could corroborate the occurrence of electron transfer, arising mainly from surface states in this system.

This work provides a detailed theoretical insight into modeling charge transfer effects at semiconductor/organic interfaces and the obtained understanding of these effects answers a number of fundamental questions concerning charge transfer processes.

Kurzfassung

Theoretische Modellierung von Ladungstransfer-Effekten an Grenzflächen zwischen Halbleitern und organischen Molekülen

von Simon Erker

In der anorganisch-organischen Elektronik wird die Funktionalität und Effizienz von Bauelementen durch die Grenzfläche zwischen anorganischen Halbleitern und organischen Molekülen bestimmt. Im Zuge dieser Arbeit werden mittels Dichtefunktionaltheorie (DFT) Rechnungen Ladungstransferprozesse an solchen Grenzflächen untersucht. Ein wesentlicher Teil davon ist die Entwicklung von Methoden, sowie die Gewinnung von Erkenntnissen für eine verlässliche Modellierung solcher Prozesse.

Der Ladungstransfer an Grenzflächen zwischen Halbleitern und organischen Molekülen hängen stark von der genauen Oberflächenstruktur des Substratmaterials ab. Die Oberflächenstruktur von Materialien wie ZnO, dem in dieser Arbeit untersuchten anorganischen Halbleiter, ist jedoch oft nicht ausreichend verstanden. In dieser Arbeit wird die Oberflächenstruktur dieses transparenten, leitenden Oxids mittels theoretischer Rechnungen als auch in Zusammenarbeit mit Experimentatoren untersucht. Um den Effekt der Dotierung auf die Phasenstabilität von O-terminierten ZnO-Oberflächen zu untersuchen, wurde eine neue Methode vorgestellt, die "band bending" Effekte direkt in DFT-Rechnungen berücksichtigt. Des Weiteren wurde, in Zusammenarbeit mit Experimentatoren, die Oberflächenstruktur von Zn-terminiertem ZnO, unter Verwendung organischer Moleküle als Sonde für die Oberflächenstruktur, untersucht.

Ausführliche Untersuchungen des Ladungstransfermechanismus wurden für eine F4TCNQ-Monolage auf der gemischt-terminierten ZnO-Oberfläche durchgeführt. An solchen anorganisch/organischen Grenzflächen tritt der Ladungstransfer in verschiedenen Formen auf, üblicherweise abhängig von der Art des Substrats. Entweder wird die übertragene Ladung gleichmäßig auf alle Moleküle verteilt (fraktioneller Ladungstransfer) oder auf einzelne Moleküle lokalisiert (Integer Ladungstransfer). Interessanterweise fanden wir für das F4TCNQ/ZnO-System heraus, dass beide Mechanismen gleichzeitig auftreten. Um den Ladungstransfer in realen Systemen zu überprüfen, haben wir mit Experimentatoren zusammengearbeitet. Der Ladungszustand von F6TCNNQ-Molekülen wurde durch IR-Spektroskopie und einer theoretischen Analyse der Schwingungsmodi bestimmt. Im Zuge dessen konnten wir das Auftreten von Elektronentransfer bestätigen, der in diesem System hauptsächlich von Oberflächenzuständen stammt.

Diese Arbeit liefert einen detaillierten theoretischen Einblick in die Modellierung von Ladungstransfereffekten an Grenzflächen zwischen anorganischen Halbleitern und organischen Molekülen. Das Verständnis dieser Effekte trägt dazu bei eine Reihe grundlegender Fragen in Bezug auf Ladungstransferprozesse zu beantworten.

Acknowledgements

I am using the opportunity to express my gratitude to everyone who supported me throughout the course of my dissertation. Such a work is never possible without the help and support from others.

First and foremost I would like to thank Oliver T. Hofmann. Your guidance and support has been crucial to my success and I benefited very much from your experience and knowledge. Without your supervision and constant help this thesis would not have been possible. I would also like to express my gratitude to my supervisor, Egbert Zojer, for your invaluably constructive criticism and advice concerning my publications and this thesis.

Scientific work is best done in a good atmosphere. I would like to thank my great coworkers, the members of the Advanced Materials Modeling Team (past and present): Alexander, Andreas, Christian, Elsi, Florian, Georgii, Giulia, Iris, Karin, Lisi, Lukas, Lukas, Markus, Michael, Natalia, Sandro, Shashank, Thomas, Tomas and Veronika. Special thanks to the ones in the list who shared the office with me, I always enjoyed your company and the activities we experienced together.

Parts of this thesis were developed together with other researches, who all made useful contributions to my work. I am particularly happy to have collaborated with Jens Niederhausen and the Norbert Koch group, Antoni Franco-Cañellas and the Frank Schreiber group, and with Christof Wöll. Thanks to Volker Blum and the members of his group for hosting me on my research stay at Duke University.

I am also very grateful for the unconditional support of my friends and family. Many thanks to my parents, you always encouraged me in my decisions and supported me on my way.
Very special thanks to Anna, I cannot express how grateful I am for you and your support.

List of Publications

This thesis is based on the following papers:

I Doping Dependence of the Surface Phase Stability of Polar O-Terminated (000$\bar{1}$) ZnO

S. Erker, P. Rinke, N. Moll and O.T. Hofmann

New J. Phys. **19**, 083012 (2017)

II X-ray standing waves evidence lack of OH-termination at ZnO(0001) surfaces

J. Niederhausen, A. Franco-Cañellas, S. Erker, T. Schultz, K. Broch, A. Hinderhofer, S. Duhm, P.K. Thakur, D.A. Dunca, A. Gerlach, T.-L. Lee, O.T. Hofmann, F. Schreiber, N. Koch

Manuscript in preparation

III Fractional and Integer Charge Transfer at Semiconductor/Organic Interfaces: The Role of Hybridization and Metallicity

S. Erker and O.T. Hofmann

Submitted manuscript

IV Electron transfer at organic/inorganic interfaces monitored by IR-spectroscopy

L. Schöttner*, S. Erker*, R. Schlesinger, N. Koch, A. Nefedov, O.T. Hofmann, Ch. Wöll

*Manuscript in preparation (*equally contributing authors)*

Reprints were made with permission from the publisher and/or the co-authors.

Preface

About the thesis

The invention of semiconductor devices was one of the most influential inventions in human history and significantly changed our world over the last decades. Many technological applications, e.g. computers, smart phones or displays, that are now an integral part of our everyday life, have become possible due to advances in semiconductor physics and surface science. Silicon as the most prominent representative of inorganic semiconducting materials became known to the general public. Another inorganic semiconducing material that was present from the very beginning of semiconductor physics is the wide-band-gap semiconductor zinc-oxide (ZnO). ZnO is a prototypical n-type semiconducting oxide that due to its stability, optical transparency, wide band gap, and high charge carrier mobility, has attracted significant attention for the use in electronic devices such as laser diodes or sensors.

Over the last years more and more research was concentrated on another class of semiconducting materials: Organic molecules. Their advantage over inorganic semiconductors is the chemical flexibility and the strong light-matter coupling. Organic molecules have shown their potential and already appear in modern electronic devices such as organic light-emitting diodes (OLEDs) for displays and lighting applications or in organic solar cells (OSCs). Their disadvantages are still their environmental instability and low charge carrier mobilities that severely limit their use in practical applications.

A lot of expectations were raised that combining these two diverse classes of semiconductors, inorganic and organic, will merge the best of the two worlds. Such hybrid materials, constituting both inorganic and organic components, are often seen as promising candidates for applications in extremely diverse fields such as electronics, spintronics, or energy storage. The main focus of this dissertation is the theoretical investigation of interfaces between inorganic ZnO and organic molecules, so-called hybrid inorganic/organic interfaces. The performance and functionality of hybrid devices is mainly governed by the hetero-interface between an inorganic semiconductor and organic molecules. Engineering and control of the interface is, therefore, the key for achieving an optimized device performance or developing new functionalities. Ultimately, this requires a comprehensive, fundamental understanding of structural features, the electronic structure, and the quantum processes at such interfaces. In particular the interfacial energy level alignment

and the charge transfer processes need to be understood in a more systematic manner. This is exactly where my research is located.

The theoretical approach I used to gain a deeper understanding of the processes at hybrid interfaces are computer experiments based on density functional theory (DFT) calculations. DFT became one of the most wide-spread computational methods in theoretical material science over the last decades and its popularity increased exponentially during this period. Its popularity is based on its good balance between computational efficiency and the accuracy of the obtained results. Nowadays computers, in combination with new sophisticated numerical methods, make DFT applicable to systems composed of hundreds or even thousands of atoms, system sizes that are so far not computationally feasible with more expensive quantum-chemistry methods rooted in wave-function theory. While in principle DFT is an exact theory, in reality a list of approximations have to be made. This causes a significant variety in DFT implementations. Some consider all electrons of an atom on the same level, while others only treat the valance electrons explicitly and use pseudo potentials for core electrons. Some use plane-waves to describe Kohn-Sham orbitals, others use Gaussian-type or numeric atom-centered basis sets. This list can be continued for a while. In most cases these approximations can be chosen in a way that a good accuracy of specific quantities are achieved. For every investigated system such convergence tests are a crucial task to assure the numerical reliability of the obtained results.

The most important and influential approximation, however, was not mentioned so far: The exchange-correlation energy functional. In general the exact exchange-correlation (xc) functional is non-analytic and, more importantly, completely unknown. Therefore, over time a whole series of various approximate functionals developed and new developments are still ongoing. The "best" functional for a system strongly depends on the investigated system itself as well as the properties or quantities of interest and people often depend on experience in this matter. However, especially in the case of hybrid inorganic/organic interfaces, where two very different classes of materials are combined, a proper choice of the xc-functional is a non-trivial task. Therefore, within this thesis the choice of the proper functional is a constant companion and different functionals were used for different questions. In this context one should give the reliability of obtained results always the top priority while keeping track of the computational costs.

The ultimate goal of theoretical material calculations is obviously to have predictive power, meaning conclusions from the theory side are predicting and fully explaining experimentally obtained findings. However, often some hidden phenomenas are not accessible when approaching a question only from one side, namely theory *or* experiment. In these cases (which are clearly the majority) theory and experiment are complementing approaches and insights from both sides are necessary to fully understand a specific system. Therefore it is also very important for a theoretician to collaborate with experimentalists, and parts of this thesis originated from such collaborations.

Outline of this thesis

This thesis is based on my research conducted at Graz University of Technology and my research stay at Duke University. Some of the results presented here have been previously published in peer-reviewed papers, while others are not yet published or were recently submitted. Therefore this thesis is assembled in a partly cumulative manner.

The goal of my dissertation was to contribute to the general understanding of the charge transfer processes at semiconductor/organic interfaces. The following outline can also be seen as a road map of my research towards this goal. Before entering into the main question we needed to overcome some theoretical limitations that are connected to the long-ranged potential that is build up within a semiconducting substrate upon charge transfer to the surface. Furthermore, knowledge about the surface structure of the substrate itself is an important prerequisite for an accurate modeling of interfaces with organic molecules. Therefore, a part of my research was devoted to the study of ZnO surface structures.

Before presenting my own research, in part one of this thesis relevant fundamentals and the theoretical background of my work are summarized. Chapter 1 introduces the reader to some fundamental background of semiconductor/organic interfaces and of the substrate material ZnO, which is the main inorganic semiconductor appearing in my research. In the second chapter relevant aspects of DFT are introduced, and important aspects of DFT for this work are discussed in more detail, including relevant xc-functionals and their limitations. Other topics that are discussed are the DFT code FHI-aims that was mainly used for my research, the calculation of finite-temperature phase diagrams from DFT calculations using *ab initio* thermodynamics, the calculation of vibrational spectra, and the calculation of surface core level shifts with DFT.

In part II of this thesis the results of my research are presented in five chapters, each chapter dealing with a stage of my research towards the goal of a better understanding of the charge transfer processes at semiconductor/organic interfaces.

Chapter 3 deals with the above described challenge to consider the effects of the long-ranged potential that is build up within a doped semiconducting substrate upon charge transfer to the surface. Standard DFT methods are limited in correctly including these effects in *ab initio* calculations. In this chapter a technique to overcome this limitation and to include the long-ranged band bending effect in DFT calculations is presented. The idea behind this technique already existed, but my work made it possible to actually apply it in a user-friendly way. The capability of this technique is shown by calculating doping-dependent surface phase diagrams of the O-terminated ZnO(000$\bar{1}$) surface. Something that was, to our knowledge, not done before. The obtained results of this work were published in **paper I**. The presented approach provides the basis for correctly modeling the charge transfer to adsorbed molecular layers and, therefore, represents an important step forward in my dissertation.

In chapter 4 we further focus on the ZnO surface structure. The presented work originated from a collaboration with experimentalists from the group of Norbert Koch and Frank Schreiber. We aimed to resolve the experimental structure of the Zn-terminated ZnO(0001) surface. Especially for the polar ZnO surfaces the actual appearing structure of the surface is still under debate. However, for theoretically modeling interfaces with organic molecules, a detailed understanding of the surface structure is key to achieve reliably results. In this work we used planar conjugated molecules as a probe to gain a deeper insight into the surface structure of Zn-terminated ZnO. By comparing experimentally obtained adsorption distances with results from DFT calculations, we were able to eliminate many proposed surface structures for this ZnO surface. We limited the possible surface structures to those for which OH groups are not appearing as adlayers, but rather appear in subsurfaces positions. This knowledge is very relevant for the adsorption behavior of organic molecules and therefore also for the charge transfer. Existing OH-adlayer would prevent a direct adsorption of the molecules to the surface by acting as a buffer layer. Although, following work specifically addressing the charge transfer investigates another ZnO surface, with the knowledge that such buffer layers are not present on Zn-terminated ZnO, the obtained results from later chapters can most probably be applied to this surface as well. The results from this collaboration are going to be published in **paper II**, which is presented in this dissertation in the form of a manuscript in an advanced state.

This dissertation focuses not only on the amount of charge transfer from a semiconducting substrate to a molecular layer, but primarily also on the localization of the transferred charge within the molecular layer. Converging DFT calculations into solutions where the charge is localized on individual molecules can be troublesome, because the charge density is often initialized to be equal on all equivalent molecules. At my research stay at Duke University in the group of Volker Blum, we implemented an alternative initial electron density guess for FHI-aims based on extended Hückel theory, as it is used in many chemistry-focused DFT codes. The aim of this work was a speed up of our calculations of semiconductor/organic interfaces, by improving the initial guess of the charge density. In chapter 5 the implementation of the extended Hückel guess for FHI-aims is presented and results for two test systems are shown.

With the preliminary chapters, that set the foundation of this work, the focus can be turned towards the main question of this dissertation. Chapter 6 deals with the major research focus of this work, the charge transfer at semiconductor/organic interfaces and its dependence on the adsorption nature of the molecules and the doping concentration of the substrate. The adsorption of the prototypical electron acceptor molecule F4TCNQ on the mixed-terminated ZnO(10$\bar{1}$0) surface is investigated by means of hybrid density functional theory. We find that two independent charge transfer mechanisms occur at this model interface as doping is introduced. The underlying physics of this charge transfer processes is studied and the results are presented in the manuscript of **paper III** entitled "Fractional and Integer Charge Transfer at Semiconductor/Organic Interfaces: The Role of Hybridization and Metallicity". An important aspect of this study, from a theoretical point of view, is the influence of the density functional used in the DFT calculations. Subsequent to the manuscript, more interesting methodological

details concerning calculations of semiconductor/organic interfaces are therefore discussed. This includes what was learned about the impact of the doping concentration of the substrate on the many-electron self-interaction error appearing in a DFT calculation of a semiconductor/organic interface. Also the question whether charge localization on individual molecules can be resolved in experiments was addressed by estimating the hopping rate of electrons between neighboring molecules within the molecular layer.

In a next step we collaborated with experimentalists to verify the charge transfer in real semiconductor/organic systems. In Chapter 7, the manuscript of **paper IV** is presented, that contains the results of this collaboration with the group of Christof Wöll and Norbert Koch. Our experimental collaborators measured infrared vibrational spectra of mono- and multilayers of the strong electron acceptor molecule F6TCNNQ adsorbed on the mixed-terminated ZnO($10\bar{1}0$) surface. Our part was to support the experimentally obtained results with a theoretical analysis of the vibrational modes. We were able to identify the impact of the charge transfer and the binding of the molecules to the ZnO surface on the vibrational frequencies. This allowed us to explain the observed IR band shifts for a molecular monolayer compared to multilayer spectra. With our contribution it was, therefore, possible to show that charge transfer into the LUMO occurs for molecules directly adsorbed on the substrate. This chapter closes the results part of my dissertation.

Concluding remarks to our findings and my thesis are written down in Chapter 8. In this chapter the major results of my research are summarized and the reader is guided through the steps that were taken to reliably model charge transfer processes at semiconductor/organic interfaces.

Charge localization on individual molecules within an adsorbed molecular layer was previously theoretically predicted[1] and experimentally observed[2] also for another class of substrate materials: Metals that were decoupled from the adsorbate layer by inserting thin insulating layers. Also for this systems the underlying physics is not yet completely understood. In an additional project we tried to gain a deeper understanding of the charge transfer to PCTDA clusters that were decoupled from an Ag(111) substrate by a bilayer of NaCl. Experiments for this system were performed by Sarah Burke and Katherine Cochrane. As the work on this system is not yet finished, first results are presented in the appendix A to this dissertation. The current status of our theoretical findings and promising ideas to continue this research in the future are described.

Contents

Part I

Theoretical Background and Methodology

Chapter 1

Fundamentals

1.1 Hybrid semiconductor/organic interfaces

One of the main goals of this thesis is to describe and gain new insights of the physics at the interface between inorganic semiconducting substrates and organic molecules. The semiconducting substrate investigated in this work is the transparent conducive oxide ZnO to which the next section is devoted. In comparison to metallic substrates, fewer experimental and theoretical studies have been conducted for metal oxide surfaces and their interfaces with organic compounds. This is partly related to the complexity of metal oxides and their surfaces in comparison to the experimentally well-controllable metal surfaces. Also from a theoretical point of view, standard electronic structure methods are often inadequate to describe the effects at semiconductor/organic interfaces. The development and application of new and often computationally more demanding approaches are necessary. More about this theoretical aspects can be found in the next chapter. In this section, some fundamentals of hybrid semiconductor/organic interfaces are presented.

In organic electronic and optoelectronic devices the goal is to combine the often complementing properties of organic and inorganic materials. It is usually the hybrid interface between an inorganic semiconducting material and organic molecules that is highly important in determining the functionality and efficiency of the device[3,4]. It is therefore essential to fully understand and gain control over the many parameters defining the relevant interface, such as the interface morphology, the presence of dopants and impurities, or the nature of the interaction between the compounds. From a physical point of view these strongly intertwined interfacial properties all have an influence on the interfacial energy level alignment. However, it is not only the knowledge of the electronic structure that is important for estimating the functionality and efficiency of a hybrid system. Also an insight into the fundamental quantum-mechanical processes, like the characteristics of the interfacial charge transfer, is of paramount importance to fully understand the rich physical properties at the interface.

1.1.1   Energy level alignment at the interface

In studies of hybrid semiconductor/organic interfaces, usually the inorganic semiconductor serves as substrate for the organic material. It is the first monolayer of organic molecules that interacts with the substrate material, defining the alignment between the discrete energy levels of the molecular orbitals and the energy bands of the inorganic substrate. For organic molecules, the two key energies are that of the highest occupied molecular orbital (HOMO) and of the lowest unoccupied molecular orbital (LUMO). The energy difference between the HOMO or LUMO and the vacuum level (VL) are the gas phase ionization energy (IE) or the electron affinity (EA) of the molecule, respectively. For the inorganic semiconductor the relative position of the valence band (VB) and the conduction band (CB) define the band gap of the material. The relevant energy level is the Fermi energy E_F that usually lies in the bandgap of a semiconductor and depends on the doping concentration of the semiconductor. A key quantity is the work function Φ of the material, which is the difference between the vacuum level and the Fermi energy. Fig. 1.1 shows a schematic of the energy levels of an inorganic semiconductor and an organic molecule when they are separated from each other.
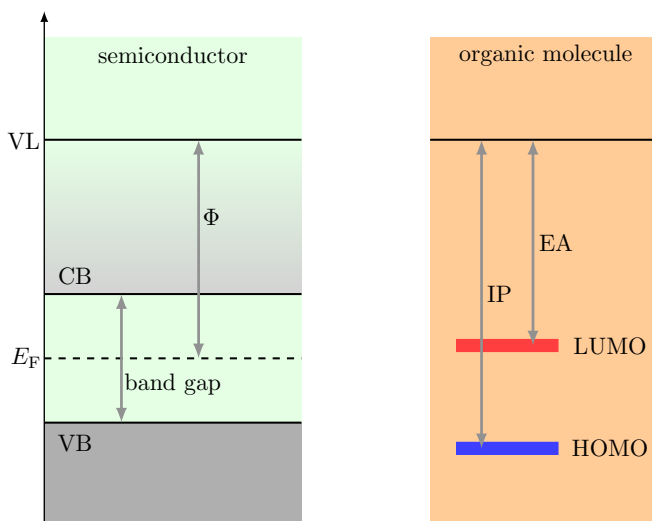
FIGURE 1.1: Schematic energy level diagram of a semiconductor and an organic molecule that are far apart, showing the relevant energetic parameters for both materials

When the molecule is brought into contact with the inorganic semiconductor the materials can interact with each other, resulting in a modification of the individual electronic structure. The interaction strength between the two diverse materials highly depend on the materials itself, varying from only weak van-der-Waals interactions (physisorption) to a formation of strong chemical bonds (chemisorption). In this discussion we focus on weakly chemisorbed molecules on semiconducting substrates, as these systems are primarily studied in this dissertation. We start with the situation where no free charge carriers are available in the inorganic semiconductor, i.e. an undoped substrate. Here the interaction is mainly governed by, first, the overlap of molecular orbitals with substrate states, i.e. the hybridization, and second, the relative position of the Fermi level to the HOMO and LUMO of the molecule after aligning the vacuum level

of both materials. If covalent bonds between molecule atoms and surface atoms are formed, the molecular orbitals hybridize with substrate bands. This leads to a broadening of occupied molecular orbitals and also might cause partial charge transfer resulting in an interface dipole. The interface dipole manifests itself in a modification of the work function of the system. In general the adsorption of organic molecules is often accompanied with the formation of an interface dipole and a modification of the work function of the semiconductor. Beside partial charge transfer due to hybridized orbitals also other effects contribute to the interface dipole. These include the push-back effect[5,6], an eventual molecular dipole, either permanent[7] or induced by the substrate[8], and charge transfer not associated with the formation of covalent bonds, either from the substrate to the molecule, or the other way around[9,6]. In general all processes that rearrange the electronic charge upon adsorption contribute to the interface dipole. The effect on the electrostatic potential of the system from such a dipole layer can be calculated from the electron density profile $n(z)$ across the interface by Poisson's equation

$$\frac{\partial^2 \phi}{\partial z^2} = -\frac{1}{\epsilon_0}(n(z) - n_0), \tag{1.1}$$

where ϕ is the electrostatic potential due to the charge in electron density, ϵ_0 is the vacuum permittivity, and is n_0 the initial electron density profile prior to adsorption. The work function change is then the induced shift in the potential across the interface

$$\Delta\Phi_{\mathrm{ID}} = \phi(\infty) - \phi(-\infty). \tag{1.2}$$

More informations on the above mentioned effects that affect the interface dipole and, thus, the work function can be found in several text books and publications[10,11,12,13]. In the following paragraph we focus on charge transfer into or from the frontier orbitals of the molecule, neglecting all other effects.

The occurrence of charge transfer and the direction is governed by the relative position of the molecular orbitals to the Fermi level. For undoped substrates no charge carriers are available above the valence band and we assume for this discussion that the Fermi level is at the VB maximum. We can distinguish between three scenarios: First, the HOMO lies above the Fermi level (IP $<$ Φ) and charge transfer can in principle occur from the molecule to the substrate assuming unoccupied states are available at the VB. However, this is not the case for defect free, intrinsic semiconductors and charge transfer is not possible due to missing acceptor states in the semiconductor. This is in contrast to metals, where empty bands are always present at the Fermi level. If empty states are available, the work function of the system decreases by $\Delta\Phi_{\mathrm{ID}}$, because a dipole with its negative part pointing towards the surfaces is established across the interface by the charge transfer. Second, the LUMO is in the band gap of the semiconductor (IP $>$ Φ $>$ EA) and no charge transfer is expected into or from the frontier orbitals of the molecule. However, still a change in the work function upon adsorption is possible due to the other above mentioned effects that cause an interface dipole. And third, the LUMO of the molecule is below the Fermi level (Φ $<$ EA) and charge can be transferred to the molecule. In

this case an interface dipole with the negative part pointing away from the surface is established across the interface, resulting in an increase of the work function by $\Delta\Phi_{ID}$. The filling of the now former LUMO also causes the molecular electronic structure to relax, which leads to new energetic positions also of the already filled molecular orbitals. Schematic representations of the three described scenarios are depicted in Fig. 1.2.
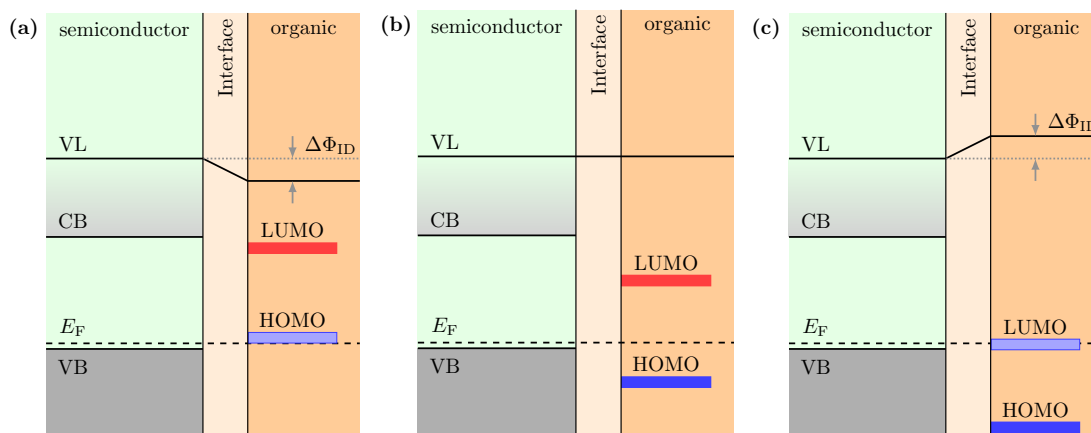
FIGURE 1.2: Scheme of the energy levels of an intrinsic semiconductor in contact with a organic molecule: (a) when the HOMO is above the valence band and charge is transferred from the molecule to the substrate (hypothetical); (b) When the LUMO is in the band gab and no charge is transferred; and (c) when the LUMO is below the valence band and charge is transferred to the molecule.

Now we turn the attention to substrates that are not intrinsic and where free charge carriers are available due to defects or intentional doping. We limit the discussion to n-type semiconductors containing impurities which give additional electrons to the system, as only this type is relevant in this thesis. In doped semiconductors the position of the Fermi level with respect to valence and or conduction band depends on various parameters. In general it shifts towards the CB as the free charge carrier concentration increases. For simplifying this discussion we assume that the doping results in free charge carriers in the conduction band of the material and the Fermi level lies at the CB minimum. In principle the scenarios are very similar to the ones mentioned above, with the difference that if the LUMO of the molecule lies below the Fermi energy and charge from the dopants is transferred to the molecule, an additional effect occurs. Free charge carriers occupying the empty LUMO orbital leave behind the ionized cores of the dopant atoms that remain spatially fixed in the semiconductor and build up an electric field resulting in a bending of the energy bands in the region adjacent to surface (space charge region). A schematic energy level diagram of this situation is depicted in Fig. 1.3. More details about band bending and associated effects are especially discussed in Chapter 3.

The energy diagrams of interfaces usually show laterally averaged energy values. In reality the electronic structure at the interface may be laterally inhomogeneous depending on e.g. the coverage of the molecular adsorbate, localized defects on the surface, or the charge transfer mechanism, which is discussed in the next section. Such inhomogeneities result in variations
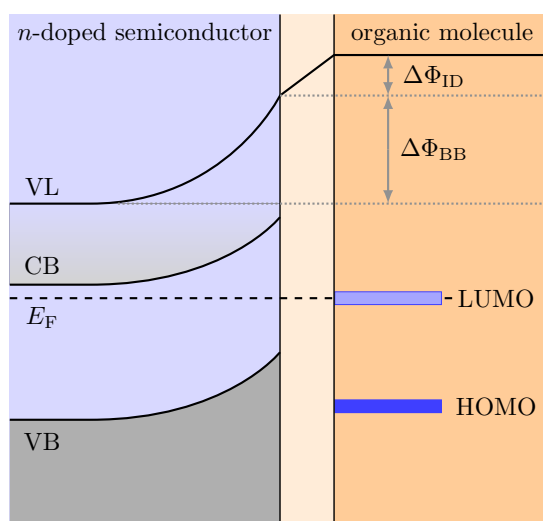
FIGURE 1.3: Scheme of the energy levels of a n-doped semiconductor in contact with an organic molecule: Charge from the bulk reservoir is transferred to the molecule resulting in a bending of the electronic bands in the semiconductor. Due to this band bending the work function is increased by $\Delta\Phi_{BB}$. Additionally the work function possibly changes due to an interface dipole by $\Delta\Phi_{ID}$.

of the electrostatic potential an might even have and impact on device relevant properties by locally altering the charge injection barrier.[14]

1.1.2 Charge transfer mechanisms

For weakly chemisorbed molecular layers, two phenomenological different types of charge transfer occur at the interface between an inorganic substrate and the organic molecular layer: Either, the charge localizes on individual molecules, which leads to a co-existence of integer charged and uncharged molecules and a semiconducting band structure, or the charge delocalizes completely within the organic layer, leading to a homogeneous distribution of fractional charged molecules with a quasi-metallic density of states.

Localization of charge from integer charge transfer (ICT) generally appears in systems where the hybridization between the molecular orbitals and the substrate wave functions is negligible[15,1,2,16]. This is the case for the adsorption of organic molecules on inert substrates, such as insulators or metals that form oxide layers, or were passivated by contaminants. For these systems electron transfer is electrostatically driven and can take place by tunneling, implying the transfer of an integer amount of charge. This results in a symmetry-breaking between differently charged molecules and a splitting of the spin channels, which can be seen in the geometry and the density of states of the differently charged molecules. Conversely, fractional charge transfer (FCT) is usuall observed upon adsorption on clean metal surfaces, where the transferred charge is equally distributed in the molecular layer[17,18,19,20,6]. The frontier orbitals of all equivalent molecules within the layer are equally fractionally charged and no symmetry breaking appears.
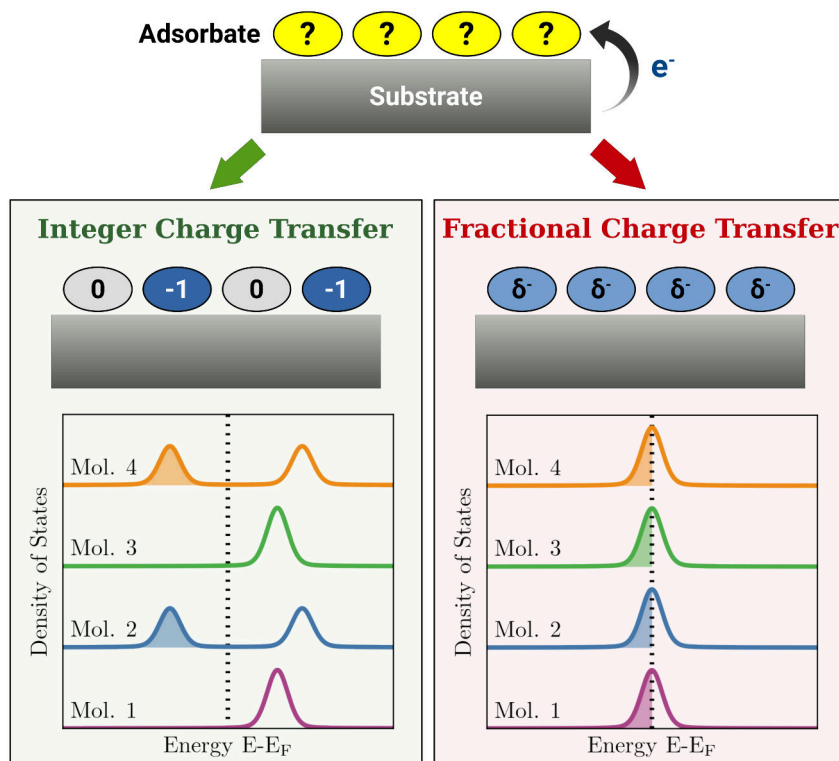
FIGURE 1.4: Schematic presentation of the two possible charge transfer mechanisms upon absorption of a molecular layer on a semiconducting substrate and molecular densities of states for an exemplarily four-molecule-system: Either the transferred charge is localized on individual adsorbate molecules while other adsorbate molecules remain neutral. This results in a spin-splitting for the charged molecules' LUMOs into filled SOMOs and empty SUMOs and no density at the Fermi energy (Integer charge transfer). Alternatively hybrid substrate-molecule states form, leading to a layer of homogeneously partially filled adsorbates with a molecular density of states at the Fermi energy (Fractional charge transfer).

The two mechanisms and their corresponding molecular density of states (DOS) are schematically depicted in Figure 1.4. Distinguishing between the two charge transfer mechanisms and gaining insight into the underlying physics that determines the charge transfer mechanism on semiconducting substrates is one of the main goals of this dissertation. Chapter 6 summarizes our findings in this context.

1.2   Zinc-Oxide

Zinc-oxide (ZnO), a prototypical n-type semiconducting oxide, appears throughout this thesis. We study the structure of various surfaces of this material and the effects of doping and charge transfer on surface and interface properties. Under ambient conditions ZnO adopts a wurtzite structure (hexagonal, space group #186, P63mc), exhibits a native n-type conductivity and a high transparency. ZnO has attracted significant attention for use in opto-electronic devices, due to its direct and wide band gap of 3.37 eV[21,22] and the large free-exciton binding energy

of 60 meV [23]. The combination of these properties makes ZnO a very attractive transparent conductive oxide, specially in combination with organic molecules for organic electronic devices [24,25,26,27].

The tunable charge carrier concentration in ZnO is one of the key properties in this thesis. Purely grown ZnO is basically insulating with a intrinsic carrier concentration below 10^{16} cm^3 [28]. The source of this intrinsic n-type doping is not unambiguously settled with zinc interstitials, oxygen vacancies and hydrogen impurities proposed as possible dopants [29,30,31]. Intentionally highly doped ZnO on the other hand can reach carrier concentrations up to 10^{21} cm^3 [32,33,34]. This makes ZnO ideal to investigate doping dependent effects on the surface or at the interface to organic molecules. Detailed descriptions of bulk and surface properties of ZnO are summarized in the literature [35,36]

1.2.1 Surfaces of ZnO

In this work we will focus on the most common low index surfaces of ZnO: The polar Zn-terminated (0001) and O-terminated (000$\bar{1}$) surfaces and the non-polar mixed-terminated (10$\bar{1}$0) surface. When a wurtzite ZnO crystal is cut perpendicular to the [0001]-axis, the two fundamentally different polar surfaces are formed. The polar surfaces exhibit a hexagonal surface structure that is, for the (0001)-surface exclusively terminated by zinc atoms, and for the (000$\bar{1}$)-surface by oxygen atoms (see Fig. 1.5(a)-(b)). Although these surfaces are used in many interface studies, the exact structure of the polar surfaces is still under debate and not fully understood. The reason is linked to the fact that the bare polar surfaces described above are electrostatically unstable (Tasker type 3 surfaces) and must therefore adopt a modified or reconstructed surface structure. Many stabilizing mechanisms for the polar surfaces have been proposed and compared in the literature [37,38,39,40,41]. For the polar surfaces a ZnO slab is build up from alternating charged planes that produces a dipole moment perpendicular to the surface. A stable surface must in principle fulfill the condition that the net surface dipole perpendicular to the surface vanishes. This is equivalent to saturating all dangling bonds at the surface. From electrostatic considerations (electron-counting model) we can conclude that removing a quarter of the surface species compensates the problematic dipole, resulting in an electrostatically stable surface structure. However, this can be achieved by many other possible surface modifications or reconstructions as well. Alternatively the dangling bonds at the surface can also be saturated by surface adsorbates. The many possible mechanisms lead to a rich surface phase diagram for both polar surfaces. The actual observed surface morphology often primarily depend on the preparation conditions. An alternative stabilization mechanism of the polar ZnO(000$\bar{1}$) surface through bulk dopants is studied in Chapter 3. A novel method to probe the surface structure of the ZnO(0001) surface with molecular adsorbates in presented in Chapter 4.

The non-polar ZnO(10$\bar{1}$0) surface has a rectangular surface unit cell and both species appear at the surface (see Fig. 1.5(c)), thus, it is also known as mixed-terminated ZnO surface. This
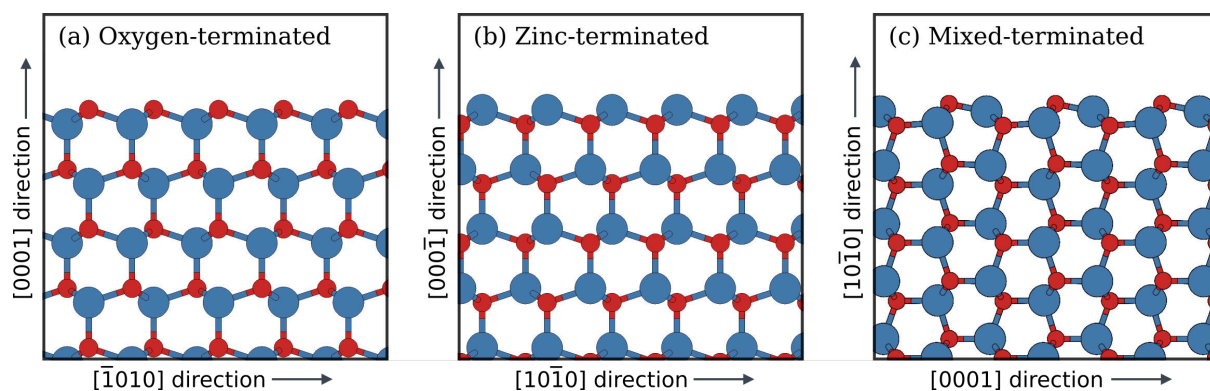
FIGURE 1.5: The three in this work studied surfaces of ZnO: (a) The Oxygen- and (b) Zinc-terminated surface are polar surfaces of ZnO. (c) Mixed-terminated ZnO($10\bar{1}0$) belongs to one of the non-polar surfaces.

surface is electrostatically stable and also energetically the most favorable surface of ZnO[42]. Therefore this surface is dominantly found in real ZnO nanostructures. Due to its electrostatic stability and the fact that the surface structure does not need to undergo any reconstructions, this surface is well accessible also from a theoretical point of view. We use this surface in Chapter 6 to study the charge transfer mechanism to a monolayer of F4TCNQ molecules and in Chapter 7 to investigate infrared vibrational spectra of adsorbed F6TCNNQ molecules.

Chapter 2

Electronic Structure Calculations

The theoretical results in this thesis are based on electronic structure calculations from density functional theory (DFT). In this chapter I give a short overview of this theory and discuss relevant aspects and applications. The basics of DFT are well known and many publications and books are available explaining DFT and providing a rigorous derivation of the theory. Therefore I refer the interested reader to standard textbooks of quantum and solid state physics or books especially on DFT (A small selection based on my own preferences is given here)[43,44,45,46,47,48,49]. After a condensed overview I want to lead the reader to the relevant aspects of applying DFT on hybrid inorganic/organic interfaces. This mainly includes the applied exchange-correlation energy functionals and their drawbacks and limitations due to their approximative nature. Finally, I introduce the reader to the FHI-aims program package. This is the code mainly used in this work to perform DFT calculations and for which I developed and implemented some features during my dissertation. The relevant aspects for this thesis are explained in more detail and include how to generate the a starting guess for the ground-state electron density, how to use DFT calculations to predict thermodynamic phase diagrams, and how to calculate surface vibrations of molecules and surface core-level shifts using DFT.

2.1   The many-body problem

The starting point of all our efforts to understand molecules, solids and their interfaces is the quantum-mechanical many-body problem. For a system of electrons and nuclei the non-relativistic time-independent Schödinger equation reads:

$$\hat{H} \left| \Psi \right\rangle = E \left| \Psi \right\rangle \tag{2.1}$$

This eigenvalue equation describes the quantum nature of matter, with $\hat{H}$ the Hamiltonian of the system. The full Hamiltonian of a condensed matter system is given, in atomic units, by

$$\hat{H} = -\frac{1}{2}\sum_i \nabla_i^2 - \sum_\alpha \frac{1}{2M_\alpha}\nabla_\alpha^2 - \sum_{\alpha,i}\frac{Z_\alpha}{|\mathbf{r}_i - \mathbf{R}_\alpha|} + \frac{1}{2}\sum_{i,i'}\frac{1}{|\mathbf{r}_i - \mathbf{r}_{i'}|} + \frac{1}{2}\sum_{\alpha,\alpha'}\frac{Z_\alpha Z_{\alpha'}}{|\mathbf{R}_\alpha - \mathbf{R}_{\alpha'}|}$$

where $\mathbf{r}_i$ and $\mathbf{R}_\alpha$ denote the position of electron i and atomic nuclei α with atomic number Z_α and nuclear mass M_α. The first two terms describe the kinetic energy of the electrons and the nuclei, respectively. The third term describes the interaction of the electrons with the nuclei, the fourth term the electron-electron interaction and the last term the interaction between the nuclei.

Writing down the equation is straight-forward, solving this equation on the other hand is another story entirely. The many-body nature of the problem makes finding the exact solution, except in the simplest cases, impossible in practice and calls for approximations. The first approximation that is usually applied is the Born-Oppenheimer approximation. It decouples the electronic degrees of freedom from the nuclear part. However, the Coulomb term which describes the interaction between the electrons and correlates every electron with all others, in general leads to an unfeasible complex many-electron problem. An approach that makes this complex problem tractable is density functional theory. Still, for solving the resulting equation further substantial approximations are required.

2.2 Density functional theory

Due to its good balance between accuracy and numerical efficiency, density-functional theory (DFT) is nowadays the standard method for electronic structure calculations in condensed matter physics. Instead of the coordinates of all electrons of a system, it uses the electron density $\mathbf{n}(\mathbf{r})$ as the central quantity and provides an in principle exact framework to solve the quantum-mechanical many-body problem.

The theorems by Hohenberg and Kohn[50] laid the basis for this theory that reduces the many-body problem to a tractable self-consistent form. Together with the Kohn-Sham (KS) scheme[51] they form the basic framework of density functional theory (DFT). The Hohenberg-Kohn theorems state that the electron density, which only depends on the three spatial coordinates, may be used as the basic variable uniquely characterizing an interacting electron system and all ground state properties of this system can be described by minimizing the total energy as a functional of the ground state electron density. Therefore these theorems provide the basics for calculating ground state properties of an interacting electron system, which can be realized in the framework of the Kohn-Sham approach. The key idea of the Kohn-Sham approach is to replace the interacting many-body system with a simpler auxiliary system of non-interacting quasiparticles that has the same ground-state density as the true interacting system.

To obtain the ground-state electron density we now need to solve the independent single-particle Schrödinger-like equations known as Kohn-Sham equations:

$$\left[-\frac{\hbar^2}{2m}\nabla^2 + v^{KS}[\mathbf{n}(\mathbf{r})] \right] \psi_{\mathbf{k}\nu}(\mathbf{r}) = \varepsilon_{\mathbf{k}\nu}\psi_{\mathbf{k}\nu}(\mathbf{r}) \tag{2.2}$$

where $\psi_{\mathbf{k}\nu}(\mathbf{r})$ are the Kohn-Sham eigenfunctions of the one-particle system, $\varepsilon_{\mathbf{k}\nu}(\mathbf{r})$ are the Kohn-Sham eigenstates and $v^{KS}[n(\mathbf{r})]$ is the Kohn-Sham potential. It is the single-particle potential that will lead to the same density $n(\mathbf{r})$ as the original interacting problem. The electron density itself is obtained from the sum of the KS-eigenfunctions

$$n(\mathbf{r}) = \sum_{\varepsilon_{\mathbf{k}\nu} \leq \varepsilon_F} |\psi_{\mathbf{k}\nu}(\mathbf{r})|^2. \tag{2.3}$$

The KS-potential depends on the density and can be written as

$$v^{KS}[n(\mathbf{r})] = v^{ext}(\mathbf{r}) + v^{hartree}(\mathbf{r}) + v^{xc}[n(\mathbf{r})]. \tag{2.4}$$

Here v^{ext} is the external potential that accounts for the interaction of the electrons with the the nuclei. The Hartree potential $v^{hartree}$ is the electrostatic mean-field potential that is induced by all electrons. It describes the classical Coulomb interaction with the charge distribution $n(\mathbf{r})$. Finally v^{xc} is the so called exchange-correlation potential in to which all difficulties of the interacting many-electron problem are transferred and which is not explicitly known. It also accounts for the difference in the kinetic energy between the fully interacting system and the non-interacting Kohn-Sham scheme. It is a truly quantum-mechanical term comprised of the non-classical exchange and correlation contributions.

The complicated many-body problem is hence simplified to a set of non-interacting one-particle problems. However, since the effective KS-potential itself depends on the density $n(\mathbf{r})$ the set of Kohn-Sham equations have to be solved self-consistently. It is important to note that up to this point no further approximations were made and if v^{xc} would be known explicitly this mapping would be exact. However, the actual form of v_{xc} or rather of the exchange-correlation energy functional E_{xc} is not known. Thus we must introduce approximate functionals based upon the electron density to describe this term. In practice, the quality of the results from a DFT calculation decisively depend on the approximations to the exchange-correlation functional.

Well known approximate functionals such as the local spin density approximation (LSDA)[51,52] or the PBE generalized gradient approximation[53] often yield reasonable accuracy for binding energies and structures[54,55]. However, over time many deficiencies of these established approximations were uncovered. Not only limitations in quantitative accuracy like the underestimation of bandgaps[56,57] or problems with electron affinities[58,59,60], but also qualitative deficiencies like erroneous charge delocalization[61,62] and problems with the dissociation behavior of radical ions and neutral molecules[63,64] became evident. Developing new and reliable density functional approximations to overcome this deficiencies became therefore an ongoing and very active field

of research. Some of these were adopted to specific systems, others are based on quantum mechanical principles with the aim of a generally improved functional. Depending on the case, such modern functionals can be better suited to successfully describe physical ground-state properties that are not well described by simpler approximations. And with increasing computational power more and more advanced approximations became applicable to also to larger systems.

A variety of deficiencies in Kohn-Sham-DFT (KS-DFT) with approximate density functionals can be traced back to a common conceptual problem: electronic self-interaction (SI). It is a result of the imperfect cancellation of the self-interaction contribution in the Hartree term, which describes the interaction of each electron with the entire electron density (including its own density), with the exchange part of the density functional. In KS-DFT the exchange part of the exchange-correlation functional should cancel this self-interaction, but since the exact amount of the self-interaction contribution can not be calculated analytically and is, therefore, not known, this cancellation is in general not perfect. The resulting self-interaction error (SIE) and the connected consequences for practical DFT calculations of hybrid inorganic/organic interfaces are discussed in more detail in the following sections.

2.3   Approximate exchange-correlation functionals

As we have seen in the last section, by transforming the many-body problem into an the effective non-interacting system we have obtained a well-defined set of equations (the KS equations), however, without knowing about the exact form of the exchange-correlation energy functional.

An approximation to $E_{xc}[n(\mathbf{r})]$ can be written in terms of the total electron density $n(\mathbf{r})$ and the exchange-correlation energy density per electron $\varepsilon_{xc}^{approx}$ as

$$E_{xc}[n(\mathbf{r})] = \int d^3r \; n(\mathbf{r}) \; \varepsilon_{xc}^{approx} \left(n(\mathbf{r}), \nabla.n(\mathbf{r}), \tau(\mathbf{r}), \dots \right) \tag{2.5}$$

By adding more and more local ingredients at $\mathbf{r}$ to the exchange-correlation energy density, additional exact constraints can be satisfied. Figuratively this can be seen as stepping up a ladder of approximations to construct $\varepsilon_{xc}^{approx}$. The rungs are defined by the number and kind of the added ingredients. Higher rungs become increasingly more complex, in general at the cost of increasing computational effort, especially at higher rungs.

Rung 1: Local (spin) density approximation (L(S)DA): Uses only the electron density $n(\mathbf{r})$ as ingredient.

Rung 2: Generalized gradient approximations (GGA): Includes also the density gradient $\nabla n(\mathbf{r})$ as additional local ingredient. Famous representative at this rung is the Perdew-Burke-Ernzerhof (PBE) functional[53].

Rung 3: <u>Meta-GGA</u>: Additionally includes a dependence on the orbital kinetic energy density $\tau(\mathbf{r})$, i.e. on the laplacian of the orbitals.

Rung 4: <u>Hybrids</u>: Requires the fully non-local ingredient of exact exchange. Usually in the form of the Hartree Fock (HF) exact exchange energy or its density.

Rung 5: <u>Double hybrids</u>: Adds a certain amount of HF exchange and second-order perturbation theory (PT2) correlation (thus double hybrid). That means that unoccupied KS orbitals are included in the calculation.

Although the density functional approximations can be ordered in this ladder, from rather simple to more sophisticated approximations, this ordering should not be mistaken in a way that a functional on a higher rung automatically gives better or more accurate results. In practice there is no systematic way to reliably improve DFT calculations by improving the density functional approximation (In contrast to wavefunction based methods where HF < second-order Møller-Plesset perturbation theory (MP2) < coupled-cluster with single and double excitations (CCSD) ...). In DFT calculations it depends on various factors, which functional fits best to a problem. Not only the system itself, but also what qualitative or quantitative informations one desires to obtain are relevant for deciding what functional to use. In the end it often comes to an trade off between computational costs and accuracy, while keeping the accuracy as high as the question one tries to answer demands. The right choice of the density functional is, therefore, a nontrivial task and often we rely on experience in this matter.

In the following only the exchange-correlation functionals used for obtaining the results in this work are presented in more detail. The interested reader is referred to the literature for information about other functionals and rungs[65,66]

2.3.1 Local and semilocal functionals

The first three rungs of the functional ladder are referred to as local and semilocal approximations. They are very popular approximations, especially the Perdew-Burke-Ernzerhof (PBE)[53] version of the generalized gradient approximation (GGA) is one of the most widely applied density functionals in condensed matter physics[67]. Also in this work the PBE functional was frequently used.

LDA as the least sophisticated representative of semilocal functionals is based on the model of the uniform electron gas. It solely depends on the electron density and works reasonable well for some simple solids with a homogeneous electron density e.g. metals with delocalized electrons. It typically suffers from overbinding, resulting in too small values of equilibrium unit cell volumes for solids. For molecular systems with localized states, LDA is not a suitable approximations and suffers from strong overbinding. It is therefore not commonly used in chemistry.

GGA functionals additionally contain the derivative of the density $\nabla n(\mathbf{r})$ and are thus better in describing inhomogeneities in the electron density. For most systems GGAs are more accurate than LDA, but there is no single universal form of GGA and functionals from this rung depend on a set of adjustable parameters. These functionals can be constructed non-empirically to satisfy different sets of exact constraints. The PBE functional preserves the accurate linear response of a uniform density that is also satisfied in LDA and additionally recovers the second order gradient expansion for correlation. The deficiencies of PBE are discussed in a separate section as they become relevant for this work. Over time several other variants of the PBE functional have been developed, playing with the adjustable parameters. Some are physically motivated like the PBEsol functional[68] that restores the second-order gradient expansion for exchange instead of correlation and claims to improve equilibrium properties of densely-packed solids and their surfaces. Others are semi-empirical with the aim to match a set of data points as good as possible. A semi-empirical offspring of PBE is the revPBE functional[69] that is constructed to fit to the exchange energy of atoms.

2.3.2   Hybrid functionals

In this work two different hybrid functional families are applied and therefore the discussion is focused on these two: The PBEh family[70] and the HSE[71,72] family of hybrid density functionals.

Hybrid functionals are constructed by admixing a portion of exact non-local exchange from Hartree-Fock (HF) theory usually into a GGA semilocal functional. Global hybrids like the PBEh functional family depend on only one parameter, the amount of mixed-in HF exchange. The mixing scheme for all global functionals is equivalent[73], therefore we exemplarily write it down for the PBEh functional:

$$E_{xc}^{\mathrm{PBEh}} = \alpha E_x^{\mathrm{HF}} + (1-\alpha)E_x^{\mathrm{PBE}} + E_c^{\mathrm{PBE}} \tag{2.6}$$

The mixing parameter $\alpha \in [0,1]$ defines the amount of HF exact exchange in the hybrid functional. The PBEh functional is based on the original PBE functional, which is restored for $\alpha = 0$. Another member of the the PBEh family it the popular PBE0 functional[74]. In PBE0 the amount of exact exchange is motivated by theoretical arguments and set to $\alpha = 0.25$ (Theoretical arguments suggest that $\alpha = 0.25$ should be optimal for predicting atomization energies with GGA hybrids). Often hybrids are used in a more empirical way and α is set such that a certain property is reproduced or a certain qualitative physical behavior is assured. The optimal value of α in this cases can differ significantly depending on the system and the property we wish to compute. As we will see later in this work, α can be tuned to minimize the many-electron self-interaction error for hybrid inorganic/organic systems.

Beside global hybrid functionals, where the mixing parameter α is a constant, in local hybrids the mixing parameter depends on the position in space[75]. The exchange energy densities are mixed

at each point in space and the resulting density functional is therefore space dependent. Local hybrids are not very common, because they are complex and computationally more expensive than global hybrids.

In recent years more and more attraction was generated by another promising class of hybrid functionals: Range-separated hybrids. As the name suggests in these functionals the exchange component is separated into a short-range (SR) and a long-range (LR) part with each part being treated differently. That means range-separated hybrids depend on at least one more parameter, namely the range-separation parameter ω. The aim of so called long-range corrected hybrid functionals is to correctly describe the asymptotic behavior of the exchange-correlation potential. The long-range asymptotic behavior of the exact xc-potential should fulfill[76,77]

$$\lim_{r \to \infty} v^{xc}(\mathbf{r}) \sim -\frac{1}{r}. \tag{2.7}$$

Instead of the correct $-\frac{1}{r}$ decay, in global hybrids the exchange part of the potential decays as $-\frac{\alpha}{r}$, i.e. proportional to the fraction of exact exchange. With the right treatment for the SR part, the erroneous potential decay in global hybrids can be lifted. The LC-ωPBE functional[78] therefore handles SR exchange interaction with PBE and the LR interaction with HF theory. In the course of my dissertation I tested this functional for one of our systems, but found it to be impractical because of missing analytical forces in the implementation of this functional family in FHI-aims at the time. Without forces DFT geometry optimizations are not possible, which are an important part for a consistent DFT study.

Besides the LC scheme, also short-range screened hybrids are available. In these functionals the HF exchange is included only in the short-range part of the electron-electron interaction. By only evaluating the non-local HF exchange in the short-range part the computational costs can be significantly reduced compared to global hybrids. In this work the screened Heyd-Scuseria-Ernzerhof (HSE) hybrid functional[71,72] was applied. HSE is also an offspring of the PBE functional but with a inverted treatment of the SR and the LR part compared to LC-ωPBE. The SR exchange interaction is described with the PBEh functional, where a certain amount α of HF exchange is mixed with $(1 - \alpha)$ PBE exchange. In the LR part only PBE exchange is considered. For $\omega = 0$ the PBEh functional family is reproduced, while for $\omega \to \infty$ one obtains the non-hybrid PBE functional. With the standard values of $\alpha = 0.25$ and $\omega = 0.2$ Å^{-1} the functional is referred to as HSE06. In this work the functional was used in an empirical way by tuning the parameters α and ω until the experimental value of the ZnO band-gap is reproduced. We found that several parameter combinations satisfied our requirement, making the solution non-unique. We decided to set the screening to the standard value to $\omega = 0.2$ Å^{-1} which is known to work well for solids[79] and only tune the α-parameter until our condition is fulfilled.

2.4   Self-interaction error and limitations of DFT

The self-interaction error (SIE) also known as delocalization problem is one of the most dominant errors in density functional approximations. As its name suggests, SI is the spurious and unphysical interaction of an electron with itself. For a single-particle system the SI is clearly defined and correction schemes can entirely compensate for this one-electron SIE. For a system with more than one electron, it is less obvious how to quantify the SIE. Over time several methods has been proposed to compensate for the many-electron SIE (MSIE).[80,81,82,83,84,85,86,87,88]. In this work I will show how the right choice of hybrid functionals can be used to reduce the MSIE to avoid the resulting charge delocalization problem.

2.4.1   One-electron self-interaction error

In KS-DFT the Hartree energy, which describes Coulomb interactions, does not vanish for a one-electron system. The reason is that the Hartree energy is a functional of the entire electron density and therefore it includes the interaction of each electron with the entire electron density. Even for a one-electron system the electron interacts with its own density and the Hartree term is non zero. KS-DFT simply does not distinguish between real two-body Coulomb interaction and self-interaction. In exact DFT the exchange-correlation energy term directly cancels the Hartree energy of the one-electron system. However, this cancellation generally does not hold true for most approximate functionals[80], which results in the one-electron self-interaction error. As a consequence local and semilocal functionals are often more accurate for many-electron systems than for systems with just one or a few electrons. A notorious example for the manifestation of the one-electron SIE is the dissociation behavior of the H_2^+ ion. Local functionals predict the energy of two infinitely separated fractionally occupied $H^{0.5+}$ ions to be lower than the energy of a separated H^+ ion and a neutral H molecule. This is obviously unphysical because fractional occupation is not possible in gas-phase molecules where orbitals are either occupied or empty. One could also say, that (semi)local functionals tend to over-delocalize the charge, therefore, the SIE is also known as delocalization error in (semi)local functionals.

Hartree-Fock theory does not suffer from one-electron SI, because all Coulomb self-interaction terms are exactly cancelled by the corresponding exchange self-interaction terms. That means HF is by construction one-electron SIE free, however, this does not mean it is free from many-electron SIE[89]. Still by admixing HF exact exchange into semilocal functionals (hybids) the one-electron SIE can be reduced and with additionally considering the many-electron SIE the deficiencies caused by SI can even be lifted[90,91].

2.4.2 Many-electron self-interaction error and its impact on charge localization

For a system containing only one electron the self-interaction can be explicitly defined. But the problem manifests itself in many-electron systems as well. Unfortunately it is less obvious how to quantify the SIE of a particular functional in a many-electron system. There is no unique and general definition of the SIE and no unique way to correct it.

While the concept of self-interaction in a one-electron system is easily understood from a physical point of view, it is not straight forward to grasp the concept the self-interaction in a many-electron systems from a pure mathematical explanation. Therefore we choose a different approach to define the SIE in a many-electron system: We use a more general concept in the form of the straight-line energy condition to explain the many-electron self-interaction error (MSIE). In this approach it is necessary to consider fractionally occupied systems, which are not necessarily physical (except when interpreted as an ensemble averaged occupation), but it allows to study the impact of the MSIE on different functionals in more detail and it allows us to use this conditions for designing MSIE-free functionals. The underlying principle of the straight-line energy condition it the postulate that the exact ground state energy of a system as a function of fractional occupation is a piece-wise linear function[92]. Between adjacent integer electron numbers the function is linear with the slope changing at integer occupations. We can now define a density functional to be free from MSIE, if the total energy is piecewise linear as a function of electron number.

Semilocal functionals like PBE give too low energies for fractionally occupied systems, resulting in a convex energy curve. On the other hand HF theory overestimates the total energy of a system at fractional occupation giving a concave energy curve[93,56,94]. The consequences of the deviation of straight line behavior for PBE and HF can be better understood from looking at the energy of the orbital, in which the occupation is increased. Janak's theorem sets a relation between the total energy derivative with respect to the occupation of a Kohn-Sham (KS) orbital and the energy of this orbital:

$$\frac{\partial E^{total}}{\partial n_i} = \varepsilon_i. \tag{2.8}$$

For a perfect straight-line behavior of the total energy between integer occupation, the orbital energy is constant. As the slope of the total energy changes abruptly at integer occupation, the orbital energy jumps to another constant value as a new orbital has started to get occupied.

For PBE the orbital energy increases with fractional occupation of the orbital. Considering a system with two degenerate orbitals e.g. from two separated molecules in a dissociation process, it would now be more favorably to split the charge between the two orbitals. This is in contrast to HF, for which the orbital energy decreases when increasing the respective occupation. For a two molecule system the negative slope of ε_i implicates an energetically favorably situation when putting the additional charge into only one of the originally degenerate orbitals. In this case integer occupations are favored, meaning that HF shows a tendency to overly localize
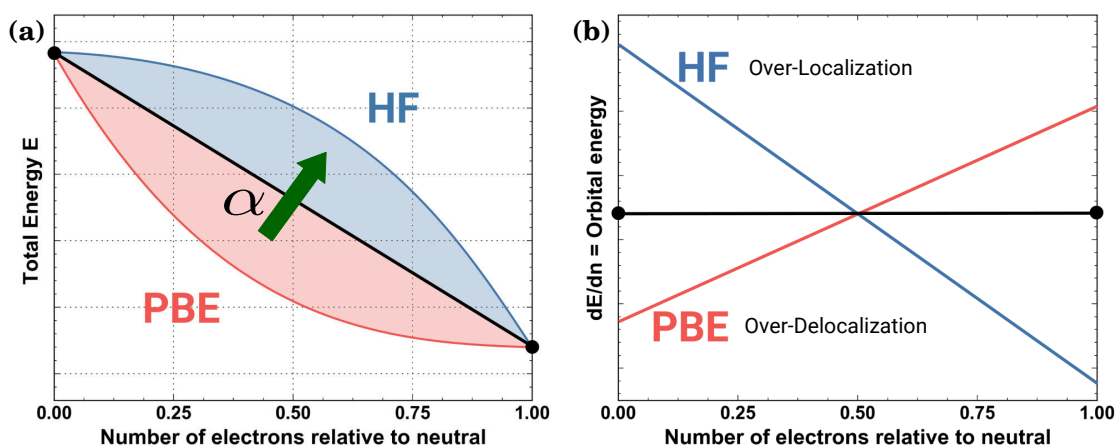
FIGURE 2.1: **(a)** Exemplary representation of the total energy evolution of a system as a function of electron number between integer occupation (e.g. neutral and singly negativity charged system). For the PBE functional and HF theory clearly the non-linear behavior can be observed. **(b)** Graph of the orbital energy dependency on the fractional occupation number for the exact density functional (black) and for PBE as well as for HF.

the charge density. It in known that also for other properties standard DFT and HF show opposing behavior as a result of the MSIE and the delocalization problem[95]. PBE in general underestimates the ionization potential (IP) whereas it is overestimated in HF. Band-gaps are therefore also affected by the MSIE. For semilocal functionals the MSIE has a stronger influence on the occupied states by over-delocalizing them and forces them up in energy. This reduced the band-gap. For HF the unoccupied states are "over-delocalized" which forces them up in energy resulting in an increased band-gap.

The fact of opposing trends for semilocal functionals and HF can be used to construct a functional that is free from MSIE in terms of fulfilling the straight line condition by mixing the two. As we already learned, this is exactly what is done in hybrid functionals and the reason why they often work better than standard semilocal density functionals. On the example of a global hybrid, one can tune the mixing parameter α until the straight line behavior is restored i.e. the orbital energy is a constant between integer occupation. Especially for theoretically describing charge transfer processes, that is one of the main foci in this work, it is important to at least know about the localization tendency of the used functional. This forms the basis to correctly assess and interpret the obtained DFT results.

We note that also several other methods has been proposed to compensate many-electron SIE to restore the straight-line condition[82,83,84,85,86,87,88]. Among these, the localized orbital scaling correction framework is a promising approach, which in addition to the density and the density gradients considered in semilocal functionals also include other information such as localized orbitals or the local occupation matrix to construct the density functional[96]. Other alternative is using range-separated hybrid functionals[97]. However the majority of these methods depend on more than only one parameter, complicating the situations without per se being better suited for semiconductor/organic interface system.

Hybrid functionals can also be optimized such that in a DFT calculation the experimental band-gap of a material is reproduced. In this context the hybrid functions behave similar to the DFT+U approach[98]. By introducing an effective on-site Hubbard U parameter in this formalism, the energy of the affected occupied orbitals are shifted down in energy by $U/2$ and the unoccupied orbitals are shifted up in energy by the same amount. This is also what is seen in hybrid functionals[99,100].

At this point it is worth noting that the KS-eigenfunctions and KS-eigenvalues ε_i are in principle quantities of the non-interacting auxiliary system which only has the same ground-state density as the original interacting system. Therefore they should not have any physical meaning. Nevertheless, the KS-eigenvalues are in general legitimately interpreted as the orbital energies of the system.

2.5 Calculations with the FHI-aims program package

In this section some aspects of the program package that was used in this work to perform DFT calculations are discussed. The main tool that was used is the all-electron code FHI-aims[101], which is a modern code that was developed at the Fritz Haber Institute in Berlin. All-electron code means that all electrons are treated explicitly and the full potential is considered. This has the advantage that the full spectrum of energy levels is calculated including core and valence electrons. One of the big advantages of FHI-aims is that it is not restricted to open or periodic boundary conditions. Periodic and non-periodic systems can be calculated on equal footing. In this work gas phase calculations of individual molecules as well as periodic bulk and surface-slab calculations were performed. By handling all individual parts of a system with the same code, a consistent picture of the system of interest is obtained. This was an important aspect for using FHI-aims in this work.

For constructing the KS-eigenfunctions, FHI-aims uses a basis set of numeric atom-centered orbitals (NAO). The advantage of NAOs is their flexibility as their radial shape is numerically tabulated and can be optimized for every element. Furthermore NAOs can be constructed such that they are spatially quite confined by cutting of the radial functions for larger distances, i.e. they are then strictly zero beyond a certain radius. This advantage is specially relevant for large systems by increasing the sparsity of the overlap matrix and the Hamiltonian matrix. For the calculation of surfaces and interfaces using the repeated slab approach it has furthermore the handy side effect that including vacuum basically comes at no or comparatively little computational cost.

For the basis set a pool of optimized basis functions are provided for all elements. They are systematically ordered in a way that the basis set, and corresponding the accuracy of the calculation, can be gradually increased, of course at increasing computational cost. For an user-friendly experience the basis functions are bundled together in "light", "tight" and "really tight"

standard settings. This standard settings also include choices for the numerical integration grids. Default "tight"-settings for basis and integration grids were mainly used in this work and usually give a very good accuracy. All settings can also be modified by hand and, of course, these settings need to be tested carefully until the desired properties are well converged. Specially for the very large systems that are studied in this work, the settings were extensively optimized for a well-balanced ratio between accuracy and computational cost.

2.6   *Ab initio* thermodynamics for surfaces

DFT is a flexible tool to accurately describe many microscopic properties of quantummechanical systems. By combing DFT with concepts from thermodynamics and statistical mechanics the microscopic information obtained from DFT can be extended to larger scales and realistic environmental conditions[102,103,104,105]. This approach is called *ab initio* thermodynamics because it employs the information of a first-principles DFT calculation to evaluate a thermodynamic potential function, the Gibbs free energy. A KS-DFT calculation gives only the ground state of the system and the obtained properties are only valid for the temperature being at absolute zero ($T = 0$ K) and for zero pressure ($p = 0$ mbar). The Gibbs free energy allows to evaluate macroscopic system properties like the equilibrium surface structure and composition of a system in contact with an environment at any temperature and pressure. In this work we applied *ab initio* thermodynamics to determine the doping dependent surface phase stability of the $ZnO(000\bar{1})$ surface in contact with a hydrogen reservoir. Different phases for this surface lie in a very narrow energy range. With *ab initio* thermodynamics it was possible to access their relative stability. More information on *ab initio* thermodynamics and how to apply it to obtain surface phase diagrams is summarized in the supporting information of **paper I** (see section 3.3).

2.7   Calculating surface vibrations

Vibrations modes and their infrared (IR) activity is strongly influenced by the charge state of a molecule. Experimentally, bands in IR reflection/absorption spectra might shift upon charging of a molecule. This fact can be used to evaluate the charge state of a molecule adsorbed on a surface. The challenge in this matter is to distinguish between the effects of charging the molecule and the effects arising from the molecule binding to the surface. The aim of my contribution in **paper II** is to theoretically predict or verify such shifts from electronic structure calculations. There are two possibilities to calculate vibrational modes from DFT: Applying an analytical algorithm on the wavefunctions, or with a numerical method via displacements of the nuclei positions in all three cartesian coordinates.

In equilibrium the nuclei of a molecule sit in minima of the effective potential created by the electronic wave functions. The shape of the potential around the minima determines the vibrational modes of the atom. We can perform a Taylor expansion of the potential around the minimum of the potential energy surface. The first order term has to be zero for a minimum. Only terms from the second order and higher are non-zero. In the harmonic approximation only the second order term is considered to model the shape of the potential, higher order terms are omitted. For the second-order term the second geometric derivatives of the energy i.e. the force constant matrix (Hessian matrix), have to be calculated either analytically or numerically. In the following we discuss the evaluation of vibrational modes and IR intensities with the numerical approach. So far a direct analytical evaluation of vibrational modes is not implemented in FHI-aims for most functionals. For the numerical evaluation an external python script was written, capable of treating open as well as periodic boundary conditions. It allows to calculate the vibrational modes from the $6 \times (number\ of\ atoms)$ calculations with displaced nuclei (in all three spatial directions x, y and z in both ways, positive and negative, resulting in 6 displacements per atom). The Hessian matrix $\mathbf{H}$ is evaluated from the forces $\mathbf{F}$ of this calculations using finite differences:

$$\mathbf{H} = \frac{\partial^2 E^{total}}{\partial x_i \partial y_j} = \frac{\mathbf{F}_i(x_j + \delta) - \mathbf{F}_i(x_j - \delta)}{2\delta} \tag{2.9}$$

with δ being the Cartesian displacement from the equilibrium position. In principle in this approach the displacements should be infinitesimally small, however we need to consider the accuracy of our DFT calculations and choose a displacement that is sufficiently large to produce a difference between the displaced systems. The obtained Hessian is then transformed to mass-weighted coordinates to get the mass-weighted Hessian matrix $\mathbf{H}'$. With the ansatz of a harmonic oscillator we can write down the equation of motion in the form of an eigenvalue problem for the system of oscillating atoms:

$$\omega^2 \mathbf{x} = \mathbf{H}' \mathbf{x} \tag{2.10}$$

The eigenvalues are the squares of the normal mode vibrational frequencies ω. The eigenvectors $\mathbf{x}$ define the amplitudes of the normal modes. At a certain normal mode, all atoms move with the same frequency ω, but with different amplitudes. IR intensities of normal modes are determined from the change in the dipole moment for the respective mode.

The calculation of vibrational spectra from DFT are connected to several uncertainties. First the limitations of the DFT calculations itself due to the applied xc-functional leads to a deviation of calculated normal mode frequencies compared to experimental results. Contrary to a widely held belief, the results from a numerical vibrational analysis, based on the displacement of atoms, show similar accuracy compared to analytic methods in most cases[106]. Still, further uncertainties arise from the harmonic approximation and the numerical evaluation of the Hessian. Anharmonicity usually accounts for $2 - 3\%$ difference from experimental frequencies[106,107]. Often multiplicative scaling factors are applied to correct for this shortcomings to

be able to better predict fundamental frequencies from experiments[108,109].

It is worth noting that frequency calculations have to be executed at the same level of theory as the associated geometry optimization. If the original atom positions are not in the minimum of the potential energy surface the here presented approach to calculate the normal modes is no longer valid and the results are worthless. The calculation of surface vibrations may also not only be interesting for vibrational spectroscopy, but also for determining the relative stability of surface morphologies or molecular layers. In *ab initio* thermodynamics the typically small vibrational contribution to the Gibbs free energy is often omitted, however, it can determine the stability of surface reconstructions or morphologies that are close in energy.

2.8 Calculating surface core-level shifts

Core-level spectroscopy can be used as a probe of the local chemical environment because the core levels are very sensitive to the local electronic structure. Here we shortly discuss DFT methods to determine the relative core level shifts as they are measured by x-ray photoelectron spectroscopy (XPS). XPS essentially measures core level electron binding energies E_{B}. The binding energy E_{B} of an electron in a core level is determined from the photon energy $h\nu$ the kinetic energy of the emitted electron E_{kin} and the work function Φ. The kinetic energy depends on the orbital of the emitted electron (see Fig. 2.2).
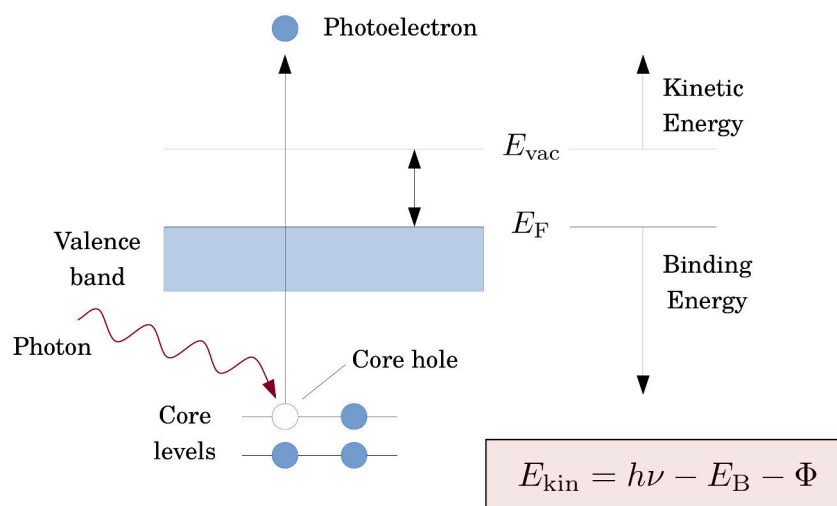
FIGURE 2.2: Basic scheme of the XPS physics (photoelectric effect): A photon with energy $h\nu$ is absorbed by an core electron. The energy gain results in a transition above the vacuum barrier. The kinetic energy of the photoelectron is measured in XPS.

Relative core level shifts can be reasonably accurately predicted from *ab initio* methods. Here we present two approaches to calculate the core level shifts from DFT calculations: The initial state approximations (IS) and the transition-potential approximation (TP, also known as half core hole approximation). The binding energy of a core electron can be calculated from the

total energy difference of the neutral system of interest (E_N) and the ionized system (E_{N-1}), with an electron missing in the selected core level.

$$E_{\mathrm{B}} = E_N - E_{N-1} \tag{2.11}$$

The surface core level shift Δ_{SCLS} is the difference in binding energies between a core electron associated with a atom in the bulk of the tested system and a core electron from a surface atom. In other words its the relative shift of core levels with respect to main (bulk) peak. It can be calculated from:

$$\Delta_{\mathrm{SCLS}} = E_{\mathrm{B}}^{\mathrm{bulk}} - E_{\mathrm{B}}^{\mathrm{surf}} = \underbrace{(E_{N-1}^{\mathrm{surf}} - E_{N-1}^{\mathrm{bulk}})}_{\text{final state shift}} - \underbrace{(E_N^{\mathrm{surf}} - E_N^{\mathrm{bulk}})}_{\text{initial state shift}}. \tag{2.12}$$

The contributions can be associated with final state and initial state effects. Since the total energy of an ionized system in periodic DFT can not easily be evaluated, in practice the binding energies are usually determined directly from the KS eigenvalues of the core levels. Different approaches have been suggested. The simplest approach is to take the core level eigenvalue of the neutral system directly to determine the binding energies of different species. This approach is called initial state approximation[110] (IS), because it completely neglects final state effects. IS is based on the assumption that when one electron is removed from a core level, the wave functions of the other electrons are unchanged. Under this assumption, one can use Koopmans' theorem from HF[111] to show that the initial-state eigenvalue of the core state ε_c, equals the difference between initial and final total energies of the system:

$$E_{\mathrm{B}} = (E_{N-1}^{\mathrm{final}} - E_N^{\mathrm{initial}}) \approx -\varepsilon_c. \tag{2.13}$$

The surface core level shift Δ_{SCLS} is then the difference between the Kohn-Sham eigenvalues of the corresponding core state for an atom at the surface and in the bulk. All binding energies can be evaluated from a single DFT calculation of the .

A more advanced approach also considers the effect of the core hole for calculating binding energies. The second approach presented here, the transition potential approximation (TP), partly takes into account the possibly different screening of the core hole near the surface and in the bulk to evaluate the surface core level shift. Motivated by Janak's theorem[112], considering fractional occupation numbers n_c of the respective core orbital, we consider the orbital energy as the derivative of the total energy with respect to the occupation number (It should be mentioned that Janak's theorem actually only applies to the highest occupied electron state, the HOMO of a molecule. However, as an approximation the theorem has been used with success for core states as well.):

$$\frac{\partial E}{\partial n_c} = \varepsilon_c \qquad E_{\mathrm{B}} = E_{N-1} - E_N = \int_1^0 \varepsilon(n_c) dn_c \tag{2.14}$$

The binding energy of the respective core electron can then be calculated form the integral of the orbital energy between the occupied ($n_c = 1$) and unoccupied ($n_c = 0$) core state. Assuming

Initial state approximation   **Transition-potential approximation**

$$\Delta_{\mathrm{SCLS}}^{\mathrm{IS}} = -\left(\varepsilon_c^{\mathrm{surf}}(n_c) - \varepsilon_c^{\mathrm{bulk}}(n_c)\right)$$

$$\Delta_{\mathrm{SCLS}}^{\mathrm{TP}} = -\left(\varepsilon_c^{\mathrm{surf}}\left(n_c - \frac{1}{2}\right) - \varepsilon_c^{\mathrm{bulk}}\left(n_c - \frac{1}{2}\right)\right)$$
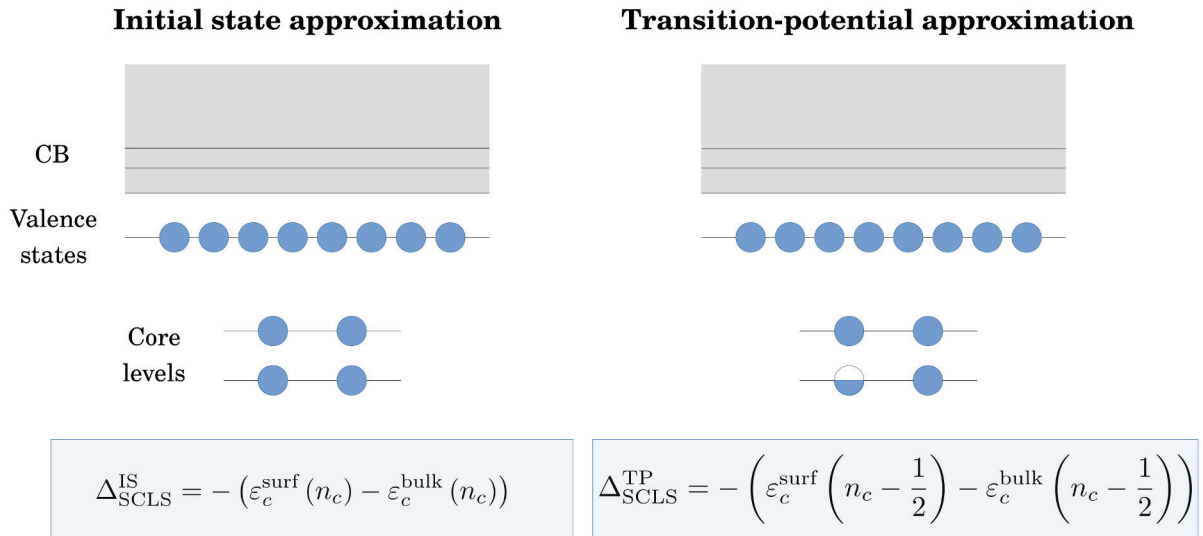
FIGURE 2.3: Overview of the two presented approach to determine core electron binding energies from DFT calculations and the corresponding equations to calculate the surface core level shift.

that the Kohn-Sham eigenvalue ε_i is a linear function of the occupation number the core-level binding energy can easily be calculated:

$$E_{\mathrm{B}} = \int_1^0 \varepsilon(n_c)dn_i = -\varepsilon_c(0) - \frac{1}{2}[\varepsilon_c(1) - \varepsilon_c(0)] \approx -\varepsilon_c(1/2) \tag{2.15}$$

This approach is also known from the Slater-Janak transition state approximation[113,114]. It has the advantage that the binding energy can be evaluated from a single DFT calculation. For obtaining the surface core level shift, calculations with a half-core hole have to be performed for the surface species and for a bulk atom[115,116]. Systems containing fractional occupation numbers, i.e. half-core holes, do not necessarily represent any physical system. Here we use it merely as a way to calculate the binding energies accounting the screening of the core hole by the other electrons by removing half an electron form the core state. A conceptual schematics of both presented methods to calculate surface core level shifts are depict in Fig. 2.3.

Part II

Results and Publications

Chapter 3

The Impact of Bulk Doping on the Phase Stability of the O-Terminated ZnO Surface

3.1 Motivation

Including the effects of bulk doping in *ab initio* simulations of semiconductor surfaces poses a difficult challenge, because the typically low concentration of dopants make an explicit treatment computationally intractable. Furthermore, if charge transfer occurs to the surface of semiconducting materials, the width of the resulting space-charge region often exceeds realistic supercell dimensions. These difficulties can be handled in a DFT calculations using the charge-reservoir electrostatic sheet technique (CREST). The original paper about CREST was presented by Ofer Sinai et al.[117]. The approach is based on including a charge sheet, mimicking the electrostatic field associated with the space charge region that typically leads to the effect of band bending. Along with the charge sheet, opposingly charged free charge carriers are introduced that represent the bulk charge carrier concentration, such that the system is overall neutral. The position of the charge sheet within the slab-cell and its charge density is determined self-consistently. The originally suggested formalism for this process is quite complicated and based on a fit of the potential inside the slab, which makes it not suitable for smaller slab thicknesses. The aim of the project was to develop a more user-friendly formalism of CREST that can be used in the following also for semiconductor/organic interfaces.

We developed such an extended CREST formalism and showed the capabilities of this new easier-to-use approach by calculating the - to our knowledge - first doping-dependent surface phase diagram of the O-terminated ZnO surface. The commonly proposed structure of this surface is the (2×1)-H reconstructed surface. Nikolaj Moll originally proposed that the H-concentration on this surface might be reduced due to available free charge carriers from dopands in the

29

bulk[118]. He showed that this is, in principle, the case for degenerately doped ZnO. However due to the missing approach to directly include long-ranged band bending into DFT calculations, it was not possible for him to quantify the H-reduction on the surface for reasonable doping concentrations. This was exactly what I then did during my dissertation using the extended CREST approach. The results were published in the following contribution.

3.2   Authors contribution

I contributed to all stages of the work. The original idea for the more user-friendly CREST formalism came from Oliver T. Hofmann. I deduced the necessary mathematical background and made the formalism accessibly by providing a python-wrapper program for CREST calculations in FHI-aims. All presented DFT calculations were performed by myself. The published manuscript was mainly written by me in close collaboration with my supervisor Oliver T. Hofmann and with the help of Patrick Rinke and Nikolaj Moll.

3.3   Publication including supporting information

New Journal of Physics

The open access journal at the forefront of physics

CrossMark

PAPER

Doping dependence of the surface phase stability of polar O-terminated (000$\bar{1}$) ZnO

Simon Erker[1], Patrick Rinke[2], Nikolaj Moll[3] and Oliver T Hofmann[1]

[1] Institute of Solid State Physics, Graz University of Technology, NAWI Graz, Austria
[2] COMP/Department of Applied Physics, Aalto University, Finland
[3] IBM Research—Zurich, Switzerland

E-mail: o.hofmann@tugraz.at

Abstract

The dependence of hydrogen coverage on the bulk doping concentration is investigated for the polar O-terminated (000$\bar{1}$) ZnO surface. We use hybrid density-functional theory in combination with *ab initio* thermodynamics to determine a doping-dependent phase diagram of this surface. For hydrogen coverages lower than 50% dangling oxygen bonds remain at the surface, where they subsequently become charged by bulk electrons. For such charged surfaces, a computational first-principles approach is presented, with which long-range band bending can now be included in first-principles supercell calculations. In this work, we use a modified and extended version of the recently introduced charge-reservoir electrostatic sheet technique (Sinai *et al* 2015 *Phys. Rev. B* **91** 075311) to incorporate band bending effects directly into our first-principles calculations. This allows us to investigate the effect of space charge layers and the resulting band bending on the hydrogen coverage of the ZnO (000$\bar{1}$) surface. After introducing a new implementation of CREST, we show that the structure and stability of polar ZnO surfaces are indeed sensitive to the amount of free charge carriers in the bulk. At low doping concentrations our results corroborate the previously reported (2 × 1) hydrogen phase, at higher doping concentrations the hydrogen coverage diminishes notably.

1. Introduction

Due to its high optical transmissivity and tunable electronic properties, zinc oxide (ZnO) is a promising material for future technological applications, e.g. as a charge-injection material in hybrid light-emitting diodes [1–3], as an acceptor material in hybrid photovoltaics [4, 5], or as a charge-transport layer and transparent electrode in organic photovoltaic devices [6–8]. In these applications, device functionality and performance critically depend on the level alignment between the ZnO and a second material, often organic molecules. The alignment is influenced by the interface dipole, which in turn critically depends on the atomistic details of the ZnO surface [9]. However, discussions on the surface structure are still controversial, in particular for the polar oxygen-terminated (000$\bar{1}$) ZnO surface. A commonly investigated stability mechanism is the adsorption of atomic hydrogen on the pristine (000$\bar{1}$) surface. A coverage of half a monolayer satisfies the electron counting rule, leading to the very stable and well-known (2 × 1) hydrogen overlayer depicted in figure 1. Theoretical investigations, however, have proposed several other energetically very similar surface structures and predict a rich surface phase diagram [10–16], indicating that the surface is highly sensitive to the environmental conditions. Also, experimentally, a wide variety of structures has been observed for similar growth conditions [17–22]. Although a lot of effort has been made, and the previously conducted studies contributed significantly to a better understanding of ZnO surfaces, the origin of its structural diversity is not satisfactorily understood, and there are still variables whose impact on the surface phase stability have not been considered so far.

Figure 1. Illustration of the (2 × 1)-H oxygen-terminated polar ZnO surface, half covered by adsorbed hydrogen atoms. The blue, red and white balls denote zinc, oxygen and hydrogen atoms, respectively.
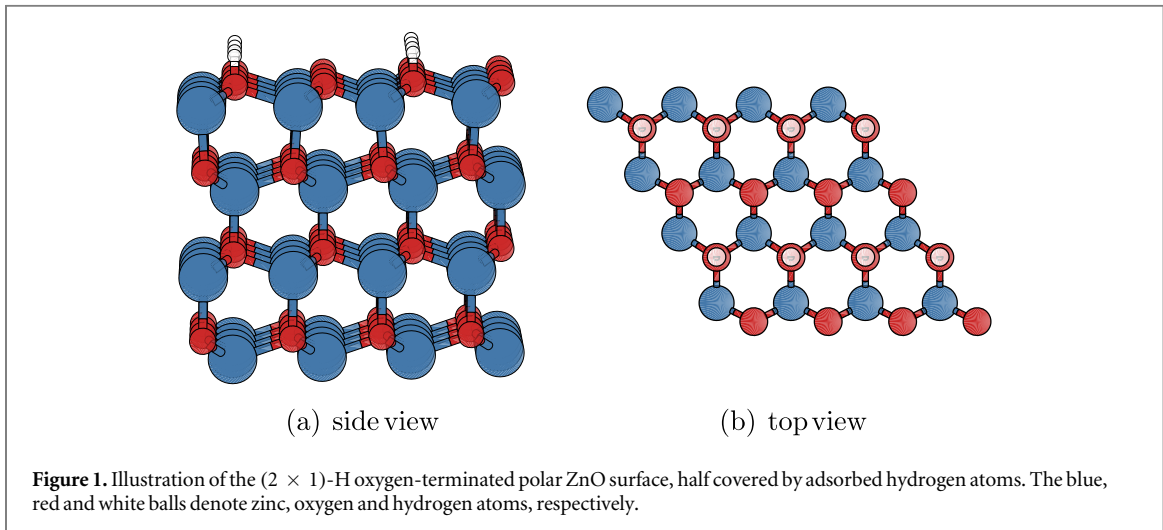
One of these variables, and a possible origin for the experimental diversity of the surface structures, is their dependence on the bulk doping concentration of ZnO. Even when grown as purely as possible, ZnO crystals always exhibit intrinsic *n*-type conductivity, whose origin has been the subject of an intensive debate [23–26]. Intrinsic carrier concentrations are typically of the order of $\sim 10^{16} - 10^{17}\,\mathrm{cm}^{-3}$ [27]. Conversely, intentionally heavily doped substrates for plasmonic applications can reach carrier concentrations of up to $\sim 10^{21}\,\mathrm{cm}^{-3}$ [28–30]. Although the doping concentration between different studies may differ by five orders of magnitude, in practice, the exact doping concentration is difficult to control and to measure [31], and is therefore not often reported in experimental studies.

Several recent computational studies indicate that free charge carriers play an essential role in the stability of different surface structures: Richter *et al* suggest that the oxygen vacancy concentration on metal oxide surfaces is determined by the doping concentration of the substrate [32]. Li *et al* investigated various surface models of zinc-terminated ZnO and concluded that *n*-type doping can stabilize the electron-acceptor states originating from the surface defects. Moreover, Moll *et al* found that for oxygen-terminated ZnO, the charge transfer from the bulk to the surface states can stabilize otherwise thermodynamically unfavorable structures, resulting in surface hydrogen atoms desorbing from the otherwise stable (2 × 1)-H reconstructed surface [33]. In all of these cases, charge carriers from the bulk are transferred to the surface to form electrically charged defects, which—depending on the position of the Fermi-level—are substantially more stable than their neutral counterparts.

However, so far a quantitative prediction of hydrogen desorption from the (2 × 1)-H surface has not been achieved, because long-range band bending, which affects the stability of surface structures as a function of the bulk doping concentration, cannot be included in first-principles calculations. In fact, to our knowledge the bulk doping concentration has not been consistently considered as a variable in the surface phase diagrams of semiconductors so far. With the recently introduced charge-reservoir electrostatic sheet technique (CREST) [34], the dependence on the bulk doping concentration can now be modeled. This approach has been previously successfully applied and tested for the well-known example of the Si(111)-surface [34]. CREST uses a two-dimensional charge sheet on the back side of a semiconducting surface slab, which mimics the effect of band bending associated with a charged surface. This makes it possible to explicitly include band bending in a slab calculation for any given bulk doping concentration.

Other approaches treat the charged surface defects by introducing an additional dopant charge into the calculation and by applying *a posteriori* correction schemes to subtract the contributions of the compensating homogeneous background in the supercell. These approaches, however, neglect the effect of the electric field in the space charge region [35, 36]. Kempisty and Krukowski presented a method to account for the electric field of the space charge region by manipulating the location and charge of passivating atoms on the back side of the slab [37–40], but did not translate the added charge into the bulk doping concentration.

In this work, we adopt the general idea of the CREST approach and present a modification that allows us to calculate the total energies as a function of the bulk doping concentration. With this modified CREST approach we can then calculate the doping-dependent surface phase diagram of the O-terminated ZnO (000$\bar{1}$) surface. With our calculations, we explore the correlation between the surface structure, the doping concentration and the resulting band bending. Our phase diagrams clearly demonstrate the connection between these three aspects. They show that at low doping concentrations, the energy cost associated with band bending prevents any hydrogen desorption and stabilizes the perfect (2 × 1) hydrogen reconstruction. In contrast, at high doping concentrations the H-coverage diminishes considerably.

The outline of this paper is as follows. The first part of section 2 briefly introduces the thermodynamic formalism we used to calculate the phase diagrams from *ab inito* density functional theory (DFT) calculations. In the second part (section 2.2), we recap the basic ideas of the CREST approach and then describe our implementation of the technique as well as its extension to the total energies. Section 3 describes the numerical details of the DFT calculations employed in this work. In section 4, we apply our revised CREST approach to obtain the phase diagram of the O-terminated (000$\bar{1}$) ZnO surface with the bulk doping concentration of ZnO as an extrinsic variable. Our conclusions are summarized in section 5.

2. Methodology

2.1. Phase diagram from *ab initio* thermodynamics

In this section, we briefly summarize how we apply *ab initio* thermodynamics to determine the stability of the various surface structures when in contact with an atomic reservoir, i.e. a surrounding gas. For the sake of brevity, we refer to the supplementary material, which is available online at stacks.iop.org/NJP/19/083012/mmedia, or [41] for further details.

When a surface is in thermodynamic equilibrium with an external reservoir at temperature T and pressure p, the most stable structure and composition of the surface is the one that minimizes the Gibbs free surface energy $\gamma(T, p)$. As we are interested in the relative surface stability, the thermodynamic quantity of interest is the change in surface free energy $\Delta\gamma$ with respect to a given reference structure. We assume that Zn is always in thermal equilibrium with the surface, and restrict the problem to the two independent gas phase reservoirs H_2 and O_2. The corresponding chemical potentials of the reservoir gases $\Delta\mu_H$ and $\Delta\mu_O$ are referenced to the total energies of the isolated H_2 ($E_{gas}^{H_2}$) and O_2 ($E_{gas}^{O_2}$) molecules:

$$\Delta\mu_H = \mu_H - \frac{1}{2}E_{gas}^{H_2}, \qquad \Delta\mu_O = \mu_O - \frac{1}{2}E_{gas}^{O_2}. \tag{1}$$

More than two external reservoirs, i.e. gas components, can be considered in principle (see e.g. [42]). We refrain from this here so as not to unnecessarily complicate the discussion of the main focus of our manuscript—the dependence on the bulk doping concentration.

The change of surface free energy per unit area for a certain surface structure with respect to the chemical potentials of the reservoir gases $\Delta\mu_H$ and $\Delta\mu_O$ is then given as

$$\Delta\gamma = \frac{1}{A}\left(E_{slab} - E_{slab}^{ref} + n_H^{rem}\left[\Delta\mu_H + \frac{1}{2}E_{gas}^{H_2}\right] + n_O^{vac}\left[\Delta\mu_O + \frac{1}{2}E_{gas}^{O_2}\right]\right) \tag{2}$$

where E_{slab} is the total energy of the surface slab with n_H^{rem} removed hydrogens and n_O^{vac} oxygen vacancies present at the surface; E_{slab}^{ref} is the energy of the reference surface. Taking into account all the considered surface structures, the most stable one for a specific set of chemical potentials ($\Delta\mu_H$, $\Delta\mu_O$) is the one with the lowest $\Delta\gamma$. With this knowledge, we can build two-dimensional phase diagrams with the axes being the two chemical potentials. Since the energy differences between the surfaces can be small, it is crucial to correctly calculate the total energies of the investigated surface structures. Therefore, it is essential to account for the energy contributions associated with the charge transfer or band bending, which we can now do with the CREST approach.

2.2. The extended CREST approach

The CREST approach was introduced by Sinai *et al* in [34]. In this section, we review the main idea and explain our extensions, which allow us to use a smaller slab to facilitate the calculation of the total energies. For ease of understanding, we explain the application of CREST with the example of the ZnO (000$\bar{1}$) surface. At this surface, the oxygen atoms are only coordinated three-fold, rather than four-fold as in the bulk. Hence, they provide an extra half an electron each, or one extra electron for every two surface O atoms. Under typical ultra-high vacuum (UHV) conditions, the surface reacts with hydrogen, which adsorbs on every other surface O atom to form the (2 × 1)-H surface structure shown in figure 1. This structure satisfies the electron counting rule and exhibits flat band conditions, as shown in figure 2(a). When individual hydrogen atoms are removed, they expose a dangling bond with an associated surface state in the ZnO band gap. Due to the intrinsic *n*-type doping of ZnO, the Fermi level is close to the conduction band minimum. Electrons from the bulk can therefore lower their energy by filling this surface state. The migration of electrons to the surface results in a net surface charge and leaves behind a depletion of charge carriers in the region adjacent to it. The depletion region is also referred to as a space charge region, and depending on the doping concentration, can reach macroscopically far into the crystal. Electrostatically, this leads to the formation of band bending, which shifts the energy levels near the surface relative to their bulk positions until they are in resonance with the bulk Fermi level, as shown in figure 2(b).

Figure 2. A schematic explanation of surface band bending due to the creation of surface states caused by dangling bonds at the ZnO (000$\bar{1}$) surface. (a) A representation of our system of interest before the charge is transferred to the surface. In the case of *n*-type conductivity, the Fermi energy E^F is close to the conduction band minimum (CBM) of the system. The work function Φ_{target} will be used as a convergence criterion in our CREST procedure. (b) The system of interest after equilibration, where charge carriers from the doped bulk now partially fill the surface state. This causes an offset of the valence band maximum (VBM) and the conduction band minimum (CBM) relative to the Fermi energy near the surface.

Figure 3. (a) Band bending as a purely electrostatic effect can be modeled semi-classically by assuming a homogeneous space charge density caused by the ionized impurities. (b) The auxiliary system contains a thin slab that is treated explicitly by a quantum-mechanical calculation (QM-region). The remaining effect of the space charge region is modeled by the insertion of a charge sheet.

With the CREST approach, band bending can be included in the first-principles calculations without having to treat the entire space charge region with first principles [34]. The concept of CREST is to only treat the near-surface region explicitly (e.g. by means of DFT), and use a classical electrostatic approach for the rest of the system. This is conceptually shown by the shaded region in figure 3(a). In the slab representing the surface, the free charge carriers are modeled using the virtual crystal approximation (VCA) [43] (see section 3 for details on how the VCA is employed in this work). The potential drop in the classical, electrostatic region that arises from ionized dopants can be adequately captured by homogeneously distributed point charges. However, for technical and numerical reasons, the homogeneously distributed charge is collapsed and is implemented as a two-dimensional charge sheet on the back side of the semiconducting slab, as shown in figure 3(b). Thus, the parabolic potential originating from the remaining ions in the space charge region is replaced by a linear drop of

the potential between the bottom side of the slab and the charge sheet. Compensating charge-carriers are introduced in the DFT calculations of the surface slab, rendering the whole system effectively charge neutral.

Sinai *et al* determined the position and charge of the charge sheet by fitting the plane-averaged electrostatic potential within the slab and extrapolating into the vacuum region below. However, when the slab thickness is reduced (e.g. to facilitate the use of computationally expensive hybrid functionals) such a fit might become unreliable. We therefore present an alternative, simplified approach to define the properties of the charge sheet, which is crucial for correctly accounting for band bending effects. Although we will explain our version of CREST using the example of *n*-type doped ZnO, we emphasize that our approach is completely general.

The major parameter of our CREST method is the work function of the 'bottom' side of the slab. In the slab approach, one of the essential convergence parameters is the slab thickness. Adsorption or desorption on one side of the slab should not affect the properties on the other side of the same slab. It is thus sensible to define the vacuum level on the 'bottom' side of the slab as our energy zero. Furthermore, it is clear that the 'bottom work function' Φ'_L (i.e. the difference between the Fermi energy and the vacuum level) must not be affected by any change to the upper side of the slab. This fact can be exploited to determine the electrostatic potential drop over the space charge region and calculate the charge and position of the charge sheet. We can therefore define a target bottom work function Φ_{target} for an ideal system that does not exhibit band bending (as shown in figure 2(a)). This target will guide us in the modified CREST scheme.

In an ideal system (e.g. the ZnO (2×1)-H surface before hydrogen desorption), where doping is modeled using the VCA, the Fermi-level is well above the mid-gap and no band bending occurs. When a hydrogen atom is now desorbed, a new acceptor-like state forms in the band gap. This state may be capable of holding one full electron. Since the state is below the Fermi energy, all free charge carriers will flow into this state. However, unless the slab is very thick, it will typically contain less than one full electron. As a result, the state becomes fractionally occupied, while the conduction band in the finite slab is completely depleted of electrons. Furthermore, the Fermi energy of the entire system (which is calculated from the electron distribution) is now in resonance with the gap state, which results in a change in the work function of the lower side of the slab Φ'_L. This change indicates a deviation from the target value Φ_{target} and requires action.

The difference between Φ'_L and Φ_{target} is equal to the electrostatic potential drop associated with band bending outside the quantum-mechanical region, i.e. outside the slab (see figure 3(a)). We refer to this part of the band bending as the tail $\Delta\varphi^{BB}_{tail}$,

$$\Delta\varphi^{BB}_{tail} = \Phi'_L - \Phi_{target}. \tag{3}$$

$\Delta\varphi^{BB}_{tail}$ will later be used to determine the position and total charge of the charge sheet that mimics band bending effects. This is where our extended CREST deviates from the procedure of Sinai *et al* [34]. Instead of fitting the electrostatic potential at the boundary of the slab we use the fact that we know the amount of band bending outside the slab and apply a self-consistent scheme to adjust the properties of the charge sheet to reproduce this amount. A flow chart covering all steps within our modified CREST approach is shown in figure 4. In the next paragraphs, we will derive the mathematical relations to define the correct properties of the charge sheet and explain the self-consistent scheme in more detail. However, for the sake of understanding, we first explain what effect the inclusion of the charge sheet has on the bottom side work function of the slab.

By including a charge sheet in the DFT calculation, we will change the bottom side work function $\Phi_{L,n}$, because the electric field between the charge sheet and the bottom side of the slab results in a potential drop, which affects the bottom side work function. Our objective in CREST is now to adjust the properties of the charge sheet iteratively (the subscript *n* denotes the iteration) such that $\Phi_{L,n} = \Phi_{target}$. If this is the case, the potential drop due to band bending would be correctly reproduced. We can interpret this procedure as finding the right amount of charge that has to be transferred to the surface, such that the distance of the conduction band to the globally defined Fermi level is correctly described. The slab states are now offset with respect to the lower vacuum level by the correct band bending, and the right amount of mobile electrons is included in the calculation.

To explain the mathematical details of our modified CREST method determining the charge and position of the charge sheet, it is useful to briefly recap the classical electrostatic equations associated with band bending in extended space charge layers. Let us consider an infinite surface parallel to the *x-y* plane with the semiconductor extending in the *z* direction. z_d denotes the extent of the space charge region in the bulk starting from the surface at $z = 0$. In the depletion approximation, we assume all donors to be ionized in the space charge region, which gives a space charge density of $\rho = eN_D$, with N_D being the doping concentration. The resulting electrostatic potential associated with the electric field in the space charge region is determined by the one-dimensional Poisson equation,

Figure 4. Flow chart of the self-consistent CREST scheme.
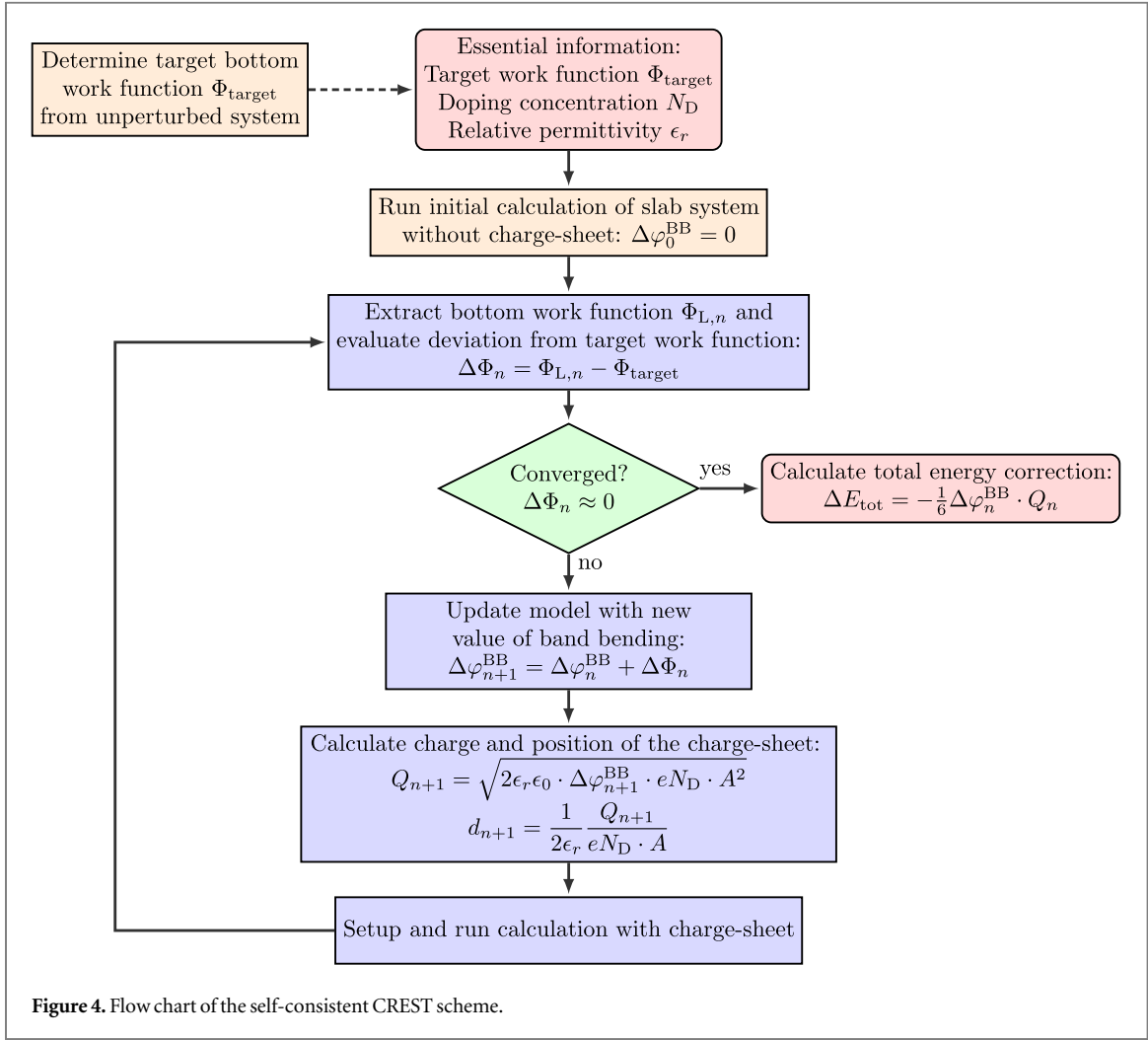
$$\frac{\mathrm{d}^2\varphi(z)}{\mathrm{d}z^2} = -\frac{\rho(z)}{\epsilon_r\epsilon_0}, \tag{4}$$

where $\varphi(z)$ is the electrostatic potential in the direction of the surface normal. The vacuum permittivity is given by ϵ_0, and ϵ_r is the relative permittivity of the material. With the boundary condition that the electric field vanishes at the edges of the space charge region, i.e. at $z = 0$ and at z_d, the solution of the Poisson equation for the electrostatic potential yields

$$\varphi_S(z) = -\frac{eN_D}{2\epsilon_r\epsilon_0}(z - z_d)^2. \tag{5}$$

The bands bend parabolically, with a total potential drop over the space charge region of

$$\Delta\varphi_S = \varphi_S(0) - \varphi_S(z_d) = -\frac{Q_S z_d}{2\epsilon_r\epsilon_0 A}; \tag{6}$$

here we replaced the charge density $\rho = eN_D$ by the total amount of charge of the ionized donors Q_S divided by the volume of the space charge region $V_{SCR} = A \cdot z_d$, where A is the base area of the slab. These equations describe the situation for homogeneously distributed dopants. In the next paragraph, we derive the equations for a system with a charge sheet as used in the CREST method.

For technical reasons, in the CREST method it is beneficial to collapse the homogeneous doping region into a single charge sheet, positioned within the space charge region. This charge sheet, combined with the quantum mechanical region, can be viewed as an auxiliary system. The properties of this auxiliary system will be defined in such a way that the original situation of the homogeneous doping region is described as accurately as possible. One difference between the original and the auxiliary system is the difference in relative permittivities. We position the charge sheet in the vacuum region on the back side of the slab calculation, and not in a medium with permittivity ϵ_r. The slope of the potential therefore changes abruptly at the interface between the back side of the slab and the vacuum region due to the change in the relative permittivity from dielectric to vacuum. Within the slab, the relative permittivity of the material ϵ_r is given by DFT. It would also be desirable to set ϵ_r in the vacuum

region between the lower slab surface and the charge sheet, which, however, has not been possible within most common DFT codes so far. Therefore, we correct for the influence of the relative permittivity in our equations, which determine the charge and distance of the sheet by considering the ϵ_r of the material in the equations of the homogeneous charge density, and setting it to the vacuum value in the following equations of the auxiliary system. With this, we introduce ϵ_r as an input parameter for our CREST (see figure 4 for reference) and ensure that the potential drop and the transferred charge is correctly reproduced.

Mathematically, the electrostatic environment of the auxiliary system can by described again by the solution of the Poisson equation. The constant charge density is now replaced by a delta function at the position d of the charge sheet

$$\rho(z) = \frac{Q_C}{A} \cdot \delta(z - d). \tag{7}$$

The two parameters that determine our auxiliary system are the surface charge density of our charge sheet Q_C/A and the distance of the sheet from the back side of the slab d. The solution of the Poisson equation returns a linear drop in the potential between the back side of the slab at $z = 0$ and the position of the charge sheet at $z = d$

$$\varphi_C(z) = \frac{Q_C}{\epsilon_0} \frac{z - d}{A}. \tag{8}$$

To ensure that our auxiliary system describes the intended system correctly, it has to fulfill two requirements to fix the two adjustable parameters of the charge sheet: first, the potential difference due to band bending $\Delta\varphi^{BB} = \Delta\varphi_S$ in the true system is reproduced by the auxiliary system

$$\Delta\varphi_S \stackrel{!}{=} \Delta\varphi_C = \varphi_C(0) - \varphi_C(d). \tag{9}$$

Second, the electric field acting on the slab is correctly described. The second criterion is fulfilled, if the charge sheet contains the same amount of charge Q_C as the total charge of the volume of the space charge region $Q_C \stackrel{!}{=} Q_S = A \cdot z_d \cdot eN_D$. Equation (9) for condition one then determines the second free parameter, which is the distance d of the charge sheet. Inserting the potential drop for the homogeneous charge distribution (6), and for the auxiliary CREST system (8) into equation (9) yields $d = \frac{z_d}{2\epsilon_r}$. This ensures that the potential difference associated with the band bending is correctly reproduced.

Finally, to obtain the correct total energy in CREST we need to correct for the incorrect potential shape that was introduced by collapsing the space charge region into a charge sheet. We subtract the energy of the effective plate capacitor U_{sheet} introduced by the charge sheet and add the contribution for the parabolic shape U_{SCR} of the desired homogeneous doping distribution. This gives a total energy correction of

$$\Delta E_{tot} = -U_{sheet} + U_{SCR} = \left(-\frac{1}{2} + \frac{1}{3}\right)\Delta\varphi^{BB} \cdot Q_C = -\frac{1}{6}\Delta\varphi^{BB} \cdot Q_C. \tag{10}$$

This correction only depends on the potential drop due to band bending $\Delta\varphi^{BB}$ and the charge within the space charge region, which is equal to the charge of the introduced sheet Q_C. The total energy of the slab system, which enters equation (2) for the phase diagram calculations, can now be written as $E_{slab} = E_{slab}^{DFT} + \Delta E_{tot}$. Additional information about the implementation of our modified CREST approach for FHI-aims can be found in the supplementary material.

3. Computational details

The structural parameters of bulk ZnO were obtained by optimizing the geometry of a primitive wurtzite bulk cell. The different surface geometries were modeled using a 4×4 slab supercell comprised of four ZnO double layers, for which the bottom two layers were fixed to their bulk positions. The top two layers were allowed to relax during the geometry optimization until the residual forces were smaller than 10^{-3} eV Å^{-1}. The surface geometries were fully optimized for the undoped case, and kept fixed for all further calculations. The bottom side of the slab was passivated with pseudo-hydrogen atoms of nuclear and electronic charge $\pm 3/2$, as is commonly done in the literature [44]. This ensures that the surface bands on the bottom side of the slab are fully occupied and charge neutralization for this side of the slab is enforced. A dipole correction was employed inside the >20 Å vacuum region between the periodic images [45].

All calculations in this work were performed with the all-electron numerical atomic orbital Fritz Haber Institute *ab initio* molecular simulation code (FHI-aims) [46–48]. We used the Heyd–Scuseria–Erzenhof (HSE*) [50, 49] functional with the optimized mixing parameter $\alpha = 0.375$ and the scaling parameter $\omega = 0.2$ Å^{-1}. These parameters are equivalent to the values of Oba *et al* [51], yielding a band gap of 3.43 eV in the bulk calculations, which is in very good agreement with the experimental value of 3.44 eV [52, 53]. Van der Waals forces were included using the vdW–TS scheme [54], employing the optimized parameters from [55]. We used
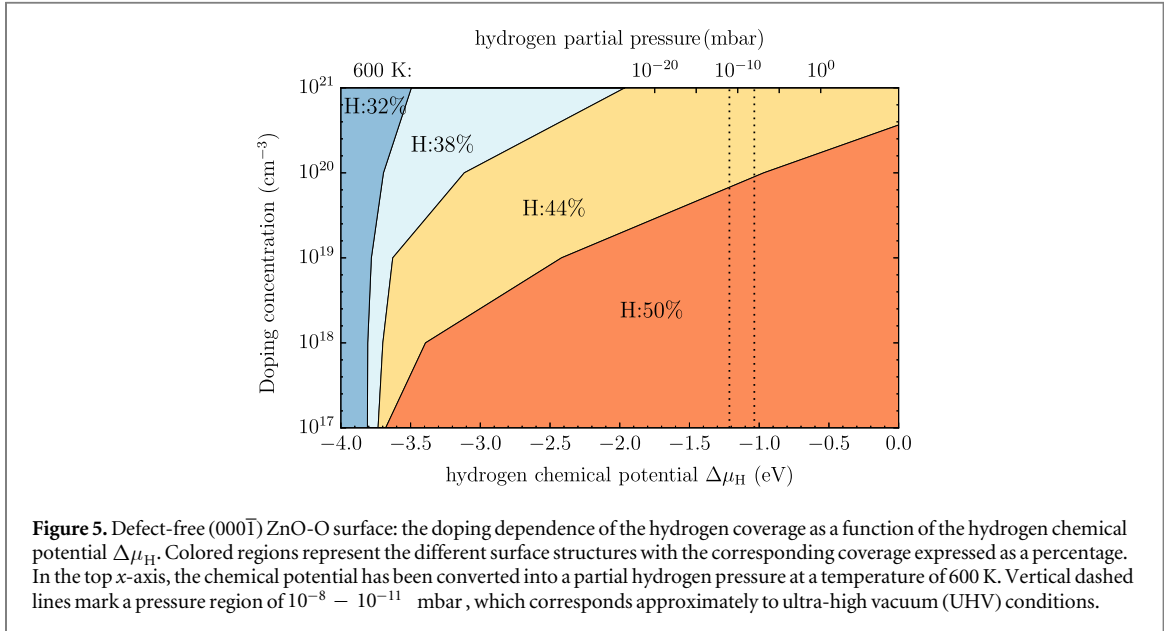
Figure 5. Defect-free (000$\bar{1}$) ZnO-O surface: the doping dependence of the hydrogen coverage as a function of the hydrogen chemical potential $\Delta\mu_H$. Colored regions represent the different surface structures with the corresponding coverage expressed as a percentage. In the top *x*-axis, the chemical potential has been converted into a partial hydrogen pressure at a temperature of 600 K. Vertical dashed lines mark a pressure region of $10^{-8} - 10^{-11}$ mbar, which corresponds approximately to ultra-high vacuum (UHV) conditions.

tight defaults for the grids and basis sets for Zn and H atoms. For the O atoms, we removed the *f* and *g* functions from the tight tier-2 defaults to reduce the computational cost. For the same reason, we increased the Hartree–Fock screening threshold to 10^{-5}. A 12 × 12 × 12 *k*-grid was used for the bulk calculations and scaled accordingly for larger supercells. All settings were carefully tested to converge within a total energy accuracy of 10^{-3} eV per primitive unit cell.

Doping in the ZnO slab was introduced by means of the virtual crystal approximation (VCA) [43, 56]. In the VCA, the O atoms are replaced by pseudo-atoms with a fractional atomic number $Z' = Z + \Delta Z$. For *n*-type doping, the corresponding change ΔZ in the electron number per atom gives rise to excess electrons, which fill the bottom of the conduction band in our calculations. This results in mobile electrons, while the counter charge remains spatially fixed at the ionic cores. The build-up of a space charge layer and the associated band bending is then included with the CREST approach.

The relative permittivity ϵ_r of ZnO required by the CREST approach was also calculated using the HSE* functional. To do so, we applied a small external field along the surface normal to the crystal and measured the resulting potential drop associated with the resulting polarization within the slab. We again kept the atomic positions fixed and thus calculated only the electronic and not the ionic contribution of the permittivity. We obtained $\epsilon_r = 4.0$, which is close to the experimental value of $\epsilon_\infty = 3.7$ [57].

4. Results

4.1. Application of CREST: doping-dependent phase diagram for O-terminated ZnO

The CREST method explained in the previous section allows us to study the influence of the doping concentration on the stability of semiconductor surfaces. As a first step, we explore the defect-free O-terminated (000$\bar{1}$) ZnO surface and the influence of the doping concentration on the hydrogen termination. The (2 × 1)-H surface with a half-monolayer of adsorbed hydrogen, shown in figure 1, completely compensates the charge from the dangling bonds on the surface and therefore has a very stable surface structure. This means the partially occupied surface bands are filled by the adsorption of hydrogen on every second oxygen atom. Alternatively, free charge carriers introduced by dopants fill and thus passivate the surface gap states. This alternative passivation introduces an energy penalty, which results from the associated build-up of band bending. The question is whether the bare, bulk-truncated O-terminated (000$\bar{1}$) ZnO surface could ever be stabilized by such free charge carriers. To investigate this question we gradually remove hydrogen from the (2 × 1)-H surface for different doping concentrations. We performed our calculations for a 4 × 4 supercell, which implies that the hydrogen coverage is reduced by ≈6% for every hydrogen atom that is removed.

Naively, one may expect the hydrogen coverage to reduce significantly for high doping concentrations, in accordance with the results reported by Moll *et al* [33] (who did not include band bending). However, figure 5, in which the coverage of the lowest energy structure is plotted as a function of the hydrogen chemical potential and doping concentration, shows that this is not necessarily the case. Converting the hydrogen chemical potential into the temperature and partial pressure of the hydrogen gas phase shows that for natively doped ZnO (i.e. approximately 10^{17} cm^{-3}), the unperturbed (2 × 1)-H surface structure is still thermodynamically preferred

Figure 6. The oxygen vacancy concentration of 1/16 at the O-terminated (000$\bar{1}$) ZnO surface: the doping dependence of the hydrogen coverage as a function of the hydrogen chemical potential $\Delta\mu_H$. Colors represent the different surface structures with the corresponding coverage expressed as a percentage. For the top *x*-axis, the chemical potential has been converted into a hydrogen partial pressure at a temperature of 600 K. Vertical dashed lines mark a pressure region of $10^{-8} - 10^{-11}$ mbar, which corresponds approximately to ultra-high vacuum (UHV) conditions.

for most realistic experimental conditions. Only at much higher doping concentrations or at very high temperatures do we find a deviation from the ideal structure. For UHV conditions and at 600 K, which is the temperature typically used for sample annealing, reduction to a surface coverage of 44% occurs for a doping concentration of $\approx 5 \times 10^{19}$ cm^{-3}. At lower temperatures, the transition would require an even higher number of free charge carriers. The stability of the (2 $\times$ 1)-H surface against hydrogen removal can be explained by the cost of band bending. To compensate for the desorption of hydrogen from the surface requires a certain amount of charge to be transferred from the bulk to the surface state that is generated in the desorption process. However, charge transfer from the bulk to the surface states is limited by the electrostatic field originating from band bending. This energy cost stabilizes surface structures close to 50% coverage under realistic conditions and illustrates the importance of including band bending in the surface calculations. At these conditions a hydrogen reduction of 6% is expected at a doping concentration of approximately 10^{20} cm^{-3}. For this case, the generated surface state becomes filled by about 0.7 electrons. For lower doping concentrations, this critical value cannot be reached because band bending limits the charge transfer. However, one needs to consider that because of the limited size of the unit cell, we can only model hydrogen reductions in increments of 6%. With this in mind, we can argue that diminishing H-coverage of <6% is to be expected already at lower doping concentrations. So far our findings cannot be compared to experimental results, because to our knowledge there is no experimental study that systematically investigates ZnO surfaces depending on the doping concentration.

4.2. Surface oxygen vacancies on the O-terminated ZnO surface

Oxygen vacancies at or near the O-terminated ZnO (000$\bar{1}$) surface have been discussed in the literature [12, 51], but from *ab inito* thermodynamics they are not considered to be stable in thermal equilibrium under realistic conditions. Still, they have been observed in experiments and might form in reality as a result of physical treatment during surface preparation procedures, which include sputtering and annealing steps. Therefore, we take a closer look at the stability of the ZnO surface including oxygen vacancies with the CREST approach. Introducing one oxygen vacancy in our 4 $\times$ 4 unit cell corresponds to an oxygen vacancy concentration of $1/16 \approx 6\%$. Figure 6 shows the doping dependency of the hydrogen coverage in this case.

One can see that there are now two competing surface structures in UHV conditions. For conditions that are richer in hydrogen, the (2 $\times$ 1)-H structure is still the most favorable. However, at smaller chemical potentials the most stable surface structure for low doping concentrations is now the one with two fewer hydrogens in the unit cell. This can easily be understood, since a structure with an oxygen vacancy and two hydrogens missing again fulfills the electron counting rule by completely filling the surface band. Thus no charge transfer from the bulk is required to saturate a dangling bond at the surface. Again, an increase in the doping concentration leads to a decrease in the hydrogen coverage. However, the desorption of hydrogen sets in at lower doping concentrations than for the defect free surface. While for the defect-free surface, hydrogen desorption is only observed for doping concentrations above 10^{20} cm^{-3}, oxygen vacancies provide additional charge carriers and lower this critical value to approximately 10^{19} cm^{-3}. This is because the oxygen vacancy pins the Fermi level at a higher energy level, a concept we recently explored for self-assembled organic monolayers at ZnO surfaces [58],

(a) dangling bond before band bending

(b) with band bending

(c) additional surface oxygen vacancy

(d) Fermi level pinning at oxygen vacancy

Figure 7. A schematic explanation of band bending and Fermi level pinning due to surface oxygen vacancies. (a) The situation at the defect-free surface before band bending. (b) A dangling bond leads to band bending that is approximately the size of the band gap. (c) The surface oxygen vacancy generates a gap state. (d) The Fermi level gets pinned at the O vacancy, significantly reducing the amount of band bending.

resulting in less band bending and a spatially smaller space charge region. The schematic band diagram explaining the position of the generated surface states and Fermi level pinning can be found in figure 7. Still, as in the defect-free case, band bending limits the charge transfer to the surface and so hinders a further decrease of its H concentration.

4.3. Complete phase diagram for various doping concentrations

Looking at the two phase diagrams with and without an oxygen vacancy, the question arises as to when the surface with an oxygen vacancy concentration of 1/16 becomes stable? To answer this question, we combine the results of the previous two sections and assume that the surface is simultaneously in equilibrium with two independent H_2 and O_2 gas reservoirs. The change in surface free energy now depends on the two chemical potentials of the surrounding gases and the doping concentration adds a third dimension. Such a three-dimensional plot would be hard to follow and therefore we representatively plot the phase diagrams for the two doping concentrations $N_D = 10^{18}$ cm^{-3} and $N_D = 10^{20}$ cm^{-3} as a function of the chemical potentials $\Delta\mu_H$ and $\Delta\mu_O$. Additionally, we added the corresponding partial pressures at a temperature of 600 K to the opposing axes of the hydrogen and oxygen chemical potentials, respectively.

Figure 8 shows that for natively doped ZnO, the (2 × 1)-H surface structure is still the thermodynamically preferred surface structure under UHV conditions at 600 K. This means that we expect surfaces with oxygen vacancies and reduced hydrogen coverage to only become stable in extremely oxygen poor conditions or at very high temperatures. The doping concentration does have an influence on the hydrogen coverage once an oxygen vacancy is present, but does not distinctively influence the stability of the vacancy itself. So, how can we justify the fact that it is still relevant to consider surface oxygen vacancies? First, an oxygen vacancy with a fifty percent coverage of hydrogen results in an empty gap state at the surface, and therefore might be the cause of Fermi level pinning, which is seen experimentally; and second, vacuum chambers are not a thermodynamic equilibrium. In the majority of surface preparation techniques, the ZnO polar surface is sputtered at least once with Ar$^+$, for

Figure 8. Phase diagrams of the O-terminated (000$\bar{1}$) ZnO surface at doping concentrations (a) $N_{\mathrm{D}} = 10^{18}$ cm^{-3} and (b) $N_{\mathrm{D}} = 10^{20}$ cm^{-3}. The hydrogen coverage of a specific phase is expressed as a percentage. Phases based on a surface including an oxygen vacancy are marked with an asterisk. Physically sensible regions of oxygen and hydrogen pressures at 600 K are indicated by vertical and horizontal dotted lines, respectively.

example. This sputtering could create oxygen vacancies that remain as metastable structures, even though they are, in principle, thermodynamically unstable.

5. Conclusion

We show for the case of ZnO that the bulk doping concentration is a parameter that needs to be included in the theoretical modeling of phase diagrams to be able to interpret the experimental results. Using a modified formalism of the recently developed CREST approach [34], we now take the bulk doping and therefore the full effects of macroscopic band bending into account in our calculations for semiconductor surfaces. By combining the modified CREST approach with a thermodynamic formalism, we have determined a doping-dependent surface phase diagram of the O-terminated (000$\bar{1}$) ZnO surface. Our work thus demonstrates the capability of the CREST approach to produce doping-dependent phase diagrams.

In this work we have focused on the O-terminated (000$\bar{1}$) ZnO surface, with and without surface oxygen vacancies, for various hydrogen terminations over a range of doping concentrations. The resulting phase diagrams show that doping can lead to a variety of the surface structures seen in experiments. However, band bending opposes the charge transfer from the bulk to the surface and thereby counteracts the hydrogen deficiency. Thus for low doping concentrations we expect almost no deviation from the most stable (2 × 1)-H

surface structure. For higher doping concentrations, the hydrogen coverage subsequently reduces, but a completely hydrogen-free surface limit appears unattainable. Deep donor states, such as oxygen vacancies, which can pin band bending at lower values, can serve as an additional source of charge carrier, leading to lower then 50% hydrogen coverage even at small doping concentrations.

Acknowledgments

References

[1] Alivov Y I, Kalinina E V, Cherenkov A E, Look D C, Ataev B M, Omaev A K, Chukichev M V and Bagnall D M 2003 *Appl. Phys. Lett.* **83** 4719–21
[2] Ohta H, Kawamura K I, Orita M, Hirano M, Sarukura N and Hosono H 2000 *Appl. Phys. Lett.* **77** 475–7
[3] Schlesinger R *et al* 2015 *Nat. Commun.* **6** 6754
[4] Ikram M, Murray R, Hussain A, Ali S and Shah S I 2014 *Mater. Sci. Eng.* B **189** 64–9
[5] Huang J, Yin Z and Zheng Q 2011 *Energy Environ Sci* **4** 3861–77
[6] Li H, Schirra L K, Shim J, Cheun H, Kippelen B, Monti O L and Bredas J L 2012 *Chem. Mater.* **24** 3044–55
[7] Schmidt-Mende L and MacManus-Driscoll J L 2007 *Mater. Today* **10** 40–8
[8] Owen J, Son M S, Yoo K H, Ahn B D and Lee S Y 2007 *Appl. Phys. Lett.* **90** 033512
[9] Hewlett R M and McLachlan M A 2016 *Adv. Mater.* **28** 3893–921
[10] Meyer B 2004 *Phys. Rev.* B **69** 045416
[11] Lauritsen J V *et al* 2011 *ACS Nano* **5** 5987–94
[12] Wahl R, Lauritsen J V, Besenbacher F and Kresse G 2013 *Phys. Rev.* B **87** 085313
[13] Jacobs R, Zheng B, Puchala B, Voyles P M, Yankovich A B and Morgan D 2016 *J. Phys. Chem. Lett.* **7** 4483–7
[14] Dulub O, Diebold U and Kresse G 2003 *Phys. Rev. Lett.* **90** 016102
[15] Kresse G, Dulub O and Diebold U 2003 *Phys. Rev.* B **68** 245409
[16] Li H, Schirra L K, Shim J, Cheun H, Kippelen B, Monti O L A and Bredas J L 2012 *Chem. Mater.* **24** 3044–55
[17] Kunat M, Gil Girol S, Becker T, Burghaus U and Wöll C 2002 *Phys. Rev.* B **66** 081402
[18] Lindsay R, Michelangeli E, Daniels B G, Ashworth T V, Limb A J, Thornton G, Gutierrez-Sosa A, Baraldi A, Larciprete R and Lizzit S 2002 *J. Am. Chem. Soc.* **124** 7117–22
[19] Kunat M, Gil Girol S, Burghaus U and Wöll C 2003 *J. Phys. Chem.* B **107** 14350–6
[20] Coppa B J, Fulton C C, Hartlieb P J, Davis R F, Rodriguez B J, Shields B J and Nemanich R J 2004 *J. Appl. Phys.* **95** 5856–64
[21] Xu H, Dong L, Shi X Q, Van Hove M A, Ho W K, Lin N, Wu H S and Tong S Y 2014 *Phys. Rev.* B **89** 235403
[22] Önsten A, Stoltz D, Palmgren P, Yu S, Göthelid M and Karlsson U O 2010 *J. Phys. Chem.* C **114** 11157–61
[23] Van de Walle C G 2000 *Phys. Rev. Lett.* **85** 1012–5
[24] Janotti A and Van de Walle C G 2007 *Phys. Rev.* B **76** 165202
[25] Oba F, Choi M, Togo A and Tanaka I 2011 *Sci. Tech. Adv. Mater.* **12** 034302
[26] Janotti A and de Walle C G V 2009 *Rep. Prog. Phys.* **72** 126501
[27] Look D, Reynolds D, Sizelove J, Jones R, Litton C, Cantwell G and Harsch W 1998 *Solid State Commun.* **105** 399–401
[28] Hu J and Gordon R G 1992 *J. Appl. Phys.* **71** 880–90
[29] Ko H J, Chen Y F, Hong S K, Wenisch H, Yao T and Look D C 2000 *Appl. Phys. Lett.* **77** 3761–3
[30] Kalusniak S, Sadofev S, Schäfer P and Henneberger F 2014 *Phys. Status Solidi* C **11** 1357–60
[31] Bierwagen O, Ive T, de Walle C G V and Speck J S 2008 *Appl. Phys. Lett.* **93** 242108
[32] Richter N A, Sicolo S, Levchenko S V, Sauer J and Scheffler M 2013 *Phys. Rev. Lett.* **111** 045502
[33] Moll N, Xu Y, Hofmann O T and Rinke P 2013 *New J. Phys.* **15** 083009
[34] Sinai O, Hofmann O T, Rinke P, Scheffler M, Heimel G and Kronik L 2015 *Phys. Rev.* B **91** 075311
[35] Komsa H P and Pasquarello A 2013 *Phys. Rev. Lett.* **110** 095505
[36] Krishnaswamy K, Dreyer C E, Janotti A and Van de Walle C G 2015 *Phys. Rev.* B **92** 085420
[37] Kempisty P, Krukowski S, Strak P and Sakowski K 2009 *J. Appl. Phys.* **106** 054901
[38] Kempisty P, Strak P and Krukowski S 2011 *Surf. Sci.* **605** 695–713
[39] Krukowski S, Kempisty P and Strak P 2013 *J. Appl. Phys.* **114** 143705
[40] Krukowski S, Kempisty P and Strak P 2013 *J. Appl. Phys.* **114** 063507
[41] Reuter K and Scheffler M 2001 *Phys. Rev.* B **65** 035406
[42] Herrmann P and Heimel G 2015 *Adv. Mater.* **27** 255–60
[43] Nordheim L 1931 *Ann. Phys.* **401** 607–40
[44] Meyer B and Marx D 2004 *Phys. Rev.* B **69** 235420
[45] Neugebauer J and Scheffler M 1992 *Phys. Rev.* B **46** 16067–80
[46] Blum V, Gehrke R, Hanke F, Havu P, Havu V, Ren X, Reuter K and Scheffler M 2009 *Comput. Phys. Commun.* **180** 2175–96
[47] Havu V, Blum V, Havu P and Scheffler M 2009 *J. Comput. Phys.* **228** 8367–79
[48] Ren X, Rinke P, Blum V, Wieferink J, Tkatchenko A, Andrea S, Reuter K, Blum V and Scheffler M 2012 *New J. Phys.* **14** 053020
[49] Krukau A V, Vydrov O A, Izmaylov A F and Scuseria G E 2006 *J. Chem. Phys.* **125** 224106
[50] Levchenko S V, Ren X, Wieferink J, Johanni R, Rinke P, Blum V and Scheffler M 2015 *Comput. Phys. Commun.* **192** 60–9
[51] Oba F, Togo A, Tanaka I, Paier J and Kresse G 2008 *Phys. Rev.* B **77** 245202
[52] Karzel H *et al* 1996 *Phys. Rev.* B **53** 11425–38
[53] Reynolds D C, Look D C, Jogai B, Litton C W, Cantwell G and Harsch W C 1999 *Phys. Rev.* B **60** 2340–4

[54] Tkatchenko A and Scheffler M 2009 *Phys. Rev. Lett.* **102** 073005
[55] Hofmann O T, Deinert J C, Xu Y, Rinke P, Stähler J, Wolf M and Scheffler M 2013 *J. Chem. Phys.* **139** 174701
[56] Parmenter R H 1955 *Phys. Rev.* **97** 587–98
[57] Ashkenov N *et al* 2003 *J. Appl. Phys.* **93** 126–33
[58] Hofmann O T and Rinke P 2017 *Adv. Electron. Mater.* **3** 1600373

Supplementary Information:
Doping dependence of the surface phase stability of polar O-terminated (0001̄) ZnO

Simon Erker[1], Patrick Rinke[2], Nikolaj Moll[3] and Oliver T Hofmann[1]

[1]Institute of Solid State Physics, Graz University of Technology, NAWI Graz, Austria
[2]COMP/Department of Applied Physics, Aalto University, Finland
[3]IBM Research−Zurich, Switzerland

E-mail: `o.hofmann@tugraz.at`

1. Practical step-by-step manual to use our CREST formalism in FHI-aims

For FHI-aims this method currently works for n-type doping and downward band bending only. To directly incorporate band bending into your surface slab calculation, follow the steps below:

(i) Determine target bottom side work function Φ_{target} from a calculation of the unperturbed system, i.e. without band bending. Actually one can set a experimental work function as target work function as well, but it is preferable to extract the target work function from a calculation of the fully passivated surface. This means a surface slab without the surface gap state present but including the doping via the Virtual Crystal Approximation (VCA).

(ii) Run an initial slab calculation of the perturbed system with the surface gap state present. Extract the bottom side work function $\Phi_{\text{L},0}$. If there is charge transfer to the surface the bottom side work function $\Phi_{\text{L},0}$ should now be larger than in the first calculation. Assume that the band bending in the region below the slab is given by $\Delta\varphi_0^{\text{BB}} = \Phi_{\text{L},0} - \Phi_{\text{target}} = \Delta\Phi_0$.

(iii) Calculate the charge of the sheet Q_n and its distance from the bottom side of the slab d_n (the subscript n denotes the CREST iteration):

$$Q_n = \sqrt{2\epsilon_r\epsilon_0 \cdot \Delta\varphi_n^{\text{BB}} \cdot eN_{\text{D}} \cdot A^2} \tag{1}$$

$$d_n = \frac{1}{2\epsilon_r}\frac{Q_n}{eN_{\text{D}} \cdot A} \tag{2}$$

Here N_{D} is the doping concentration and A the surface area of the slab cell.

(iv) Set up a calculation with the charge-sheet as determined through equation (1) and (2): Use a set of point charges to mimic the charge-sheet. For point charges simply take the species defaults for an H atom (light settings) without basis functions.

Replace all basis function by the line "`include_min_basis .false.`" and set the values for nucleus and valence accordingly to collectively hold the determined total charge of the sheet. Also include the lines "`override_warning_nobasis`" and "`override_warning_negative_nucleus`" in your `control.in` file. If you use Van-der-Waals correction make sure to switch it off for the point charges.

(v) Run the calculation, extract the bottom side work function of the CREST system $\Phi_{L,n}$ and calculate the new value of the band bending $\Delta\varphi_{n+1}^{BB} = \Delta\varphi_n^{BB} + (\Phi_{L,n} - \Phi_{target})$.

(vi) Repeat (iv)-(vi) until $\Delta\Phi_n = \Phi_{L,n} - \Phi_{target} = 0$, i.e., is smaller than a defined threshold.

(vii) Calculate the correction to the total energy $\Delta E_{tot} = -\frac{1}{6}\Delta\varphi_n^{BB} \cdot Q_n$.

2. ZnO parameters

For all our calculations we use the Heyd-Scuseria-Erzenhof (HSE*) [4] functional with an optimized mixing parameter $\alpha = 0.375$ and a scaling parameter $\omega = 0.2\,\text{Å}^{-1}$. As seen in table 1 this functional reproduces very well the experimental band gap of bulk ZnO. Using the commonly used PBE functional [5] the band gap is highly underestimated. This would result in a systematic error in our CREST formalism since the band bending would not be correctly described.

Table 1. Measured and calculated lattice constants and u parameter of bulk ZnO (Wurtzite structure, space group #186 (hexagonal, P63mc)).

a (Å)	c (Å)	c/a	u	bandgap (eV)	Reference
		1.633	0.375		Ideal
3.2496	5.2042	1.6018	0.3819	3.4370	Experiment [2, 3]
3.2780	5.2911	1.6141	0.3791	0.7486	pbe+vdW
3.2170	5.1616	1.6046	0.3810	3.4326	hse06*+vdW

3. Considered Surface structures

In our calculation of the ZnO surface phase diagram we did not consider all proposed surface structures that can be found in literature but rather restricted out investigation on the hydrogen coverage of the surface. We considered the defect-free surface was well as surface oxygen vacancies with multiple hydrogen adsorption rates and patterns. The in the literature well known (2×1)-H structure of the O-terminated polar ZnO surface can be seen as the initial structure of our investigation. At this structure every second surface oxygen is saturated by an H atom. Starting from this hydrogen adsorption pattern the number of adsorbed hydrogen is reduced one by one, for our 4×4 cell this means to reduce the hydrogen coverage by about 6% every step. When it is possible to

remove non-symmetry equivalent hydrogens from the surface, always the lowest energy configuration was considered in the determination of the phase diagram for a specific hydrogen coverage. We also considered structures with one oxygen vacancy at the surface and again several sub-structures with a reduced hydrogen concentration. One oxygen vacancy in the unit cell corresponds to a vacancy concentration of $1/16 \approx 6\%$. A schematic representation of the surface layer of our considered structures is shown in figure 1.

| (a) H:50% | (b) H:44% | (c) H:38% | (d) H:32% |

| (e) O_{vac}-H:50% | (f) O_{vac}-H:38% | (g) O_{vac}-H:32% | (h) O_{vac}-H:25% |
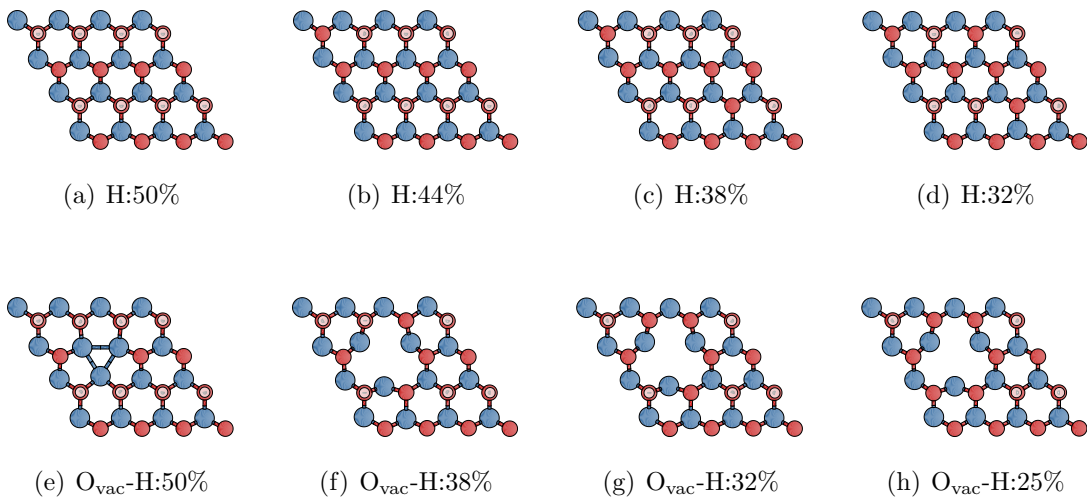
Figure 1. Topmost layer of the various surface structures appearing in our phase diagrams of the O-terminated ZnO surface. Zn atoms are colored in blue, O atoms in red and H atoms are white. Hydrogen coverages are expressed as a percentage. (a) is the defect free (2×1)-H surface with half monolayer hydrogen. (b)-(c) are the structures with a reduced hydrogen concentration. In the second row (e)-(h) the structures with one oxygen vacancy per unit cell are shown.

4. Phase diagrams from *ab-initio* thermodynamics

In this section we will give a brief summary of the thermodynamic formalism we used to determine the stability of the various surface structures when in contact with an atomic reservoir, i.e., a surrounding gas. There is a significant literature on *ab-initio* thermodynamics and their use for obtaining surface phase diagrams of ZnO [6,7]. We refer the reader to [8] for a detailed description of the formalism, and summarize below the basic information relevant to this paper.

When in contact with an external reservoir at temperature T and pressure p, thermodynamic equilibrium is defined by the minimization of the surface grand-potential

$$\gamma(T,p) = \frac{1}{A}\left(G(T,p,\{n_x\}) - \sum_x n_x \mu_x(T,p_x)\right) \tag{3}$$

where n_x is the number of particles in the solid and μ_x and p_x are the chemical potential and the partial pressure of the various species respectively. The Gibbs free energy G of a solid inducing the surface of interest comprises of several contributions:

$$G(T, p) = E_{\text{tot}} + F_{\text{vib}} - TS_{\text{conf}} + pV \qquad (4)$$

The total energy E_{tot} can be directly obtained from the electronic structure calculation. The second term, the vibrational free energy F_{vib}, accounts for all vibrational contributions in the system. The third term TS_{conf} includes the configurational entropy. A crucial aspect in our analysis is that we are only interested in the relative stability of a surface and therefore in differences of surface free energies. In our case, the thermodynamic quantity of interest to determine the relative stability of a certain surface structure is the change in surface free energy $\Delta\gamma$ from a reference surface structure. We choose the reference structure to be the ideal (2×1)-H structure where every second surface oxygen is bound to an adsorbed H atom. As a consequence one can argue that contributions to the Gibbs free energy from vibrations or configurational entropy can be neglected. This approximation has been shown to be valid for oxides and hydroxylated surfaces [8, 9] but might become relevant at finite temperatures or out of equilibrium.

In the present study of the O-terminated ZnO surface we would have to considering three different species x that is Zn, O and H. To reduce the complexity we assume that Zn is always in thermal equilibrium to the surface and restricting the problem to two independent reservoirs of H_2 and O_2 gas. This implies that we do not consider the formation of water which would normally happen in thermal equilibrium. This can be justified for the conditions of interest which are usually ultra high vacuum conditions (UHV) by arguing that water vapor is much more efficiently pumped from of a vacuum chamber, and that water does not readily form from H_2 and O_2 without proper activation.

As it is usually done in *ab-initio* thermodynamic studies all energies and chemical potentials are referenced to the total energies of the isolated hydrogen and oxygen molecules $E_{\text{gas}}^{H_2}$ and $E_{\text{gas}}^{O_2}$:

$$\Delta\mu_{\text{H}} = \mu_{\text{H}} - \frac{1}{2}E_{\text{gas}}^{H_2}, \qquad \Delta\mu_{\text{O}} = \mu_{\text{O}} - \frac{1}{2}E_{\text{gas}}^{O_2}. \qquad (5)$$

With this we can write down the change of surface free energy for a certain surface structure with respect to the chemical potentials of the reservoir gases $\Delta\mu_{\text{H}}$ and $\Delta\mu_{\text{O}}$:

$$\Delta\gamma = \frac{1}{A}\left(E_{\text{slab}} - E_{\text{slab}}^{\text{ref}} + n_{\text{H}}^{\text{rem}}\left[\Delta\mu_{\text{H}} + \frac{1}{2}E_{\text{gas}}^{H_2}\right] + n_{\text{O}}^{\text{vac}}\left[\Delta\mu_{\text{O}} + \frac{1}{2}E_{\text{gas}}^{O_2}\right]\right) \quad (6)$$

with E_{slab} the total energy of the surface slab with $n_{\text{H}}^{\text{rem}}$ removed hydrogens and/or $n_{\text{O}}^{\text{vac}}$ oxygen vacancies present at the surface. $E_{\text{slab}}^{\text{ref}}$ is the energy of the reference (2×1)-H surface slab. Taking into account all the considered surface structures described in the section above the most stable one for a specific set of chemical potentials $(\Delta\mu_{\text{H}}, \Delta\mu_{\text{O}})$ is the one with the lowest $\Delta\gamma$. From this we can now build a two dimensional phase diagram with the axes being the two chemical potentials. In a next step assuming the surface being in a thermodynamic equilibrium the chemical potentials can be related to a partial pressure of the gas components at a specific temperature.

This relational between chemical potential and partial pressure of a gas component presumes a thermodynamic equilibrium of the gas component with the surface. For an ideal gas we can use the well know equation to relate the partial pressure p_x to the chemical potential $\Delta\mu_x$

$$\Delta\mu_x(T, p_x) = \widetilde{\mu}_x(T, p^0) + \frac{k_B T}{2} \ln\left(\frac{p_x}{p^0}\right) \tag{7}$$

$$p_x = p^0 \cdot \exp\left(\frac{2[\Delta\mu_x - \widetilde{\mu}_x(T, p^0)]}{k_B T}\right) \tag{8}$$

where $k_B = 8.6173303 \cdot 10^{-5}$ eV/K is the Boltzmann constant. Furthermore one needs to know the temperature dependence of the chemical potential at standard conditions (standard pressure p^0). $\widetilde{\mu}_x(T, p^0)$ can be calculated from values in thermodynamic reference tables e.g. the JANAF table (kinetics.nist.gov/janaf) via

$$\widetilde{\mu}_x(T, p^0) = \frac{1}{2}\left[H(T, p^0, x) - H(0, p^0, x)\right] - \frac{1}{2}T\left[S(T, p^0, x) - S(0, p^0, x)\right] \tag{9}$$

with the enthalpy H and the entropy S and T the temperature. The values for the enthalpy H and the entropy S at standard conditions can be found in the thermodynamic reference table. In table 2 the chemical potential of molecular hydrogen and oxygen gas as well as for water vapor are listed for various temperatures.

Table 2. Chemical potential of molecular hydrogen and oxygen gas as well as for water vapor at standard conditions ($p^0 = 0.1$ MPa $= 1 \cdot 10^3$ mbar) for various temperatures.

Temperature (K)	$\mu_{H_2}(T, p^0)$ (eV/particle)	$\mu_{O_2}(T, p^0)$ (eV/particle)	$\mu_{H_2O}(T, p^0)$ (eV/particle)
100	-0.03666	-0.07476	-0.06193
300	-0.15929	-0.27394	-0.24225
600	-0.38020	-0.61120	-0.55670
700	-0.45970	-0.72987	-0.66861
800	-0.54137	-0.85100	-0.78330
1000	-0.71031	-1.09961	-1.02002

References

[1] Sinai O, Hofmann O T, Rinke P, Scheffler M, Heimel G and Kronik L 2015 *Phys. Rev. B* **91**(7) 075311

[2] Karzel H, Potzel W, Köfferlein M, Schiessl W, Steiner M, Hiller U, Kalvius G M, Mitchell D W, Das T P, Blaha P, Schwarz K and Pasternak M P 1996 *Phys. Rev. B* **53**(17) 11425–11438

[3] Reynolds D C, Look D C, Jogai B, Litton C W, Cantwell G and Harsch W C 1999 *Phys. Rev. B* **60**(4) 2340–2344

[4] Krukau A V, Vydrov O A, Izmaylov A F and Scuseria G E 2006 *J. Chem. Phys.* **125** 224106

[5] Perdew J P, Burke K and Ernzerhof M 1996 *Phys. Rev. Lett.* **77**(18) 3865–3868

[6] Kresse G, Dulub O and Diebold U 2003 *Phys. Rev. B* **68**(24) 245409

[7] Meyer B 2004 *Phys. Rev. B* **69**(4) 045416

[8] Reuter K and Scheffler M 2001 *Phys. Rev. B* **65**(3) 035406

[9] Sun Q, Reuter K and Scheffler M 2003 *Phys. Rev. B* **67**(20) 205424

3.4 Appendix

3.4.1 ZnO bulk calculations

In our CREST approach that introduces free charge carries into the conduction band of the semiconductor, the maximum amount of band bending is limited by the band gap of the semiconducting material. Therefore, for correctly considering the maximum amount of band bending, it is important that the band gap in the DFT calculation is accurately reproduced. In Figure 3.1 the dependence of the band gap of bulk ZnO is plotted as a function of the hybrid mixing parameter α in the HSE functional.
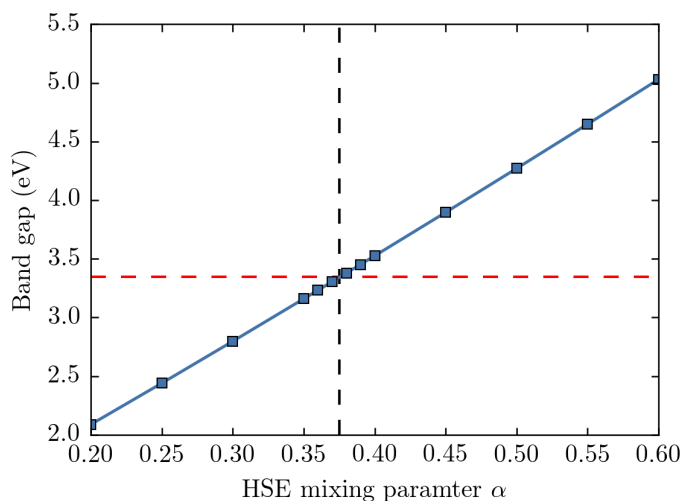
FIGURE 3.1: Evolution of the ZnO band gap as a function of the hybrid mixing parameter α in the HSE functional ($\omega = 0.2$ Å^{-1}). The red horizontal line mark the value of the experimental band gap, which is reproduced with $\alpha = 0.375$.

We find a linear dependence of the band gap as a function of α. The experimental band gap of 3.37 eV is almost perfectly reproduced using HSE with $\omega = 0.2$ Å^{-1} and $\alpha = 0.375$. This is in good agreement with results obtained with the VASP code[119]. The bandstructure of bulk ZnO for this parameters is plotted in Fig. 3.2.

3.4.2 Comments on slab calculations of polar ZnO surfaces

The theoretical treatment of the polar ZnO surfaces in slab calculations comes with some complications. Even when the surfaces are perfectly saturated, such that no dangling bonds are present on both side of the slab, a small dipole moment remains through the slab. This leads to a closing of the band gap with increasing number of ZnO layers in the slab. The evolution of the valence and conduction band with increasing slab thickness is plotted Fig. 3.3.
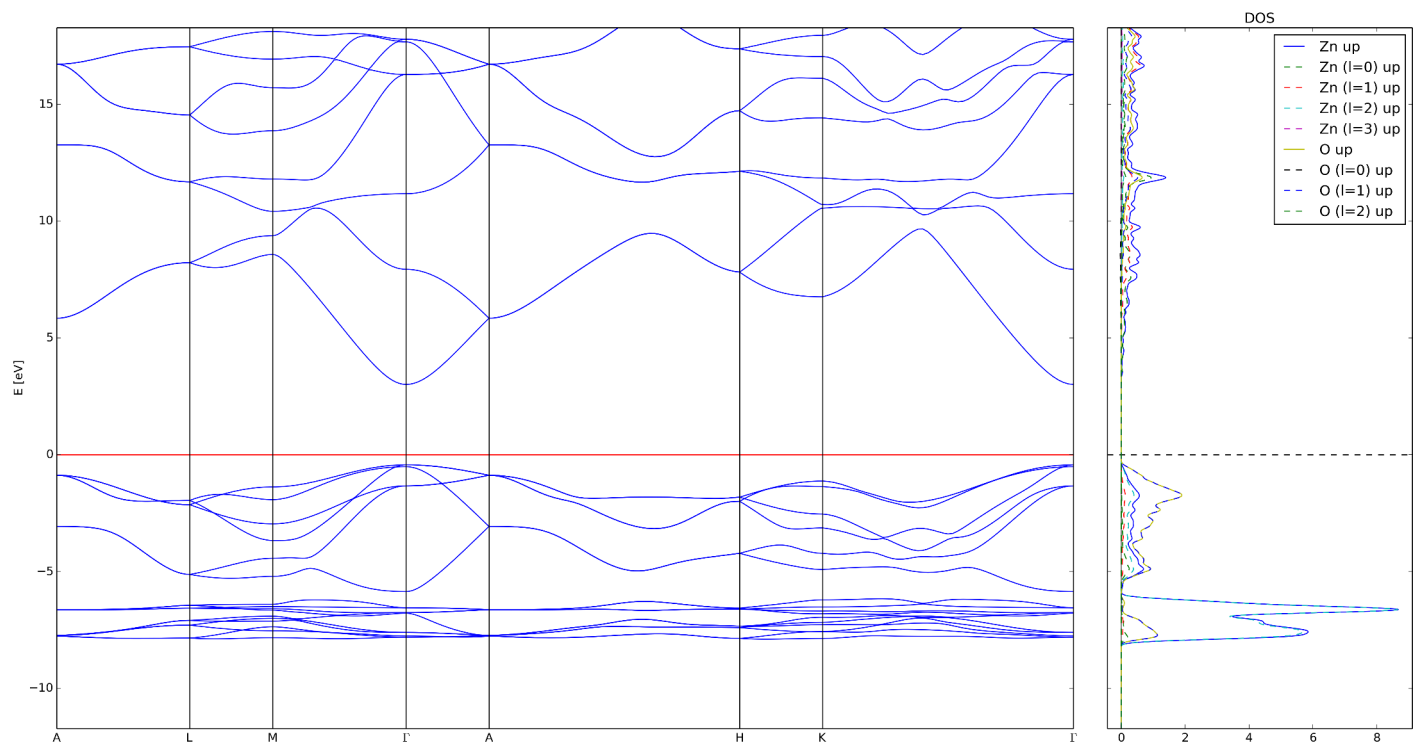
FIGURE 3.2: Bandstructure and density of states of bulk ZnO calculated with HSE ($\omega = 0.2$ Å^{-1}, $\alpha = 0.375$) + vdW-TS
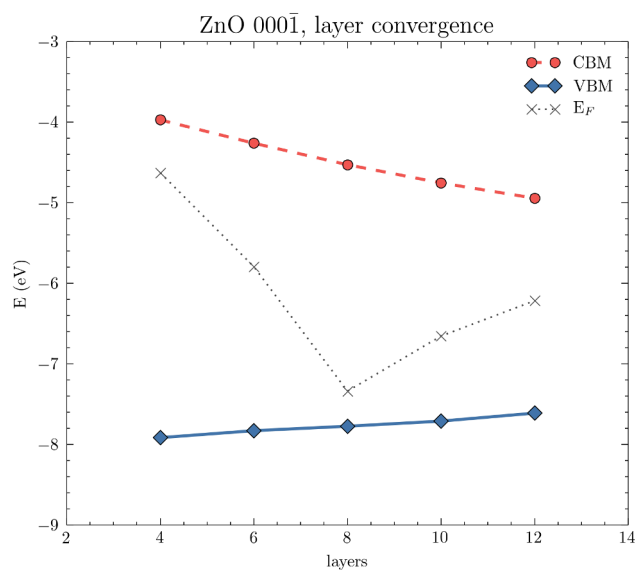
FIGURE 3.3: ZnO layer convergence: Valence band maximum (VBM) and conduction bang minimum (CBM) as a function of numbers of ZnO layers in the slab. The Fermi energy E_F is plotted as output by FHI-aims, but, due to the algorithmic implementation, has no physical meaning here.

3.4.3 Calculating the dielectric constant of ZnO

The dielectric constant (or relative permittivity) of the substrate material is one of the input variables of the CREST scheme. We calculated the dielectric constant of ZnO from the dielectric response to an external electric field.

In the linear response regime we assume that external field varies on a length scale that is much larger than the atomic distances. When applying such a small external electric field normal to the slab surface (in z-direction in our system, corresponds to the [0001] crystal direction), a response field is build up inside the ZnO slab. The dielectric response generally consists of electronic and ionic contributions. As described in the publication, only the electronic part is relevant for CREST calculations. Therefore, we are looking for the optical dielectric constant (also known as high-frequency dielectric constant $\epsilon_r(\infty)$), which only considers the electronic part. In the static value $\epsilon_r(0)$ also the ionic part would be included.

When performing a DFT slab calculation without geometry relaxation the response field is generated only by the induced change in the charge density, i.e. only the electronic part is active. The total macroscopic field E inside the ZnO slab can be written as:

$$E = E_{\text{ext}} - \frac{P}{\epsilon_0} \tag{3.1}$$

where E_{ext} the external applied electric field introduced in the DFT calculation, P the polarization, that is the response of the system to the external field, and ϵ_0 be the vacuum permittivity. The dielectric constant can be calculated from the ratio:

$$\epsilon_r = \lim_{E_{\text{ext}} \to 0} \frac{E_{\text{ext}}}{E} \tag{3.2}$$

Note that in general the dielectric constant is a tensor, i.e. the dielectric response depends on the direction of the applied field. As we are only interested in electric fields along the surface normal we only calculated the dielectric constant for this direction. Our calculations were performed with an external field in the z-direction of $E_{\text{ext}} = 0.1$ V/Å. The response field was determined from a linear fit of the Hartree potential difference inside the slab between the perturbed system and the system without applying an external field (see Fig. 3.4). The obtained values also depend on the applied density functional. For HSE ($\omega = 0.2$ Å^{-1}, $\alpha = 0.375$) we find $\epsilon_r^{\text{HSE}*} = 3.43$, and for PBE $\epsilon_r^{\text{PBE}} = 5.19$. The HSE value is close to the experimental value of $\epsilon_r(\infty) = 3.72$[120].
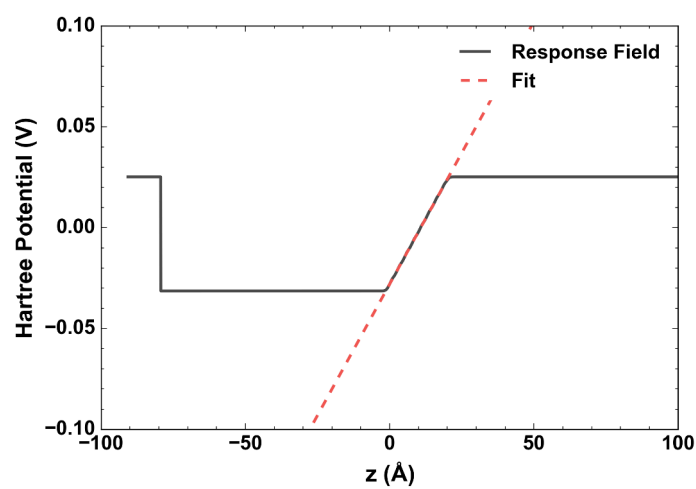
FIGURE 3.4: Difference of the plane integrated Hartree potential with and without an external electric field. The difference shows the response field $(E - E_{ext})$ build up in the ZnO slab due to the small field $(E_{ext} = 0.1 \text{ V/Å})$. The ZnO slab extends approximately from $z = 0$ to $z = 20$ Å.

Chapter 4

Molecular Probes: Organic Molecules as a Probe to Identify the Surface Structure of ZnO

4.1 Motivation

One of the biggest challenges, not only for experiments, but also for computations of ZnO interfaces, is that the exact surface structure, especially of the polar ZnO surfaces, is still not unambiguously resolved. In a collaboration with people from the groups of Norbert Koch and Frank Schreiber we aimed to contribute to this ongoing discussion by approaching the quest for the surface structure from a new side. From experimentalists a lot of insight and knowledge was obtained by Jens Niederhausen and Antoni Franco-Cañellas concerning the preparation of ZnO surface samples. X-ray standing wave (XSW) and X-ray photoelectron spectroscopy (XPS) measurements were conducted at various stages of the surface preparation process. The aim was to identify the surface structure at these stages to understand the impact of typical surface preparation techniques like sputtering or annealing. Furthermore they investigated how the surface evolves over time after those steps. The original idea of our collaboration was to compare experimental XPS spectra with surface core-level shifts calculated from DFT, to be able to identify the surface structure at the various stages. We performed calculations for many different surface structures and a constant exchange of ideas took place between me and especially Jens Niederhausen and Antoni Franco-Cañellas. However, we had to find out that from the computational side we where not able to provide unambiguous assignments, since several possible surface structures gave similar results that lie within the accuracy of the theoretically obtained core-level shifts (The challenges that emerged in simulating surface core-level shifts and some obtained results are presented in the appendix of this chapter; the experimental results from the surface preparation were published in Antoni Franco-Cañellas' dissertation[121]). Therefore no trustworthy conclusions could be drawn from comparing the

theoretically obtained shifts with experimental results, and we needed the find a new approach to gain insight into the structure of the polar ZnO surfaces. The idea emerged in discussions with Jens Niederhausen, Oliver T. Hofmann and me: We can use organic molecules as a probe for the surface. We assumed that the adsorption heights of the molecules allows us to draw conclusions concerning the surface structure of the substrate. This idea was a very elegant way to omit many computational challenges for this surfaces because adsorption heights are usually quite well reproduced by DFT, but still gives valuable insight into the surface structure. XSW measurements were conducted for PTCDI molecules adsorbed on the Zn-terminated ZnO(0001) surface to experimentally determine the adsorption heights.

4.2 Authors contribution

The idea for using probe molecules to explore ZnO surfaces originated from Jens Niederhausen. My part was to plan, perform, and analyze the theoretical calculations for the different surface structure models. By comparing the results we indeed were able to eliminate a wide range of proposed surface structures for this polar ZnO surface. Our joint findings are summarized in the following manuscript. The coordination of this project and the writing of the manuscript was mainly organized by Jens Niederhausen, who also wrote the main part of the manuscript. My contribution was in co-authoring the manuscripts, especially writing the parts about the computations and producing the images of the investigated surface models.

4.3 Manuscript

X-ray standing waves evidence lack of OH-termination at ZnO(0001) surfaces.

Jens Niederhausen[1,2], Antoni Franco-Cañellas[3], Simon Erker[4], Thorsten Schultz[2], Katharina Broch[3], Alexander Hinderhofer[3], Steffen Duhm[5], Pardeep K. Thakur[6], David A. Duncan[6], Alexander Gerlach[3], Tien-Lin Lee[6], Oliver T. Hofmann[4,7], Frank Schreiber[3], and Norbert Koch[1,2]

[1]*Helmholtz-Zentrum Berlin für Materialien und Energie GmbH,*
12489 Berlin, Germany
[2]*Humboldt-Universität zu Berlin, Institut für Physik & IRIS Adlershof, 12489 Berlin, Germany**
[3]*Institut für Angewandte Physik, Universität Tübingen, 72076 Tübingen, Germany*
[4]*Institut für Festkörperphysik, Graz University of Technology, NAWI Graz, 8010 Graz, Austria*
[5]*Institute of Functional Nano & Soft Materials (FUNSOM),*
Jiangsu Key Laboratory for Carbon-Based Functional Materials and Devices,
Soochow University, Suzhou, Jiangsu 215123, People's Republic of China
[6]*Diamond Light Source, Harwell Science and Innovation Campus, Oxfordshire OX11 0DE, UK and*
[7]*Fritz-Haber-Institut der Max-Planck-Gesellschaft, Theory Department, 14195 Berlin, Germany*
(Dated: December 29, 2018)

We present a novel way of exploiting molecules as surface structure probes. In this approach, the vertical adsorption distances of planar conjugated organic molecules are determined with the X-ray standing wave technique and compared to simulated adsorption geometries based on different models of the surface structure. Surprisingly, the obtained results for 3,4,9,10-perylenetetracarboxylicdiimide (PTCDI) on Zn-terminated ZnO(0001) (Zn-ZnO) do not agree with the popular notion of protruding hydroxyl (OH) groups for a range of surface preparations. Conversely, good agreement is found for PTCDI molecules in direct contact with the topmost Zn layer. Our findings thus assign OH groups to subsurface sites and call for a reconsideration of the prevailing surface models with important implications for the understanding and modification of electronic and morphological properties of Zn-ZnO surfaces.

The surface structure of ZnO exposed to water and hydrogen is of major importance not only for the understanding of heterogeneous catalytic processes [1–5], but also because it controls the morphologies of condensed water [6] and organic or metal adlayers [7, 8], which are relevant for self cleaning and (opto)electronic applications, respectively. Hydroxyl (OH) formation is generally found in these cases [9–12]. Zn-polar ZnO(0001) (Zn-ZnO) is the only ZnO facet that does not feature O atoms in the surface layer. Therefore, OH formation is particularly intriguing in this case and pinpointing the location of the OH groups is extremely relevant.

The most stable Zn-ZnO surface structures under typical ultra-high vacuum (UHV) conditions and room temperature have been calculated for half a OH monolayer (ML, 1 ML = 1 OH per Zn-ZnO surface unit cell) adsorbed on top of the non-reconstructed Zn-ZnO surface [5, 13]. This theoretical prediction justifies that such protruding OH groups are often employed when rationalizing results from spectroscopy and diffraction experiments [10, 11, 13–17]. Strikingly though, the protrusions so far reported in scanning probe studies had much lower abundances than 1/2 ML and an assignment to OH groups was implicitly or explicitly dismissed by the authors[18]. However, a problem with scanning probe experiments is that often the surface structure can be unambiguously identified for only a part of the probed surface area. This is particularly true for Zn-ZnO, for which atomic resolution is only occasionally obtained [19–21]. Further evidence is thus needed to resolve this discrepancy.

It was shown that surface structures can be probed by means of molecular adsorbates: in a pioneering work, Staemmler *et al.* confronted the binding energy of CO found from thermal desorption spectroscopy with calculated binding energies for different surface models and could successfully solve several ZnO surface structures [22]. However, CO does not stick to hydroxylated Zn-ZnO surfaces even at temperatures as low as 50 K, leaving the OH location at Zn-ZnO surfaces an open question [5, 23].

Here, we present an alternative approach, namely, employing a planar π-conjugated molecule [here: 3,4,9,10-perylenetetracarboxylicdiimide, PTCDI, see Fig. 1 (d)] as probe for the surface structure. To this end, we employ the X-ray standing wave technique (XSW), a powerful, but yet unexplored tool for the study of ZnO-organic semiconductor interfaces. Adsorption at room temperature is guaranteed for such large molecules (PTCDI has a footprint of approx. 10 times the surface unit cell area of Zn-ZnO) by considerable van der Waals attraction. For the PTCDI-ZnO interface, appreciable interaction well beyond pure physisorption was reported [24]. Therefore, PTCDI can be expected to wet the Zn-ZnO surface well and films in the sub-monolayer regime can be used to probe a large fraction of the surface area. This is an important prerequisite for arriving at results that are truly representative of the Zn-ZnO surface structure.

To achieve maximal sensitivity to the surface struc-
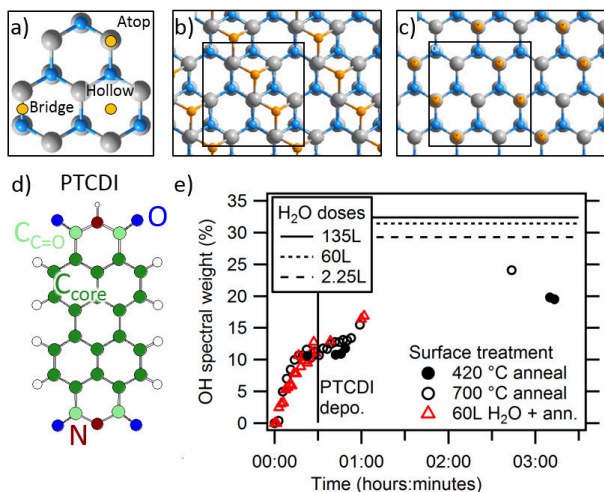
FIG. 1. (a) Top view of the three possible adsorption sites of Zn-ZnO-terminating OH groups. Of these, the hollow and top site are considered in this work. The top-views of the corresponding models *2* and *3* that both feature a 1/2 ML OH coverage are shown in (b) and (c), respectively. (d) Chemical structures of PTCDI in its protonated (top) and deprotonated state (bottom). (e) OH spectral contribution determined from O1s core level fits (hν = 700 eV, *cf.* Suppl. Fig. 4). Data points present the OH signal evolution as function of time after the respective annealing was stopped. The horizontal lines show the OH spectral weight after water exposures of the indicated doses. The vertical line indicates when PTCDI was deposited onto sample *C*. For samples A and B, the deposition was done after four hours, i.e., beyond the axis range.

ture, we employ adsorption geometries to compare experiment and theory instead of binding energies. By doing so, this approach is lenient toward details of the molecule-ZnO interaction: The electronic structure calculations of PTCDI/ZnO in Ref. 24 report very different binding energies when Zn interstitials or O vacancies are assumed as dopants in ZnO (2.3 eV vs. 1.1 eV). In contrast, the same work predicts the PTCDI adsorption distance to be only very slightly affected by the dopant species. This shows that accurate binding energies can only be calculated if the electronic surface structures are established, whereas the geometric adsorption structure is much more robust. Vice versa, different surface structures can result in identical binding energies: Different ZnO facets were used in Ref. 24 and "the experimental data were found to be insensitive to the specific surface chosen", suggesting that binding energy differences might be hard to resolve experimentally. In contrast, using structural observables promises to be able to distinguish different surface structures with similar reactivity towards the molecular probe.

We consider three different Zn-ZnO surface models for the simulation of PTCDI adsorption geometries. They consider a bare Zn surface and two different surfaces with OH adsorbates. These models represent the controversial

discussion of the Zn-ZnO surface in the literature, as rationalized below.

In a purely ionic treatment, a stoichiometric Zn-ZnO surface is not neutral but carries a positive 1/2 extra elementary charge per surface Zn atom that gives rise to a divergent surface energy. Neutral surfaces can be achieved with surface stoichiometries that have 1/4 ML less Zn than O atoms in the form of defects and/or surface reconstructions [5, 23]. Indeed, stoichiometric surfaces have not been observed by scanning probe microscopy. The structures that have been resolved can be roughly separated in microscopically reconstructed but macroscopically flat surface areas [19, 20, 25] and areas that are reconstructed into triangular islands and holes (and thus macroscopically rough) and additionally exhibit high densities of vacancies and pits [20, 21, 25–29]. The models that were proposed to rationalize the structures observed in scanning probe experiments often do not explicitly consider OH groups. However, the presence of OH in the surfaces investigated in these experiments can be expected even if the samples were not intentionally exposed to water or hydrogen. This is because under typical UHV conditions, residual water and H$_2$, as well as atomic H created by the pressure gauge filament and/or ion getter pump [7, 26, 30] amount to non-intentional doses of 1 langmuir (L) on the timescale of a few hours. Exposure of clean Zn-ZnO surfaces to only a few L of hydrogen or water results in clear changes of the surface structure [2, 31] and OH fingerprints are consistently found for non-intentionally exposed samples [11, 25, 32]. If the OH presence was explicitly accounted for in the structures resolved by scanning probe experiments, those subsurface sites were used where oxygen atoms would otherwise be undercoordinated, e.g., next to single Zn vacancies [25] or at the edge of the triangular islands/holes [23]. With this approach, up to a full ML OH can be accounted for: By removing three Zn atoms from the first layer and one O atom from the subsurface layer, the "ZnO3-H sat" structure simulated by Valtiner *et al.* represents the smallest possible triangular geometry and has all remaining subsurface oxygen sites located at the edge and filled with OH [23].

Importantly, the footprint of PTCDI is too large to fit into the small surface openings (pits, rows, and stripes of missing atoms as well as individual vacancies) but still small compared to the flat parts of the macroscopically rough surface areas. **Model *1*** thus employs bare Zn as the surface layer (see Fig. 1) and is expected to be representative for realistic Zn-ZnO surfaces with a terminating Zn layer. It does not explicitly include OH groups, but implicitly limits them to subsurface sites.

Models *2* and *3* represent Zn-ZnO surfaces for which compensating the positive surface charge is achieved via negatively charged OH adsorbates instead of surface reconstructions. Several OH locations have been suggested: In an early work, Wander and Harrison located the OH

groups atop the terminal Zn atoms, which is where the next oxygen atoms would be found if simply extending the bulk lattice [1]. Later studies reported that the fcc hollow site is significantly more stable [3, 5, 13]. A surface model that assumes vacancies in the top Zn layer favors OH in the bridge site between the two remaining Zn atoms [32]. Finally, a recent work reports both bridge and fcc hollow sites as reasonable OH locations for ideal surfaces [33]. To account for the two extremes in terms of degree of protrusion and OH bond orientation (perpendicular vs. almost parallel to the surface, *cf.* Fig. 2), models *2* and *3*, assume (2×1) overlayers of OH groups in fcc hollow sites and atop sites, respectively (see Fig. 1).

The chemical structure of PTCDI in contact with ZnO is not fully established. X-ray photoelectron spectroscopy (XPS) yields chemical shifts of PTCDI's C1s and N1s core-level binding energies at the PTCDI/ZnO interface compared to bulk-like PTCDI. From ultraviolet photoelectron spectroscopy (UPS), additional occupied density of states in the HOMO-LUMO gap in the interface regime is apparent (see Suppl. Figs. 4 and 7 as well as Refs. 24 and 34 for XPS and UPS results). These observations are equivalent to those reported for the PTCDI/TiO$_2$ interface, for which a deprotonation reaction of PTCDI at the oxide surface was suggested as possible origin [35]. However, the same observations were also reported for N,N'-dibutylperylene-3,4,9,10-dicarboxyimide (C$_4$-PTCDI) on ZnO [34], for which the N atoms are bound to dibutyl groups and a deprotonation reaction is not possible. Charge redistribution rather than a change of the PTCDI's chemical structure was thus proposed to explain the chemical shifts [24, 34].

In order to cover both possible chemical structures of the molecular probe, we simulated models *1–3* for protonated and deprotonated PTCDI. The associated structural differences represent the uncertainty that derives from the unknown molecule-substrate interaction.

We used the FHI-aims electronic structure code [36] to carry out quantum mechanical calculations based on density functional theory (DFT) of the proposed models. The Perdew-Burke-Ernzerhof (PBE) exchange-correlation functional [37] was employed, together with the method of Tkatchenko and Scheffler (vdW-TS) [38] with parameters optimized for ZnO [39] to model the long-range London dispersion interactions. Element specific *tight* settings for the integration grids and basis sets were used, which ensured convergence within 1 meV for the total energy of the primitive bulk unit cell. A reciprocal k-grid of $24 \times 24 \times 18$ was used for the primitive hexagonal unit cell and scaled accordingly for surface calculations such that a similar spacing of k-points in the reciprocal space was maintained. Optimizations of the structures were performed until residual forces on all atoms were less than 10^{-3} eV/Å. With this set-

tings, we obtained lattice constants of $a = 3.278$ Å and $c = 5.291$ Å for the bulk ZnO unit cell, which is in good agreement with the experimental values of $a = 3.250$ Å and $c = 5.204$ Å [40, 41]. All surfaces in this study were modeled by surface slabs consisting of six ZnO double-layers, having a surface area of 335.0 Å^2 (6×6 primitive unit cells). The bottom side of the slab was passivated by attaching pseudo-hydrogens of nuclear and electronic charge $\pm 1/2$ onto the oxygen atoms in order to enforce charge neutralization for this side of the slab and avoid the buildup of an unphysical dipole moment through the slab [8]. Surface structure optimizations were performed keeping two bottom layers fixed at their relaxed bulk positions and relaxing the rest of the slab as well as the molecule during the optimization. A vacuum region of > 50 Å was added and a dipole correction was applied to avoid unphysical interactions between the periodic images.

For each model, several possible local molecular adsorption sides were considered based on chemical intuition. Here we report only the energetically lowest structure for each model, however, adsorption distances were similar for other possible adsorption sites. For model *3*, the oxygen atoms of the OH groups were constrained to stay on top of surface Zn atoms, because otherwise they relax into the energetically more favorable hollow position (model *2*). For the position of the top-most oxygen layer, the average of all top-most oxygen atoms within the unit cell was used.

The theoretically calculated adsorption distances for the three models were confronted with PTCDI's vertical adsorption distances that can be determined with high accuracy with the XSW technique [42, 43]. XSW employs a crystalline substrate to create an X-ray standing wave field that extends above the surface. The atoms of an adsorbate can be located by monitoring their photoabsorption in the X-ray field while the phase of the standing wave is continuously shifted (by a total of π) via scanning through the Bragg condition of the employed reflection [here: ZnO(0002)]. Using XPS to detect the absorption signal enables selectively probing individual chemical elements and even different chemical species of the same element [42–45]. Fitting the XSW scans based on the dynamical theory of X-ray diffraction yields the coherent position (P_H) and coherent fraction (f_H) as fit parameters that quantify the location of a chemical species within the standing wave field and its positional disorder, respectively. The partial photoelectron yield was separately resolved for carbonyl C (C$_{C=O}$) and N (both representative of PTCDI's functional groups) and all other C (C$_{core}$, representative of its perylene core), O and Zn of ZnO (O$_{ZnO}$ and Zn$_{ZnO}$), as well as hydroxyl O (O$_{OH}$). The vertical distance between two species A and B can then be calculated according to

$$d_{A,B} = d_H(n + P_{H,B} - P_{H,A}) \,, \tag{1}$$

where $d_H = 2.602$ Å is the diffraction plane spacing for $H = (0002)$ and $P_{H,A}$ and $P_{H,B}$ are the coherent positions for species A and B, respectively. $n = 0, 1, 2, \ldots$ is a free parameter that reflects the fact that the XSW technique is only sensitive to the vertical position modulo the period of the standing wave field. XSW experiments were performed at the beamline I09 of the Diamond Light Source [46].

Zn-ZnO surfaces were prepared according to three different recipes (labeled A–C). These represent the range of annealing temperatures employed in most previous Zn-ZnO surface studies and also include water exposure as additional surface treatment. All crystals were hydrothermally grown (*CrysTec*, Berlin) and annealed under atmospheric conditions at 1000 °C for two hours before being loaded into the UHV system. This procedure is designed to yield crystals with flat and relatively clean surfaces [47] as well as very low mosaicity. As shown in Suppl. Fig. 8, the resulting surfaces exhibited a $\left(\sqrt{3} \times \sqrt{3}\right) R30°$ low-energy electron diffraction pattern that remained after an initial 10 min annealing step at ca. 420 °C but was completely removed by 15 min Ar^+ sputter-cleaning (E = 0.5 keV). The sputter procedure successfully removes surface contaminants, but causes an effective outward relaxation of the ca. 10 topmost ZnO double layers due to Ar incorporation [48]. After undergoing the above procedure, samples A and B underwent final 10 min annealing steps at ca. 420 °C and 600 °C, respectively.

Sample C was used to elucidate the OH formation dynamics under UHV conditions and the effect of deliberate water exposure. To this end, it was first treated following the same protocol as used for sample A, followed by a 700 °C annealing. Subsequently, the UHV chamber was backfilled through a leak valve at a pressure of 5×10^{-8} mbar with water that had been cleaned by several freeze/thaw cycles. Two water exposures were performed with respective doses of 60 L and 135 L. Doses of this magnitude were reported to result in significant surface topology changes towards a disordered surface layer [31]. Each water exposure was followed by a 700 °C annealing. We monitored the OH fingerprint in the O1s spectrum (*cf.* Suppl. Fig. 4) following every post-sputtering annealing. For the 700 °C annealings we also monitored the sample while it was heated and could confirm complete OH desorption (see Suppl. Fig. 4). The OH intensity evolution with time is presented in Fig. 1 (e) and shows a gradual reformation of OH groups from the UHV environment after each annealing and suggests a saturation at the intensities observed after deliberate water dosing, also included in the figure. Within the experimental error of ca. 10% that mostly results from minor radiation damage, no changes were observed when comparing the successive 420 °C and 700 °C annealing treatments of the pristine surface (directly after the sputter procedure) as well as the 700 °C annealing after the

TABLE I. Theoretically calculated adsorption heights (in Å) of PTCDI and OH on different Zn-ZnO surface structures and for different PTCDI chemical structures. The adsorption heights are measured from the top-most oxygen layer of the ZnO crystal.

Model	*1*		*2*		*3*	
PTCDI state	prot.	deprot.	prot.	deprot.	prot.	deprot.
N	2.67	2.55	5.10	4.51	5.37	5.01
$\mathbf{C_{C=O}}$	2.82	2.81	5.09	4.69	5.38	5.17
$\mathbf{C_{core}}$	3.23	3.45	5.20	5.26	5.48	5.50
$\mathbf{O_{OH}}$	–	–	1.93	1.92	2.43	2.43

60 L water exposure. [49]

Submonolayer films of PTCDI were deposited from a custom-built Knudsen cell onto samples A and B ca. 4 hours after they had undergone their final annealing. As can be extrapolated from our OH-vs-time analysis, this marks just enough time to roughly saturate their surface with OH. In contrast, the time was reduced to only 30 min for sample C in order to increase the chance that a relevant fraction of PTCDI adsorbs onto OH-free surface patches. We estimate that the surface of sample C was OH-depleted by at least 50% during PTCDI deposition compared to samples A and B.

The theoretically calculated adsorption distances for models *1–3* are given in Tab. I and Tab. II reports the XSW results for samples A–C. To compare experiment and theory, one could select n in Eq. (1) according to the respective surface model, as illustrated in Fig. 1.

A more concise and established [42, 45, 50] way is to instead plot the data in an Argand diagram by using P_H as angle, with a full circle set to 1 for clarity. To that end, the theoretical distances are converted into quasi coherent positions via $d_{A,B}/d_0$. A common reference plane for theoretical and experimental data is achieved by subtracting P_H of a selected reference species. The ΔP_H values obtained this way for the three PTCDI signals are presented in Fig. 3. For Figs. 3 (a) and (b), O_{ZnO} was used as reference, whereas Fig. 3 (c) shows the XSW data referenced to O_{OH}. For the experimental values, f_H was used as the radius, whereas for the theoretical values the radius was set to 1.

The comparison between theory and experiment is guided by the following observables:

Adsorption geometry: Generally, the XSW fits are of very high quality (*cf.* Suppl. Fig. 5) and the f_H values are representative of face-on molecules. However, Zn-ZnO surfaces are generally rather disordered. A recent theoretical study even suggests that "disorder is the source of the stability", with ordered reconstructions being merely the result of the surface energy distributions associated with particular values of the chemical potential [51]. A high degree of disorder is indeed characteristic for many of the morphologies reported by means of scan-
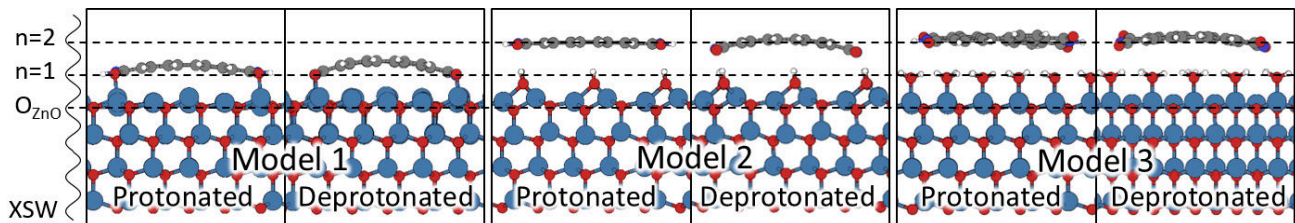
FIG. 2. The six calculated geometries for three different Zn-ZnO surface models and two different chemical structures of PTCDI (see text for description). The X-ray standing wave (XSW) is included to illustrate the ambiguity of the vertical adsorption distances determined with the XSW technique. The height of the O_{ZnO} layer, used as reference in Figs. 3 (a) and (b), is also indicated.

TABLE II. XSW results for PTCDI/Zn-ZnO (samples A–C). The carbonyl O of PTCDI ($O_{C=O}$) has a very similar core-level binding energy as O_{OH} and thus only the joint signal from both species can be determined for the PTCDI/Zn-ZnO system. To check for consistency, we confirmed that P_H for the joint signal is in between those for O_{OH} before PTCDI adsorption and $C_{C=O}$. The XSW scans before PTCDI deposition were used for the substrate signals unless otherwise noticed. We confirmed that the O_{ZnO} signal stayed unchanged by PTCDI adsorption. The sputter-induced outward relaxation is only completely removed for the extensively annealed sample C and needs to be taken into account for samples A and B when deriving the PTCDI adsorption heights with respect to the ZnO lattice [48]. Values of f_H that are larger than 1 are not physically meaningful and stem from the uncertainty of the fit.

Sample	A		B		C	
	P_H	f_H	P_H	f_H	P_H	f_H
O_{ZnO}	0.88[a]	0.81	0.82[a]	0.89	0.77	0.94
O_{OH}	0.78	0.54	0.63	0.60	0.66	0.67
Zn_{ZnO}	0.09[a]	0.85	0.04[a]	0.98	0.00[b]	1.01[b]
N	0.87	0.55	0.81	0.81	0.74	1.07
$C_{C=O}$	0.97	0.65	0.92	0.80	0.87	0.71
C_{core}	0.11	0.28	0.15	0.35	1.00	0.55

[a] Corrected for surface relaxations by 0.02 and 0.01 for samples A and B, respectively.
[b] Determined after PTCDI deposition

ning probe microscopy [19–21] and the same surface usually contains macroscopically flat and rough areas [19]. This explains why f_H for C_{core} is slightly lower than for perylene derivatives on coinage metals [44, 45, 50]. A significant intramolecular bending is apparent from the fact that the experimental data for C_{core}, $C_{C=O}$, and N are found at very different angles in Fig. 3 (a). The notion of bent PTCDI is also consistent with significant larger f_H values for PTCDI's functional groups than its perylene core. These observations are at variance with the simulations of protonated PTCDI on top of OH (models *2* and *3*, see Fig. 2): protonated PTCDI assumes an almost planar adsorption geometry for model *2*, and for model *3* an intramolecular twist, but no bending is observed. In contrast, the calculations for deprotonated PTCDI in-
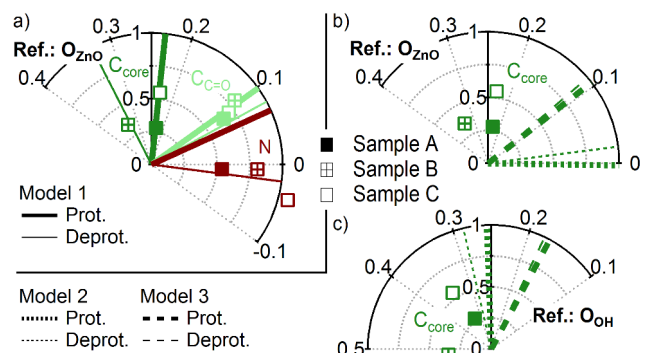
FIG. 3. (a) Experimentally determined ΔP_H, referenced to O_{ZnO}, and f_H for the PTCDI signals (symbols) and the corresponding theoretical values (lines) for surface model *1*. The data is presented by employing ΔP_H as angle (full circle = 1) and f_H as radius. (b) The same as (a) but for models *2* and *3* and for C_{core} only. (c) The same as (b) but using O_{OH} as reference height.

deed predict bent molecules for the same two models, induced by hydrogen bond formation between the OH groups and PTCDI's O and N atoms. In the case of bare Zn-ZnO (model *1*), already protonated PTCDI exhibits a bent adsorption geometry, which, however, is significantly enhanced in the case of deprotonated PTCDI.

OH depletion-induced effect: Sample C allows to test whether the OH-depletion has an effect on the adsorption structure that can, in turn, be related to protruding OH. Assuming that PTCDI molecules adsorb on top of OH groups in the case where these saturate the surface, the OH-depletion should result in a trend towards *larger* ΔP_H – despite an expected *decrease* in $d_{A,B}$. This is because of the different n in Eq. (1) required for models *2* and *3* and model *1*, respectively (*cf.* Fig. 2). PTCDI films on both the OH-depleted sample C as well as the OH-saturated samples A and B give overall similar ΔP_H values, but the ΔP_H variations when comparing samples A–C are ca. twice of the experimental error bars found, e.g., for perylene derivatives on coinage metals [44, 45, 50]. However, in contrast to the expectation stated above, sample C does not yield smaller ΔP_H val-

ues than samples *A* and *B*. In addition, the observed difference with respect to samples *A* and *B* is similar to the ΔP_H variations between the two OH-saturated samples *A* and *B*. The ΔP_H variations between the three samples therefore rather stem from differences in the samples' surface roughness that, as discussed above, can indeed be expected in view of the large number of possible surface reconstructions when also taking into account that the composition of the reconstructions plausibly depends on the sample history.

Adsorption heights with respect to O_{ZnO} and O_{OH}: Starting with models *2* and *3* and using O_{ZnO} as reference [Fig. 3 (b)], we find that both models are incompatible with the experimental ΔP_H for C_{core}. The data for $C_{C=O}$ and N is included in the Suppl. Fig. 6. We refrain from showing them here, because when using the structures of deprotonated and protonated PTCDI as limits and permitting all intermediate geometries as conceivable configurations, the theoretical ΔP_H uncertainty (apparent from Fig. 2) is too large to warrant a meaningful comparison. Since models *2* and *3* explicitly include OH, we can use O_{OH} as alternative reference to obtain an independent confrontation of experiment and theory. This is particularly interesting for the model that deviates less from experiment when referenced to O_{ZnO}, namely model *3*. Even though due to the lower data quality of O_{OH} vs. O_{ZnO} the experimental values in Fig. 3 (c) have a larger spread than those shown in Fig. 3 (b), it is clear that model *3* is at variance with experiment also when using the OH groups as reference. The agreement is better for model *2*, the difference apparently being the hydrogen atoms of the OH groups pointing upwards and acting as spacer in this case. However, in summary both models predict significantly too low adsorption heights. Since we covered the highest and lowest OH adsorption sites with respect to the topmost Zn layer, this assessment is going to hold for alternative configurations of terminating OH as well. The agreement between theory and experiment is much better for model *1*. Within the experimental uncertainty discussed above, the XSW results and the simulated values for model *1* are consistent. A better agreement for N is achieved in the case of deprotonated PTCDI compared to protonated PTCDI. However, we want to stress that details of the interfacial interaction, e.g., the effect of ZnO surface dopants discussed in Ref. 24, will likely affect the adsorption geometry and prevents to identify PTCDI's chemical structure from the current data. Nonetheless, the drastically better agreement for model *1* than for models *2* and *3* shows that the geometric structure prediction for PTCDI is sufficiently accurate even when the chemical state is not *a priori* known, because the adsorption distance is significantly more influenced by the OH group configuration.

To rationalize the absence of protruding OH groups for the investigated Zn-ZnO surfaces, we consider their genesis, starting with sputter/annealing-cleaned OH-free

Zn-ZnO surfaces. Electronic neutrality of such surfaces is guaranteed by a suitable surface stoichiometry via one of several possible surface reconstructions. Once the annealing is stopped and the surface temperature lowered to room temperature, the formation of OH groups is observed. Possible reaction pathways are water dissociation at the surface [33, 52], hydrogenation and consecutive surface migration of subsurface oxygen atoms [53], and Zn etching [54]. While non-reconstructed surfaces with a half OH overlayer are predicted to give the lowest total energy [5, 13], two driving forces potentially stabilize the reconstructed surfaces during OH formation: Firstly, kinetic barriers severely impede reaching thermodynamic equilibrium. This was emphasized in Ref. 23 by Valtiner *et al.*, who deemed the structural changes needed to transform surfaces that exhibit triangular reconstructions into ideal Zn-ZnO surfaces with OH termination "very unlikely within the constraints of the performed UHV experiments, if not impossible.". Secondly, as reported by Iachella *et al.*, a OH surface concentration of > 0.5 ML can be sustained only with a reconstructed surface [33], whereas saturation at 1/2 ML OH is predicted for non-reconstructed Zn-ZnO [5, 33, 52]. OH surface concentrations exceeding 1/2 ML are indeed suggested by experiments and a value of ca. 1 ML OH was determined for water- or hydrogen-exposed Zn-ZnO by XPS [11, 12] and nuclear reaction analysis [55], although with a significant uncertainty.

In conclusion, we have introduced a novel scheme to determine surface structures via the adsorption geometry of molecular probes. We exploit this method to study Zn-ZnO surfaces and find the data to be not consistent with the common notion of the formation of protruding OH groups on sputter/annealing-cleaned Zn-ZnO surfaces. Our findings instead strongly hint towards OH in subsurface sites. In addition, this work lays the groundwork for employing XSW as a powerful tool to elucidate the still elusive chemical and structural details at hybrid inorganic-organic interfaces.

* jens.niederhausen@helmholtz-berlin.de

[1] A. Wander and N. M. Harrison, J. Chem. Phys. **115**, 2312 (2001), https://doi.org/10.1063/1.1384030.

[2] C. Wöll, J. Phys.: Condens. Matter **16**, S2981 (2004).

[3] B. Meyer, Phys. Rev. B **69**, 045416 (2004).

[4] C. Wöll, Prog. Surf. Sci. **82**, 55 (2007).

[5] G. Kresse, O. Dulub, and U. Diebold, Phys. Rev. B **68**, 245409 (2003).

[6] M. M. Gentleman and J. A. Ruud, Langmuir **26**, 1408 (2010), pMID: 20000328, https://doi.org/10.1021/la903029c.

[7] O. Dulub, L. A. Boatner, and U. Diebold, Surf. Sci. **504**, 271 (2002).

[8] B. Meyer and D. Marx, Phys. Rev. B **69**, 235420 (2004).

[9] H. Noei, H. Qiu, Y. Wang, E. Löffler, C. Wöll, and M. Muhler, Phys. Chem. Chem. Phys. **10**, 7092 (2008).

[10] M. Valtiner, S. Borodin, and G. Grundmeier, Phys. Chem. Chem. Phys. **9**, 2406 (2007).

[11] R. Heinhold, G. T. Williams, S. P. Cooil, D. A. Evans, and M. W. Allen, Phys. Rev. B **88**, 235315 (2013).

[12] B. S. Mun, Z. Liu, M. A. Motin, P. C. Roy, and C. M. Kim, Int. J. Hydrogen Energy **43**, 865 (2018).

[13] M. Valtiner, M. Todorova, G. Grundmeier, and J. Neugebauer, Phys. Rev. Lett. **103**, 065502 (2009).

[14] C. M. Schlepütz, Y. Yang, N. S. Husseini, R. Heinhold, H.-S. Kim, M. W. Allen, S. M. Durbin, and R. Clarke, J. Phys.: Condens. Matter **24**, 095007 (2012).

[15] L. L. Kelly, D. A. Racke, P. Schulz, H. Li, P. Winget, H. Kim, P. Ndione, A. K. Sigdel, J.-L. Brédas, J. J. Berry, S. Graham, and O. L. A. Monti, J. Phys.: Condens. Matter **28**, 094007 (2016).

[16] S. Ito, T. Shimazaki, M. Kubo, H. Koinuma, and M. Sumiya, J. Chem. Phys. **135**, 241103 (2011), https://doi.org/10.1063/1.3675680.

[17] N. Abedi and G. Heimel, Phys. Status Solidi B **252**, 755 (2015).

[18] The protrusions were instead identified as zinc-hydride in the case of the 3×1 missing row phase [19] and as oxygen adatoms for so-called "eyes" found on the triangular islands [29].

[19] S. Torbrügge, F. Ostendorf, and M. Reichling, J. Phys. Chem. C **113**, 4909 (2009), https://doi.org/10.1021/jp804026v.

[20] J. Dumont, B. Hackens, S. Faniel, P.-O. Mouthuy, R. Sporken, and S. Melinte, Appl. Phys. Lett. **95**, 132102 (2009), https://doi.org/10.1063/1.3238288.

[21] F. Ostendorf, S. Torbrügge, and M. Reichling, Phys. Rev. B **77**, 041405 (2008).

[22] V. Staemmler, K. Fink, B. Meyer, D. Marx, M. Kunat, S. Gil Girol, U. Burghaus, and C. Wöll, Phys. Rev. Lett. **90**, 106102 (2003).

[23] M. Valtiner, M. Todorova, and J. Neugebauer, Phys. Rev. B **82**, 165418 (2010).

[24] P. Winget, L. K. Schirra, D. Cornil, H. Li, V. Coropceanu, P. F. Ndione, A. K. Sigdel, D. S. Ginley, J. J. Berry, J. Shim, H. Kim, B. Kippelen, J.-L. Brédas, and O. L. A. Monti, Adv. Mater. **26**, 4711 (2014).

[25] M. Hellström, I. Beinik, P. Broqvist, J. V. Lauritsen, and K. Hermansson, Phys. Rev. B **94**, 245433 (2016).

[26] O. Dulub, L. A. Boatner, and U. Diebold, Surf. Sci. **519**, 201 (2002).

[27] O. Dulub, U. Diebold, and G. Kresse, Phys. Rev. Lett. **90**, 016102 (2003).

[28] J. H. Lai, S. H. Su, H.-H. Chen, J. C. A. Huang, and C.-L. Wu, Phys. Rev. B **82**, 155406 (2010).

[29] H. Xu, L. Dong, X. Q. Shi, M. A. Van Hove, W. K. Ho, N. Lin, H. S. Wu, and S. Y. Tong, Phys. Rev. B **89**, 235403 (2014).

[30] T. Becker, S. Hövel, M. Kunat, C. Boas, U. Burghaus, and C. Wöll, Surf. Sci. **486**, L502 (2001).

[31] A. Önsten, D. Stoltz, P. Palmgren, S. Yu, M. Göthelid, and U. O. Karlsson, J. Phys. Chem. C **114**, 11157 (2010), https://doi.org/10.1021/jp1004677.

[32] H. Li, L. K. Schirra, J. Shim, H. Cheun, B. Kippelen, O. L. A. Monti, and J.-L. Brédas, Chemistry of Materials **24**, 3044 (2012), http://dx.doi.org/10.1021/cm301596x.

[33] M. Iachella, J. Cure, M. Djafari Rouhani, Y. Chabal, C. Rossi, and A. Estève, J. Phys. Chem. C **0**, null (2018), https://doi.org/10.1021/acs.jpcc.8b04967.

[34] L. K. Schirra, "Charge transfer at metal oxide/organic interfaces," PhD thesis (2012).

[35] V. Lanzilotto, G. Lovat, G. Fratesi, G. Bavdek, G. P. Brivio, and L. Floreano, J. Phys. Chem. Lett. **6**, 308 (2015), pMID: 26263468, https://doi.org/10.1021/jz502523u.

[36] V. Blum, R. Gehrke, F. Hanke, P. Havu, V. Havu, X. Ren, K. Reuter, and M. Scheffler, Comput. Phys. Commun. **180**, 2175 (2009).

[37] J. P. Perdew, K. Burke, and M. Ernzerhof, Phys. Rev. Lett. **77**, 3865 (1996).

[38] A. Tkatchenko and M. Scheffler, Phys. Rev. Lett. **102**, 073005 (2009).

[39] O. T. Hofmann, J.-C. Deinert, Y. Xu, P. Rinke, J. Stähler, M. Wolf, and M. Scheffler, J. Chem. Phys. **139**, 174701 (2013), http://dx.doi.org/10.1063/1.4827017.

[40] H. Karzel, W. Potzel, M. Köfferlein, W. Schiessl, M. Steiner, U. Hiller, G. M. Kalvius, D. W. Mitchell, T. P. Das, P. Blaha, K. Schwarz, and M. P. Pasternak, Phys. Rev. B **53**, 11425 (1996).

[41] D. C. Reynolds, D. C. Look, B. Jogai, C. W. Litton, G. Cantwell, and W. C. Harsch, Phys. Rev. B **60**, 2340 (1999).

[42] D. P. Woodruff, Rep. Prog. Phys. **68**, 743 (2005).

[43] A. Gerlach, C. Bürker, T. Hosokai, and F. Schreiber, "X-ray standing waves and surfaces x-ray scattering studies of molecule-metal interfaces," in *The Molecule-Metal Interface* (Wiley-Blackwell, 2013) Chap. 6, pp. 153–172.

[44] A. Franco-Cañellas, Q. Wang, K. Broch, D. A. Duncan, P. K. Thakur, L. Liu, S. Kera, A. Gerlach, S. Duhm, and F. Schreiber, Phys. Rev. Materials **1**, 013001 (2017).

[45] B. Stadtmüller, M. Willenbockel, S. Schröder, C. Kleimann, E. M. Reinisch, T. Ules, S. Soubatch, M. G. Ramsey, F. S. Tautz, and C. Kumpf, Phys. Rev. B **91**, 155433 (2015).

[46] T.-L. Lee and D. A. Duncan, Synchrotron Radiation News **31**, 16 (2018), https://doi.org/10.1080/08940886.2018.1483653.

[47] J. Götzen and G. Witte, Appl. Surf. Sci. **258**, 10144 (2012).

[48] The corresponding XSW-based analysis will be detailed in a forthcoming publication.

[49] In contrast, the sticking coefficient of H_2 was reported to increase by three orders of magnitude by

the first hydrogen exposure/thermal desorption cycle of sputter/annealing-cleaned Zn-ZnO [30]. Such a high sensitivity to the sample history is clearly not found in the current case even though it was shown that the water dose used in the current experiment and the H_2 dose of $> 10^4$ L in Ref. 30 both result in similar surface topology changes towards a disordered surface layer [31, 56]. Thus, the disordered surface topology assists adsorption much more in the case of the less reactive H_2 than for water and atomic hydrogen, which are the main sources for OH formation in the current UHV environment (base pressure $= 3 \times 10^{-10}$ mbar; running ion getter pump and hot-filament ionization gauge, both out of line of sight of the sample).

[50] C. Bürker, N. Ferri, A. Tkatchenko, A. Gerlach, J. Niederhausen, T. Hosokai, S. Duhm, J. Zegenhagen, N. Koch, and F. Schreiber, Phys. Rev. B **87**, 165443 (2013).

[51] D. Mora-Fonz, T. Lazauskas, M. R. Farrow, C. R. A. Catlow, S. M. Woodley, and A. A. Sokol, Chem. Mater. **29**, 5306 (2017), https://doi.org/10.1021/acs.chemmater.7b01487.

[52] H. Ye, G. Chen, H. Niu, Y. Zhu, L. Shao, and Z. Qiao, J. Phys. Chem. C **117**, 15976 (2013), https://doi.org/10.1021/jp312847r.

[53] K. Nishidate and M. Hasegawa, Phys. Rev. B **86**, 035412 (2012).

[54] K. Ozawa and K. Mase, Phys. Rev. B **83**, 125406 (2011).

[55] F. Traeger, M. Kauer, C. Wöll, D. Rogalla, and H.-W. Becker, Phys. Rev. B **84**, 075462 (2011).

[56] E. D. Batyrev and J. C. van den Heuvel, Phys. Chem. Chem. Phys. **13**, 13127 (2011).
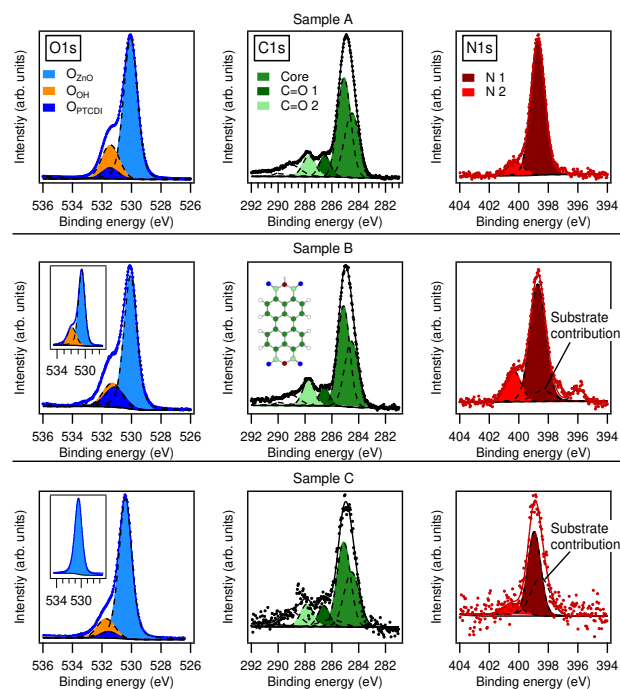
FIG. 4. XPS results for PTCDI on Zn-ZnO. For samples *B* and *C*, the O1s spectra shortly before PTCDI deposition are included as inset. The color code of the spectra derives from the colored atoms in PTCDI's chemical structure in the inset. The light and dark hues are explained in the text. $h\nu = 700$ eV

X-ray photoelectron spectroscopy

Figure 4 reports the O1s, C1s, and N1s spectra for sub-monolayer coverages of PTCDI on Zn-ZnO (samples *A*-*C*) and the O1s spectra for samples *B* and *C* before PTCDI deposition. For sample *C*, the presented spectrum was taken with the sample still at 700 °C. Afterward, the heater was turned off and the sample transferred to the deposition position. The O1s component at 1.4 eV higher binding energy corresponds to O_{OH}. The PTCDI deposition gives rise to additional spectral intensity not found for Zn-ZnO that stems from the carbonyl oxygen of PTCDI.

The C1s spectra exhibit a peak with its center at ca. 285 eV that stem from the molecule's perylene core ("Core"). Since the composition of the peak is not unambiguously established in literature and the fine structure cannot be resolved in the scans used in the XSW analysis, we did not attempt to fit the presented highly resolved spectra with a physically accurate model. Two additional peaks at higher binding energy are due to the carbon atoms in the carbonyl groups ("C=O"). Species 1 at 287.7 eV (light green) corresponds to a feature that is also found for bulk-like PTCDI in multilayer films, whereas species 2 at 286.5 eV (dark green) derives from
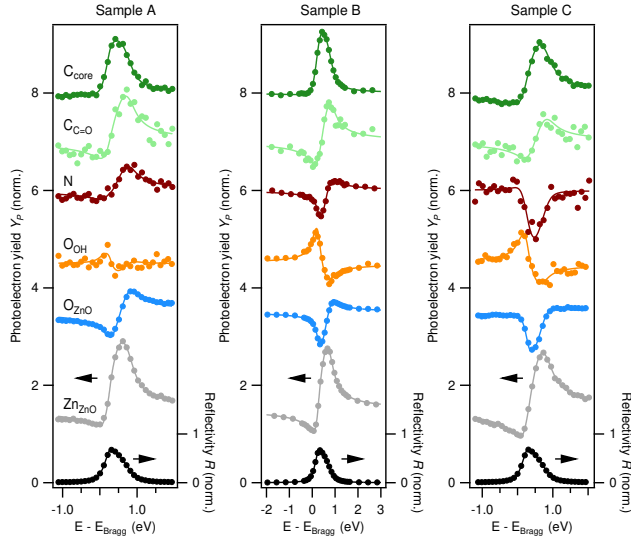
FIG. 5. XSW results for PTCDI on Zn-ZnO. The bottom curve shows the reflectivity and the upper curves present the partial photoelectron yield for the core-level peaks shown in Fig. 4. The latter are offset for clarity.

an interfacial interaction between PTCDI and Zn-ZnO and is absent from multilayer films [24, 34, 44]. Two corresponding species are also found in the N1s spectra, a minor one at ca. 400.5 eV (light red) that is the one also found for bulk-like PTCDI and a major one at 398.5 eV (dark red) that stems from the interfacial interaction [34].

X-ray standing wave

The photoelectron yield Y_p corresponding to the XPS signals shown in Fig. 4 as well as the reflectivity R are presented as function of excitation energy in Fig. 5. The Y_p data have been fitted according to

$$Y_p = 1 + R + 2\sqrt{R} f_H \cos(\nu - 2\pi P_H)$$

where ν is the relative phase of the standing wave field [42, 43].

Ultraviolet photoelectron spectroscopy

Ultraviolet photoelectron spectroscopy (UPS) measurements were performed at the Humboldt-University Berlin, using a UHV system consisting of interconnected preparation and analysis chambers and a SPECS Phoibos 100 hemispherical energy analyzer. He I (21.21 eV) radiation was used for sample excitation and a voltage of -10 V was applied between sample and analyzer during measurements of the secondary electron cut-off (SECO). PTCDI was evaporated from resistively heated quartz
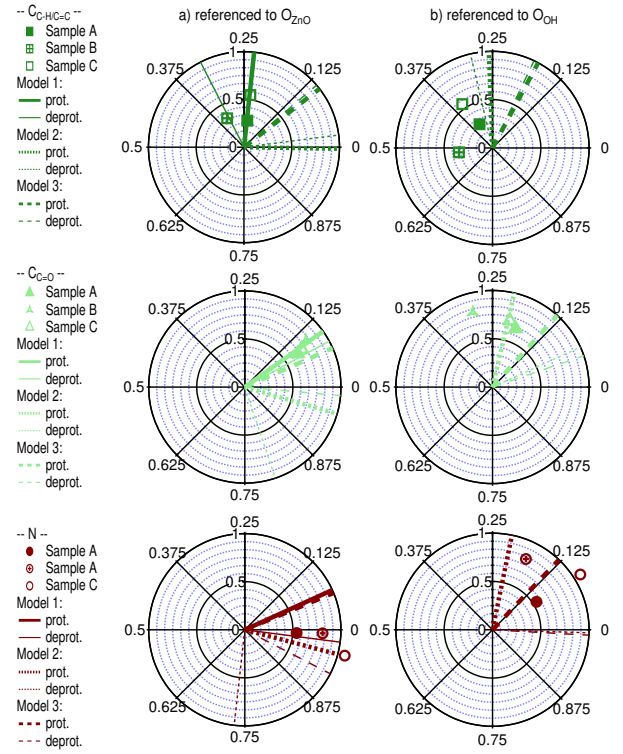
FIG. 6. (a) Experimentally determined ΔP_H, referenced to O_{ZnO}, and f_H for the PTCDI signals and the corresponding theoretical values for surface model *1-3*. The data is presented by employing ΔP_H as angle (full circle = 1) and f_H as radius. (b) The same as (a) but only for models *2* and *3* using O_{OH} as reference height.
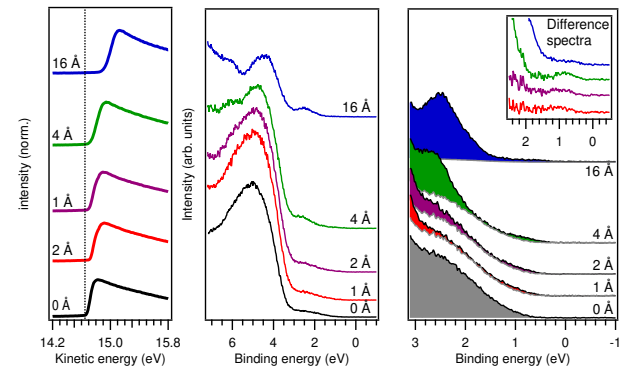
FIG. 7. UPS results for pristine Zn-ZnO (0 Å) and after deposition of PTCDI films of the indicated nominal thicknesses. The left panel shows the SECO region, whereas the right two panels show different energy ranges of the valence band region. The inset in the top right presents the spectra after the Zn-ZnO contribution was subtracted to illustrate the extra peak in the interface regime.

crucibles and the nominal thicknesses were determined with a quartz-crystal microbalance.

Figure 7 presents UPS experiments performed on the pristine Zn-ZnO surface (prepared like sample A) and after deposition of PTCDI films of increasing thicknesses. A small electron transfer to PTCDI's lowest unoccupied molecular orbital is apparent from the spectral intensity in the HOMO-LUMO gap region of PTCDI in the interface regime. This charge transfer gives rise to an interfacial dipole that causes the work function of Zn-ZnO to increase upon PTCDI film formation. Both observations are consistent with the results presented in Ref. 24. However, the atomic layer deposition-grown ZnO in this other study has a lower initial work function and thus gives rise to a more pronounced interfacial charge transfer.

LEED

Figure 8 shows the low-energy electron diffraction patterns obtained after the indicated surface preparation steps. Note that the $\left(\sqrt{3} \times \sqrt{3}\right) R30°$ pattern only disappears after the sputter-cleaning.
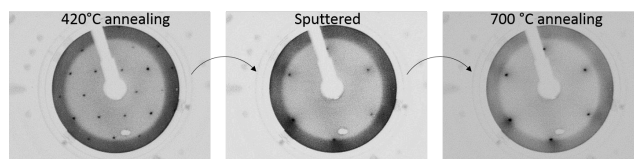
FIG. 8. LEED patterns recorded for selected surface preparation steps. $E = 97.5\ eV$

4.4   Appendix: Calculations of surface core-level shifts

As described in the introduction, from the theory side we first tried to contribute in resolving the ZnO surface structure by simulating XPS spectra for various proposed surface structures. Similar calculations for some ZnO surface structures were published in the paper of Navid Abedi et al[122]. However, some of the proposed structures were missing in this publication and additionally we also wanted to better understand the uncertainties linked to calculations of core-level shifts in DFT. We found that calculated XPS spectra strongly depend on the applied density functional. Also for the two approaches to determine surface core-level shifts, the initial state and the transition potential method, we found significant differences. Therefore, we concluded that the absolute values of the surface core-level shifts we obtained are not accurate enough to distinguish between structures resulting in similar XPS spectra. A comprehensive investigation of the nature of the uncertainties was not within the scope of my dissertation, but it would be very interesting for future studies. An expert in this field is Georg Michelitsch, formally TU Munich, who studied the simulation of X-ray spectroscopy data in his dissertation (not published yet). He found that the creation of a half-core hole in FHI-aims can be problematic. The problem arise from a possible delocalization of the core hole states in the calculations. Such delocalized core states are obviously not physical. This problem could in principle be lifted by applying localization methods like Foster-Boys[123] or maximally-localized Wannier projections[124,125,126]. However, such projections are currently not available for periodic systems in the electronic structure code FHI-aims. But also if the core hole delocalization problem is not present, additional challenges may arise from creating a core hole within a surface slab. One has to make sure that surface area of the periodically repeated slab is large enough that a missing half-core-electron has no significant effect on the surface potential, i.e. no artificial dipole layer is produced at the surface. The effect of a periodically repeated dipole on the surface potential ("collective electrostatic effects") were extensively investigated in our group[127,128]. The impact of this effects on core-level shifts is currently investigated by Thomas Taucher.

The conclusions for our project were the following: Simulated XPS spectra of ZnO surfaces are not suited to identify a specific surface structure. At best we can give trends, but the absolute values should be considered with care. Some of our XPS results are presented in the following sections.

4.4.1   Computational details

We were interested in the O1s surface core-level shifts of ZnO surface structures that have been predicted to occur under certain condition. To model the ZnO surface, we used a 6-layer slab with the bottom 3 layers fixed to their bulk equilibrium position. The top 3 layers were allowed to relax during the geometry optimization (force convergence criterion of 10^{-3} eV/Å). We investigated both, the the zinc- and oxygen-terminated polar surface. For these polar surfaces the bottom sides of the slabs were passivated with pseudo-hydrogens of nuclear and

electronic charge $\pm 3/2$ and $\pm 1/2$, respectively. We used the FHI-aims program package with numerical "tight" setting for basis sets and grids. Calculations with the PBE functional were performed with a $18 \times 18 \times 1$ k-grid for the primitive surface unit cell, and for HSE calculations ($\omega = 0.2$ Å^{-1}, $\alpha = 0.375$) with a $12 \times 12 \times 1$ k-grid (scaled accordingly for larger cells). We considered the oxygen atoms in the 5th layer (from the top) as bulk atoms. The presented core-level spectra are all aligned to the core-level energies of these bulk oxygens. For the line profiles of the core-level spectra we used a sum of Gaussian and Lorentzian distribution functions (65% Gaussian and 35% Lorentzian to account for thermal and natural line broadening) with a full width at half maximum of 1.0 eV.

4.4.2 Influence of the functional

We investigated the influence of the functional by calculating the O1s core-level spectrum for the O-terminated ZnO(000$\bar{1}$) surface with a (2×1)-H overlayer. For this surface two chemically different surface oxygen species are present at the surface: Bare oxygens and oxygens with adsorbed hydrogen atoms. We evaluated the core-level spectrum from calculations with the PBE functional as well as the HSE functional, with the corresponding lattice constants and geometries for both functionals. The core-level shifts were obtained from the initial state (IS) approximation and the transition potential (TP) approximation. For the IS approximation all binding energies can be evaluated from a single DFT calculation. For the TP approximation, three calculations were necessary to evaluate the binding energy for bulk oxygen and the two surface species. In Figure 4.1 the four obtained spectra are plotted, including the absolute values for the surface core-level shifts for the two surface species. We find that the general trend of the shifts is equal in all four simulated spectra. However, the absolute values show a significant variation up to a factor of two.

4.4.3 Surface core-level shifts of selected ZnO surfaces

In the following the simulated XPS spectra for some selected surface structures of Zn-terminated ZnO(0001) are presented. The spectra were obtained using the PBE functional and the IS approximation. The aim was to investigate the impact of adsorbed hydrogen on oxygen atoms that are present at the surface due to surface reconstructions. Adsorbed or intercalated hydrogen might be the reason for the changes in the XPS spectra occurring over time after a sputtering process of ZnO(0001) samples. Considering only the trends of the core-level shifts, our simulated spectra of the triangular reconstructed surface with hydroxyl groups at the step edges, show a good agreement with the measures XPS spectra. This corresponds to the findings described in the manuscript. Figures 4.2 - 4.5 show the calculated surface core-level spectra for selected surface structures of ZnO(0001).
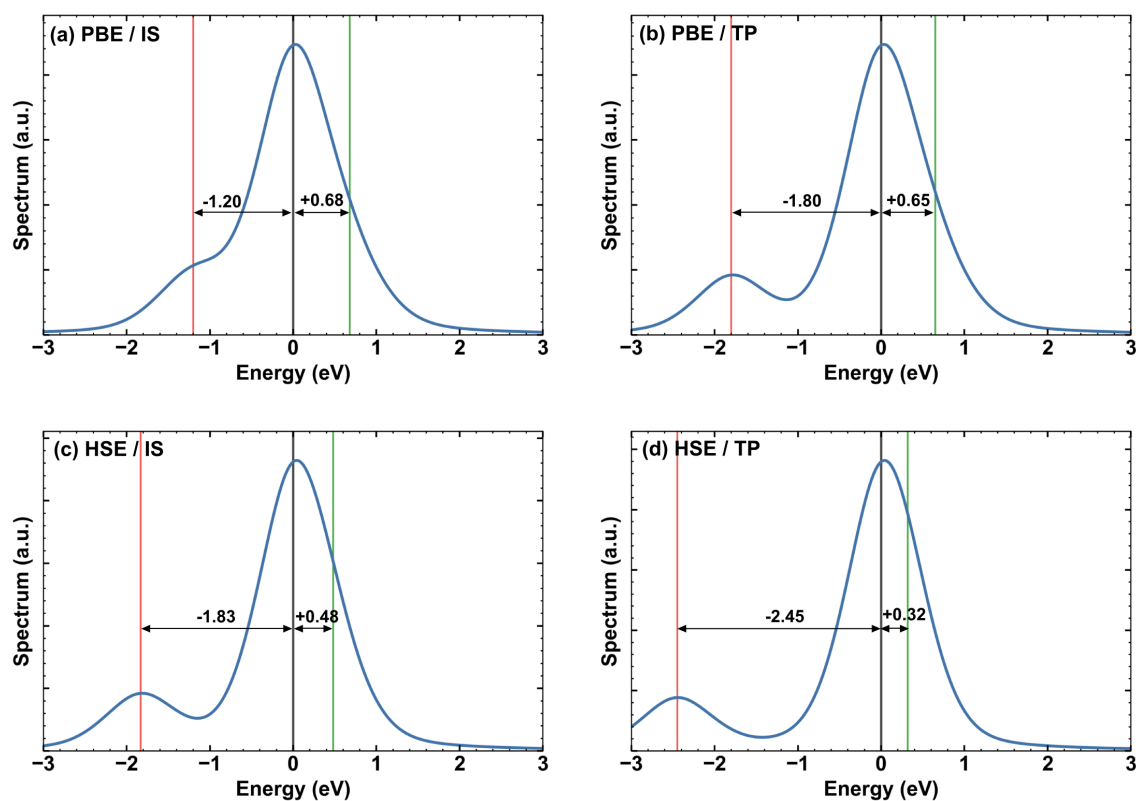
FIGURE 4.1: Simulated XPS spectra for the polar O-terminated ZnO(000$\bar{1}$) surface with an (2 × 1)-H overlayer using different density functionals and methods. Values are aligned to the position of the bulk peak. The green line makes the relative surface core-level energy for the bare surface oxygen atoms, and the red line marks the energy for the H-saturated surface oxygens. (a) Calculated with the PBE functional and the initial state method, (b) PBE and the transition potential method, (c) with the HSE functional ($\omega = 0.2$ Å^{-1}, $\alpha = 0.375$) and IS method, and (d) with HSE and the TP method.
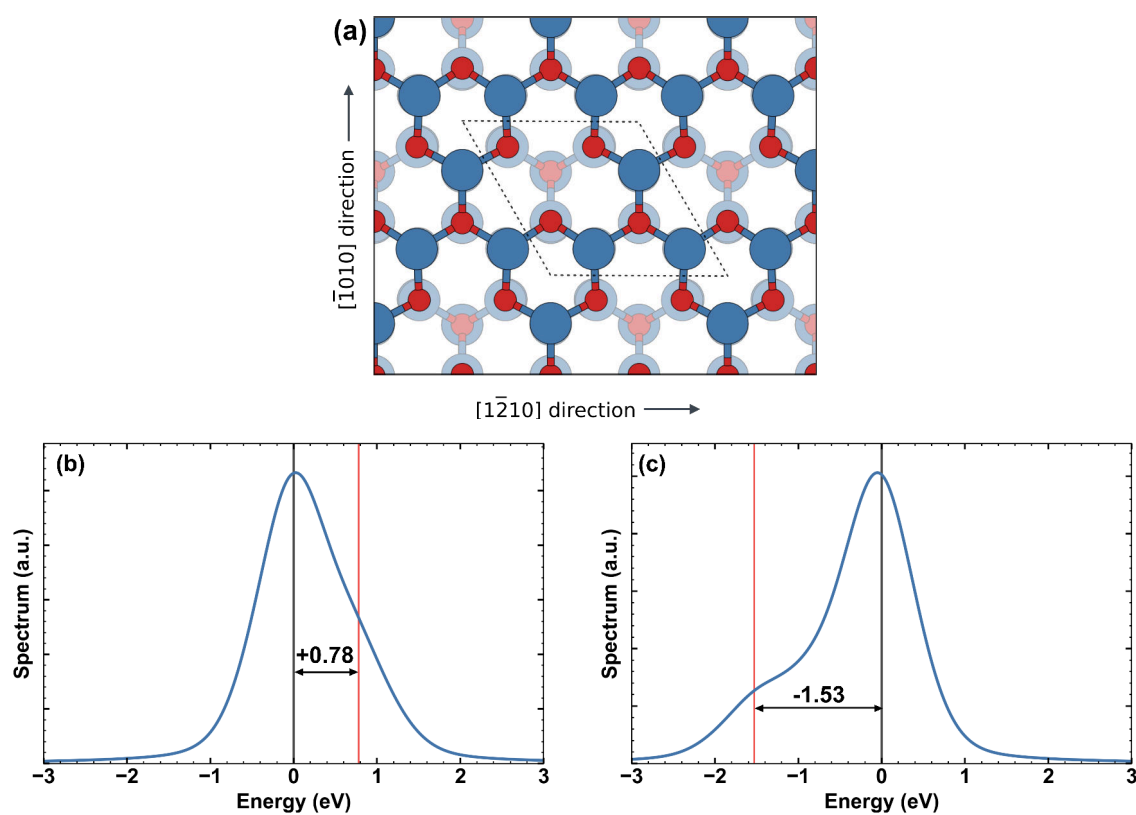
FIGURE 4.2: (a) Structure of polar Zn (0001) surface with Zn vacancies present at the surface (1/4 of the Zn atoms in the top layer were removed). Zinc atoms are shown in blue, oxygens in red, and the surface unit cell is indicated by the black dashed lines. (b) Simulated O1s core-level spectrum. Energies are relative to bulk-oxygens. The relative O1s binding energy for O atoms at the edge of the Zn-vacancy are marked by the red-line. (c) Simulated XPS spectra for a structure with hydrogens adsorbed on the edge-oxygens.
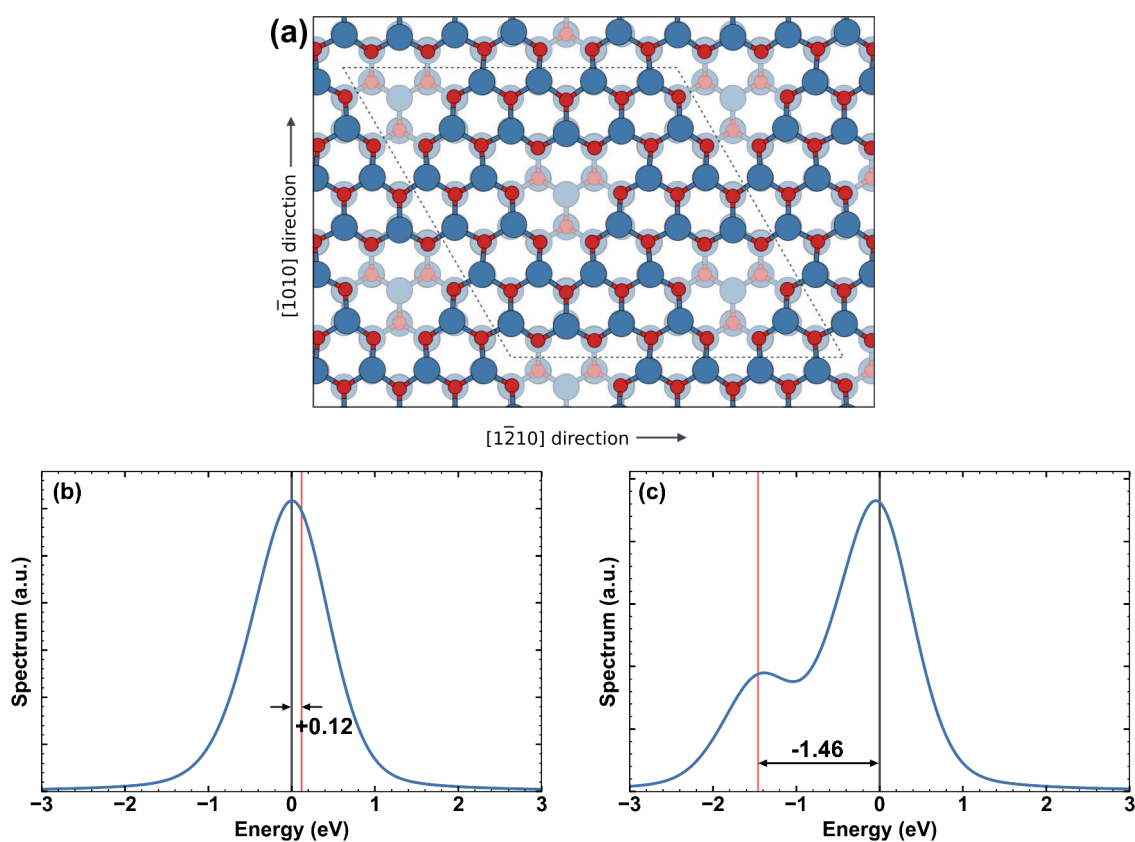
FIGURE 4.3: (a) Structure of polar Zn (0001) surface with (4 × 4)-triangular reconstructions. The surface unit cell is indicated by the black dashed lines. (b) Simulated O1s core-level spectrum. Energies are relative to bulk-oxygens. The relative O1s binding energy for O atoms at the edge of the triangular reconstructions are marked by the red-line. (c) Simulated XPS spectra for a structure with hydrogens adsorbed on the step edges.
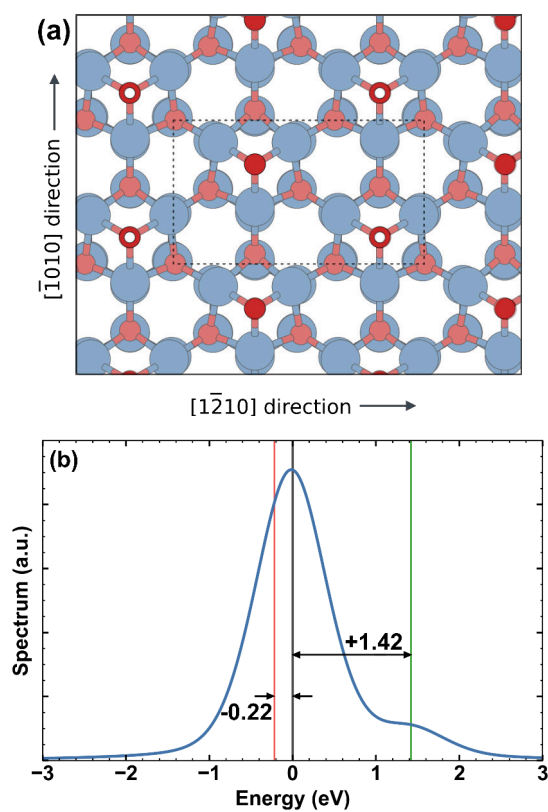
FIGURE 4.4: (a) Structure of the mixed $(\sqrt{3} \times \sqrt{3})R30°$-O+$(2 \times 1)$-H overlayer on the polar ZnO(0001) surface. The surface unit cell is indicated by the black dashed lines. (b) Simulated O1s core-level spectrum. Energies are relative to bulk-oxygens. The red and green vertical lines mark the relative O1s binding energies for the surface hydroxy group and oxygen adatom, respectively.
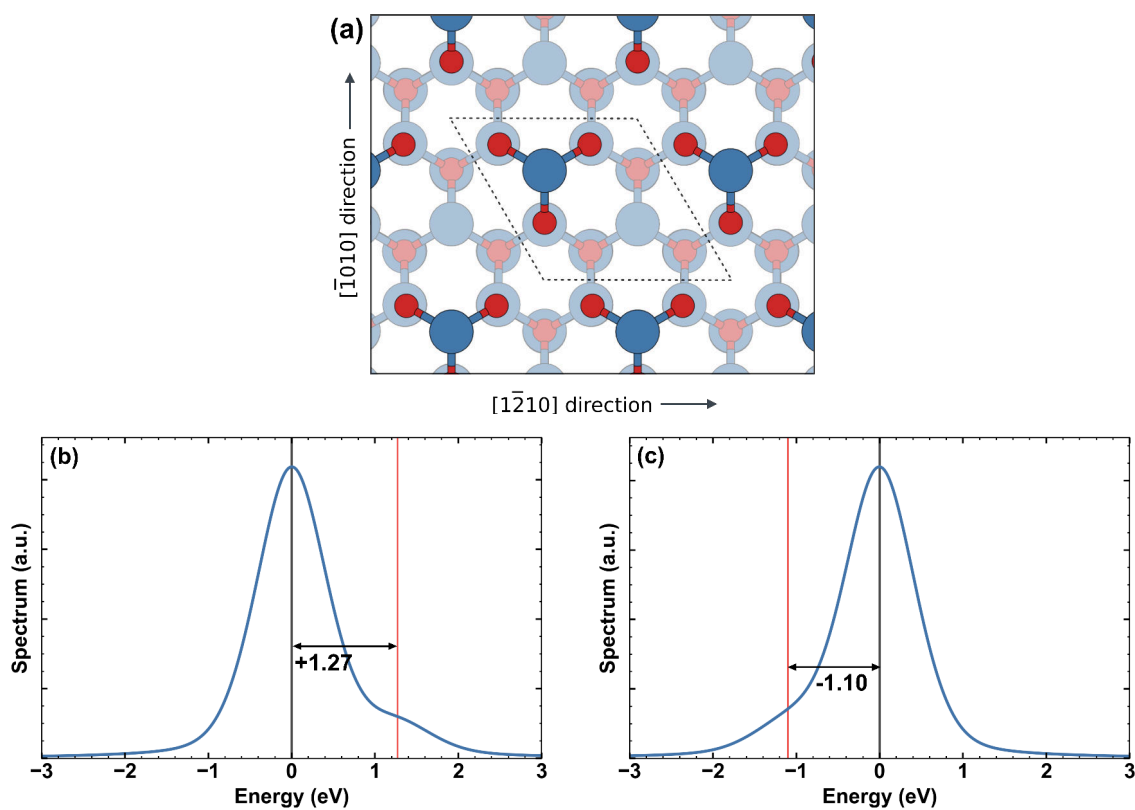
FIGURE 4.5: (a) Structure of polar Zn (0001) with small triangular pits at the surface. The unit cell is indicated by the black dashed lines. (b) Simulated O1s core-level spectrum. Energies are relative to bulk-oxygens. The relative O1s binding energy for O atoms at the edge of the small pits are marked by the red-line. (c) Simulated XPS spectra for a structure with hydrogens adsorbed on the oxygens at the edge of the pits.

Chapter 5

An Extended Hückel Based Initialization for FHI-aims

5.1 Motivation

An important factor that determines the computational costs of a DFT calculation is the speed of convergence. There are many factors that define how fast the self-consistent-field (SCF) cycle of a DFT calculation converges. Ideally as few as possible SCF iterations are needed to reach self-consistency of the charge density and orbitals, such that all desired convergence criteria are matched. Very clever ways to improve the convergence speed have been developed and also implemented in FHI-aims over time, such as preconditioning and sophisticated charge mixing schemes. One of the most decisive factors that influences the speed of convergence is the quality of the initial guess for the electron density. The aim of my work was to implement an improved initialization based on Extended Hückel theory in the FHI-aims code. I tested the reliability of the new initialization to show how it influences the number of SCF steps for selected systems compared to the standard initialization based on the superposition of atomic densities. This work was mainly done during a research stay at Duke University in Durham, North Carolina, in the group of Prof. Volker Blum.

5.2 Initial guess of the electron density

One of the most crucial steps in a practical DFT calculation is the initialization of the charge density. Starting from a sensible initial guess can significantly reduce the amount of time needed to reach a converged result. Furthermore, the electronic structure can exhibit multiple minima and the initial guess for the electron density might therefore have an impact on the qualitative result of the calculation. This is a common issue for magnetic solids, but was also relevant in this work for charge transfer systems. If we use a hybrid functional with a mixing parameter

that satisfies the straight-line energy condition, two solutions are stable (although not both are minima[129]). In a two-molecule system with one additional electron, the additional charge is either localized at only one molecule, or the charge is fractionally distributed on both. With the right initialization one can enforce either solution. For a localized solution the charge density is initialized in a spin-polarized manner with the defined initial moment lifting the symmetry of the spin-up and spin-down channel. For the delocalized solution the charge density should be initialized fully spin-symmetric.

For the discussion in this section we want to focus on the aspect of convergence speed and its relation to the quality of the initial guess. There is no unique way how to define the initial guess for the electron density $n(\mathbf{r})$ and several methods are used in the different DFT codes. Popular choices are the superposition of atomic densities (SAD), the one-electron guess from the core Hamiltonian, and the extended Hückel method. In solid-state band structure codes a initial guess from a superposition of spheric atomic densities is most common. It is straight-forward to implement but does not consider any chemical insight one might have of the system. SAD is currently used as the default guess in FHI-aims. Many quantum chemistry codes like Gaussian or Turbomole, on the other hand, use the semi-empirical extended Hückel method to generate a initial guess for the electron density. With this approach, the first SCF iteration should be closer in energy to the converged solution, and a speedup of the calculations should be obtained compared to a naïve initial guess from SAD. The extended Hückel (EH) method was described by Roald Hoffmann[130] and takes into account all the valence electrons of a system but ignores core electrons. For using EH method as initial guess in an all-electron code the core orbitals are usually approximated by Slater orbitals with exponents defined by Slater's rules[131]. The strength of EH is that it gives a good qualitative picture of the molecular orbitals and it is therefore well suited to provide a first chemical insight into a system. As basis set to express the molecular orbitals (MOs) minimal valence atomic-orbitals (AOs) are used. The AOs are represented by Slater-type orbitals (STOs). Knowing the atom positions the overlap of the MOs can be calculated. With the resulting overlap matrix $\mathbf{S}$ the hamiltonian matrix $\mathbf{H}$ is set up from a very simple recipe: For the diagonal elements H_{ii} empirical parameters are used. Its value should be equal to the energy of an electron in the respective AO of the isolated atom, i.e. the valence state ionization energy of the atomic orbital. Parameters are available for almost all elements but recommended values differ slightly between authors[132,133,134,135] Because of the very approximate nature of the EH method, the slight variations should be of little consequence[136]. The off-diagonal elements of H depend on the overlap and are evaluated according to

$$H_{ij} = K S_{ij} \frac{H_{ii} + H_{jj}}{2} \tag{5.1}$$

where K is an adjustable weighting parameter also known as Wolfsberg-Helmholtz constant. The idea behind the expression for the off-diagonal elements is that energy of interaction between electrons should depend on the overlap between the orbitals. The interaction energy should be greater when the overlap between the AOs is greater. Furthermore, the interaction energy between AOs with lower on-site energy should be lower compared to the interaction energy

between AOs with higher on-site energy and an equal amount of overlap. The value of K suggested by Hoffmann and frequently used for molecules is 1.75. In this region of K the energetic order of the MO should be in good agreement with experimental results.

With the Hamiltonian $\mathbf{H}$ and the overlap Matrix $\mathbf{S}$ we can set up the generalized eigenvalue problem

$$\mathbf{HC} = \mathbf{SC}\varepsilon \tag{5.2}$$

and solve it for the eigenvalue spectrum ε, i.e. the valence orbital energies, and the eigenvectors $\mathbf{C}$, i.e. the coefficients for the MOs. From this solution one gets a good first picture of the molecular orbitals and one can use chemical insight to choose a sensible occupation of the obtained MOs to build a good initial guess of the electron density in a SCF cycle. This flexibility of a controlled occupation of orbtials is one of the strengths of an EH based initialization and should yield faster convergence especially for chemical systems compared to the naïve SAD.

5.3   Implementation in FHI-aims

A new initialization for the electron density based on Extended Hückel theory was implemented into FHI-aims. It can be used for initializing calculations of isolated molecules and periodic systems. Instead of the originally proposed method that is based on Slater-type atomic orbitals, I used orbitals available in FHI-aims. Since we are interested in constructing the MOs from atomic-like orbitals, we choose the orbitals from the FHI-aims minimal basis (type "atomic"). Most important for the quality of the Extended Hückel results are the empirical parameters defining the diagonal elements of the Hamiltonian. The parameters for our implementation are collected from various sources. The parameter set is mainly based on Pyykkoe's table[137]. Additional sources are used for transition elements and elements that are on the bottom of the periodic table[138,139]. Parameters that were not available form this sources were interpolated from neighboring elements.

Here the keywords, which control the initialization are briefly explained (The notation used is as follows: Words in `typewriter style` are keywords. Words in *italic type* are variable names used within the program).

The initial guess in a FHI-aims calculations can be controlled via the `scf_init` keyword in the control file. `scf_init ehueckel` K_{EH} requests the Extended Hückel based initialization; `scf_init sad` requests the default initialization based on the superposition of atomic densities. K_{EH} is the adjustable off-diagonal weighting parameter, which can be set optionally (default value is 1.75). As explained above, standard values for the diagonal elements of the Extended Hückel Hamiltonian are available for all elements, but they can also be defined manually in the species definition of the control with the keyword `ehueckel_param` n l E_{ii} (n is an integer that defines the principal quantum number (1,2,...); l in a string that defines the azimuthal quantum number (s,p,d,...); E_{ii} is the diagonal element of the specified orbital).

In the following the performance of the new initialization is tested on tow test systems: The O_2 molecule and a TTF-TCNQ dimer.

5.4   Test systems

5.4.1 O_2 molecule

The ground state of the oxygen molecule is triplet oxygen. In this configuration the molecule has two unpaired electrons occupying two degenerate molecular orbitals (see Fig. 5.1). We tested our new initialization on this system using the B3LYP (Becke, three-parameter, Lee-Yang-Parr) hybrid functional[140]. Using the default initialization, the symmetric spin density can be perturbed by defining an initial moment in a spin-polarized calculation. For this system we assumed that the chemically motivated Extended Hückel guess performs better than the default guess. For the default guess the required number of SCF cycles depend on the value of the default initial moment (dim). A good choice of the initial moment already simplifies the calculation. The best performance is achieved if the initial moment is set to a numerical value close to the final converged moment on the atoms (i.e. for triplet oxygen the best value is 1.0). Comparing with the new guess, we find that with best initialization for both methods, the same number of SCF iterations are needed to reach convergence. That means no speed-up was achieved. The default initialization already gives a very good starting point if you choose the right initial moment. The evolution of the total energy difference unit convergence is achieved for both initialization methods is plotted in Fig. 5.1.
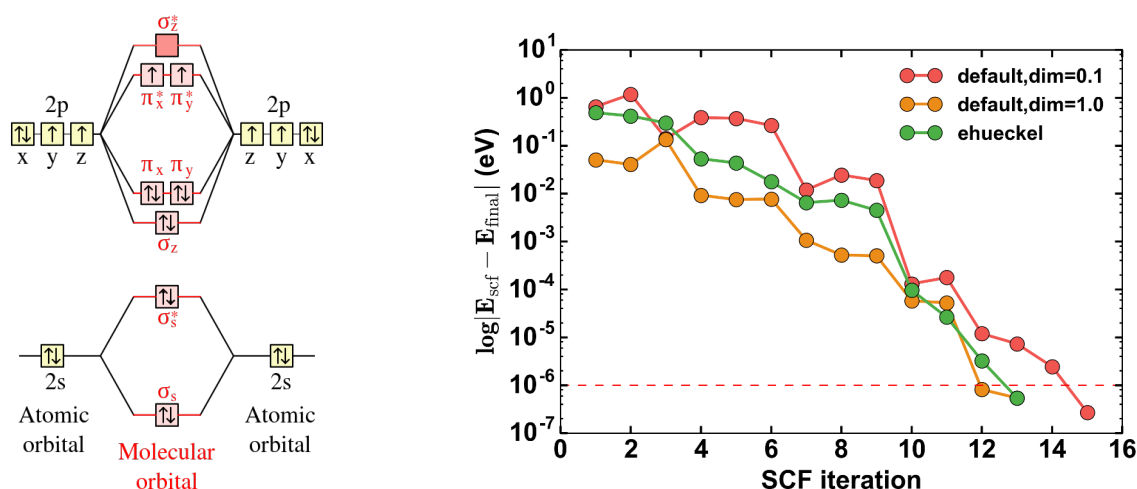
FIGURE 5.1:   *(left):* The valence orbitals of molecular oxygen in the triplet ground state (from[141]). *(right):* Evolution of the change in total energy during the calculation using the default initialization with an initial moment (dim) of 0.1 and 1.0 compared to the new initialization based on Extended Hückel.

5.4.2 TTF-TCNQ charge transfer complex

The second model system investigated was a tetrathiafulvalene (TTF) - tetracyanoquinodimethane (TCNQ) dimer. This is a typical example of molecular organic donor-acceptor charge transfer complex, where TTF acts as a donor and TCNQ as an acceptor. An organic metal from these molecules was discovered already in 1973[142]. For our test system we used a parallel configuration of the two molecules with the intermolecular distance fixed at 3.5 Å. The strongest electronic coupling between the two molecules is achieved when the TTF molecule is shifted by 3.0 Å along the long axis of the molecules (see Fig. 5.2). In this configuration it is known that an external electric field perpendicular to the planes of the two molecules induces electron transfer from the donor to the acceptor molecule in a HF calculation[143]. For this test we have applied an external electric field of 1 V/Å to the TTF-TCNQ pair.
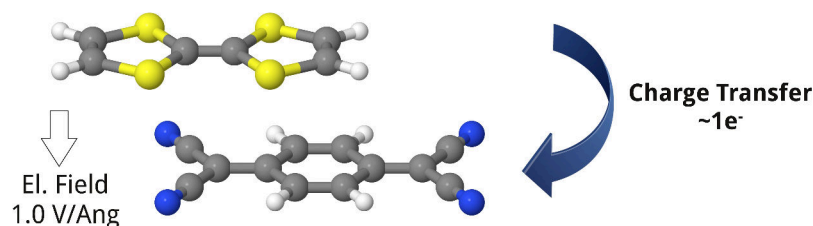
FIGURE 5.2: TTF-TCNQ dimer, where an electric field is applied in the direction perpendicular to the long molecular axis. The electric field induces electron transfer from the TTF to the TCNQ molecule.

To test the different initialization methods we performed unrestricted Hartree-Fock calculations of the dimer, with an convergence criterion for the total energy of 10^{-6} eV. For this test system we found that the off-diagonal weighting factor K_{EH} in the EH initialization can have an significant impact on the convergence speed of the calculation. The weighting factor basically defines the strength of the contribution of the off-diagonal elements. For our test system we found that a smaller weighting factor of 1.25 gave better performance compared to the suggested default value of 1.75. Still, when looking at the evolution of the change in total energy over the SCF run (top part of Fig. 5.3) we again find a similar performance of the EH guess and the default guess. With the right weighting factor the EH guess converges a bit faster than the default guess. What sticks out is that the EH initialization gives a worse total energy in the beginning of the calculation. The reason for this is not complected clear and need further investigations, but for a faster convergence the initial total energy should be closer to the finally converged one. To gain a better understanding of the quality of the orbital ordering for the two initialization methods we looked at the Mulliken charge difference between the TCNQ and TTF molecule (bottom part of Fig. 5.3). In the converged result, we obtain a charge transfer of one electron, i.e. the charge difference should converge to 1. We find that the EH guess gives a better initial charge transfer value, i.e. the initial charge density is closer to the final converged one, compared to the default guess. This is an indicator that the orbital ordering in the EH guess is better than in the default guess, which is what we expect for the semi-empirical method compared to the naïve SAD guess.
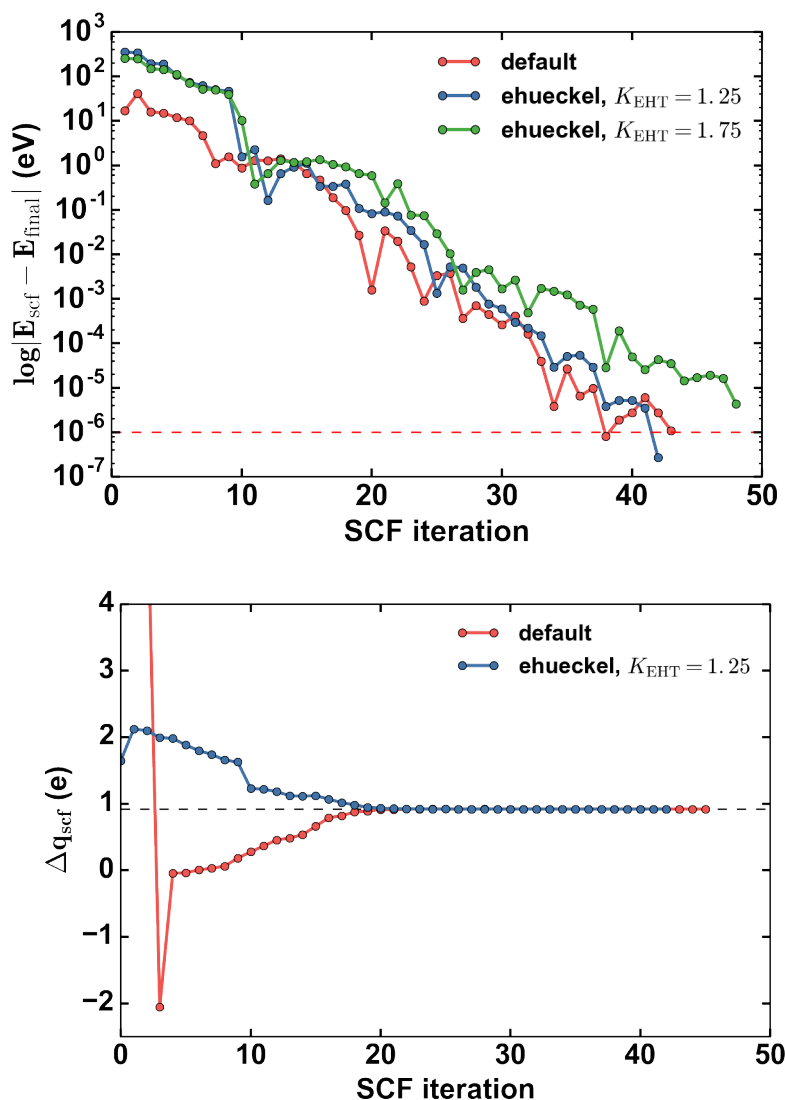
FIGURE 5.3: *(top):* Evolution of the change in total energy during the calculation using the default initialization compared to the new EH initialization with weighting factors of 1.25 and the default value of 1.75. *(bottom):* Evolution of the Mulliken charge difference between the two molecules over the number of SCF cycles.

5.5   Conclusion

The new implemented initialization based on Extended Hückel theory gives a similar performance compared to FHI-aims standard guess. We found no significant improvement of the convergence speed for the selected test systems. Is was surprising that for the test systems the total energy of the EH guess was further away from the converged values compared to the default guess. The problem could be linked to the selection of the empirical EH parameter set. Like I described in the introduction, the parameter sets that are available were constructed for Slater-type orbitals. Since in our implementation we use the numerical atomic orbitals of FHI-aims, the used parameter set might not be suitable. An optimized parameter set for the

NAOs might improve the initial guess in terms of the total energy. Furthermore to improve the EH guess an keyword that allows to gain control over the occupation of specific orbitals would further be helpful to manually choose a reasonable initial guess of the electron density.

Chapter 6

Charge Transfer Mechanisms at Hybrid Interfaces: F4TCNQ on ZnO

6.1 Motivation

This chapter is concerned with the main research focus of my dissertation. The funding for my PhD position stems from the FWF-project (P27868) "Tuning the Interaction Strength at Inorganic/Organic Interfaces". The aim of this project was a description of the charge transfer at semiconductor/organic interfaces with the focus of finding a phase transition from integer charge transfer (ICT) to fractional charge transfer (FCT) as the charge carrier concentration is gradually increased in the semiconducting substrate material. ICT is mainly expected to occur at inert substrates like undoped semiconductors, while FCT is observed at clean metal surfaces. One might suspect that it is the metallictiy of the substrate that determines the charge transfer mechanism. Therefore, the original assumption was that by tuning the charge carrier concentration in a semiconductor from intrinsic concentrations to concentrations similar to metals, the charge transfer mechanism changes somewhere in between. However, on the way to find such a phase transition we faced many obstacles mainly attributed to the commonly applied standard theoretical methods. This prompted us to investigate and find ways to overcome these limitations. The CREST method, that was introduced in Chapter 3.3, builds the foundation to perform DFT calculations for any charge carrier concentration of the substrate. However, because of the computational costs of hybrid DFT calculations, the size of the supercell surface area is limited. This also limits the number of molecules in the supercell and, hence, the range of doping concentrations for which we can obtain ICT solutions. At the outset of this project we wanted to use the F6TCNNQ molecule as organic part in our system, but soon had to find out that we have to look for a smaller molecule. Instead we focused on the smaller sibling, the well studied F4TCNQ molecule. We studied monolayers of F4TCNQ molecules adsorbed on two ZnO surfaces, the bare mixed-terminated ZnO($10\bar{1}0$) surface and the O-terminated ZnO($000\bar{1}$) surface. On the two surfaces the binding behavior of the F4TCNQ molecule is fundamentally

different. On the mixed-terminated surface, Zn atoms act as docking groups for the molecule, which primarily covalently bind to the surface (chemisorption). On the O-terminated surface the (2×1)-hydrogen overlayer acts as a spacer layer, preventing the molecule to directly bind to the surface. In this case the molecules bind to the surface primarily due to Van-der-Waals interaction (physisorption). In the following publication only the findings for the mixed-terminated surface are presented.

One of the big setbacks in achieving the original aim of this project was coming from a finding that has been made in our research group during the ongoing research. This finding has a significant effect on all studies using hybrid DFT calculations to describe charge transfer systems. Basically we found that with hybrid DFT calculations we are not able to predict the charge transfer mechanisms at interfaces. Rather both solutions for the case of ICT and FCT can be obtained and conclusions for the actually appearing charge transfer mechanism are only possible by comparing computed properties with experimental results[129]. We had to accept that in terms of the charge transfer mechanisms we do not posses predictive power and we needed to change our focus instead on conceptual findings for charge transfer effects on semiconductor/organic interfaces. Our presented findings in this chapter show in principle that both charge transfer mechanisms can appear even simultaneously, without predicting that ICT from ZnO to the LUMO of the F4TCNQ molecule will occur for the specific system.

6.2 Authors contribution

As this chapter summarizes my main research interests during my dissertation, I contributed to all stages of the work. A lot of preliminary work was necessary to obtain the presented results. All DFT calculations were performed my myself spending in total almost 3 million CPU hours. This should give the reader a feeling how demanding hybrid DFT calculations for such large systems are. The manuscript of the paper resulted from a close collaboration with my supervisor Oliver T. Hofmann, who also had the original idea to study the impact of doping on the charge transfer mechanism at semiconductor/organic interfaces. The manuscript was submitted to a journal on 12.12.2018 and is not yet published. Subsequently to the submitted manuscript and the corresponding supporting information, further findings are presented in additional sections. These findings include the doping dependence of the optimal hybrid mixing parameter for interface systems, and considerations on how fast electrons might hop between molecular sites in a molecular monolayer.

6.3 Submitted manuscript and supporting information

Fractional and Integer Charge Transfer at Semiconductor/Organic Interfaces: The Role of Hybridization and Metallicity

Simon Erker and Oliver T. Hofmann*

Institute of Solid State Physics, Graz University of Technology, NAWI Graz, Petersgasse 16, 8010 Graz Austria

ABSTRACT

Inorganic/organic interfaces show to phenomenologically different types of charge transfer: On inert substrates, a coexistence of charged and neutral molecules is found, while on metals, which have more available charge carriers and a larger propensity to hybridize, the organic component is homogeneously, fractionally charged. In this contribution, we use hybrid density functional theory to study the adsorption of the strong electron acceptor F4TCNQ on ZnO(10-10) as function of the substrate's doping concentration. This system undergoes a joint charge donation/backdonation reaction. Since the former is driven by hybridization, but the latter is not, this allows us to discuss the impact of hybridization and charge carrier availability separately. We find that while the hybridization determines the mechanism, the charge-carrier concentration (i.e., "metallicity") crucially impacts the amount of transferred charge. This leads to the counterintuitive situation that at low doping concentrations, most of the molecules are positively, rather than negatively, charged.

KEYWORDS

doping, band-bending, zinc oxide, F4TCNQ, hybrid density functional theory, charge localization, charge reservoir electrostatic sheet technique

Hybrid interfaces between inorganic semiconducting materials and organic molecules represent particularly interesting systems to study fundamental quantum-mechanical effects, since the flexibility of organic chemistry and the adjustability of the inorganic substrate's free charge-carrier concentration allows systematically tuning the strength of the interaction between the two components. Also from a practical viewpoint, the properties of organic and inorganic materials complement each other, which already led to many practical applications, such as light-emitting diodes for displays, lighting applications[1,2] or organic photovoltaic cells.[3,4] Other applications are still in their infancy, such as organic thermoelectric materials,[5] molecular switches,[6,7] or spintronic[8] devices. For their final success, an in-depth atomistic understanding of the quantum processes at the relevant interfaces is critical. Of particular interest in this context is the nature and mechanism of charge-transfer across the interface, since this critically affects the device performance.

Experimental investigations of inorganic/organic interfaces often find that the average charge-transfer amounts to less than a full electron per molecule. This allows for two different interpretations: Either, the charge is transferred in integer units and is localizes on individual molecules, which leads to a co-existence of integer charged and uncharged molecules. This is known as the integer charge transfer (ICT) model.[9–11] Alternatively, the charge delocalizes within the organic layer, leading to a homogeneous distribution of fractionally charged molecules. This is called the fractional charge transfer (FCT) model.[9,12] Experimentally, localized charge is mainly observed for adsorption on inert substrates, such as semiconductors or passivated metals[10,11,13,14] . Conversely, delocalized charges are found for adsorption on weakly reactive metal surfaces.[15–19]. Thus, there seem to be two properties of the *substrate* that potentially influence the charge-transfer mechanism: the propensity to hybridize with the adsorbate, and the availability of free charge-carriers. Although these properties are often correlated (i.e., metals have a larger charge-carrier concentration and tend to be more reactive than

2

semiconductors), they are not necessarily causally related. The open question at the heart of this contribution is to what extend these two different aspects impact the charge-localization at the interface.

Ideal systems to address this issue are monolayers of small organic molecules on weakly reactive substrates, which are in between the prototypical cases of physisorption (i.e., inert systems) and chemisorption (i.e., the formation of covalent bonds between substrate and adsorbate). In this study, we use theoretical modeling based on hybrid density functional theory to exemplarily investigate the adsorption of tetrafluorotetracyanoquinodimethane (F4TCNQ) on the wide-bandgap semiconductor ZnO. We focus on the question how the localization of charge is affected when the nature of the substrate is gradually changed from insulating to metallic by tuning its free charge-carrier concentration.

Zinc oxide is a prototypical semiconducting oxide that has attracted significant attention for use in organic electronic devices due to its optical transparency and wide band gap ($E_g = 3.4$ eV).[20,21] Natively grown, ZnO has a free carrier concentration below 10^{16} cm^{-3},[22] while highly doped ZnO, on the other hand, can reach carrier concentrations up to 10^{21} cm^{-3}.[23–25] The chosen adsorbate, F4TCNQ (see inset of Figure 1), is a prototypical organic acceptor that is used both in practical applications[26,27] and in many surface science studies.[10,16,28–32] It is susceptible to both charge-transfer mechanisms, depending on the nature of the substrate.[10,16]

Furthermore, F4TCNQ can undergo charge-transfer via two separate "channels": One the one hand, the peripheral cyano groups can form dative covalent bonds, donating electrons to the substrate ("charge donation"). On the other hand, the energetically low-lying lowest unoccupied molecular orbital (LUMO) readily accepts electrons from the Fermi-level ("charge backdonation")[16] of materials with a sufficiently low work function.[9,33] The latter process also occurs in the absence of hybridization[30] and is caused by the difference of the electronegativity of the components. Due to its similarity with the

charge-transfer bonding of ionic materials, such as NaCl, we refer to it as "ionically driven" hereafter. For the present study, it is important to note that the LUMO of F4TCNQ molecules lies in the band gap of ZnO. Hence, for intrinsic (undoped) ZnO, one a priori expects no charge-transfer into the LUMO, whereas for n-doped ZnO, the amount of charge transferred should depend critically on the charge carrier concentration.[30] In other words, the charge carrier concentration of the substrate can be used as a handle to modify the charge-transfer, rendering this material combination ideal for the present computational study.
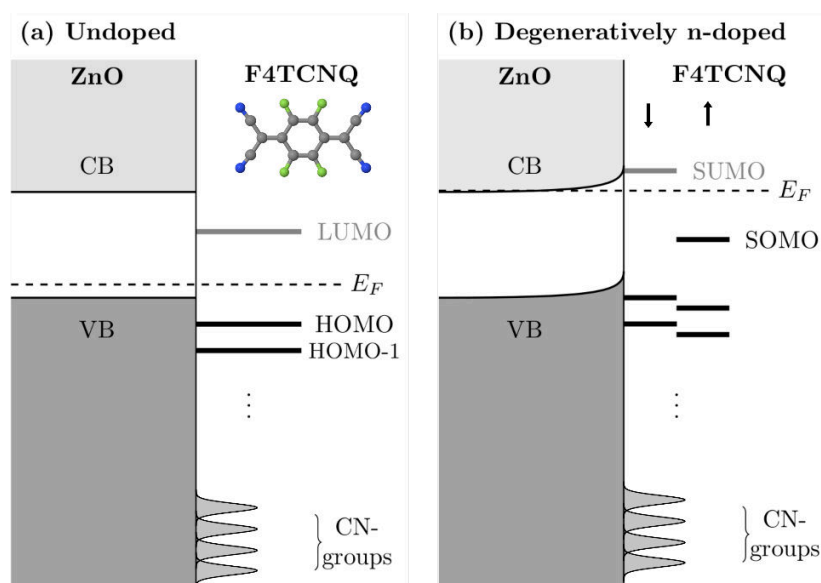
Figure 1. Qualitative level alignment for the F4TCNQ/ZnO interface. (a) shows the level alignment for intrinsic ZnO, where only the CN-groups hybridize, while (b) depicts the qualitative level alignment for degenerately doped ZnO, where also the LUMO splits into a SOMO and a SUMO

The major issue in charge-transfer studies based on density functional theory (DFT) is the choice and impact of the exchange-correlation functional. This is mainly due to the so-called many-electron self-interaction error (MSIE), which leads to the tendency of charge over-delocalization for common local and semilocal functionals.[34–36] Hybrid functionals, which contain a fraction of Hartree-Fock-like (HF) exchange, in general perform better in in terms of charge transfer, but too much HF exchange leads to

the converse problem of over-localizing charge.[35,37,38] Arguably, the best results are obtained when choosing the amount of HF exchange such that the functional becomes MSIE-free. In this case the functional neither over-localizes nor it over-delocalizes charge, and the charge transfer at the interface can be driven into either solution depending on the initialization.[39,40]

For the F4TCNQ molecule, the MSIE-free situation is achieved by using the PBEh[41] functional with 63% HF exchange. Due to screening, the required amount for HF exchange of the F4TCNQ/ZnO interface to achieve MSIE-free behavior would be notably smaller.[39] However, at too low values the energy level ordering at the interface is no longer correctly reproduced, as the LUMO shifts below the valence band of the ZnO. This gives rise to spurious charge-transfer from the valence band of ZnO.[30] Therefore, the calculations presented in this work were performed with 63% HF exchange, which thus tendentially lead to charge over-localization. We discuss the impact of this at the end of this paper. Further methodological details are given in the method section and the Supporting Information.

The ideal starting point for our investigation is a perfect, intrinsic ZnO substrate. We acknowledge that, to the best of our knowledge, such a substrate is hypothetical, since already trace amounts of hydrogen (e.g., in the residual gas of UHV chambers) lead to n-type doping of ZnO.[42] Nonetheless, because the ionization energy of ZnO (ca. 8 eV) [43] is much larger than the electron affinity of F4TCNQ (EA = 5.2 eV),[44] we do not expect any ionically driven charge (back-)transfer for the intrinsic substrate. Rather, all charge redistributions occurring at the interface should be due to wave-function overlap between substrate and adsorbate, allowing us to first focus on this effect only.

Indeed, as shown in Figure 2b, our DFT calculations yield the F4TCNQ LUMO to be in the ZnO band gap. Although F4TCNQ is a strong electron acceptor, adsorption on intrinsic ZnO leads to a reduction of the work function by -0.83 eV. The reason for this, besides a small molecular dipole induced by the bent geometry on the surface, is that the molecule acquires a small, *positive* Mulliken charge (ca. 0.1 electrons). In principle, there are several possible reasons for this: Besides covalent interactions, these

include Pauli push-back[45] or polarization of the electron cloud. To demonstrate that the positive charge is indeed due to bond formation, in Fig. 2a we plot the line-integrated charge rearrangements upon adsorption of the molecule (i.e, the difference between the charge density of the combined system and the sum of the charge densities of the isolated components, integrated along the line of sight of the figure.). The charge rearrangements are dominated by a reduction of the electron density of C≡N triple bond (red regions) and a concomitant increase between the peripheral nitrogen atoms and the substrate Zn atoms. The overall shape of the charge rearrangements strongly resembles the cyano-orbitals, that are also relevant for charge donation on variety of other substrates.[16,28] The observation that the adsorption energy of F4TCNQ on ZnO is exothermic (E_{ads} = -2.31 eV) even when disregarding van-der-Waals interactions (which amount to -1.37 eV) further corroborates the notion that this is a covalent interaction due to the hybridization of the substrate's and adsorbate's wave function.

6
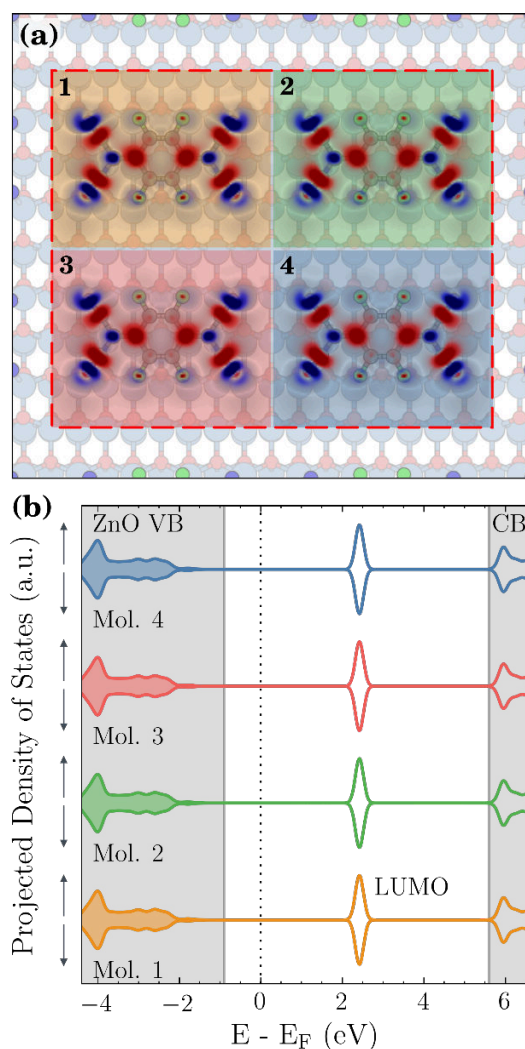
Figure 2. (a) Line-averaged charge rearrangements within the surface supercell containing four F4TCNQ molecules. Blue areas indicate an increase in electron density, red areas a reduced electron density. (b) DOS projected on the individual molecules adsorbed on undoped ZnO. The gray areas indicate the conduction and valence band of ZnO.

The other important question for the present situation, however, is whether in a closed monolayer, the positive charge is delocalized, or whether it localizes on individual molecules. To answer this, we have performed the calculation in a supercell containing four molecules. Despite several efforts to break the translational symmetry (via initialization of the SCF guess or small geometry distortions of the molecules), and despite the tendency of our functional to over-localize charge (see above), we find that

the charge remains fully *delocalized*, i.e. all molecules in the layer remain equivalent as clearly be seen in the charge rearrangement of the four molecules in the supercell as well as in the density of states projected onto the individual molecules (Fig. 2).

The situation changes fundamentally for an n-doped substrate. Doping nominally introduces free charge carriers into the conduction band of ZnO. However, as shown in Fig 1a and Fig 2b, for the undoped substrate the (empty) F4TCNQ LUMO lies below the conduction band. Thus, F4TCNQ molecules act as p-dopants at the surface with a very high local concentration. Hence, the energy of the combined system can be lowered if (some of) the introduced charge carriers are transferred to the molecule. However, in contrast to the cyano-groups, the LUMO does not hybridize notably with the substrate. This is evident from Figure 2b by the fact that the orbital remains a sharp peak in the band gap, without additional contributions in resonance in the substrate bands. Hence, any doping-induced charge backdonation from the substrate to the molecule must be a primarily non-covalent, ionic process.

Such charge transfer leads to the formation of an interface dipole between substrate and adsorbate, which shifts the LUMO upwards in energy (relative to the conduction band). This interface dipole is not confined to the region between the components, but, for a doped semiconductor, also extends into the substrate itself – in other words, it leads to band-bending, as schematically indicated in Fig 1b. This interface dipole and its associated energetic cost limits how much charge the molecular layer receives. Importantly, this is directly dependent on the charge carrier concentration, and can vary from negligible charge transfer in the case of low charge carrier concentrations to very large charge transfer for high charge carrier concentrations.[30]

In our simulations, we account for doping using the CREST approach,[46] which allows to explicitly introduce doping in DFT calculations by mimicking the long ranged electrostatic effect of band-bending (for further details see SI). Like for the undoped case, we use a supercell (2x2 containing four

8

molecules, see Figure 3a) to conceptually allow for charge localization in the layer. For the following discussion, it is useful to consider the evolution of charge donation (i.e., the contribution of the cyano groups) and backdonation (the filling of the molecular LUMO) separately. We will focus on backdonation first.
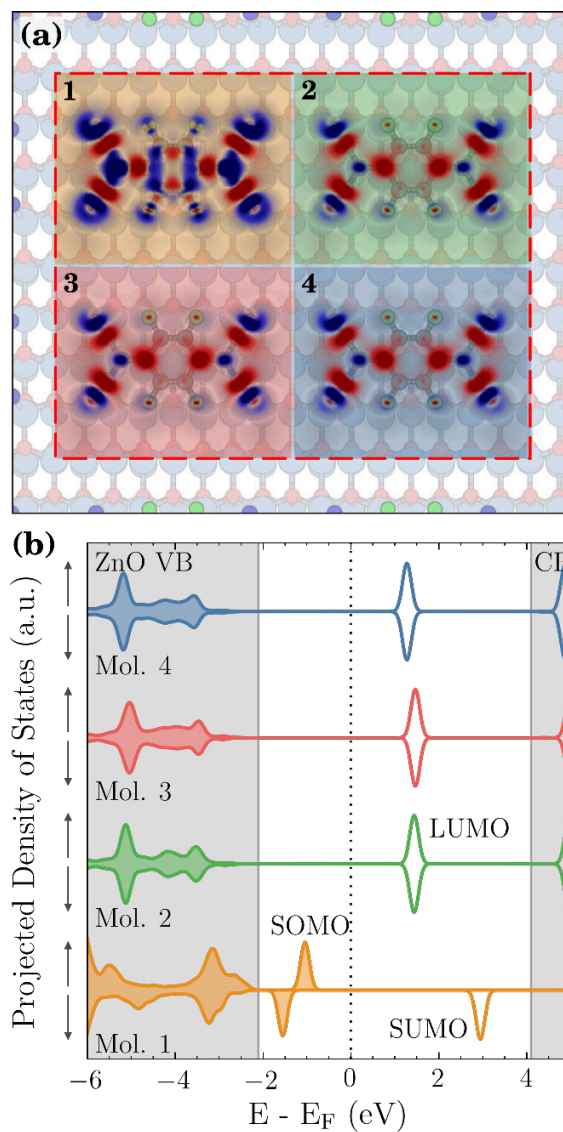
Figure 3. (a) Line-averaged charge rearrangements within the surface supercell containing four F4TCNQ molecules. Blue areas indicate an increase in electron density, red areas a reduced electron density. (b) DOS projected on the individual molecules adsorbed on ZnO with a free carrier concentration of 1.9×10^{19} cm^{-3}. The gray areas indicate the conduction and valence band of ZnO.

Any finite n-type doping activates the backdonation channel. At a charge carrier concentration of 1.9×10^{19} cm^{-3}, ZnO back-donates one electron per supercell, i.e. ¼ electron per F4TCNQ molecule. This exceeds the donated charge, leading to an overlayer that is overall negatively charged, as one would expect for the adsorption of a strong electron acceptor. However, as evident from Figure 3a, our calculations show that, in contrast to the charge-donation, the backdonated charge is *not* equally distributed. Rather, while all molecules still show the telltale density redistribution of charge donation, only molecule 1 (top left corner) additionally shows charge rearrangements reminiscent of the molecular LUMO. This is further corroborated by the density of states shown in Figure 3b, which shows that the molecule becomes a radical, i.e. the LUMO splits into a singly occupied molecular orbital (SOMO) and a single unoccupied molecular orbital (SUMO). Thus, the electron-backtransfer occurs in the same way it would for a free molecule in the gas phase, but is in stark contrast to charge-transfer on metallic surfaces, where no spin-polarization occurs. Interestingly, this means that although the overall charge of he F4TCNQ monolayer is negative on average, at this doping concentration most of the molecules are positively charged.

As also predicted by simpler models,[30] increasing the carrier concentration increases the charge backdonation: 2, 3, or 4 electrons per supercell are backdonated at charge carrier concentration of approximately 6.4×10^{19} , 1.5×10^{20} , and 2.9×10^{20} cm^{-3}, respectively (see Figure 4). Importantly, the additional charge always localizes onto individual molecules and renders them radicalic (i.e. spin-polarized, without molecular density of states at or near the Fermi-edge). We can thus conclude that even for degenerate doping, where the charge-carrier concentration is close to that of a metal, the charge-transfer mechanism does not change qualitatively, and the backdonated charge does not become delocalized within the molecular layer as it is on pristine metals.
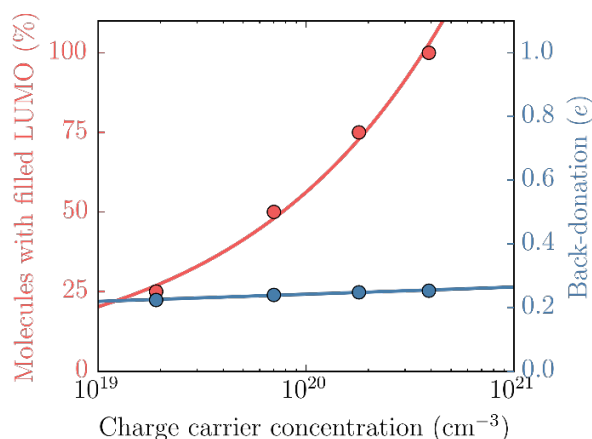
Figure 4. Red: Number of molecules with singly occupied orbitals within the molecular layer as the charge carrier concentration is increased. Blue: Charge donation per molecule from the cyano orbitals only.

In contrast to the backdonation channel, the amount of charge donated by the cyano groups hardly sensitive to the charge carrier concentration in the ZnO. Qualitatively, filling the LUMO of one molecule in the supercell (e.g., at 2×10^{19} cm^{-3}), affect neither its own charge-donation significantly, nor that of the other molecules in the unit. This shows that the two mechanisms, donation and backdonation, are of different nature and act independently of each other. Since the LUMO of some molecules remain unfilled, they still exhibit a net positive charge, which leads to a coexistence of positively and negatively charged molecules on the surface.

We note at this point that, as mentioned initially, the chosen functional has a tendency to overlocalize charge. This raises the question whether our results might be artefacts from the employed method. However, we stress that we find localization for only one channel and delocalization for the other, rather than localization for both. Moreover, the same qualitative results are obtained when using the default PBE0 functional (which employs a much smaller fraction of HF-like exchange, 25%). Thus, at the very least our results are a proof of concept that different charge localization for different charge-transfer channels, as we have described here, is conceptually possible and can be modelled within

11

hybrid functional DFT. However, since the degree of hybridization (which appears to be the governing factor) is essentially independent of the employed functional, we are also confident that our results are robust and will hold up to experimental scrutiny. Moreover, we expect our findings to be directly transferrable to other semiconductor/organic interfaces which show a combination of charge donation and backdonation. Such systems are, indeed, quite common, and include small molecules frequently used for surface science studies, such as carbon monoxide,[47] as well as large molecules used in the context of organic electronics, such as PTCDA.[48]

In summary, we have investigated the F4TCNQ/ZnO(10-10) interface, which undergoes a charge donation/backdonation reaction. The charge donation is driven by hybridization between the components. It affects all molecules equally, rendering them fractionally positive independent of the doping of the substrate. Conversely, the backdonation is driven by the difference of the component's electron chemical potentials. Our calculations indicate that only some molecules receive an integer electron in the process, rendering them negative. The LUMO of the other molecules at the interface remains empty. This leads to a coexistence of positively and negatively charged molecules on the surface. The number of negatively charged molecules depends critically on the number of free charge-carriers of the substrate (i.e,. its "metallicity"). For low doping concentrations, we find that the number of positive molecules may even exceed that of negative moieties, even if the overall charge of the monolayer is net negative. As we increase the charge carrier concentration the fundamental mechanisms do not change, but the density of molecules within the monolayer with integer charged LUMOs increases. The two mechanisms are found to be essentially independent from each other. This indicates that only the hybridization, and not the "metallicity" of the substrates, determines the charge transfer mechanism, even if the latter plays a major role for the amount of charge transferred.

Methods

All DFT calculations presented here are performed with the FHI-aims package.[49–51] Van der Waals forces are included with the vdW-TS scheme,[52] employing parameters for the substrate that are optimized for ZnO interfaces.[53] The interface is modeled with a four double-layer ZnO surface slab cell that contains four F4TCNQ molecules at a surface area of 548.6 $Å^2$ (See Fig. 2). Geometry relaxations for this surface unit cell were performed using a single Gamma centered k-point (This corresponds to a k-point grid of 8x4x1 for the primitive ZnO (10-10) surface unit cell) and with the default element-specific "light" settings for the integration grids and basis sets. For final single point calculations a reciprocal k-grid of 2x2x1 was used with default "tight" setting (without the "tier-2" f and g basis functions for oxygen). The k-grid was scaled accordingly for smaller unit cells containing only one molecule. To further reduce memory consumption we increased the Hartree-Fock screening threshold ("crit_val") to 10^{-5}.

The ZnO lattice constant was obtained from a PBE calculation and was kept fixed for all hybrid calculations because geometry optimizations for the ZnO substrate were only performed on the PBE level (see below). We carefully checked that the lattice constant of the substrate has no significant influence on our results. Since in the case of integer charge transfer the system undergoes a symmetry breaking in the charge density that is accompanied by a symmetry breaking in the geometry of the monolayer, it is essential to optimize the geometry of the monolayer for all calculations with the corresponding functional. The geometry relaxation strategy is therefore as follows: The interface was pre-relaxed using the PBE functional, fixing the bottom two double-layers of the substrate at their bulk position while allowing the other layers, as well as the molecules, to relax. The final relaxation was performed with the Perdew-Burke-Ernzerhof hybrid (PBEh) functional with the mixing parameter α = 0.63. For all hybrid calculations the substrate was kept fixed and only the molecular monolayer was allowed to relax until the residual forces are smaller than 10^{-4} eV/Å. All electronic structure results

reported int his paper were also obtained with this functional. More details about the computations including how we used CREST[46] to mimic the effect of band bending in our DFT calculations and information about the spin-polarized charge density initialization can be found in the supplementary information.

ASSOCIATED CONTENT

Supporting Information

Further computational details (doping and band-bending model, spin-polarized charge density initialization), adsorption site and geometry of the monolayer, molecular orbital density of states, discussion on the applied density functional

AUTHOR INFORMATION

Corresponding Author

*E-mail: o.hofmann@tugraz.at

ACKNOWLEDGMENT

REFERENCES

(1)   Hung, L. S.; Chen, C. H. Recent Progress of Molecular Organic Electroluminescent Materials and Devices. *Mater. Sci. Eng., R* **2002**, *39* (5–6), 143–222. https://doi.org/10.1016/S0927-796X(02)00093-1.

(2)   Meredith, P.; Bettinger, C. J.; Irimia-Vladu, M.; Mostert, A. B.; Schwenn, P. E. Electronic and Optoelectronic Materials and Devices Inspired by Nature. *Reports on Progress in Physics* **2013**, *76* (3), 034501. https://doi.org/10.1088/0034-4885/76/3/034501.

(3)   Cao, H.; He, W.; Mao, Y.; Lin, X.; Ishikawa, K.; Dickerson, J. H.; Hess, W. P. Recent Progress in Degradation and Stabilization of Organic Solar Cells. *Journal of Power Sources* **2014**, *264*, 168–183. https://doi.org/10.1016/j.jpowsour.2014.04.080.

(4)   Kaur, N.; Singh, M.; Pathak, D.; Wagner, T.; Nunzi, J. M. Organic Materials for Photovoltaic Applications: Review and Mechanism. *Synthetic Metals* **2014**, *190*, 20–26. https://doi.org/10.1016/j.synthmet.2014.01.022.

(5)   Paulsson, M.; Datta, S. Thermoelectric Effect in Molecular Electronics. *Physical Review B* **2003**, *67* (24). https://doi.org/10.1103/PhysRevB.67.241403.

(6)   McNellis, E.; Meyer, J.; Baghi, A.; Reuter, K. Stabilizing a Molecular Switch at Solid Surfaces: A Density Functional Theory Study of Azobenzene on Cu(111), Ag(111), and Au(111). *Physical Review B* **2009**, *80* (3). https://doi.org/10.1103/PhysRevB.80.035414.

(7)   Maurer, R. J.; Reuter, K. Bistability Loss as a Key Feature in Azobenzene (Non-)Switching on Metal Surfaces. *Angewandte Chemie* **2012**, *124* (48), 12175–12177. https://doi.org/10.1002/ange.201205718.

(8)   Sanvito, S. Molecular Spintronics. *Chemical Society Reviews* **2011**, *40* (6), 3336. https://doi.org/10.1039/c1cs15047b.

(9)   Braun, S.; Salaneck, W. R.; Fahlman, M. Energy-Level Alignment at Organic/Metal and Organic/Organic Interfaces. *Advanced Materials* **2009**, *21* (14–15), 1450–1472. https://doi.org/10.1002/adma.200802893.

(10)   Braun, S.; Salaneck, W. R. Fermi Level Pinning at Interfaces with Tetrafluorotetracyanoquinodimethane (F4-TCNQ): The Role of Integer Charge Transfer States. *Chem. Phys. Lett.* **2007**, *438* (4–6), 259–262.

(11)   Hofmann, O. T.; Rinke, P.; Scheffler, M.; Heimel, G. Integer *versus* Fractional Charge Transfer at Metal(/Insulator)/Organic Interfaces: Cu(/NaCl)/TCNE. *ACS Nano* **2015**, *9* (5), 5391–5404. https://doi.org/10.1021/acsnano.5b01164.

(12)   Hofmann, O. T.; Atalla, V.; Moll, N.; Rinke, P.; Scheffler, M. Interface Dipoles of Organic Molecules on Ag(111) in Hybrid Density-Functional Theory. *New Journal of Physics* **2013**, *15* (12), 123028. https://doi.org/10.1088/1367-2630/15/12/123028.

(13)   Hollerer, M.; Lüftner, D.; Hurdax, P.; Ules, T.; Soubatch, S.; Tautz, F. S.; Koller, G.; Puschnig, P.; Sterrer, M.; Ramsey, M. G. Charge Transfer and Orbital Level Alignment at Inorganic/Organic Interfaces: The Role of Dielectric Interlayers. *ACS Nano* **2017**, *11* (6), 6252–6260. https://doi.org/10.1021/acsnano.7b02449.

(14)   Gruenewald, M.; Schirra, L. K.; Winget, P.; Kozlik, M.; Ndione, P. F.; Sigdel, A. K.; Berry, J. J.; Forker, R.; Bredas, J.-L.; Fritz, T.; et al. Integer Charge Transfer and Hybridization at an Organic Semiconductor / Conductive Oxide Interface. *The Journal of Physical Chemistry C* **2015**, *119* (9), 4865–4873. https://doi.org/10.1021/jp512153b.

(15)   Duhm, S.; Glowatzki, H.; Cimpeanu, V.; Klankermayer, J.; Rabe, J. P.; Johnson, R. L.; Koch, N. Weak Charge Transfer between an Acceptor Molecule and Metal Surfaces Enabling Organic/Metal Energy Level Tuning. *J. Phys. Chem. B* **2006**, *110* (42), 21069–21072. https://doi.org/10.1021/jp0644715.

(16) Romaner, L.; Heimel, G.; Brédas, J.-L.; Gerlach, A.; Schreiber, F.; Johnson, R.; Zegenhagen, J.; Duhm, S.; Koch, N.; Zojer, E. Impact of Bidirectional Charge Transfer and Molecular Distortions on the Electronic Structure of a Metal-Organic Interface. *Phys. Rev. Lett.* **2007**, *99* (25), 256801. https://doi.org/10.1103/PhysRevLett.99.256801.

(17) Heimel, G.; Duhm, S.; Salzmann, I.; Gerlach, A.; Strozecka, A.; Niederhausen, J.; Bürker, C.; Hosokai, T.; Fernandez-Torrente, I.; Schulze, G.; et al. Charged and Metallic Molecular Monolayers through Surface-Induced Aromatic Stabilization. *Nature Chemistry* **2013**, *5* (3), 187–194. https://doi.org/10.1038/nchem.1572.

(18) Glowatzki, H.; Bröker, B.; Blum, R.-P.; Hofmann, O. T.; Vollmer, A.; Rieger, R.; Müllen, K.; Zojer, E.; Rabe, J. P.; Koch, N. "Soft" Metallic Contact to Isolated C 60. *Nano Lett.* **2008**, *8* (11), 3825–3829. https://doi.org/10.1021/nl8021797.

(19) Crispin, X.; Geskin, V.; Crispin, A.; Cornil, J.; Lazzaroni, R.; Salaneck, W. R.; Brédas, J.-L. Characterization of the Interface Dipole at Organic/ Metal Interfaces. *J. Am. Chem. Soc.* **2002**, *124* (27), 8131–8141. https://doi.org/10.1021/ja025673r.

(20) Roth, A. P.; Webb, J. B.; Williams, D. F. Absorption Edge Shift in ZnO Thin Films at High Carrier Densities. *Solid State Communications* **1981**, *39* (12), 1269–1271. https://doi.org/10.1016/0038-1098(81)90224-6.

(21) Srikant, V.; Clarke, D. R. On the Optical Band Gap of Zinc Oxide. *Journal of Applied Physics* **1998**, *83* (10), 5447–5451. https://doi.org/10.1063/1.367375.

(22) Look, D. C.; Reynolds, D. C.; Sizelove, J. R.; Jones, R. L.; Litton, C. W.; Cantwell, G.; Harsch, W. C. Electrical Properties of Bulk ZnO. *Solid State Communications* **1998**, *105* (6), 399–401. https://doi.org/10.1016/S0038-1098(97)10145-4.

(23) Hu, J.; Gordon, R. G. Textured Aluminum☐doped Zinc Oxide Thin Films from Atmospheric Pressure Chemical☐vapor Deposition. *Journal of Applied Physics* **1992**, *71* (2), 880–890. https://doi.org/10.1063/1.351309.

(24) Ko, H. J.; Chen, Y. F.; Hong, S. K.; Wenisch, H.; Yao, T.; Look, D. C. Ga-Doped ZnO Films Grown on GaN Templates by Plasma-Assisted Molecular-Beam Epitaxy. *Applied Physics Letters* **2000**, *77* (23), 3761–3763. https://doi.org/10.1063/1.1331089.

(25) Kalusniak, S.; Sadofev, S.; Schäfer, P.; Henneberger, F. Heavily N-Type ZnO: A Plasmonic Material at Telecommunication Wavelengths: Heavily n-Type ZnO: A Plasmonic Material at Telecommunication Wavelengths. *physica status solidi (c)* **2014**, *11* (7–8), 1357–1360. https://doi.org/10.1002/pssc.201300738.

(26) Chen, D.-Y.; Tseng, W.-H.; Liang, S.-P.; Wu, C.-I.; Hsu, C.-W.; Chi, Y.; Hung, W.-Y.; Chou, P.-T. Application of F4TCNQ Doped Spiro-MeOTAD in High Performance Solid State Dye Sensitized Solar Cells. *Physical Chemistry Chemical Physics* **2012**, *14* (33), 11689. https://doi.org/10.1039/c2cp41855j.

(27) Liu, D.; Li, Y.; Yuan, J.; Hong, Q.; Shi, G.; Yuan, D.; Wei, J.; Huang, C.; Tang, J.; Fung, M.-K. Improved Performance of Inverted Planar Perovskite Solar Cells with F4-TCNQ Doped PEDOT:PSS Hole Transport Layers. *Journal of Materials Chemistry A* **2017**, *5* (12), 5701–5708. https://doi.org/10.1039/C6TA10212C.

(28) Rangger, G.; Hofmann, O.; Romaner, L.; Heimel, G.; Bröker, B.; Blum, R.-P.; Johnson, R.; Koch, N.; Zojer, E. F4TCNQ on Cu, Ag, and Au as Prototypical Example for a Strong Organic Acceptor on Coinage Metals. *Phys. Rev. B* **2009**, *79* (16). https://doi.org/10.1103/PhysRevB.79.165306.

(29) Gerbert, D.; Hofmann, O. T.; Tegeder, P. Formation of Occupied and Unoccupied Hybrid Bands at Interfaces between Metals and Organic Donors/Acceptors. *The Journal of Physical Chemistry C* **2018**, *122* (48), 27554–27560. https://doi.org/10.1021/acs.jpcc.8b09606.

(30)   Xu, Y.; Hofmann, O. T.; Schlesinger, R.; Winkler, S.; Frisch, J.; Niederhausen, J.; Vollmer, A.; Blumstengel, S.; Henneberger, F.; Koch, N.; et al. Space-Charge Transfer in Hybrid Inorganic-Organic Systems. *Physical Review Letters* **2013**, *111* (22), 226802. https://doi.org/10.1103/PhysRevLett.111.226802.

(31)   Mukai, K.; Yoshinobu, J. Observation of Charge Transfer States of F4-TCNQ on the 2-Methylpropene Chemisorbed Si(100)(2×1) Surface. *Journal of Electron Spectroscopy and Related Phenomena* **2009**, *174* (1–3), 55–58. https://doi.org/10.1016/j.elspec.2009.04.006.

(32)   Topham, B. J.; Kumar, M.; Soos, Z. G. Profiles of Work Function Shifts and Collective Charge Transfer in Submonolayer Metal-Organic Films. *Advanced Functional Materials* **2011**, *21* (10), 1931–1940. https://doi.org/10.1002/adfm.201002677.

(33)   Koch, N. Organic Electronic Devices and Their Functional Interfaces. *ChemPhysChem* **2007**, *8* (10), 1438–1455. https://doi.org/10.1002/cphc.200700177.

(34)   Mori-Sánchez, P.; Cohen, A. J.; Yang, W. Many-Electron Self-Interaction Error in Approximate Density Functionals. *J. Chem. Phys.* **2006**, *125* (20), 201102. https://doi.org/10.1063/1.2403848.

(35)   Cohen, A. J.; Mori-Sanchez, P.; Yang, W. Insights into Current Limitations of Density Functional Theory. *Science* **2008**, *321* (5890), 792–794. https://doi.org/10.1126/science.1158722.

(36)   Zheng, X.; Liu, M.; Johnson, E. R.; Contreras-García, J.; Yang, W. Delocalization Error of Density-Functional Approximations: A Distinct Manifestation in Hydrogen Molecular Chains. *The Journal of Chemical Physics* **2012**, *137* (21), 214106. https://doi.org/10.1063/1.4768673.

(37)   Gani, T. Z. H.; Kulik, H. J. Where Does the Density Localize? Convergent Behavior for Global Hybrids, Range Separation, and DFT+U. *Journal of Chemical Theory and Computation* **2016**, *12* (12), 5931–5945. https://doi.org/10.1021/acs.jctc.6b00937.

(38)   Atalla, V.; Zhang, I. Y.; Hofmann, O. T.; Ren, X.; Rinke, P.; Scheffler, M. Enforcing the Linear Behavior of the Total Energy with Hybrid Functionals: Implications for Charge Transfer, Interaction Energies, and the Random-Phase Approximation. *Physical Review B* **2016**, *94* (3), 035140. https://doi.org/10.1103/PhysRevB.94.035140.

(39)   Wruss, E.; Zojer, E.; Hofmann, O. T. Distinguishing between Charge-Transfer Mechanisms at Organic/Inorganic Interfaces Employing Hybrid Functionals. *The Journal of Physical Chemistry C* **2018**, *122* (26), 14640–14653. https://doi.org/10.1021/acs.jpcc.8b03699.

(40)   Sai, N.; Barbara, P. F.; Leung, K. Hole Localization in Molecular Crystals from Hybrid Density Functional Theory. *Physical Review Letters* **2011**, *106* (22), 226403. https://doi.org/10.1103/PhysRevLett.106.226403.

(41)   Perdew, J. P.; Ernzerhof, M.; Burke, K. Rationale for Mixing Exact Exchange with Density Functional Approximations. *The Journal of Chemical Physics* **1996**, *105* (22), 9982. https://doi.org/10.1063/1.472933.

(42)   Van de Walle, C. G. Hydrogen as a Cause of Doping in Zinc Oxide. *Physical Review Letters* **2000**, *85* (5), 1012–1015. https://doi.org/10.1103/PhysRevLett.85.1012.

(43)   Woll, C. The Chemistry and Physics of Zinc Oxide Surfaces. *Progress in Surface Science* **2007**, *82* (2–3), 55–120. https://doi.org/10.1016/j.progsurf.2006.12.002.

(44)   Gao, W.; Kahn, A. Controlled *p* -Doping of Zinc Phthalocyanine by Coevaporation with Tetrafluorotetracyanoquinodimethane: A Direct and Inverse Photoemission Study. *Applied Physics Letters* **2001**, *79* (24), 4040–4042. https://doi.org/10.1063/1.1424067.

(45)   Bagus, P.; Käfer, D.; Witte, G.; Wöll, C. Work Function Changes Induced by Charged Adsorbates: Origin of the Polarity Asymmetry. *Physical Review Letters* **2008**, *100* (12). https://doi.org/10.1103/PhysRevLett.100.126101.

(46)   Erker, S.; Rinke, P.; Moll, N.; Hofmann, O. T. Doping Dependence of the Surface Phase Stability of Polar O-Terminated (000$\bar{1}$) ZnO. *New Journal of Physics* **2017**, *19* (8), 083012. https://doi.org/10.1088/1367-2630/aa79e7.

(47)   Blyholder, G. Molecular Orbital View of Chemisorbed Carbon Monoxide. *The Journal of Physical Chemistry* **1964**, *68* (10), 2772–2777.

(48)   Tautz, F. S. Structure and Bonding of Large Aromatic Molecules on Noble Metal Surfaces: The Example of PTCDA. *Progress in Surface Science* **2007**, *82* (9–12), 479–520. https://doi.org/10.1016/j.progsurf.2007.09.001.

(49)   Blum, V.; Gehrke, R.; Hanke, F.; Havu, P.; Havu, V.; Ren, X.; Reuter, K.; Scheffler, M. Ab Initio Molecular Simulations with Numeric Atom-Centered Orbitals. *Computer Physics Communications* **2009**, *180* (11), 2175–2196. https://doi.org/10.1016/j.cpc.2009.06.022.

(50)   Ren, X.; Rinke, P.; Blum, V.; Wieferink, J.; Tkatchenko, A.; Sanfilippo, A.; Reuter, K.; Scheffler, M. Resolution-of-Identity Approach to Hartree–Fock, Hybrid Density Functionals, RPA, MP2 and *GW* with Numeric Atom-Centered Orbital Basis Functions. *New Journal of Physics* **2012**, *14* (5), 053020. https://doi.org/10.1088/1367-2630/14/5/053020.

(51)   Ihrig, A. C.; Wieferink, J.; Zhang, I. Y.; Ropo, M.; Ren, X.; Rinke, P.; Scheffler, M.; Blum, V. Accurate Localized Resolution of Identity Approach for Linear-Scaling Hybrid Density Functionals and for Many-Body Perturbation Theory. *New Journal of Physics* **2015**, *17* (9), 093020. https://doi.org/10.1088/1367-2630/17/9/093020.

(52)   Tkatchenko, A.; Scheffler, M. Accurate Molecular Van Der Waals Interactions from Ground-State Electron Density and Free-Atom Reference Data. *Physical Review Letters* **2009**, *102* (7), 073005. https://doi.org/10.1103/PhysRevLett.102.073005.

(53)   Hofmann, O. T.; Deinert, J.-C.; Xu, Y.; Rinke, P.; Stähler, J.; Wolf, M.; Scheffler, M. Large Work Function Reduction by Adsorption of a Molecule with a Negative Electron Affinity: Pyridine on ZnO(10-10). *The Journal of Chemical Physics* **2013**, *139* (17), 174701. https://doi.org/10.1063/1.4827017.

Supporting Information :

Fractional and Integer Charge Transfer at Semiconductor/Organic Interfaces: The Role of Hybridization and Metallicity

Simon Erker and Oliver T. Hofmann[*]

Institute of Solid State Physics, Graz University of Technology, NAWI Graz, Austria

E-mail: o.hofmann@tugraz.at

Further Details on the Applied Computational Methods

In this section we give additional computational details that were not mentioned in the main part of this publication. In particular, we want to explain how doping and the corresponding band-bending are considered in our DFT calculations and how we choose the initial charge density at the beginning of the self-consistent field cycle.

In principle, with choosing a hybrid functional containing a certain amount exact exchange in a DFT calculation, the solution for the transferred charge being localized on individual molecule (integer charge transfer, ICT) *and* the solution for charge being homogeneously distributed on all molecules (fractional charge transfer, FCT) can be obtained[1] (See section below, where we discuss the influence of the exchange-correlation functional). Both charge transfer solution are fundamentally different: For ICT electrons are transferred

---

[*]To whom correspondence should be addressed

in integer numbers, resulting in a splitting of the spin-channels. The LUMO gets spit up in a singly occupied molecular orbital (SOMO) and a singly unoccupied molecular orbital (SUMO). This leads to a semiconducting band structure (no density at the Fermi energy). In contrast, for FCT the spin channels stay degenerate as all molecules get fractionally charged. This leads to a quasi-metallic density of states. Therefore, a prerequisite to obtain the ICT solutions is to perform spin-polarized calculations (unrestricted, which increases the computational cost). As both charge transfer mechanisms are stable solutions in our DFT calculation, we enforced either solution be choosing the "right" initial charge density. FCT solutions were initialized with a fully spin-symmetric charge density. For the ICT solution the symmetry breaking of the spin channels can be enforced by an unsymmetric initial spin density. For that, we define individual molecules within our unit cell to have a non-vanishing initial moment (0.1 per atom). This allows us to select which molecules preferably end up with an extra electron. The breaking of the spin-density in the molecular layer and the coexistence of molecules with filled and empy LUMOs in the supercell is accompanied by a spontaneous breaking in translation symmetry. The geometry of a molecule with empty LUMO differs from the geometry of the molecule with a filled SOMO. Therefore, geometry relaxations on the same theoretical level (same density functional) for the whole molecular layer within the supercell are an essential part of correctly describing the charge transfer mechanism and the resulting effects.

Considering Doping of Semiconductors in our DFT Calculations

A special focus of this work is on how an organic/inorganic interface system behaves as the charge carrier concentration of the substrate is changed. Therefore, explicitly including doping in our DFT calculation of hybrid interfaces is of utmost importance for this work. We include bulk doping of the ZnO substrate in our calculations by using our recently developed CREST method[2,3]. CREST allows explicitly considering doping in DFT calculations by mimicking the long-ranged electrostatic effect of band-bending. In this approach doping

within the slab itself is introduced by means of the virtual crystal approximation (VCA).[4,5] In the VCA some of the bulk atoms are replaced by pseudo-atoms whose nuclear charge Z' (and the corresponding electron number) is fractionally altered from the bulk atom integer number Z. The added or subtracted fraction of charge, ΔZ, is set such that it corresponds to the desired bulk charge carrier concentration of the substrate. In our case of n-doped ZnO only the oxygen atoms in the slab are replaced by the pseudo-atoms with a fractional atomic number $Z' = Z + \Delta Z$. The additionally introduced change ΔZ per oxygen atom gives rise to excess electrons, which fill the bottom of the conduction band, resulting in a corresponding amount of mobile electrons. The counter charge remains spatially fixed at the ionic cores. This mobile charge carriers are then available to be eventually transfered into a molecular layer. The spatially fixed ionized cores build up the electric field that leads to band-bending. However, at lower charge carrier concentrations the size of the space-charge region drastically exceeds the size of a computational feasible slab. Therefore a different approach is necessary to treat the region below the slab. In CREST a charge-sheet is introduced below the slab that mimics the electrostatic field associated with band-bending. In practice the sheet is build up by a grid of positive point charges. We use a total of 480 equally distributed point charges for the charge-sheet in the 2×2 supercell (i.e., a grid of 3×5 point charges for the primitive surface unit cell with the dimensions 3.26×5.26 Å. This corresponds to a density of 0.87 point charges per Å^2). Along with the charge-sheet, the corresponding amount of electrons are introduced such that the system remains overall neutral. The additional electrons represent the bulk charge carrier concentration that is transfered to the interface. The distance of this charge-sheet from the slab and the amount of charge within the sheet is determined self-consistently, requiring the bottom side work functions to coincide with the bottom side work function of the ZnO slab without a molecular layer (i.e. without charge transfer or band-bending). The work function of the unperturbed slabs were determined for each doping concentration separately and a work function accuracy of 100 meV was required in the self-consistent CREST scheme. With this procedure we assure to obtain the correct

amount of charge transfer into the molecular layer at a specific charge carrier concentration and reproduce the charge-transfer-limiting effect of the band-bending. As described in more detail in the original publication,[2] the only input we need for CREST is the desired bulk charge carrier concentration and the dielectric constant ϵ_r of the ZnO substrate. In this work we use $\epsilon_r = 4.0$, which is agreement with experimental values of the high frequency dielectric constant of ZnO.[6]

At this point it should be emphasized that with the CREST approach a homogeneous bulk charge carrier concentration is considered without the explicit introduction of defect sites in the ZnO substrate. Surface or sub-surface defects, which are not explicitly considered, might drastically reduce the band-bending. Such defects can additionally influence the local potential at the surface and therefore locally alter the charge transfer and the charge transfer mechanism.

Surface Geometry and Monolayer Structure

We constructed a reasonable molecular monolayer structure of F4TCNQ molecules adsorbed on the mixed terminated ZnO (10-10) surface without performing a full structure search. We like to mention that there are advanced methods to predict the morphology of monolayers available or currently under development,[7,8] but for our conceptional study such an intensive search is not required. We used a simpler, more straight-forward process to find the monolayer structure. Starting from the lowest energy local adsorption site of a single molecule on the surface (which was found by chemical intuition, see below), we build the densest possible monolayer that only contains this geometry. The calculations to find the monolayer structure were performed with the PBE functional, which is computationally more efficient than hybrid functions. For the local adsorption site we used specific starting geometries motivated by chemical intuition and performed a geometry relaxation for the molecule only, fixing the substrate atoms at their initial position. We found that the cyano groups of the

molecule prefer binding to surface Zn atoms, that act as docking sites for the molecule. We looked at upright-standing as well as flat-lying adsorption geometries. For a single molecule the flat-lying geometries are energetically favorable. The two lowest-energy local adsorption sites are plotted in Fig. S1.
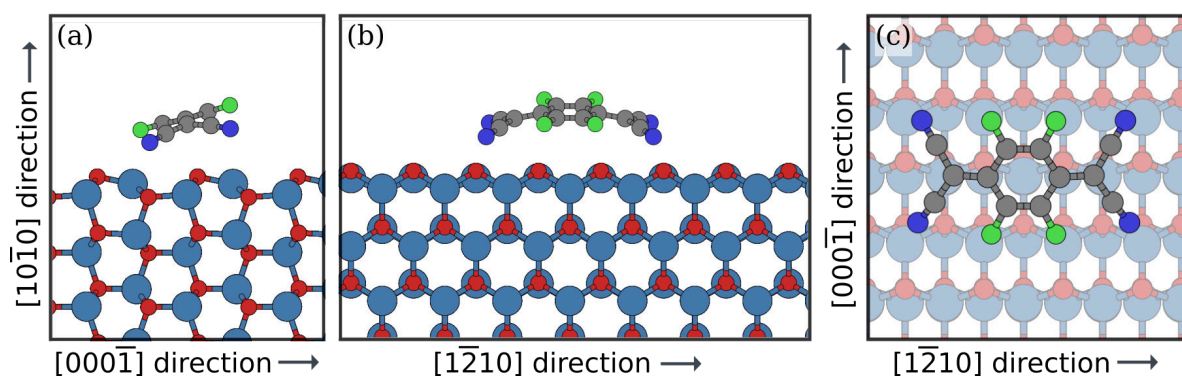
Figure S1: Adsorption geometry found for F4TCNQ on ZnO (10-10): (a-b/c) Side-view/topview of the lowest energy local adsorption site, that was further on used in this work to build the monolayer surface structure.

The energetically preferred adsorption site for the F4TCNQ molecule is parallel to the rills of the ZnO surface (parallel to the $[11\bar{2}0]$ direction). In this configuration each of the four cyano groups can bind to surface Zn atoms and the molecule covers a surface of six Zn atoms in total. The smallest surface unit cell in this case is then a orthogonal unit cell comprised of six surface zinc and six surface oxygen atoms, with the dimensions of 13.05 Å × 10.41 Å in the $[11\bar{2}0]$ and $[0001]$ directions, respectively. From the smallest surface unit cell for a single molecule we build the monolayer structure by using this unit cell in a periodic slab approach. This means the applied coverage is defined by the structure of the ZnO surface, and we used the highest packing density allowing the commensurate adsorption of F4TCNQ in a flat-laying manner. For the bigger unit cell containing four molecules, a 2×2 supercell was used (See Fig. S2). We do not claim the monolayer morphology considered in this work to be the one that should be found in experiments.

We calculated the adsorption energy ΔE^{ads} of the F4TCNQ molecule on the undoped
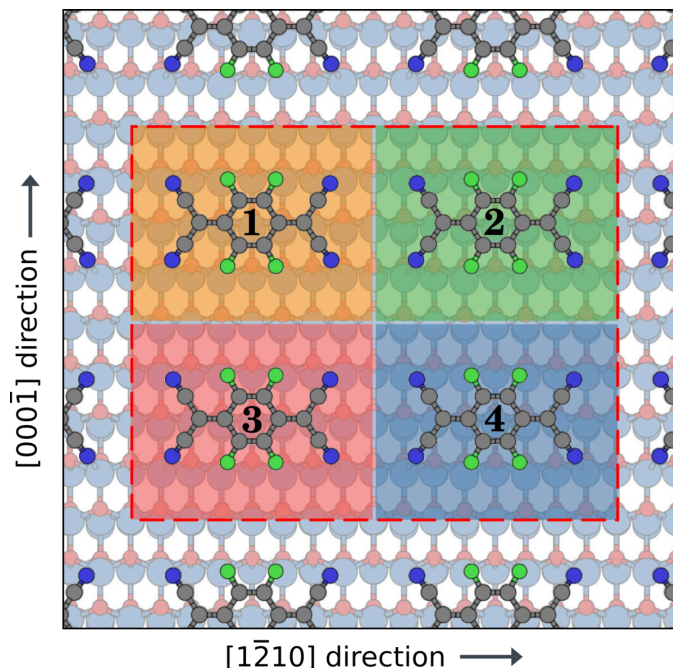
Figure S2: The red dashed line indicates the 2×2 supercell containing four molecules used in this work for the F4TCNQ monolayer on ZnO (10-10)

ZnO (10-10) surface using the following equation:

$$\Delta E^{\mathrm{ads}} = E^{\mathrm{sys}} - E^{\mathrm{sub}} - E^{\mathrm{mol}} \tag{1}$$

where E^{sys} and E^{sub} are the total energies of the combined system and the bare substrate, and E^{mol} is the total energy of the neutral molecule. The energy for the combined system was calculated from a PBEh ($\alpha = 0.63$) calculation with the small unit cell containing one molecule and the relaxation strategy described in the methods section of the main publication. The energy for the bare substrate was calculated in an equivalent manner without the adsorbate. The energy E^{mol} was obtained from a gas-phase calculation of the molecule. For the adsorption energy values neglecting van-der-Waals (vdW) interaction, we subtracted the vdW contribution to the total energies (the geometries were obtained including vdW interaction).

Molecular Orbital Density of States

In Fig. S3(a) we plot the molecular orbital density of states (MODOS) for the F4TCNQ molecule on undoped ZnO (10-10). Integration of each state up to the Fermi-energy then yields its formal occupation, as shown in Figure S3(b). The orbitals associated with the cyano groups (HOMO-10 to HOMO-13) show clearly a reduced occupation, because of the covalent bonding to surface Zn atoms. We find a notable occupation depletion of ca. 5%. This leads to a net positive charge transfer from this deeper laying states of 0.1 e- (value from Mulliken analysis of the cyano groups). For the other orbitals we find a rather weak hybridization with the substrate. The HOMO of the molecule is broadened to some extent. The LUMO basically does not hybridize at all with the bands of the semiconductor substrate, showing no broadening and remaining essentially empty (The nominal LUMO occupation of 2% and occupation numbers to be above 100%, that can be seen in Fig. S3(b), can be ascribed to artefacts of the Mulliken scheme).
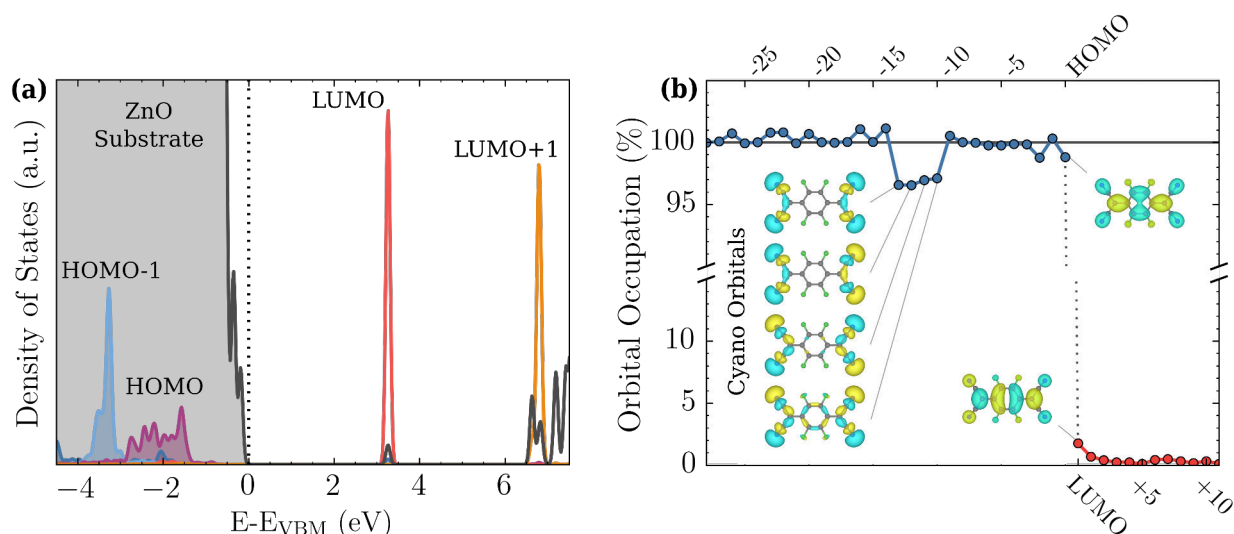
Figure S3: (a) Molecular orbital density of states (MODOS) projected on the free F4TCNQ orbitals and (b) molecular orbital population analysis of a single F4TCNQ molecule on undoped ZnO (10-10).

Discussion of the Applied Exchange-Correlation Functional: Determining the Hybrid Mixing Parameter

Describing the charge transfer, including the amount and particularly the localization of charge, is a non-trivial task using computational methods based on density functional theory (DFT). This is mainly attributed to the many-electron self-interaction error (MSIE) from which most approximate density functionals suffer.[9] This leads to a tendency of charge over-delocalization for common local and semilocal functionals. Therefore, these functionals favor FCT solutions for weakly hybridizing organic molecules adsorbed on inorganic substrates.[10] For describing the physics of such systems it is important to at least know whether the used functional does favor charge delocalization or localization.

In practice, the MSIE associated with approximate density functionals manifests itself as the convexity or concavity of the total energy as a function of fractional number of electrons N. In exact theory the ground-state energy with respect to N is known to be described by a series of straight-line segments.[11–13] The MSIE can, therefore, be defined indirectly using the straight-line energy condition.[11] A functional is defined as being free from many-electron SIE if the total energy $E(N)$ of an N electron system is a piecewise linear function between integer particle numbers. A deviation from this straight-line condition in form of a concave or convex E versus N curve is also referenced in the literature as localization error or delocalization error, respectively. Commonly used semilocal functionals underestimate the total energy of a system at factional occupation, leading to a convex energy curve and an over-delocalization of charge.[9,10,14] Hartree-Fock (HF), on the other hand, while being one-electron SI free by construction, still suffers from many-electron SI resulting in an overestimation of the total energy at factional occupation and charge over-localization.[9,10,14]

Because of this opposing trend for semilocal functionals and HF theory the deviation from the straight-line condition can be reduced and even lifted by employing a portion of the HF like exchange in a semilocal functional, resulting in so-called hybrid functionals.[15]

The disadvantage of such functionals is that they are computationally much more costly than their semilocal cousins. In this work, we apply the Perdew-Burke-Ernzerhof (PBEh) family of hybrid functionals:[16]

$$E_{xc}^{\text{PBEh}} = \alpha E_x^{\text{HF}} + (1 - \alpha)E_x^{\text{PBE}} + E_c^{\text{PBE}} \tag{2}$$

for which the amount HF exchange can be tuned by the hybrid mixing parameter $\alpha \in [0, 1]$ ($\alpha = 0$ corresponds to the common PBE functional,[17] the PBE0 functional is obtained by setting $\alpha = 0.25$[18,19]). The parameter α can be chosen to enforce the straight-line condition by requiring that the derivative of the total energy with respect to the number of electrons in the system, i.e. the orbital energy, does not change between integer electron numbers. This criterion can be enforced, for example, between the neutral and the singly-ionized system. It has recently been shown that when using hybrid functional DFT with an optimized mixing parameter α^* (i.e., the value at which the functional becomes MSIE-free), both solutions, the ICT and the FCT case, are stable and energetically degenerate if the straight line condition is fulfilled.[1] This limits our possibility to use DFT to predict the correct charge transfer mechanism, but gives us the opportunity to gain a deeper insight into charge transfer systems by studying both possible solutions. Therefore, our study should be seen as a proof of concept that both charge transfer mechanisms can in principle occur simultaneously.

In the following we show how we determined the mixing parameter α used in this work. We used the fact that the hybrid mixing parameter can be chosen to enforce the straight-line condition by requiring that the derivative of the total-energy with respect to the number of electrons in the system (in Kohn-Sham DFT this equals the energy of the orbital $\epsilon(N)$ that is filled) does not change between integer electron numbers N. We enforced this criterion for the free F4TCNQ molecule between the neutral and the singly-charged system and obtained the optimal mixing parameter $\alpha^* = 0.63$ (For a specific system we denote the optimal mixing parameter that fulfills the straight-line condition as α^*). This is the mixing parameter that

is used throughout this work, although the surface system should require less HF exchange than the molecule in the gas phase due to screening effects of the substrate.[1] We note that at α values below 0.2 the energy level alignment of the system is qualitatively no longer reproduced correctly. There, the LUMO of the F4TCNQ molecule is shifted below the valence band of the ZnO substrate, leading to a spurious charge transfer to the molecule already without doping. Therefore, possibly not all aspects of the F4TCNQ/ZnO interface can simultaneously be described correctly using hybrid functional DFT. To reproduce the correct energy level alignment, we need to accept that the charge localization for the chosen α parameter is driven towards over-localization and the integer charge transfer solutions are energetically favored by the applied functional. In other words, we apply the gas phase parameter because if using the α^* for the interface system (which would be less than 0.2) we obtain a spurious energy level alignment between the molecule and the substrate. We want to stress here that the qualitative results in this contribution are not influenced by the used functional as long we use a mixing parameter $\alpha > 0.2$ and a correct energy level ordering is assured. We tested that qualitatively equivalent results are obtained when using $\alpha = 0.25$, which is the default value for the PBE0 functional.[18,19]

Straight-Line Condition for F4-TCNQ in the Gas Phase

Determining the straight-line mixing parameter α^* for gas phase molecules using a DFT code capable of applying open boundary conditions is a straight forward procedure. We calculated the molecular orbital energies for the neutral molecule and the anion (i.e. singly charged molecule) using the optimized geometries of for various mixing parameters α. As FHI-aims allows to calculate fractional occupations of the orbital energies as well we can directly observe the concavity or convexity for the total energy curve (see Fig. S4). For PBE ($\alpha = 0.0$) the curve is clearly convex and for HF exchange ($\alpha = 1.0$) the curve is clearly concave. The total energies of the neutral molecule for every α are set to zero in this graph. We can also see that the electron affinity (EA) calculated from the total energy difference

between the anion and the neutral molecule obviously slightly depends on the amount of HF exchange, as the curves for the different αs do net meet again for the single negatively charged molecule.
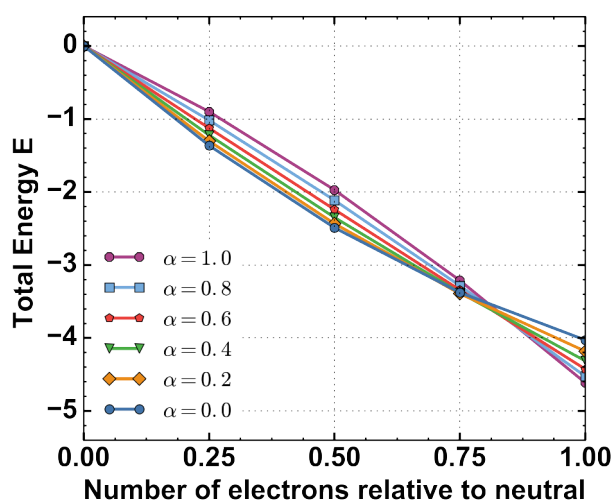
Figure S4: Total energy as a function of LUMO occupation between a neutral molecule and a anion for various hybrid mixing parameters α. Five charging levels have been considered ($N = 0$, $N = 0.25$, $N = 0.5$, $N = 0.75$ and $N = 1$). The energy curves are aligned to be zero for the neutral molecule.

To determine the optimal mixing parameter α^* we use the orbital energy of the LUMO (i.e. the derivative of the total energy curve). For a singly charged molecule, the LUMO of the neutral molecule now becomes the SOMO of the charged molecule. The energetic evolution of the LUMO as it becomes filled is plotted in Fig. S5(a) for various mixing parameters α. In agreement with the total energy curves we find a increase of the LUMO orbital energy as is become occupied for small mixing values $\alpha < 0.6$ and an decrease for higher mixing values $\alpha > 0.8$. The slope of the orbital energies are obtained from a linear fit and plotted in Fig. S5(b). A linear interpolation between the points results in a vanishing slope at the straight-line mixing parameter $\alpha^* = 0.63$. This is similar to the value of 0.7 obtained for the chemically similar TCNQ molecule.[15]
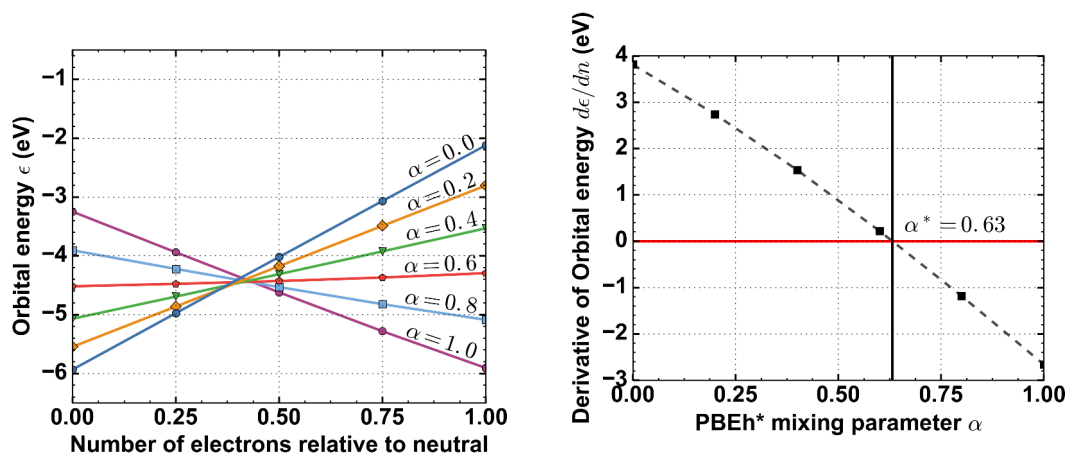
Figure S5: (left) Evolution of LUMO orbital energy of F4TCNQ in the gas phase as is gets (partially) occupied for different hybrid mixing parameters α. (right) Slope of the orbital energy plotted as a function of α. At $\alpha^* = 0.63$ the slope is zero and the straight line condition is fulfilled.

References

(1) Wruss, E.; Zojer, E.; Hofmann, O. T. *The Journal of Physical Chemistry C* **2018**, *122*, 14640–14653.

(2) Erker, S.; Rinke, P.; Moll, N.; Hofmann, O. T. *New Journal of Physics* **2017**, *19*, 083012.

(3) Sinai, O.; Hofmann, O. T.; Rinke, P.; Scheffler, M.; Heimel, G.; Kronik, L. *Phys. Rev. B* **2015**, *91*, 075311.

(4) Nordheim, L. *Annalen der Physik* *401*, 607–640.

(5) Sinai, O.; Kronik, L. *Phys. Rev. B* **2013**, *87*, 235305.

(6) others,, et al. *Journal of Applied Physics* **2003**, *93*, 126–133.

(7) Scherbela, M.; Hörmann, L.; Jeindl, A.; Obersteiner, V.; Hofmann, O. T. *Phys. Rev. Materials* **2018**, *2*, 043803.

(8) Packwood, D. M.; Han, P.; Hitosugi, T. *Nature Communications* **2017**, *8*, 14463.

(9) Mori-Sánchez, P.; Cohen, A. J.; Yang, W. Many-electron self-interaction error in approximate density functionals. 2006.

(10) Mori-Sánchez, P.; Cohen, A. J.; Yang, W. *Physical review letters* **2008**, *100*, 146401.

(11) Perdew, J. P.; Parr, R. G.; Levy, M.; Balduz, J. L. *Phys. Rev. Lett.* **1982**, *49*, 1691–1694.

(12) Perdew, J. P.; Ruzsinszky, A.; Csonka, G. I.; Vydrov, O. A.; Scuseria, G. E.; Staroverov, V. N.; Tao, J. *Phys. Rev. A* **2007**, *76*, 040501.

(13) Li, C.; Yang, W. *The Journal of Chemical Physics* **2017**, *146*, 074107.

(14) Stein, T.; Autschbach, J.; Govind, N.; Kronik, L.; Baer, R. *The journal of physical chemistry letters* **2012**, *3*, 3740–3744.

(15) Atalla, V.; Zhang, I. Y.; Hofmann, O. T.; Ren, X.; Rinke, P.; Scheffler, M. *Phys. Rev. B* **2016**, *94*, 035140.

(16) Perdew, J. P.; Ernzerhof, M.; Burke, K. *The Journal of chemical physics* **1996**, *105*, 9982–9985.

(17) Perdew, J. P.; Burke, K.; Ernzerhof, M. *Phys. Rev. Lett.* **1997**, *78*, 1396–1396.

(18) Ernzerhof, M.; Scuseria, G. E. *The Journal of Chemical Physics* **1999**, *110*, 5029–5036.

(19) Adamo, C.; Barone, V. *The Journal of Chemical Physics* **1999**, *110*, 6158–6170.

6.4 Appendix: Determining the straight-line mixing parameter for interface systems

In the following sections we present several methods to determine the straight-line hybrid mixing parameter α^* for interface systems. As we have seen in the supporting information of the publication, for gas phase molecules this is a straight forward procedure. For interface systems, however, there is no unique method to determine α^*. First we use the fact that at α^* both solutions are energetically degenerate and find that the optimal mixing depend on the charge carrier concentration of the substrate. As the charge carrier concentration is increased the screening increases as well, leading to a smaller α value to fulfill the straight line condition. We also present two other methods to determine α^* for the surface system based more directly on the straight line condition. We use the total energy itself and determine the orbital energy from the total energy derivative with respect to the occupation number. In this case we need to subtract the energy contribution from our doping model. This is basically the energy of a plate capacitor with the plates sitting at the level of the molecular layer and the other one at the position of the charge-sheet of the CREST. The third method presented is based on determining the orbital energies of the molecule directly from molecular orbital density of states (MODOS) and again require the orbital energy to be constant as the occupation is increased between zero and one. The evaluation of the straight-line hybrid mixing parameter is in general more of computational interest, as it marks the transition point between the delocalization error and the localization error for the used density functional family for the specific system. It determines whether the DFT calculation favors an FCT or ICT solution and is hence worthwhile being studied to be able to better classify the computationally obtained results of a charge transfer system. Furthermore by understanding the factors that influence the α^* value we can also gain some more knowledge about the physics of the investigated system.

6.4.1 Straight-line condition for F4TCNQ/ZnO from the degeneracy of the ICT and FCT Solutions

Since at the straight-line value α^* the hybrid functional neither favors localization nor delocalization, at this point the ICT and the FCT solution are energetically degenerate. We can use this to determine α^* for interface systems. We find that this method is the most reliable one to determining α^* for interface systems. We need to mention that the energetic difference between the two possible solutions can only be evaluated for α values that are greater than α^* of the interface system. This is because the ICT solution can only be obtained for $\alpha \geq \alpha^*$ [129]. For hybrid functionals with less HF exchange mixed in only the FCT solution is stable. Calculations to obtain the ICT solution at a specific charge carrier concentration and hybrid mixing parameter were performed with the unit cell containing four molecules. With this unit cell we can simulate charge transfer at charge carrier concentrations at which a quarter, half, three-quarter and all

molecules in the molecular monolayer hold one electron in their LUMO (in the following discussion we refer to molecules with an integer filled LUMO as charged molecules and molecules with empty LUMOs as neutral molecules). This corresponds to charge transfer of one, two, three and four electrons per unit cell from the substrate to the monolayer. The FCT solutions were enforced by performing spin-restricted calculations (i.e. without spin-polarization). As all four molecules in the unit cell are equivalent we performed the FCT calculations in the smaller unit cell containing only one molecule.

At the four charge carrier concentrations that correspond to the integer electron charge transfer values, calculations were performed with $\alpha = 0.25$, 0.45 and 0.63. The total energy difference for this α values between the FCT and the ICT solution are plotted in Fig. 6.1 for the different charge carrier concentrations. Since all the values are negative, the ICT solutions is the energetically preferred solution for the considered α values. We might assume that the two solutions should become equal when there are no free charge carries available (at $N_D = 0$) and no charge is transferred at all. This should be valid independently of the hybrid mixing parameter. We do not know the exact functional dependence of these curves, however, it seems that as the charge carrier concentration is decreased the energy difference approaches zero, which is what we expect. Evaluations at lower charge carrier concentrations are limited by the required unit cell size and the resulting computational costs. The energy differences found are rather small for the large unit cell sizes we are considering and the points in this graphs are subject to numerical uncertainties. The drawn conclusions should thus be seen qualitatively only.
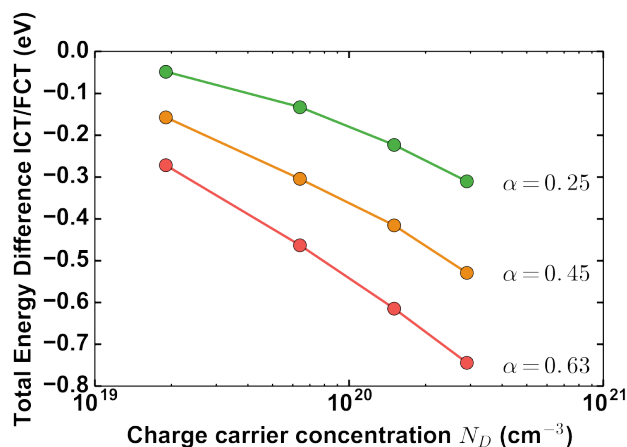
FIGURE 6.1: Total energy difference between FCT and ICT solution plotted at the four charge carrier concentrations that correspond to change transfer of one, two, three and four electrons per unit cell for three differed hybrid mixing parameters $\alpha = 0.25$, 0.45 and 0.63.

We see in the graph above that the slope of the total energy difference increases with increasing mixing parameter α. In Fig. 6.2 we plotted the total energy difference as a function of α for the four considered charge carrier concentrations. We linearly fitted the curves for the four charge carrier concentrations to evaluate the straight line hybrid mixing parameter α^* from the

intersection of this fit with the line where the energy difference vanishes, i.e. the FCT and the ICT solution are energetically degenerate.
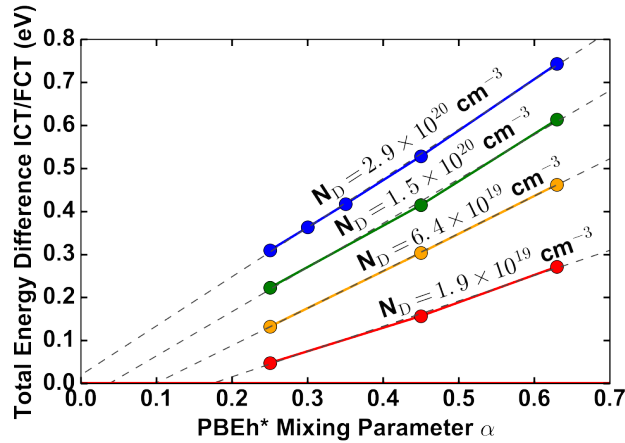
FIGURE 6.2: Absolute value of the total energy difference between FCT and ICT solution plotted as a function of hybrid mixing parameter α for the four charge carrier concentrations that correspond to charge transfer of one, two, three and four electrons per unit cell. The intersection of the linear fit for each charge carrier concentration with the y-axis (i.e. if the total energy difference is zero) gives the straight line mixing α^* for the specific charge carrier concentration.

We find that the α^* value needed to fulfill the straight-line condition for the F4TCNQ/ZnO interface system clearly depends on the charge carrier concentration of the substrate and decreases as the charge carrier concentration increases. For a clearer visual confirmation of this claim we plotted the straight-line mixing α^* as is depends on the charge carrier concentrations in Fig. 6.3.
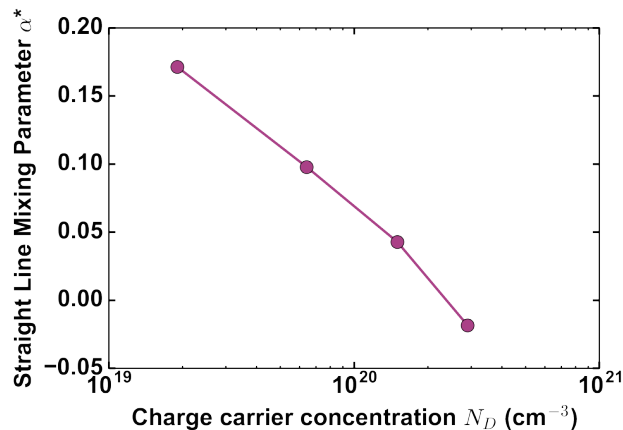
FIGURE 6.3: Dependence of the straight-line hybrid mixing parameter α^* from the charge carrier concentration of the substrate. The amount HF exchange needed to fulfill the straight line condition decreases as the charge carrier concentrations increases.

We find that at very high charge carrier concentrations the required amount of HF exchange to satisfy the straight line condition essentially becomes zero, i.e. PBE in this case seems to

be many-electron SIE free. That the required amount of HF exchange decreases as the charge carrier concentrations increases can be explained from a stronger surface screening at higher charge carrier concentrations. This is consistent with the fact that the surface screening energy scales with the dielectric substrate and a higher charge carrier concentration results in a more polarizable substrate.

6.4.2 Straight-line condition from the total energy of the interface system

In this section we briefly want to present another method to evaluate the hybrid mixing parameter to fulfill the straight line condition for organic/inorganic interface systems. We use the total energy of the system and evaluate the orbital energy from its derivative with respect to the partial LUMO occupation. Here we do not consider a specific charge carrier concentration of the substrate but rather artificially include electrons into our system without using the self-consistent CREST approach. We instead use a CREST-like approach by placing the charge-sheet at a fixed distance to the slab and introducing the equivalent amount of negative charge into our unit cell. The overall positive charge within the sheet should be the desired LUMO filling. The extra electrons are available to occupy empty states, i.e. the LUMO of the F4TCNQ, while the unit cell stays overall charge neutral. For this evaluation of α^* we use a unit cell containing only one F4TCNQ molecule. Because of the charged sheet within our unit cell we need to subtract the energy contribution from the electric field being build up between the positively charged sheet and the negatively charged molecular layer. This energy contribution is basically the electrostatic energy of a plate capacitor and can be easily calculated form

$$E_{\text{capacitor}} = \frac{Q^2 d}{2\epsilon_0 A} \tag{6.1}$$

with Q the summed up charge within the layer of point charges, d the distance between the two plates, i.e. the distance between the charge sheet and the molecular layer (we used the average z-coordinate of all carbon atoms of the F4TCNQ molecule as position of the molecular layer), ϵ_0 being the vacuum permittivity and A the surface area of the unit cell. Using this approach, calculations were performed for a LUMO occupation with 0.0, 0.5 and 1.0 e^- and for α values of 0.25, 0.5, 0.63 and 0.75. The derivative of the total energy was then evaluated using finite differences. We plotted the obtained difference quotients for the used α values in Fig. 6.4(a). The slope of the orbital energies at each considered α is plotted in Fig. 6.4(b). From a linear fit of those points the straight-line α^* is evaluated and found to be approximately zero. Again we find that α^* drastically decreases for the interface system compared to the gas phase value. Again this result suffers from numerical uncertainties and the quantitative α^* value should be considered with care.
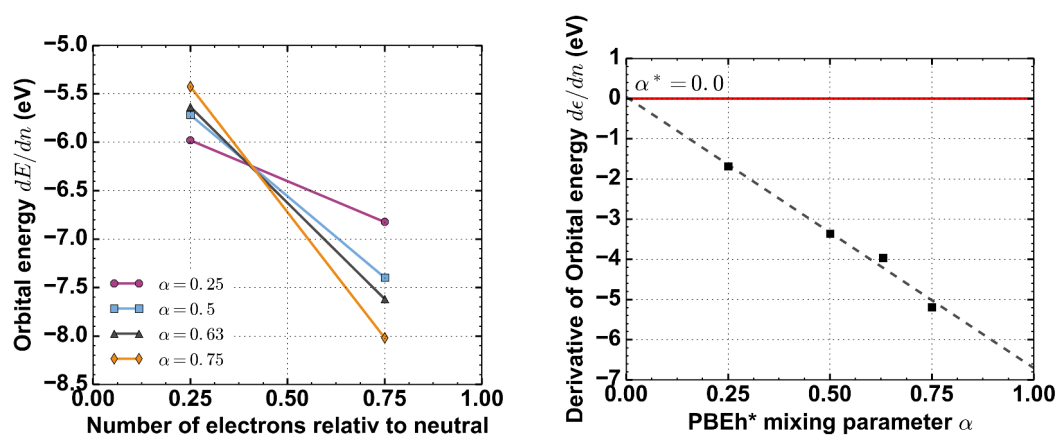
FIGURE 6.4: (left) LUMO orbital energies for $\alpha = 0.25$, 0.5, 0.63 and 0.75 obtained from the derivative of the total energies of the interface system at F4TCNQ LUMO occupation 0.0, 0.5 and 1.0 e^-. (right) Change of LUMO energy for the considered α values. A linear fit yields a value of $\alpha^* = 0.0$ for $d\epsilon/dN = 0$.

6.4.3   Straight line condition from MODOS orbital energies

The α^* value can also be evaluated from the orbital energies obtained from the molecular orbital density of states (MODOS). As in the method above no specific charge carrier concentration was considered, but rather an artificial charging of the molecule was enforced by a CREST-like approach (see description above). The MODOS was evaluated for α values 0.25, 0.45 and 0.63 for a "neutral" F4TCNQ molecule on the surface (neutral in the sense that the LUMO of the molecule is essentially empty, although overall the molecule is slightly positively charged from charge back-donation) and a single negatively charged molecule (the LUMO is split into a filled SOMO and an empty SUMO). The MODOS allows to separate the LUMO contribution to the total density of states. We evaluated the energy of the orbital from the weighted mean of the LUMO contribution (Integrate ($MODOS \times energy$) and divide by the integrated MODOS to obtain the weighted mean energy position of the orbital). To be able to compare the orbital energies of differently charged systems the obtained orbital energies were aligned to the upper vacuum level of the specific system. The development of the LUMO energy as a function of occupation and the change in orbital energy as a function of α is plotted in Fig.6.5.

Equivalently to the previous methods we find a significant reduction of the α^* for the interface system compared to the gas phase result. Using the orbital energy obtained from the MODOS we find $\alpha^* = 0.11$.
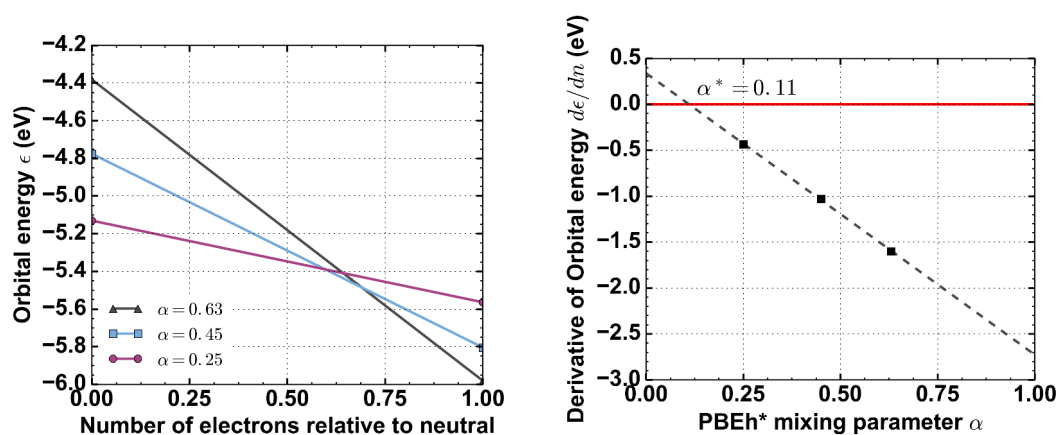
FIGURE 6.5: (left) LUMO orbital energies for $\alpha = 0.25$, 0.45, and 0.63 obtained from the MODOS of the interface system for an empty LUMO and a singly occupied LUMO (i.e. SOMO). Orbital energies are given relative to the upper vacuum level. (right) Change of LUMO energy upon filling as a function of the considered α values. A linear fit yields a value of $\alpha^* = 0.11$ for $d\epsilon/dN = 0$.

6.5 Appendix: Change in the molecular geometry upon charge transfer

Upon surface adsorption and charging, the intra-molecular bond lengths of F4TCNQ change noticeably. The bond-lengths for the molecules on the surface with empty LUMOs and with integer filled LUMOs are plotted in Fig. 6.6. Interestingly, the bond lengths of a neutral free molecule are basically identical with the bond lengths of an "uncharged" (empty LUMO) molecule adsorbed on the surface. With the change in bond lengths upon charge transfer into the LUMO we expect also a change in the vibrational normal modes of the molecules. Therefore the coexistence of "charged" and "uncharged" molecules on the surface might be resolvable in infrared vibrational spectra.
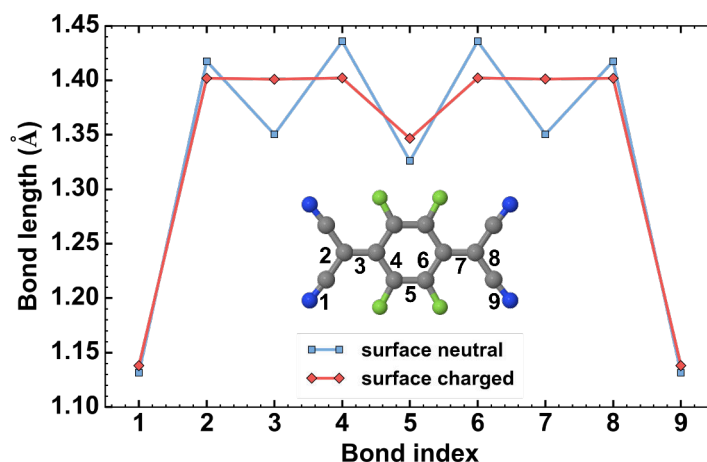
FIGURE 6.6: Bond lengths of a molecule with an unoccupied LUMO ("neutral") and a molecule with an integer filled LUMO ("charged") absorbed on the ZnO (10-10) surface.

6.6 Appendix: Charge transfer rates calculated from Marcus theory

A question that arose during this work was whether imaging experimental methods are able to capture ICT scenarios at organic/inorganic interface systems. It is presently not completely clear if the electrons remain localized on individual molecules or hop between the molecules in the monolayer at a certain hopping rate. In principle the charges are confined normal to the surface, i.e. in the molecular layer, but are free to move parallel to the surface. In case the electrons hop at a rate faster than the time resolution in experiments, it would not be possible to identify the ICT nature of charge transfer. In a time averaged image we would rather obtain a charge distribution that erroneously looks like to be homogeneous within the monolayer, which would be expected for FCT. So the question is if the coexistence of charged and uncharged molecules can be observed from imaging experimental methods or only an averaged image can be obtained because of a limited time-resolution. To answer this question we calculated the electron transfer rate or hopping time within the molecular layer from Marcus theory[144,145]. The Marcus formula for electron transfer rate reads

$$k = \frac{V^2}{\hbar} \sqrt{\frac{\pi}{\lambda k_{\mathrm{B}} T}} \exp\left(-\frac{(\Delta G^0 + \lambda)^2}{4 \lambda k_{\mathrm{B}} T}\right). \tag{6.2}$$

where $\hbar$ is the reduced Planck constant and k_{B} is the Boltzmann constant. ΔG^0 is the free energy difference between the molecular sites of the initial electron position and final electron position. Since in our molecular layer we only have one type of molecules and all the molecular sites within the layer are equivalent, $\Delta G^0 = 0$. The two remaining parameters are the most important ones and are the key characteristics that control charge mobility in organic electronics: The electronic coupling V and the reorganization energy λ. Both strongly depend on the material and the arrangement of the molecules within the molecular layer. In the case of electron hopping between two molecules the intramolecular reorganization energy λ is the energy that is required for the transition of a neutral molecule to a anion and vice versa for the former anion to a neutral molecule. Since this is mainly the energy cost due to geometry modifications, we can calculate it from a geometry relaxation with DFT. We therefore used the unit cell containing four molecules and performed a geometry relaxation at a charge carrier concentration of $N_D = 2 \times 10^{19}$ cm^{-3} (at which one out of the four molecules in the unit cell gets charged by one electron) starting from the geometry of a neutral monolayer (i.e. all molecules without a filled LUMO). We obtained a energy difference between the initial neutral geometry and the final unit cell with one charged molecule of 0.42 eV. This value is the relaxation energy for a transition of a single molecule from a neutral geometry to the anion geometry on the ZnO substrate. The total reorganization energy for electron hopping between two molecules is then twice the relaxation energy for a single molecule.

The second important parameter is the electronic coupling V between neighboring molecules in the monolayer. It is also known as adiabatic coupling or effective or generalized charge transfer

integral. It can be written as an expectation value of the Hamiltonian of the system,

$$V = H_{ab} = \langle \Psi_a | \hat{H} | \Psi_b \rangle \tag{6.3}$$

where Ψ represents the multielectron wavefunction of the molecule with the label a and b, respectively. $\hat{H}$ is the Hamiltonian of the system. There are several DFT based methods proposed to calculate this parameter, e.g. constrained density-functional theory (cDFT)[146], frozen-density embedding[147] or fragment-orbital (FO)[148,149]. In this work we use the fragment-orbital density-functional theory (FO-DFT) scheme as implemented in FHI-aims for the calculation of electronic coupling values. The basic idea behind the fragment orbital (FO) family of methods is that only the frontier orbitals directly participate in the charge transfer process while all other orbitals remain unperturbed. The fragments in our case are two neighboring molecules within the molecular monolayer. In our model we considered the neighboring molecule in x and y direction and calculated the electronic coupling for these two possible pairs of molecules.
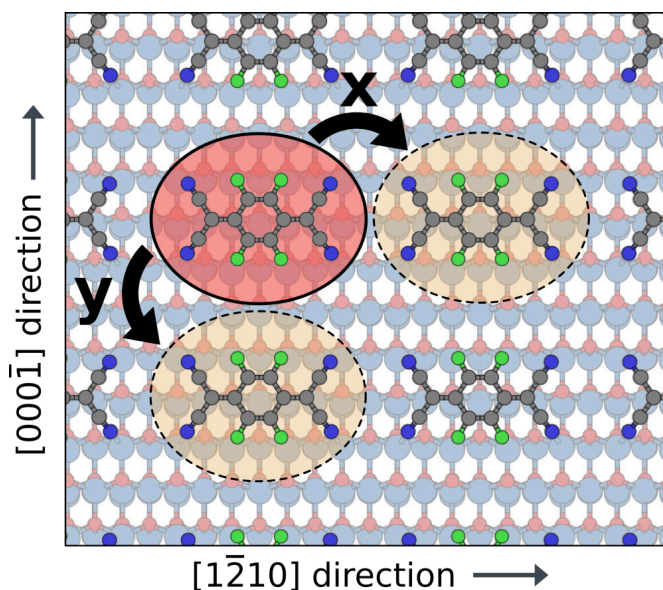
FIGURE 6.7: Electron hopping rates between the LUMO's of the molecules within our molecular monolayer model were calculated for the x-direction (along the [1$\bar{2}$10] direction) and the y-direction (along the [0001] direction).

In the original FO method the Hamiltonian is always constructed from the orbitals of the neutral fragments and for electron transfer the reference states are taken as the LUMOs of the molecules. There are also other "flavors" of FO-DFT available that considers the right number of electrons in the system, but in the work of Schober et al.[150] it was shown that the original formulation of FO-DFT with neutral fragments shows similar accuracy compare to charged fragment schemes in the case of electron transport. Also the used functional has a noticeable influence on the absolute value of the electronic coupling. Is was shown that V has a nearly linear dependence on the amount of HF exchange of a hybrid functional. Values almost vary by a factor of two between $\alpha = 0.0$ and $\alpha = 1.0$[150]. In this work we therefore use the original scheme with neutral fragments in combination with a hybrid functional including an intermediate amount of

HF exchange (PBEh*, $\alpha = 0.63$). The obtained electronic coupling value should give a sufficient accuracy for a rough estimation of the electron hopping time within the monolayer.

All FO-DFT calculations were performed with the FHI-aims *tight* defaults for integration grids and basis sets. For the electronic coupling between the LUMOs of two molecule next to each other in x-direction (along the $[1\bar{2}10]$ direction) we obtained a value of $V_x = -2.82$ meV and in y-direction (along the $[0001]$ direction) a value of $V_y = -0.08$ meV. The sign of V depend on the phase of the fragments, but since V^2 is used in the Marcus formula (6.2), the sign does not affect the hopping rates. Putting the obtained values in Markus equation we get electron hopping rates at room temperature ($T = 298$ K) in x and y direction of $k_x = 3.3 \times 10^7$ s^{-1} and $k_y = 2.7 \times 10^4$ s^{-1}, respectively, corresponding to hopping times of $\tau_x \approx 30$ ns and $\tau_y \approx 40$ μs. Both hopping rates are far from common experimental time resolutions of surface imaging techniques. Our calculations therefore imply that charge hopping within molecular monolayers at organic/inorganic interfaces may happen at such high rates that experimental imaging methods would not be able the see the coexistence of charged an uncharged molecules at the surface. Therefore integer charge transfer of single electrons would not be able to be resolved, but rather a time averaged charge distributions would be observed. We would like to mention that these results apply for a perfect monolayer and a defect free substrate. Charge localization at a single molecule in the monolayer for a longer time still might occur due to surface defects at the inorganic substrate.

6.7   Appendix: Results for the O-terminated surface

Originally we studied the charge transfer mechanism also on the oxygen-terminated ZnO surface that is saturated by a (2×1)-hydrogen overlayer. Due to the hydrogen overlayer, that acts as a buffer layer, the cyano groups can not bind directly to surface atoms and the molecule is rather weakly bound to the surface, primarily due to vdW interactions. Therefore, we do not observe hybridization of the cyano orbitals and, therefore, also no resulting fractional positive charge transfer, as we found it for the mixed terminated surface. The charge transfer to the LUMO of the molecule is also on this surface "ionically driven" and occurs in integer units for the chosen density functional. The calculations were performed with the PBEh* functional ($\alpha = 0.63$), equivalent to the calculations presented in the publication. Also the numerical settings and the k-grid were chosen equivalently to the settings for the mixed terminated surface.

In the lowest energy local adsorption geometry of the F4TCNQ molecule on the O-terminated ZnO surface the molecule is oriented parallel to the rows of the hydrogen overlayer (see Fig. 6.8). In this configuration the cyano groups lie on top of hydrogen atoms of the (2×1)-H overlayer.

In Figure 6.9(a) we plot the molecular orbital density of states (MODOS) for the F4TCNQ molecule on the O-terminated ZnO (000-1) surface. The corresponding occupation analysis is
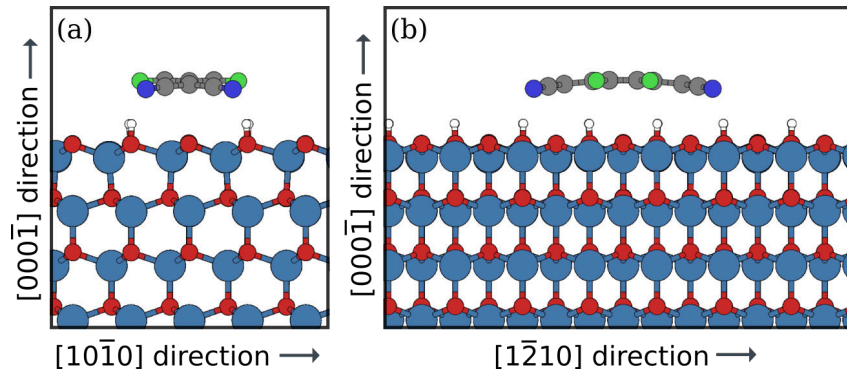
FIGURE 6.8: Adsorption geometry found for F4TCNQ on ZnO (000-1): (a-b) Sideview of the lowest energy local adsorption site.

shown in Figure 6.9(b). On this surface the orbitals associated with the cyano groups (HOMO-10 to HOMO-13) show a negligible reduction in the occupation (below 1%). Also all other orbitals show no significant hybridization with the substrate, only the HOMO of the molecule is broadened to some extend, but also shows no reduced occupation. The LUMO lies in the band gap of ZnO and does not hybridize with substrate. Thus the orbital remains empty.
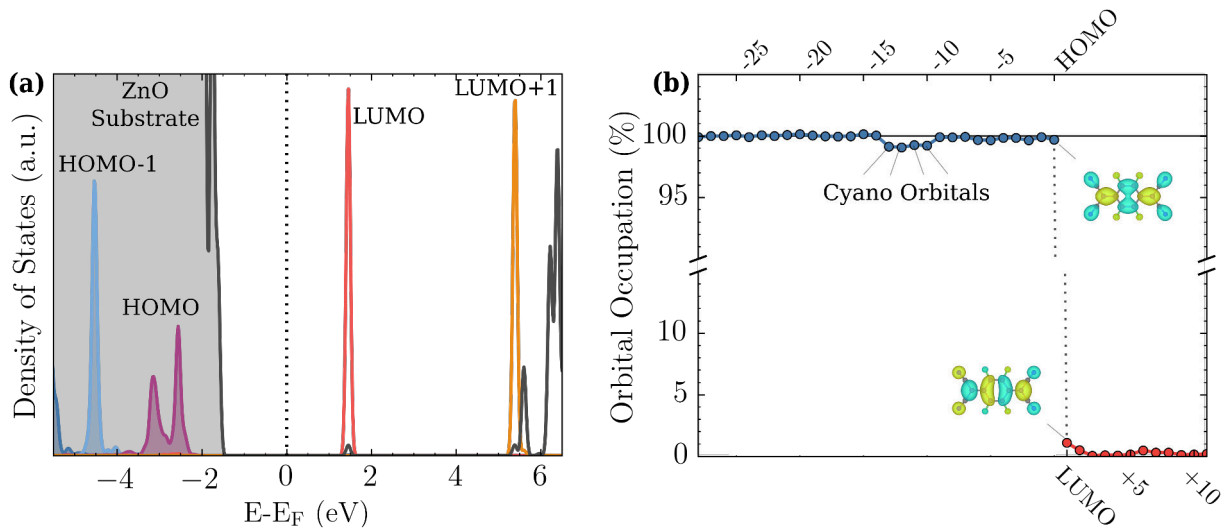
FIGURE 6.9: (a) Molecular orbital density of states (MODOS) projected on the free F4TCNQ orbitals and (b) molecular orbital population analysis of a single F4TCNQ molecule on undoped ZnO (000-1).

Assuming a monolayer coverage of F4TCNQ molecules, charge transfer to the LUMO of the molecules can be achieved by doping of the substrate. We simulated the charge transfer to a surface supercell containing four molecules (see Fig. 6.10).

The charge carrier concentrations that lead to charge transfer of integer electron numbers into the 2×2 supercell containing four molecules are similar to the values obtained for the mixed-terminated surface. We find charge transfer of 1, 2, 3 and 4 electrons within the unit cell of the molecular layer at charge carrier concentrations of approximately 2.0×10^{19}, 6.8×10^{19}, 1.6×10^{20}, and 3.1×10^{20} cm^{-3}, respectively. Equivalently to the mixed-terminated surface
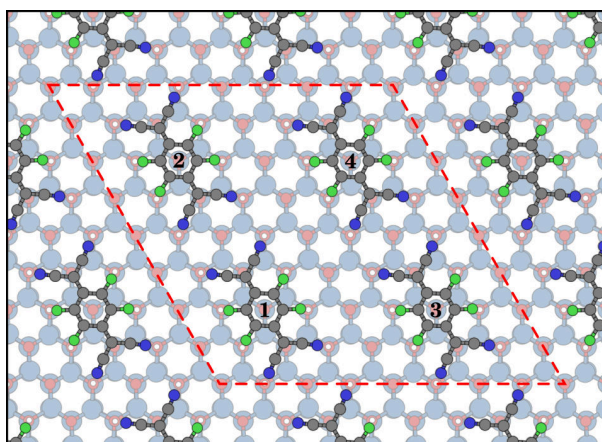
FIGURE 6.10: The red dashed line indicates the 2×2 supercell containing four molecules for the F4TCNQ monolayer on O-terminated ZnO (000-1)

the additional charge always localizes onto individual molecules. Due to Coulomb repulsion between the on individual molecules localized electrons, it is energetically favorable that the charge localizes on molecules being furthest apart in our 2×2 supercell. Assuming charge transfer of two electrons within our supercell and that the first electron localizes on molecule 1 (according to the labeling in Fig. 6.10), it is energetically favorable to place the second electron onto molecule 4, as it is the furthest apart. It needs to be mentioned again, that the charge localization is a result of the used density functional, and the results for O-terminated ZnO do not predict ICT for the specific system.

For the F4TCNQ monolayer on O-terminated ZnO we also simulated constant height STM images at a charge carrier concentration of 2.0×10^{19} cm^{-3}, i.e. when one molecule within the 2×2 supercell is charged. We used the Tersoff-Hamann model as implemented in FHI-aims to simulate a map of the tunneling current at voltages of -3.0 V and +2.0 V. A sideview of the simulated system and the obtained STM images are shown in Figure 6.11. If the charge is localized on individual molecules during the time a STM images is experimentally obtained, we expect that the inhomogeneous charge distribution should be clearly visible in the obtained image (*cf.* section 6.6 about the hopping rate).
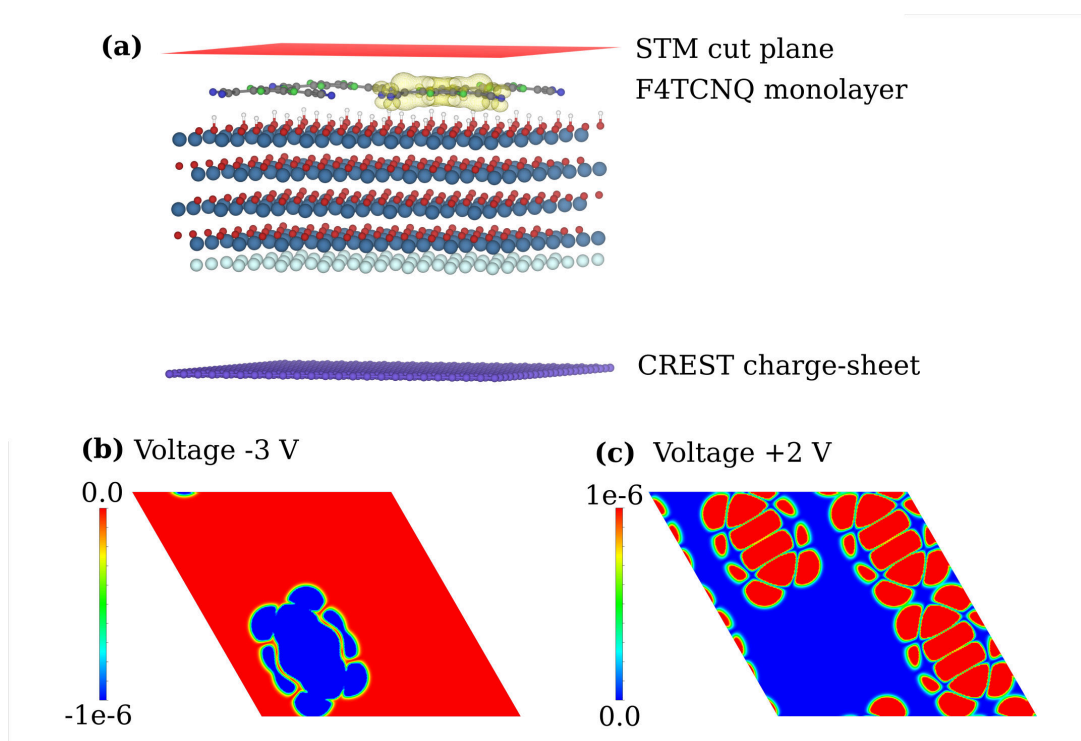
FIGURE 6.11: (a) Sideview of the supercell of a F4TCNQ monolayer adsorbed on O-terminated ZnO used for calculating STM images. The STM plane is placed ≈ 3 Å above the molecular monolayer. (b) Simulated constant-height STM image at a doping concentration of 2.0×10^{19} cm^{-3} and an applied voltage of -3.0 V, and (c) an applied voltage of +2.0 V.

Chapter 7

Charge Transfer at Inorganic/Organic Interfaces Probed by IR-Spectroscopy

7.1 Motivation

Vibrational spectroscopy is a sensitive probe of the atomic structure and chemical bonding and thus of the electronic structure of a molecule on a surface. Members of the Wöll-group in collaboration with the Koch-group performed infrared (IR) spectroscopy experiments of the strong electron acceptor F6TCNNQ adsorbed on the non-polar mixed-terminated ZnO(10$\bar{1}$0) surface. Experiments were done for a monolayer coverage as well as for multilayers. The aim of the experiments was to detect the charge state of the molecules in the first monolayer. To gain a better understanding of the source of charge transfer at hybrid inorganic/organic interfaces, the experiments were conducted on intrinsic and n-doped substrates. Interestingly the obtained IR-spectra showed no clear differences for both substrates, indicating that the charge carrier concentration in the substrate plays a smaller role for the charge transfer as originally anticipated. Our role was to provide complimentary insight from first principles theory in resolving the charge state of the molecules on the surface. We have done this by simulating vibrational spectra of the interface system and the molecule in the gas phase. In particular, the calculations focused on the impact of *charge transfer* and the *bonding chemistry*, i.e. the covalent bonding of the cyano-groups to surface Zn atoms. With our approach to study the impact of charge transfer into the LUMO of the molecule by gas phase calculations, we were able to distinguish between the impact of charge transfer and surface bonding on the vibrational spectra for the studied interface system. Our calculations together with the experimentally obtained IR-spectra indicate that the molecules in the first monolayer are charged by one electron. We suggest that the source of this charge transfer primarily stems from surface defects.

7.2   Authors contribution

The initiator of this project was Prof. Christof Wöll from the Karlsruhe Institute of Technology (KIT). He approached my supervisor Oliver T. Hofmann with the idea to corroborate their experimentally obtained results with computational input. Part of my contribution was to perform the DFT calculations and to evaluate the simulated vibrational spectra. To determine the vibrational spectra from FHI-aims calculations, it was necessary to improve the available script for numerical vibration analysis in FHI-aims and extend it to periodic systems. From the experimental side the responsible person for writing the manuscript was Ludger Schöttner. From the theory side I was responsible for the manuscript in close collaboration with my supervisor Oliver T. Hofmann. The experimental and the theory side are equally important for this work and also contributed equally to the final manuscript. As the manuscript itself focuses primary on the results of the experiment, additional details and insights gained from the computations are available in the supporting information, that was entirely written by me (except for section 7. 'Additional Experimental Data').

7.3   Manuscript and supporting information

Electron transfer at organic/inorganic interfaces monitored by IR-spectroscopy

L. Schöttner*[1], S. Erker*[2], R. Schlesinger[3], N. Koch[3], A. Nefedov[1], O. T. Hofmann[2], Ch. Wöll[1]

[1]*Karlsruhe Institute of Technology, Hermann-von-Helmholtz-Platz 1, 76344 Eggenstein-Leopoldshafen, Germany*

[2]*Graz University of Technology, NAWI Graz, Petersgasse 16, 8010 Graz, Austria*

[3]*Humboldt Universität zu Berlin, Brook-Taylor-Straße 6, 12489 Berlin, Germany*

Abstract

Charge transfer at organic/inorganic interfaces critically influences the properties of molecular adlayers. Here, we demonstrate that the transfer of electrons from an oxide semiconductor into an aromatic compound can be determined directly by infrared spectroscopy. For a prototype organic acceptor, hexafluoro-tetracyano-naphthoquinodimethane (F_6-TCNNQ) deposited on a $(10\bar{1}0)$ oriented ZnO single crystal substrate we recorded IRRAS (infrared reflection-absorption spectroscopy) data. By comparing the vibrational spectrum obtained for a F_6-TCNNQ monolayer with those of multilayers, we find unambiguous evidence for electron transfer from the inorganic substrate to F_6-TCNNQ. Since there are no previous works of similar type, we have carried out a thorough theoretical analysis using density functional theory (DFT). The calculations reveal that two mechanisms govern the pronounced vibrational band shifts of the adsorbed molecule seen in the experiments: in addition to electron transfer into unoccupied molecular levels of the organic acceptor, also polarization effects arising from the fairly strong electric field generated by the ions at the interface strongly affect vibrational frequencies.

Introduction

Organic/inorganic interfaces attract substantial interest because of the prospect to use unusual effects occurring at such heterojunctions for applications in optics, electronics, energy storage and conversion, catalysis, and sensing[1]. These interesting phenomena result from combining two materials with rather different properties, e.g. electronic structure, dielectric constants and polarizabilities. In general, electric fields form at these hybrid interfaces, and depending on the relative energies of the flat bands originating from the molecular orbitals and the more dispersive electronic bands in the inorganic semiconductor, charge transfer may result[2]. A unique prospect for engineering the properties of devices exploiting these effects is the possibility to engineer these charge density rearrangements by doping, in particular of the inorganic part.

However, even for an easy-to-realize class of organic/inorganic interfaces - organic adlayers on inorganic substrates – the nature of the charge-transfer remains incompletely understood. An interesting large band-gap semiconductor to create organic/inorganic interfaces by organic molecular beam deposition (OMBD) is ZnO, a wide band gap metal oxide semiconductor, and a number of recent studies have been reported in this context[3-6]. Previous investigations on the deposition of F_4-TCNQ (tetrafluoro-tetracyano-quinodimethane) have yielded apparently inconsistent results: On metals, charge transfer to the molecule is accompanied by the appearance of a (partially) filled state near the Fermi energy[7]. The electric field is localized between the molecule and the metal surface, giving rise to an interface dipole $\Delta\Phi_{ID}$. On semiconductors, a similar level alignment may be expected (at least for highly doped systems), as shown in Figure 1a. However, near-Fermi states associated with the former molecular LUMO appear are absent in UPS studies of semiconductor/organic interfaces [3, 8].
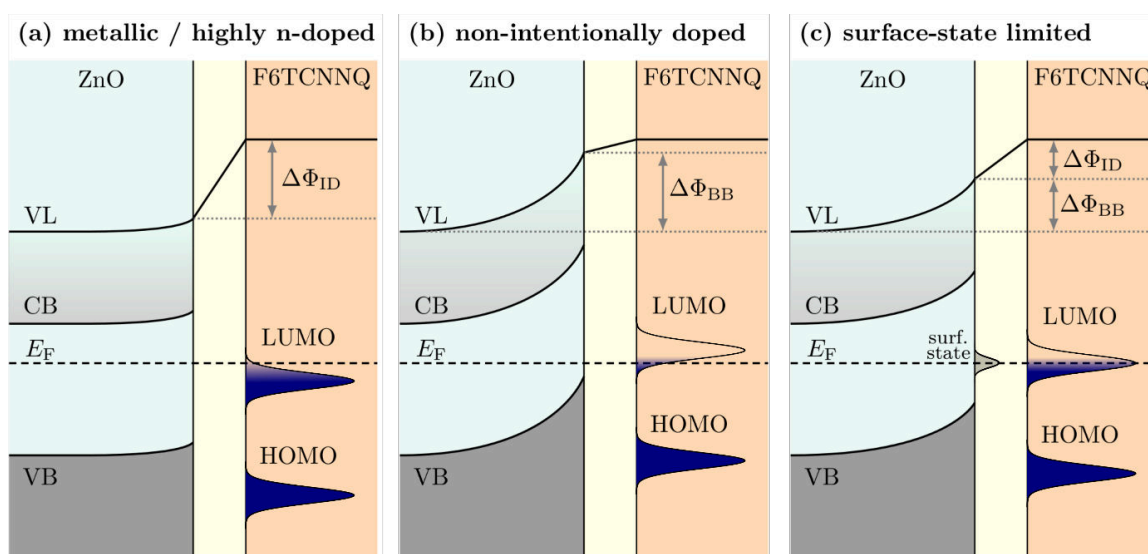
Figure 1. Schematic energy level diagram after the deposition of acceptor molecules on **(a)** a highly doped substrate, **(b)** a nominally undoped substrate, and **(c)** a substrate with surface states present e.g. due to surface defects. The interface dipole $\Delta\Phi_{ID}$ and the band bending $\Delta\Phi_{BB}$ illustrate the contributions to the work function change.

For semiconducting substrates, the electric field can extend significantly into the substrate, giving rise to band bending ($\Delta\Phi_{BB}$), as shown in Figure 1b. This band bending can significantly reduce the amount of charge that is transferred at the interface, depending on the doping concentration [3, 9, 10]. In the limit of low doping concentrations (e.g., intrinsic or non-intentionally doped substrates), one would expect band bending to be the major contribution to the adsorption-induced work-function increase. In practice, however, the band bending typically only amounts to a small fraction of it [3, 8].

It has been shown that reason for this effect is the presence of surface states, which eventually pins the band-bending [8], as schematically shown in Figure 1c. However, this implies that there is, again, significant charge transfer to the molecule (which, in contrast to the highly-doped situation depicted in Fig 1a, now originates from the surface states).

To verify the qualitative picture painted in Figure 1c, it is imperative to determine the charge state of the adsorbed molecule. Still, as initially mentioned, evidence for a corresponding molecular state appears to absent in UPS experiments. However, the absence of evidence in UPS is not the same as the evidence of absence. Also computational considerations provide only limited insight into the correct level alignment. One problem is that the nature of the surface (e.g. the density and structure of OH groups [11]) is usually unknown. On the other hand, just as importantly, semilocal density functional theory (which is the workhorse of computational surface science) suffers from the infamous band-gap problem, which leads to energetically too high occupied and energetically too low unoccupied states. Especially for interfaces between very different types of materials, such as inorganic/organic interfaces, this may lead to qualitatively wrong level alignment and ensuing spurious charge transfer [10, 12-14]. In principle, hybrid functionals that admix a certain fraction of exact exchange can mitigate this problem [14, 15]. However, the fraction of exchange required to obtain correct level positions for the adsorbate depends heavily on the nature of the substrate [14] and its doping concentration. Moreover, the fraction is almost always different for the substrate and the adsorbate [14]. Higher-level theory, such as GW, could provide authoritative results [12], but is currently computationally too expansive to be tractable for pertinent systems. In practice, these complications prevent a fully ab-initio prediction of the charge transfer, which calls for a complimentary experimental technique.

In the present study we apply infrared reflection-absorption spectroscopy (IRRAS) to study a prototypic organic acceptor molecule, hexafluoro-tetracyano-naphthoquinodimethane (F_6-TCNNQ), a strong electron acceptor, often used as a p-dopant in organic semiconductors [16-18] deposited on a structurally well-defined $ZnO(10\bar{1}0)$ surfaces. In contrast to other low-indexed ZnO surfaces, $ZnO(0001)$ and $ZnO(000\bar{1})$, for this surface orientation electrostatic instabilities are absent [19].

In case of metal substrates, IRRAS has been applied successfully in several cases to evidence charge-transfer by detecting frequency shifts of vibrations in molecular adsorbates [20]. To our knowledge, however, similar studies on large-band gap inorganic semiconductors have not yet been reported. The absence of such experimental information for dielectric single crystal substrates is mainly due to severe challenges in measuring IR-spectra in reflection for insulating substrates. However, during the last decade, these problems have been overcome by a number of groups (for a review see Ref. [21]). IRRAS allows detecting charge transfer across the interface by measuring the shifts of molecular vibrational frequencies. Such shifts are well known from studies for solvated molecules, for F_4-TCNQ they can be as large as 70 cm^{-1} [22].

Experimental

The experiments were conducted in a state-of-the-art ultrahigh vacuum (UHV) multi-chamber system (Prevac)[21]. The apparatus allows measuring infrared spectroscopy (IR) in combination with other surface sensitive techniques like X-ray-photoelectron spectroscopy (XPS) and low-energy electron diffraction (LEED). The IR spectra were obtained in reflection absorption mode (IRRAS) using a Fourier-Transform (FT)-IR spectrometer (Bruker Vertex 80v) directly coupled to the UHV chamber via differentially pumped KBr-windows. The base pressure of the entire chamber is in 10^{-10} mbar range.

As substrates, one nominally undoped and two Ga-doped (n-type) ZnO crystals were used. In the latter case the charge carrier density was determined by analyzing reflectivities in the context of the Drude model, yielding n-doping levels of $7.8 \cdot 10^{19}$ cm^{-3} and $2.9 \cdot 10^{20}$ cm^{-3}, respectively.

The ZnO($10\bar{1}0$) single crystal (CrysTec) was cleaned by repeated cycles of Ar$^+$ sputtering ($1 \cdot 10^{-6}$ mbar, 10 min) and annealing at 800 K for 10 min. As a final step, the sample was annealed in oxygen atmosphere ($1 \cdot 10^{-6}$ mbar) at 840 K. The cleanliness and structural quality of the surface was monitored by XPS and LEED.

Deposition of F$_6$-TCNNQ (Novaled) on ZnO($10\bar{1}0$) was carried out by directing the flux of an effusion cell towards the substrate. Deposition rates were determined using a quartz crystal microbalance. All IR spectra shown here are difference spectra obtained by subtracting a spectrum recorded for the clean ZnO substrate before F$_6$-TCNNQ deposition from that measured after molecule deposition. All IRRAS experiments were carried out at room temperature; the IR light angle of incidence was set to 80° with respect to the surface normal. An internal polarizer module allowed to record IR spectra with s- and p-polarized light.

Computational details

As mentioned in the introduction, obtaining a reliable prediction of the charge state of the molecule via semilocal DFT is challenging. This is because the LUMO is spuriously below the valence band of ZnO, which yields spurious charge transfer, independent of the substrate's actual Fermi level. Thus, rather than calculating the charge state directly, the aim of the calculations is to predict the shift of vibrational frequencies as consequence of charging and binding to the surface. We do this separately by calculating the shift due to charging for a free molecule in the gas phase, and by calculating the vibrational frequencies for the molecule on the surface (where, in our calculations, it assumes a charge transfer of approx. one electron). Assuming these two effects are independent, we can combine these to estimate the vibrational shift for arbitrarily charged molecules on the surface, as explained in more detail in the supporting information.

All computed vibrational modes presented here were obtained by density functional theory (DFT) calculations using the FHI-aims program package[23]. The Perdew-Burke-Ernzerhof (PBE) [24] density functional was used and van der Waals forces were included with the vdW-TS scheme [25] using the appropriate parameters for the ZnO substrate[26]. The vibrational modes were computed numerically via the finite displacement method, using a displacement amplitude of 0.005 Å. Initial geometries were optimized until residual forces were smaller than 10^{-4} eV/Å with 'tight' basis sets and numerical settings.

Calculations for the free molecule were performed with open boundary conditions. The electronic structure of the F$_6$-TCNNQ/ZnO interface was determined using a periodic slab approach. The ZnO substrate was modeled by a five double-layer slab cell. For the geometry optimization, the bottom three double-layers were fixed at their bulk position and the top two layers are allowed to relax. For the vibrational analysis, we restrict the discussion to vibrations of the molecule within the harmonic approximation. By keeping the substrate fixed, we omit changes in pure surface and pure bulk modes. To avoid artifacts arising from artificial surface states located at the bottom side of the slab, the bottom layer was passivated

with hydrogen atoms. Calculations for the primitive surface unit-cell are performed with a 16x24x1 k-grid and scaled accordingly for larger cells. The 4x4 supercell including the molecule was chosen such that there is no significant intermolecular interaction between the adjacent molecular adsorbates when employing periodic boundary conditions.

The adsorption of the F_6-TCNNQ molecules on the ZnO($10\bar{1}0$) surface is governed by a weak binding of the protruding cyano groups to the surface Zn atoms, which act as docking sites, leading to a planar molecular adsorption geometry. Two different azimuthal orientations were considered: oriented along the rills of the mixed-terminated ZnO surface (i.e. along the ZnO[$1\bar{2}10$] direction), and oriented perpendicular to the rills (the ZnO[0001] direction). The orientation perpendicular to the rills is energetically more favorable by 33 meV and was therefore used for the vibrational analysis in this work.

Vibrational frequencies usually strongly depend not only on the physics of the system but also on the density functional and the basis set used in the DFT calculations. Because of the systematic nature of the deviations, it is customary to apply uniform multiplicative scale factors to correct the computed vibrational frequencies [27-29]. The scale factor used here was determined from experimental and theoretical data for F_4-TCNQ [30, 31]. This procedure yields a scale factor of 1.0095 for the C≡N and of 1.0198 for the C=C/C-C vibrational frequencies. (More details on the computational methods including how we obtained the scale factors can be found in the Supporting information).

Results and discussion

In order to determine the charge state of the molecules in direct contact with the substrate, it is useful to first characterize the spectrum of a deposited molecular multilayer, where the molecules are clearly charge-neutral. This provides a baseline for the expected vibrations, allowing us to analyze the shifts due to charging and binding to the surface afterwards. In the following, we will focus on the results for the nominally undoped substrate (which is still effectively n-type doped), since the results are qualitatively equivalent to that of the doped samples.

The inspection of the multilayer IRRAS data (Figure 1, top curves) reveals several well-defined, sharp vibrational bands. In the frequency regime below 1700 cm^{-1} (C=C/C-C region), four strong bands are seen in the experimental multilayer data, centered at 1639 cm^{-1}, 1552 cm^{-1}, 1460 cm^{-1}, and 1396 cm^{-1}. In addition, a weak feature is seen at 1424 cm^{-1}. For their assignment, we rely on the comparison to corresponding data for a structurally related molecule, F_4-TCNQ[22, 30, 31], and to the results of DFT calculations for the F_6-TCNNQ molecule in the gas phase (see Table 1).
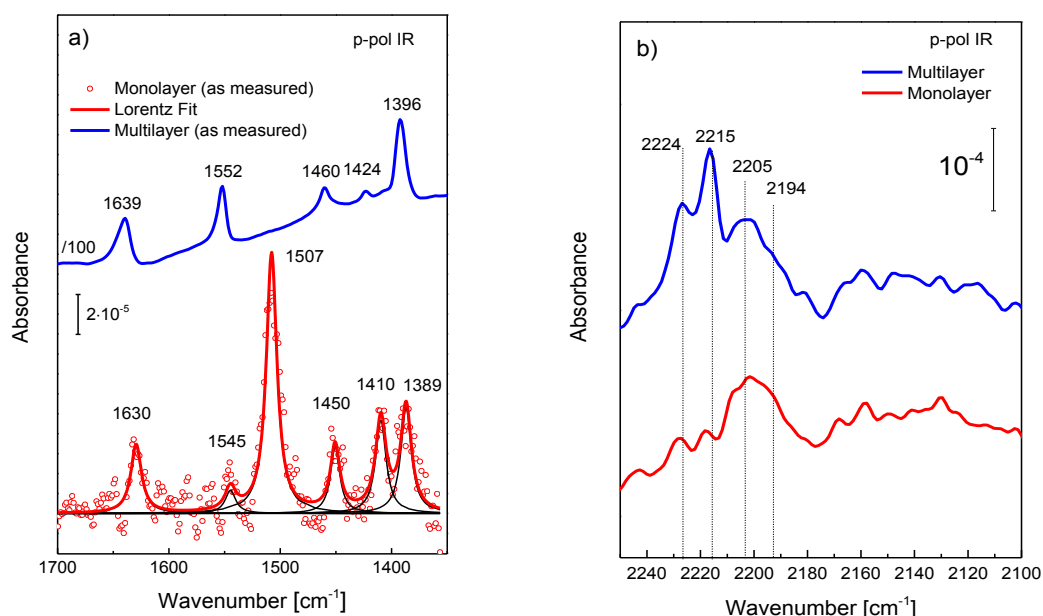
Figure 2. Experimental IRRAS spectra of F6-TCNNQ on the nominally undoped ZnO($10\bar{1}0$): **a)** C=C/C-C region, the intensity of the multilayer data are scaled by a factor of 100; **b)** C≡N region.

On the basis of a comparison with the theoretical results for the uncharged free molecule provided in Table 1 (column "Theory, gas phase, neutral") we can assign the four strong bands to the C-C vibrations $b_u\nu_{51}$, $b_u\nu_{52}$, $b_u\nu_{53}$, $b_u\nu_{55}$ and the weak feature to $b_u\nu_{54}$. In the C-N stretch regime we observe 3 bands at 2224 cm^{-1}, 2215 cm^{-1}, 2205 cm^{-1} and a weak feature at 2194 cm^{-1} (Fig. 1b, top curve). We assign the bands at 2224 cm^{-1} and at 2215 cm^{-1} to the $b_u\nu_{49}/a_g\nu_1$ (see Table 1) for the first band and $b_u\nu_{50}/a_g\nu_2$ for the second one, respectively. The calculations yield frequencies of 2248/2246 cm^{-1} for the first pair of modes and 2221 cm^{-1} for the second pair. This assignment is in analogy with that reported for F$_4$-TCNQ multilayers [31].

All the vibrations discussed above have their transition dipole moments (TDM) oriented within the molecular plane of F$_6$-TCNNQ. The fact that we do not see any vibrational bands with negative intensity (for a discussion of the interplay between orientation of TDMs and the sign of IR-bands in IRRAS at dielectric surfaces see SI) for these vibrations in the p-polarized IRRAS-data reveals that all F$_6$-TCNNQ molecules must be orientated with their molecular plane parallel to the ZnO substrate. IRRAS data recorded for F$_6$-TCNNQ multilayers using s-polarized light do yield negative peaks at the same wavenumbers, with the same intensities as for p-polarized spectra (see Figure S10 in SI). This observation is fully consistent with a parallel stacking of this aromatic compound.

Unfortunately, the bulk structure of F$_6$-TCNNQ is unknown. Also in the case of thin films, Duva et al.[32] were unable to detect out-of-plane diffraction peaks for F$_6$-TCNNQ films.

Overall, the agreement between the positions of the bands in the experimental multilayer IR-spectra and the DFT results for the free molecule is very good. Note, that the small deviation between experiment and theory is similar to that reported in previous work for F_4-TCNQ multilayers [31].

For the F_6-TCNNQ monolayer on ZnO($10\bar{1}0$), the IRRAS data reveal pronounced differences compared to the multilayer spectra (see Fig. 1a, bottom curve). For the monolayer, the most pronounced peak is that at 1507 cm^{-1}. Smaller bands are observed at 1630, 1450, 1410 and 1389 cm^{-1}.

In case of a neutral F_6-TCNNQ adsorbate, the DFT results predict a small blue shift (15 cm^{-1}) of the strong $b_u\nu_{52}$ band at 1552 cm^{-1} relative to the molecule in the gas phase. Since, experimentally, no such shift is observed in this region, we tentatively conclude that the presence of neutral F_6-TCNNQ molecules at the inorganic/organic interface is unlikely. Conversely, for a negatively charged molecular species, the calculations predict a red shift of 30 cm^{-1} for the $b_u\nu_{52}$ band (see Fig.S5 in SI), in excellent agreement with the experimentally observed shift of 42 cm^{-1}. Such a substantial lowering of frequencies is typical for electron transfer to this organic acceptor. In line with this hypothesis, the second sharp band for the monolayer observed at 1450 cm^{-1} can assigned to the $b_u\nu_{53}$ band (1460 cm^{-1} in the multilayer). In this case, the red shift observed for the monolayer amounts to 10 cm^{-1}. Also in this case, the DFT results for the neutral species predict a small blue-shift, whereas for the charged species a small red-shift is expected (5 cm^{-1}). Inspection of Table I confirms, that also the other vibrations agree well with the theoretical results for a F_6-TCNNQ anion at the interface between organic semiconductor and ZnO.

In the C-N-stretch regime, the experimental monolayer data reveals only one rather broad feature (2212-2188 cm^{-1}) centered at 2205 cm^{-1} (Fig. 1b, bottom curve). The center of this band is red-shifted by 10-20 cm^{-1} with respect to the multilayer features. Although the lower intensity of the C-N bands in the experimental data prohibits a more detailed analysis, the red-shift in the measured data is consistent with the theoretical results for the negatively charged species, where for all C-N stretch vibrations red shifts between 40 cm^{-1} and 60 cm^{-1} are observed.

A question at this point is whether a negative charging of the molecule is plausible at all. According to results obtained with inverse photoemission spectroscopy [33] the electron affinity (EA) of F_6-TCNNQ films amounts to 5.6 eV, similar to the value of F_4-TCNQ (5.2 eV [34]). This value is clearly above the valence band maximum of ZnO($10\bar{1}0$) (ca. 8 eV). Therefore, for undoped ZnO, no electron transfer from the semiconductor substrate to the adsorbed molecules should occur at all. However, ZnO is generally found to exhibit n-type behavior resulting from unintentional doping, most likely by residual hydrogen [35]. As a result, the Fermi-energy of this inorganic semiconductor is found close the ZnO conduction band, which is at 4.5 eV and larger than the F_6-TCNNQ electron affinity. As a result, for the non-intentionally doped sample, one does expect a significant change of the work function (which is also experimentally observed[8]). An idealized surface (which is commonly assumed in theoretical calculations) would then yield the schematic level alignment shown in Figure 1b, i.e. the work-function increase should be mainly due to bend bending, which limits the charge-transfer into the molecule to infinitesimally small values. This picture is clearly

refuted by the pronounced red shift of the C-C-vibrational bands, which evidence strongly charged molecules in the first monolayer.

Rather, our results are consistent with earlier experimental results that indicate that band-bending is limited, and which imply – but could not conclusively evidence – a corresponding strong charge transfer between surface and adsorbate. Thus, our findings strongly corroborate the schematic level alignment in Figure 1c, where band-bending is limited by surface states.

As a final remark, we note that neither our experimental nor our theoretical findings provide a conclusive explanation for the apparent absence of filled molecular state in UPS experiments. Possible origins include strong charge localization in the molecular layer, which would shift the filled states away from the Fermi-energy[36, 37], or surface states acting as reaction centers, which would lead to molecular states in the valance band (rather than in the gap), where they could not be easily detected by means of UPS. However, a conclusive answer would require significant improvements over state-of-the-art theory for the former, and atomistic knowledge over the type of surface states and defects for latter, both of which are outside the scope of the present contribution.

Table 1. The experimental and theoretical results for F6-TCNNQ.

Symmetry/ Vibration	Experiment, multilayer	Experiment, monolayer	Theory, gas phase, neutral	Theory, gas phase, charged	Theory, surface, neutral	Theory, surface, charged
C-N vibrations						
$b_u\nu_{49}$	2227	2205	2248	2222	2229	2202
$a_g\nu_1$	2227	2205	2246	2223	2219	2196
$b_u\nu_{50}$	2215	2194	2221	2189	2197	2165
$a_g\nu_2$	2215	2194	2221	2189	2191	2158
C-C vibrations						
$b_u\nu_{51}$	1639	1630	1638	1629	1632	1622
$a_g\nu_4$	1552	1545	1552	1551	1551	1550
$b_u\nu_{52}$	1552	1507	1552	1508	1567	1522
$b_u\nu_{53}$	1460	1450	1470	1445	1490	1465
$b_u\nu_{54}$	1424	1410	1431	1412	1434	1415
$b_u\nu_{55}$	1396	1389	1402	1379	1420	1397

Conclusions

The experimental IRRAS data recorded for F_6-TCNNQ molecules deposited on a $ZnO(10\bar{1}0)$ surface reveal the formation of multilayers with the molecular plane orientated strictly parallel to the substrate. In the monolayer regime, two sharp vibrational bands are observed, with pronounced red shifts relative to the multilayer. Since DFT results obtained for a neutral adsorbate predict a blue shift for these bands, we feel such a neutral state can be excluded. From the good agreement with the theoretical results obtained for a negatively charge species we conclude that the F_6-TCNNQ molecules are negatively charged, even though the substrate has not been doped intentionally.

References

[1] Delville, M. H. & Taubert, A. in *Hybrid Organic-Inorganic Interfaces: Towards Advanced Functional Materials* (John Wiley & Sons, 2018).

[2] Hörmann, U. *et al*. Stark effect of hybrid charge transfer states at planar ZnO/organic interfaces. *Physical Review B* **98**, 155312 (2018).

[3] Schlesinger, R. *et al*. Controlling the work function of ZnO and the energy-level alignment at the interface to organic semiconductors with a molecular electron acceptor. *Physical Review B* **87**, 155311 (2013).

[4] Pal, S., Maiti, S., Maiti, U. N. & Chattopadhyay, K. K. ZnO-(Cu/Ag) TCNQ heterostructure network over flexible platform for enhanced cold cathode application. *Nanotechnology* **27**, 265601 (2016).

[5] Liu, H. *et al*. Fabrication of large-area hybrid nanowires arrays as novel field emitters. *Journal of Materials Chemistry* **19**, 1031-1036 (2009).

[6] Hosaka, H. & Meguro, K. The solvent effect on the charge-transfer adsorption of TCNQ onto metal oxides and silica. *Colloid Polym. Sci.* **252**, 322-326 (1974).

[7] Braun, S., Salaneck, W. R. & Fahlman, M. Energy-level alignment at organic/metal and organic/organic interfaces. *Adv Mater* **21**, 1450-1472 (2009).

[8] Schultz, T., Niederhausen, J., Schlesinger, R., Sadofev, S. & Koch, N. Impact of surface states and bulk doping level on hybrid inorganic/organic semiconductor interface energy levels. *J. Appl. Phys.* **123**, 245501 (2018).

[9] Schultz, T. *et al*. Tuning the work function of GaN with organic molecular acceptors. *Physical Review B* **93**, 125309 (2016).

[10] Xu, Y. *et al*. Space-charge transfer in hybrid inorganic-organic systems. *Phys. Rev. Lett.* **111**, 226802 (2013).

[11] Staemmler, V. *et al*. Stabilization of polar ZnO surfaces: validating microscopic models by using CO as a probe molecule. *Phys. Rev. Lett.* **90**, 106102 (2003).

[12] Draxl, C., Nabok, D. & Hannewald, K. Organic/inorganic hybrid materials: Challenges for ab initio methodology. *Acc. Chem. Res.* **47**, 3225-3232 (2014).

[13] Gruenewald, M. *et al*. Integer charge transfer and hybridization at an organic semiconductor/conductive oxide interface. *The Journal of Physical Chemistry C* **119**, 4865-4873 (2015).

[14] Wruss, E., Zojer, E. & Hofmann, O. T. Distinguishing between Charge Transfer Mechanisms at Organic/Inorganic Interfaces Employing Hybrid Functionals. *The Journal of Physical Chemistry C* (2018).

[15] Caruso, F. *et al*. First-principles description of charge transfer in donor-acceptor compounds from self-consistent many-body perturbation theory. *Physical Review B* **90**, 085141 (2014).

[16] Kleemann, H. *et al*. Structural phase transition in pentacene caused by molecular doping and its effect on charge carrier mobility. *Organic Electronics* **13**, 58-65 (2012).

[17] Weichsel, C. *et al*. Storage of charge carriers on emitter molecules in organic light-emitting diodes. *Physical Review B* **86**, 075204 (2012).

[18] Tietze, M. L., Burtone, L., Riede, M., Lüssem, B. & Leo, K. Fermi level shift and doping efficiency in p-doped small molecule organic semiconductors: a photoelectron spectroscopy and theoretical study. *Physical Review B* **86**, 035320 (2012).

[19] Wöll, C. The chemistry and physics of zinc oxide surfaces. *Prog Surf Sci* **82**, 55-120 (2007).

[20] Zaitsev, N., Jakob, P. & Tonner, R. Structure and vibrational properties of the PTCDA/Ag (1 1 1) interface: bilayer versus monolayer. *Journal of Physics: Condensed Matter* **30**, 354001 (2018).

[21] Yang, C. & Wöll, C. IR spectroscopy applied to metal oxide surfaces: adsorbate vibrations and beyond. *Advances in Physics: X* **2**, 373-408 (2017).

[22] Meneghetti, M. & Pecile, C. Charge–transfer organic crystals: Molecular vibrations and spectroscopic effects of electron–molecular vibration coupling of the strong electron acceptor TCNQF4. *J. Chem. Phys.* **84**, 4149-4162 (1986).

[23] Blum, V. *et al*. Ab initio molecular simulations with numeric atom-centered orbitals. *Comput. Phys. Commun.* **180**, 2175-2196 (2009).

[24] Perdew, J. P., Burke, K. & Ernzerhof, M. Generalized gradient approximation made simple. *Phys. Rev. Lett.* **77**, 3865 (1996).

[25] Tkatchenko, A. & Scheffler, M. Accurate molecular van der Waals interactions from ground-state electron density and free-atom reference data. *Phys. Rev. Lett.* **102**, 073005 (2009).

[26] Hofmann, O. T. *et al*. Large work function reduction by adsorption of a molecule with a negative electron affinity: Pyridine on ZnO (10 1⁻ 0). *J. Chem. Phys.* **139**, 174701 (2013).

[27] Merrick, J. P., Moran, D. & Radom, L. An evaluation of harmonic vibrational frequency scale factors. *The Journal of Physical Chemistry A* **111**, 11683-11700 (2007).

[28] Laury, M. L., Carlson, M. J. & Wilson, A. K. Vibrational frequency scale factors for density functional theory and the polarization consistent basis sets. *Journal of computational chemistry* **33**, 2380-2387 (2012).

[29] Wong, M. W. Vibrational frequency prediction using density functional theory. *Chemical Physics Letters* **256**, 391-399 (1996).

[30] Furuhashi, M. & Yoshinobu, J. Charge Transfer and Molecular Orientation of Tetrafluoro-tetracyanoquinodimethane on a Hydrogen-Terminated Si(111) Surface Prepared by a Wet Chemical Method. *J. Phys. Chem. Lett.* **1**, 1655-1659 (2010).

[31] Pingel, P. *et al*. Charge-Transfer Localization in Molecularly Doped Thiophene-Based Donor Polymers. *J. Phys. Chem. Lett.* **1**, 2037-2041 (2010).

[32] Duva, G. *et al*. Thin-Film Texture and Optical Properties of Donor/Acceptor Complexes. Diindenoperylene/F6TCNNQ vs Alpha-Sexithiophene/F6TCNNQ. *J. Phys. Chem. C* **122**, 18705-18714 (2018).

[33] Zhang, F. & Kahn, A. Investigation of the High Electron Affinity Molecular Dopant F6-TCNNQ for Hole-Transport Materials. *Adv. Funct. Mater.* **28**, 1703780 (2018).

[34] Ma, L. *et al*. Single photon triggered dianion formation in TCNQ and F4TCNQ crystals. *Scientific Reports* **6**, 28510 (2016).

[35] Zhang, S. B., Wei, S. -. & Zunger, A. Intrinsic n-type versus p-type doping asymmetry and the defect physics of ZnO. *Phys. Rev. B* **63**, 075205 (2001).

[36] Sau, J. D., Neaton, J. B., Choi, H. J., Louie, S. G. & Cohen, M. L. Electronic Energy Levels of Weakly Coupled Nanostructures: ${\mathrm{C}}_{60}$-Metal Interfaces. *Phys. Rev. Lett.* **101**, 026804 (2008).

[37] Hofmann, O. T., Rinke, P., Scheffler, M. & Heimel, G. Integer versus Fractional Charge Transfer at Metal(/Insulator)/Organic Interfaces: Cu(/NaCl)/TCNE. *ACS Nano* **9**, 5391-5404 (2015).

SUPPORTING INFORMATION:

Electron transfer at organic/inorganic interfaces monitored by IR-spectroscopy

L. Schöttner*[1], S. Erker*[2], R. Schlesinger[3], N. Koch[3], A. Nefedov[1], O. T. Hofmann[2], Ch. Wöll[1]

[1]*Karlsruhe Institute of Technology, Hermann-von-Helmholtz-Platz 1, 76344 Eggenstein-Leopoldshafen, Germany*

[2]*Graz University of Technology, NAWI Graz, Petersgasse 16, 8010 Graz, Austria*

[3]*Humboldt Universität zu Berlin, Brook-Taylor-Straße 6, 12489 Berlin, Germany*

1. Further Details on the Applied Computational Methods

A python script was used to evaluate the vibrational frequencies and intensities from DFT calculations computed with the FHI-aims program package [1]. The vibrational modes has been obtained numerically by diagonalizing the mass weighted Hessian matrix of the system. The Hessian was built from forces that were acquired from 6 x *number of atoms* calculations (6 displacements per atom, displacement distance = 0.005 Å). In the case of F6-TCNNQ with its 26 atoms, this sums up to 156 single point DFT calculations for the molecule. For the surface system the substrate was kept fixed in order to save computational costs, i.e. only the atoms of the molecule were displaced in the calculations. Due to the large number of involved calculations, we did not employ a supercell approach, i.e. only the phonons at the Γ point were calculated.

IR intensities were calculated from a finite difference approximation of the gradient of the dipole moment (For more details on numerical calculation of IR frequencies see [2]). For gas phase calculations, the change of the dipole moment can be determined in all three directions in space. For the surface systems, where a slab-call approach with periodic boundary conditions was employed, the potential parallel to the surface vanishes by construction. Therefore, only the dipole component perpendicular to the surface could be determined. More precisely only the change in dipole moment could be evaluated from the work function change between a calculation with displaced atom and the molecule in equilibrium. The dipole change $\Delta\mu$ can be calculated from $\Delta\mu = \varepsilon_0 \cdot A \cdot \Delta\Phi$, where ε_0 is the vacuum permittivity, A is the surface area taken up by one molecule, i.e. the unit cell surface area, and $\Delta\Phi$ is the change in work function evaluated in the calculation.

In experiments, vibrations with a dipole moment parallel to the surface might occur. It is to mention that the vibrational frequencies were of course calculated, however, their intensity is null in our results. Therefore, absolute values of intensities in the case of the surface system should be considered with care.

In general, vibrational modes and intensities strongly depend on the electronic structure of a system. At inorganic/organic interfaces, this poses a notable challenge for computations: Using the PBE functional (or any other semi-local functional), the bandgap of ZnO is underestimated. For PBE it amounts only to 0.65 eV, compared to the experimental band gap of 3.44 eV [3,4]. As a result of the band-gap problem, the F6-TCNNQ LUMO is located below the valence band of ZnO. This leads to a spurious charge transfer at the interface, even in the absence of doping or defects (or for hypothetical, p-type material) [5,6].

The charge transfer results in a filling of the LUMO with one electron. Therefore, our calculations of the adsorbed molecules are always for molecules with an occupied LUMO (Mulliken analysis of the overall molecule gives only a negligible total charging because of charge back donation from orbitals located at the binding cyano groups. For more details see Section 3 of the SI). However, the advantage of using FHI-aims in addition to the fact that periodic surface slabs ca be calculated, is that for gas phase calculations every charge state can be evaluated including factional occupations. Form gas phase calculations we can therefore extract the influence of changing the LUMO occupation and back-extrapolate for the surface system to determine the vibrational frequencies for any charge state at the interface. In fact, with this approach we can distinguish between the influence of charging and surface adsorption on the vibrational frequencies.

We note that a more sensible level alignment could be obtained by employing hybrid functionals [7] in combination with an approach to include bulk doping [8]. However, this would lead to intractable computationally costs for numerical vibrational analysis calculations without significantly improving the physical insight for this specific problem.

2. Local adsorption geometry: F6-TCNNQ on mixed terminated ZnO (10$\bar{1}$0)

At the F6-TCNNQ/ZnO interface, the surface Zn atoms act as docking sites for the protruding cyano groups of the molecule. This limits the number of sensible, low-energy adsorption geometries. In the case of a flat-laying molecule, two different orientations were considered: oriented along the rills of the mixed-terminated ZnO surface, and oriented perpendicular to the rills. The orientation perpendicular to the rills, depicted in Fig. SI1 is energetically more favourable by 0.03 eV. This is a rather small difference and at finite temperatures, both adsorption sides might be observable in a monolayer structure.
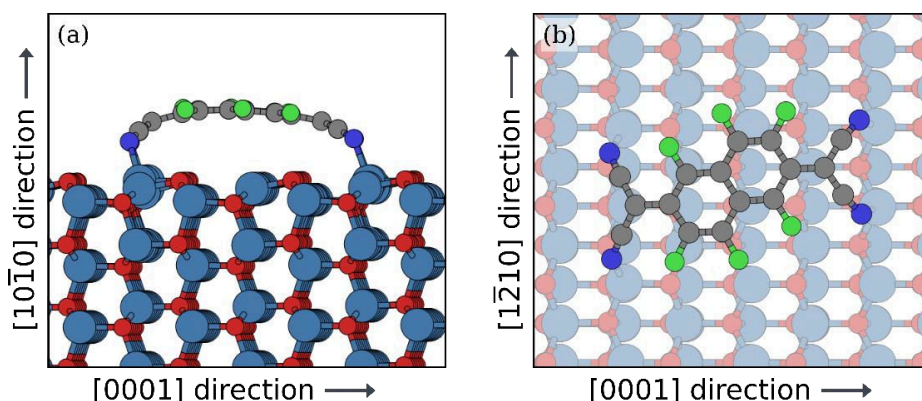
Figure SI1: *Top and side view of the theoretically found lowest energy local adsorption site of F6-TCNNQ on the ZnO ($10\bar{1}0$) surface.*

3. Electronic structure: Flat-lying molecule

A Mulliken analysis of the molecule on the surface yields a negligible net charge transfer from the substrate to the molecule. The total additional charge of the molecule amounts only to 0.03 e$^-$. This is, at first glance, very surprising, since the molecular LUMO is below the valence band edge and hence becomes at least partially filled. To understand the origin of the fact that overall, the molecule is charge-neutral, we calculated the molecular orbital density of states (MODOS) projected on the orbitals for F6-TCNNQ on ZnO ($10\bar{1}0$) [9,10]. By integrating the DOS of each molecular orbital up to the Fermi energy, a formal occupation of each orbital is obtained.
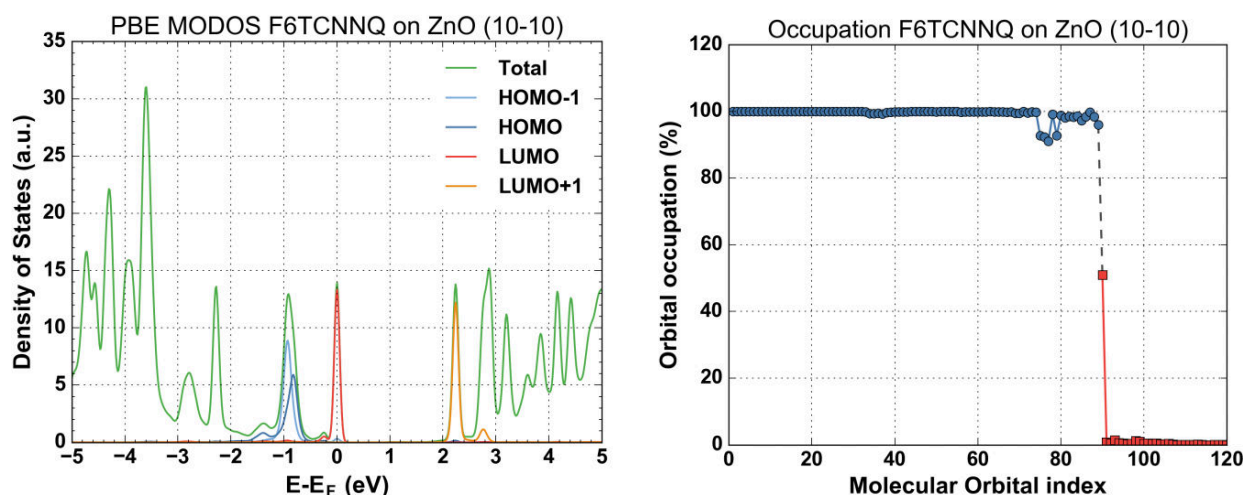
Figure SI2: *(left) MODOS and (right) orbital population analysis of F6-TCNNQ on ZnO ($10\bar{1}0$). The LUMO of the Molecule is occupied by one electron (50% filling). A significant reduction from full occupation can be observed for the cyano orbitals at orbital indices 79-75.*

The MODOS of F6-TCNNQ on ZnO and the corresponding occupation values of the molecular orbitals are shown in Fig. SI2. Because of hybridization of the initial molecular states with the substrate, the molecular states become broadened and shifted, such that the LUMO is now in resonance with the Fermi edge. This leads to an occupation of ~50%, i.e. the LUMO is filled with one electron. However, from the Mulliken analysis we know that the overall molecule is practically neutral, which suggests that other orbitals are donating charge back to the substrate. This charge back-donation, indeed, can be seen in the occupation analysis in Fig. SI2 (right) for orbital indices 79-75. These orbital indices correspond to molecular orbitals located at the cyano groups of the F6-TCNNQ molecule (see Fig. SI3).

(a) LUMO (90)

(b) HOMO (89)

(c) HOMO-10 (79)

(d) HOMO-12 (77)

(e) HOMO-13 (76)

(f) HOMO-14 (75)
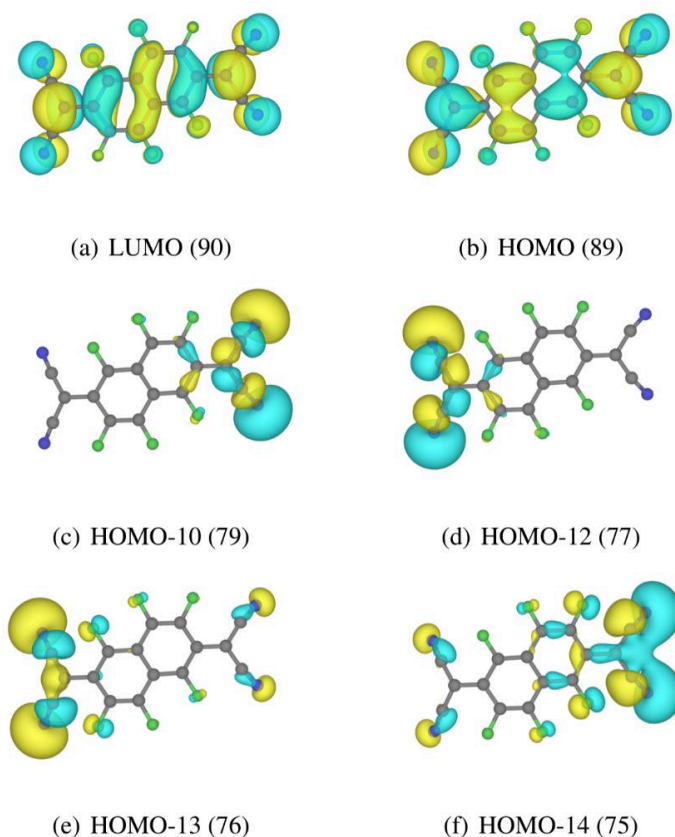
Figure SI3: *Most relevant molecular orbitals for charge transfer upon adsorption of F6-TCNNQ on ZnO* ($10\bar{1}0$)

4. Determining Scale Factors

It is a common approach for ab-initio calculations of vibrational frequencies to determine harmonic frequencies and use a multiplicative scale factor to correct shortcomings of the method to be able to predict frequencies observed via experiment. The scaling strongly depends on the ab-initio method used including e.g. the density functional and the basis set. In general, it should compensate for two problems: First, the approximate nature of DFT based electronic structure calculations (shortcomings of the functional like missing electronic correlation, basis set truncation effects, etc.). And second, missing

anharmonic effects (in the frequency evaluation the harmonic approximation is used although the potential energy surface is in general not harmonic).

For some ab-initio programs that are commonly used for theoretical vibrational frequency calculations (e.g. Gaussian09) universal scaling factors often can be looked up in tables for specific density functional / basis set combinations (e.g. NIST Computational Chemistry Comparison and Benchmark DataBase). FHI-aims does not use one of the widely used basis set like Pople basis sets [11] or the correlation-consistent basis sets developed by Dunning [12], but instead uses individual pre-constructed hierarchical basis functions [1]. Therefore scale factors for other basis sets are not applicable. This makes it necessity to determine a scale factor for our system by us ourselves.

We determined the scale parameter by comparing theoretically obtained results of neutral F4-TCNQ in gas phase with experimental and theoretical data based on work by Furuhashi *et al.* [13] and Pringel *et al.* [14]. The calculations for F4-TCNQ were obtained using the same methods we applied for F6-TCNNQ in this work.

Experimentally for F4-TCNQ a very sharp peak appears at 2227 cm^{-1} attributed to the symmetric stretching vibration $b_{1u}v_{18}$ of the cyano groups. This vibration can be clearly identified in our calculations and appears at 2206 cm^{-1} From this comparison we assign a scale factor of 1.0095 for C≡N vibrations obtained for FHI-aims using PBE functional and *tight* settings.

For the C=C/C-C vibrational frequencies we determine the scale factor from the stretching vibration $b_{2u}v_{33}$. Experimentally it appears at 1601 cm^{-1} whereas in our computations we find at 1570 cm^{-1}. This deviation can be corrected by a scale factor of 1.0198, that is therefore used in this work for C=C/C-C vibrational frequencies.

Gas phase calculations of the F6-TCNNQ molecule were furthermore compared to Gaussian09 results with PBE functional and the 6-311G** basis set. The results were very similar with a maximum deviation in frequency values of +/- 6 cm^{-1} wavenumbers for the C=C/C-C and C≡N stretching region

5. Theoretical IR Vibrational Spectra

To investigate the impact of charge transfer, i.e. occupying the LUMO, on the IR frequency spectrum, we first perform gas phase calculations of the molecule in the neutral and some negatively charged states. The main difference between the two spectra is a shift in frequency and an increase in intensity of the C≡N vibrations for the negatively charged molecule. The two peaks can be attributed to the symmetric $b_u v_{49}$ and antisymmetric $b_u v_{50}$ stretching modes (see Fig. SI4).
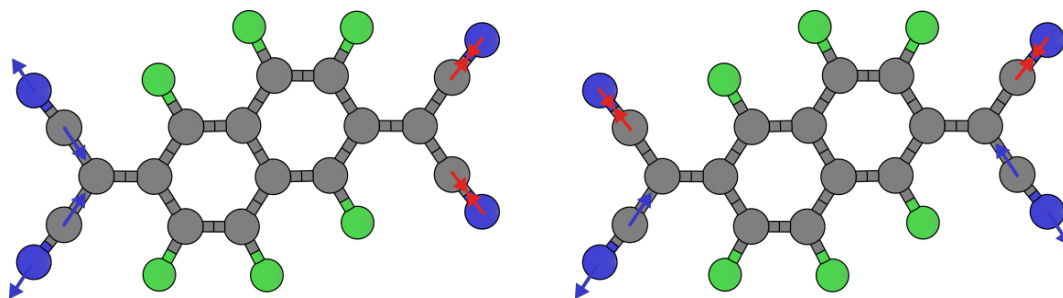
Figure SI4: *The two most prominent features that appear in gas phase calculations upon charging of the molecule are the symmetric* $b_u\nu_{49}$ *and the antisymmetric* $b_u\nu_{50}$ *stretching of the cyano groups at wavenumber 2222 cm^{-1} (left) and 2189 cm^{-1} (right), respectively.*

In a next step, the charged molecule adsorbed on the surface is considered. Fig. SI5 graphically summarizes the IR-band shifts between a neutral molecule in gas phase and a charged molecule on the surface for the cyano- and the carbon-vibrations. With our approach to determine the influence of LUMO filling by gas phase calculations, we can assign the total band shifts to contributions from charging and surface adsorption. The impact of surface-adsorption on the vibrational frequencies of the carbon vibrations is a bit weaker or even in the opposite direction compared to the significant influence on the cyano-group vibrations. Explanations for the frequency shift direction can be found in the next section 5. A graphical overview of the theoretical results for the most important vibrations including the band shifts due to charging and adsorption, and the development of IR intensities upon charging can be found in x Fig. SI6 and SI7 for the C-C/C=C region and in Fig. SI8 for the C≡N region.
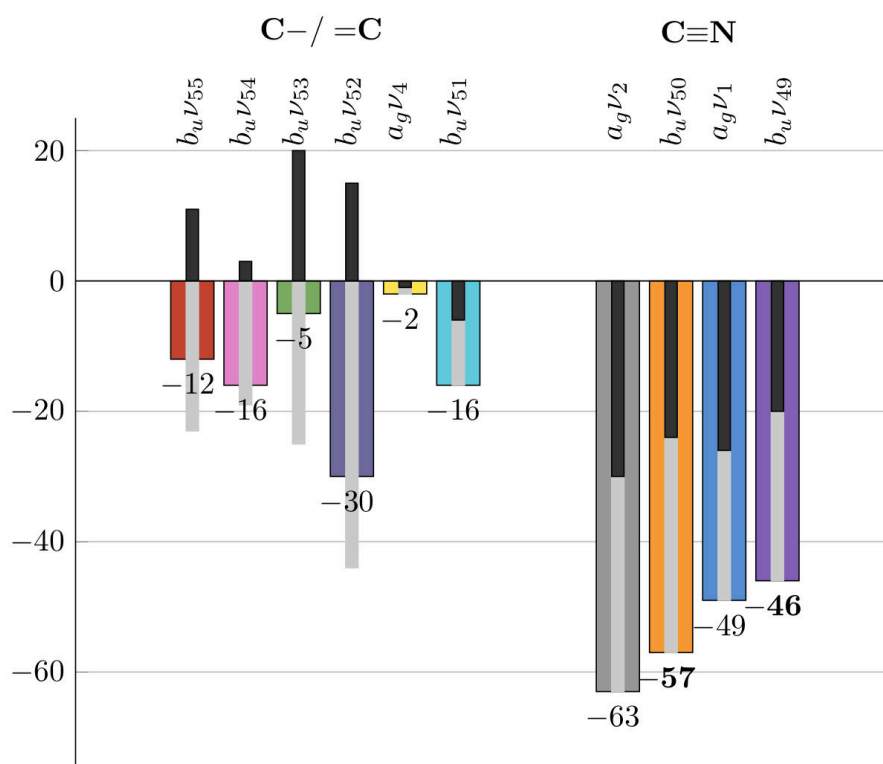
Figure SI5: *Depiction of C=C/C-C and C≡N frequency shifts of flat-laying F6-TCNNQ on the mixed terminated ZnO surface with respect to neutral gas-phase vibrations. With our approach we can clearly distinct the different contributions from surface adsorption an occupying the LUMO of the molecule. The nominal contribution of the surface bonding is depict by the back bars. For the C≡N surface bonding results in general in a red shift of vibrational frequencies. For C=C/C-C modes a blue shift or a rather weak red shift is observed. The contribution of LUMO-charging is shown by the light gray bars and always results in a red shift of IR vibrational frequencies.*
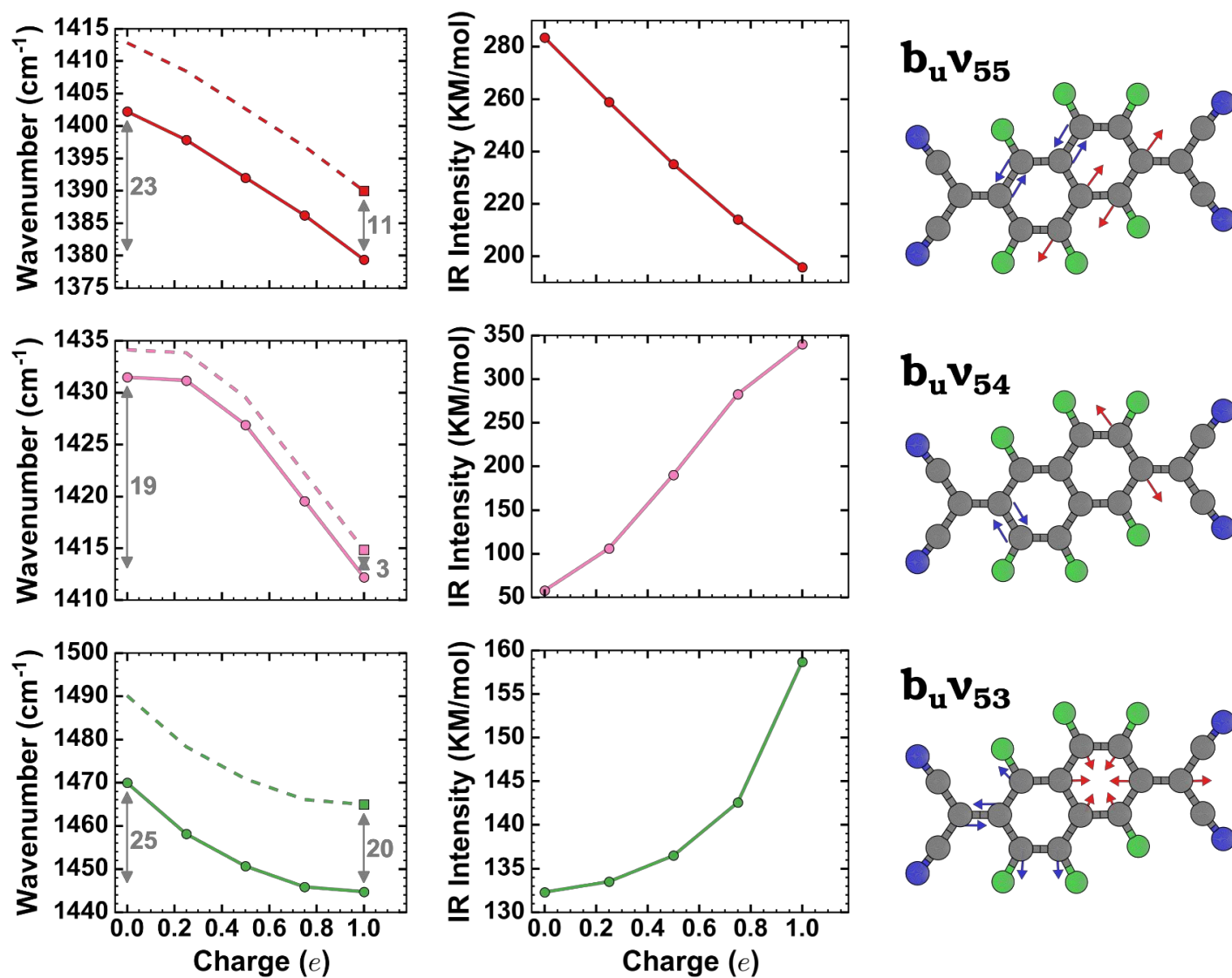
Figure SI6: *Theoretical results of C-C/C=C stretching vibrations for F6-TCNNQ on ZnO Part 1: (left) Evolution of vibrational frequency shifts upon filling the LUMO with one electron in gas phase (solid lines). The dashed lines represent the back extrapolation from the obtained result of a charged molecule adsorbed on mixed-terminated ZnO to a neutral molecule on the surface. (middle) Development of IR intensities upon charging for gas phase calculations. (right) Graphical representation of the vibrational modes.*
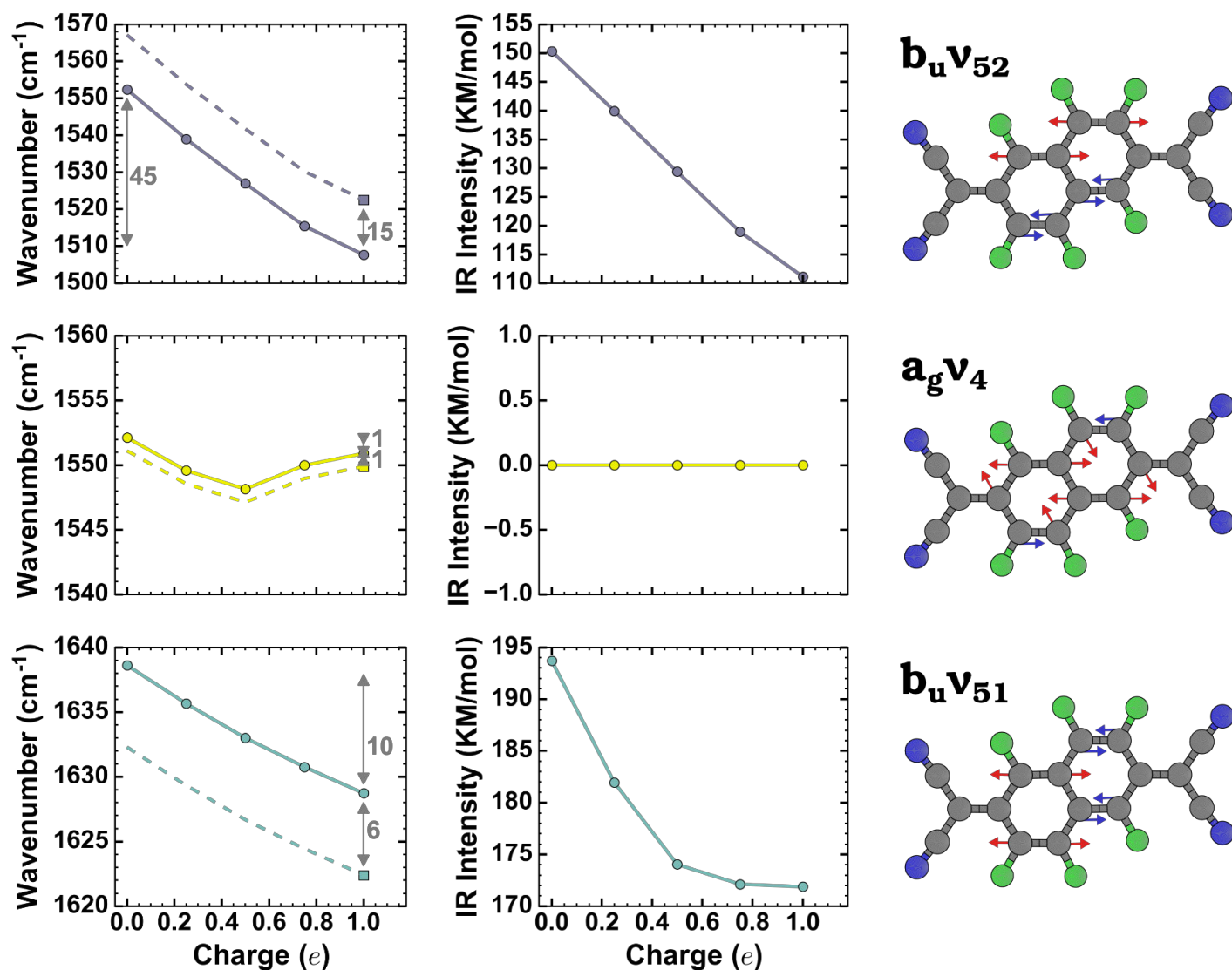
Figure SI7: *Theoretical results of C-C/C=C stretching vibrations for F6-TCNNQ on ZnO Part 2: (left) Evolution of vibrational frequency shifts upon filling the LUMO with one electron in gas phase (solid lines). The dashed lines represent the back extrapolation from the obtained result of a charged molecule adsorbed on mixed-terminated ZnO to a neutral molecule on the surface. (middle) Development of IR intensities upon charging for gas phase calculations. (right) Graphical representation of the vibrational modes.*
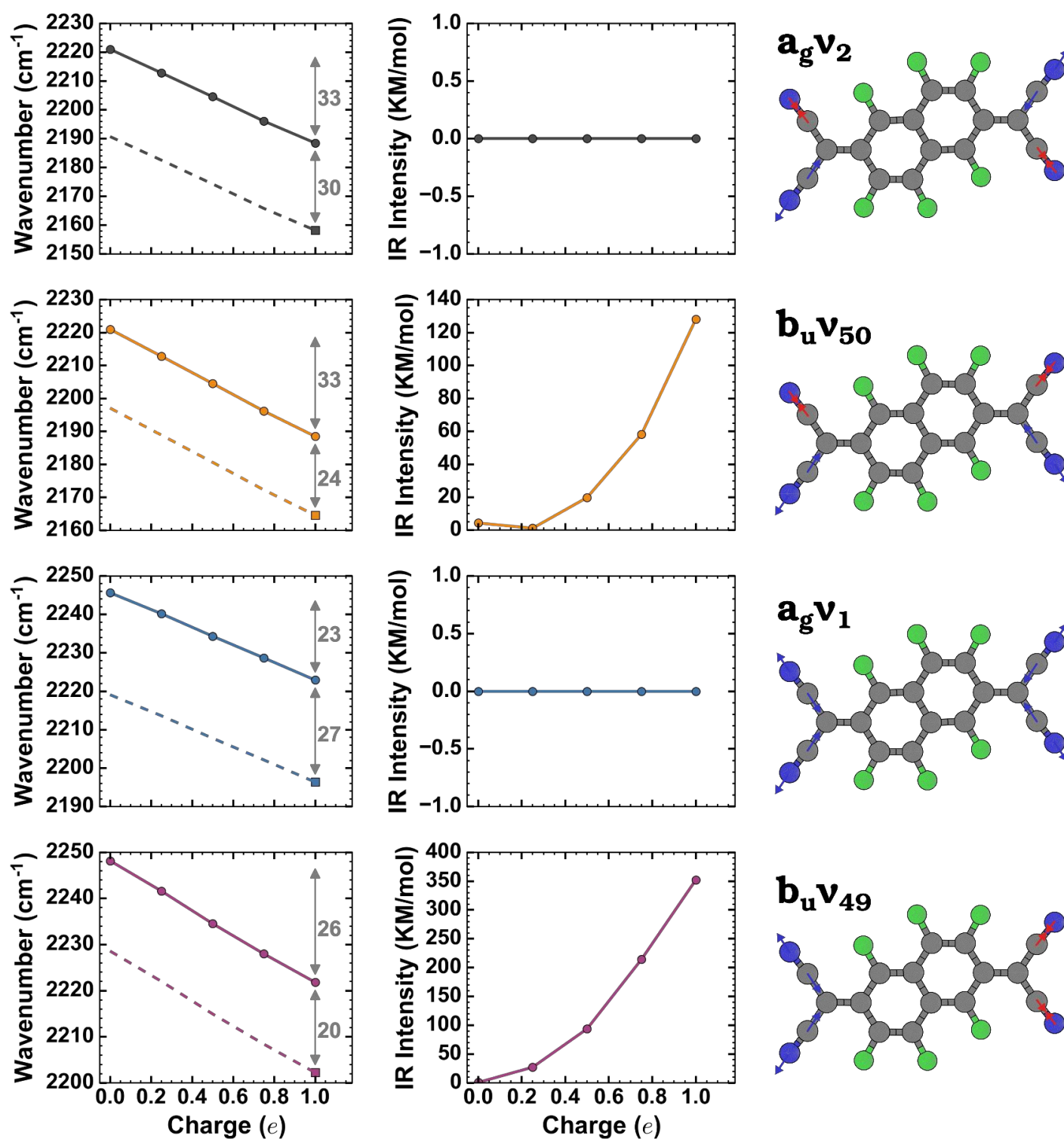
Figure SI8: *Theoretical results of C≡N stretching vibrations for F6-TCNNQ on ZnO: (left) Evolution of vibrational frequency shifts upon filling the LUMO with one electron in gas phase (solid lines). The dashed lines represent the back extrapolation from the obtained result of a charged molecule adsorbed on mixed-terminated ZnO to a neutral molecule on the surface. (middle) Development of IR intensities upon charging for gas phase calculations. The intensities of IR active vibrations significantly increases with increased charging of the molecule. (right) Graphical representation of the vibrational modes.*

6. Explanation for IR-Shift Directions

We find that in the monolayer the IR bands from cyan vibrations shift to lower frequencies (red shift). Due to the covalent nature of bonding between cyano groups and surface Zn atoms, electrons from the nitrogen atoms are shared with the substrate, weakening the C≡N triple bond (Charge back donation to the substrate can be attributed to orbitals located at the cyano groups - see MODOS Fig. SI2). This results in a shift to smaller wave numbers or frequencies. The covalent bonding of the cyano groups upon surface adsorption initialize an electron flipping through the whole molecule and results in a shift of the double bonds within the molecule (See Fig. SI8).
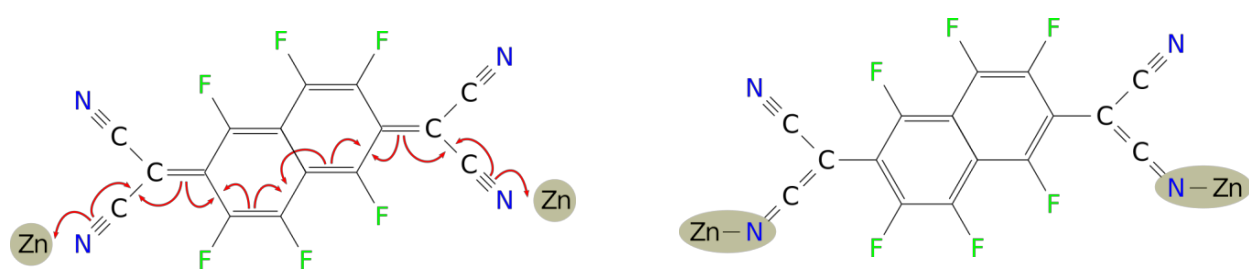
Figure SI9: *Chemical structure and double bond locations within the molecule (left) in gas phase and (right) upon adsorption (symbolically shown if two cyano groups bind to surface Zn atoms). Due to covalent bonding of the molecule's cyano groups to surface Zn atoms the location of the double bonds get shifted (because of electron flipping), increasing the aromatic character of the molecule.*

It is interesting that the covalent bonding of the edges of the molecule has an influence on vibrational frequencies of the whole molecule. This process of electron flipping with the result of shifted double bonds can be demonstrated by the bond-length change upon adsorption of the molecule to the ZnO surface (Fig. SI10). A shifted double bond and the resulting bond length change has obviously an effect on the molecular vibrations as double bonds have a higher force constants compared to single bonds. As a result, the carbon rings of the molecules becomes more aromatic and the bonds within the carbon rings get stronger. For some most C-C/C=C vibrations this results in a blue shift of vibrational frequencies to higher wavenumbers when only considering the process of adsorption. Similar behaviour can be can be observed for the transition from p-Benzoquinone to a more aromatic p-Hydroquinone [15].

Charging of the molecule, i.e. occupying the LUMO, on the other hand always results in a red-shift within the studied frequency range. Due to filling of the LUMO the population in antibonding states increases, which results in a shift to lower frequencies. Similar behaviour was found for other molecules, e.g. for CO stretching vibrations [16]. For C≡N vibrations, we find that the red shift advances linearly with increasing LUMO occupation (Fig. SI8). In the C-C/C=C region, however, not always a strict linear behaviour can be observed (Fig. SI6 and Fig. SI7). The reason for the rather curved increase in red shift upon charging of the molecule is currently not known.
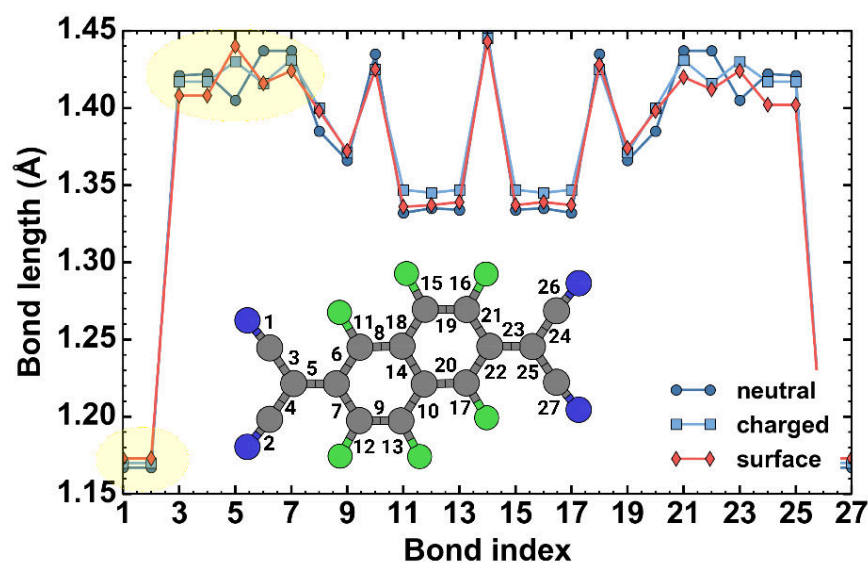
Figure SI10: *Bond lengths of all bonds within the F6-TCNNQ molecule in a neutral gas phase geometry, charged gas phase geometry and adsorbed on the ZnO surface (charged).*

7. Additional Experimental Data

Polarisation dependency of absorbance

When applying IRRAS to characterize molecular adsorbates on metal oxide surfaces, the situation is rather complicate: both s- and p-polarized components of the incident light can couple to adsorbate vibrations. The sign of the vibrational signals on dielectric materials can be explained by the reflectivity calculations described in Refs. [17-21]. The s-polarized light is oriented parallel to the surface and perpendicular to the incidence direction. The absorbance bands excited by s-polarized light (E_s) are always negative. For p-polarized light, it is more complicated, the electric field can be orientated parallel to the surface (tangential p-polarized light $E_{p,t}$) and normal to the surface (normal p-polarized light $E_{p,n}$). The IRRAS bands excited by p-polarized light can be negative or positive depending on the incidence angle θ and the refractive index of the substrate. The $E_{p,n}$ component couples only to vibrations with a component of the TDM perpendicular to the surface. The component of the TDM parallel to the surface can be excited either by E_s or by $E_{p,t}$ component, depending on the azimuth orientation.
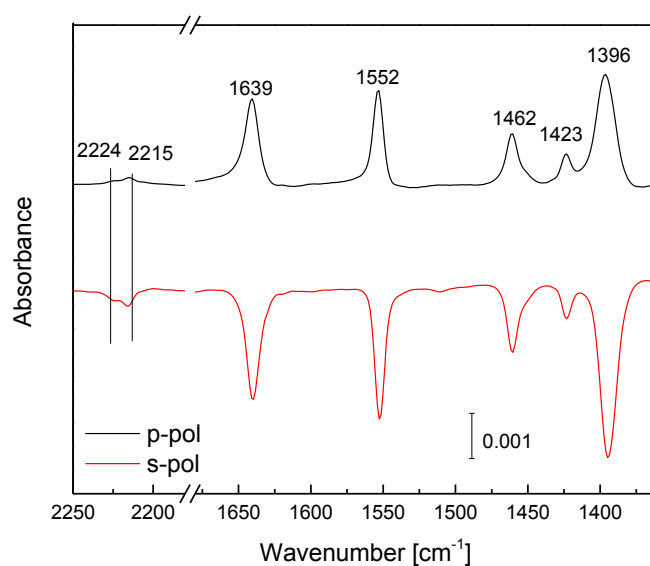
Figure SI11: *Experimental IRRAS spectra of F6-TCNNQ on the ZnO* (**10$\bar{1}$0**) *measured with p- (black curve) and s-polarized (red curve) light.*

References:

[1] Blum V, Gehrke R, Hanke F, Havu P, Havu V, Ren X, et al. Ab initio molecular simulations with numeric atom-centered orbitals. Computer Physics Communications. 2009; 180(11):2175-2196.

[2] Porezag D, Pederson MR. Infrared intensities and Raman-scattering activities within density-functional theory. Physical Review B. 1996; 54(11):7830-7836.

[3] Karzel H, Potzel W, Köfferlein M, Schiessl W, Steiner M, Hiller U, et al. Lattice dynamics and hyperfine interactions in ZnO and ZnSe at high external pressures. Physical Review B. 1996; 53(17):11425-11438.

[4] Reynolds DC, Look DC, Jogai B, Litton CW, Cantwell G, Harsch WC. Valence-band ordering in ZnO. Physical Review B. 1999; 60(4):2340-2344.

[5] Schlesinger R, Xu Y, Hofmann OT, Winkler S, Frisch J, Niederhausen J, et al. Controlling the work function of ZnO and the energy-level alignment at the interface to organic semiconductors with a molecular electron acceptor. Physical Review B. 2013; 87(15):155311.

[6] Schlesinger R. Energy-Level Control at Hybrid Inorganic/Organic Semiconductor Interfaces. : Springer International Publishing; 2017.

[7] Hofmann OT, Deinert J, Xu Y, Rinke P, Stähler J, Wolf M, et al. Large work function reduction by adsorption of a molecule with a negative electron affinity: Pyridine on ZnO(10-10). The Journal of Chemical Physics. 2013; 139(17):174701.

[8] Erker S, Rinke P, Moll N, Hofmann OT. Doping dependence of the surface phase stability of polar O-terminated (000-1) ZnO. New Journal of Physics. 2017; 19(8):083012.

[9] Nelin CJ, Bagus PS, Philpott MR. The nature of the bonding of CN to metals and organic molecules. The Journal of Chemical Physics. 1987; 87(4):2170-2176.

[10] Romaner L. Modelling of organic semiconductors and their interaction with metallic surfaces. Graz University of Technology; 2007 .

[11] Ditchfield R, Hehre WJ, Pople JA. Self-Consistent Molecular-Orbital Methods. IX. An Extended Gaussian-Type Basis for Molecular-Orbital Studies of Organic Molecules. The Journal of Chemical Physics. 1971; 54(2):724-728.

[12] Dunning TH. Gaussian basis sets for use in correlated molecular calculations. I. The atoms boron through neon and hydrogen. The Journal of Chemical Physics. 1989; 90(2):1007-1023.

[13] Furuhashi M, Yoshinobu J. Charge Transfer and Molecular Orientation of Tetrafluoro-tetracyanoquinodimethane on a Hydrogen-Terminated Si(111) Surface Prepared by a Wet Chemical Method. The Journal of Physical Chemistry Letters. 2010; 1(10):1655-1659.

[14] Pingel P, Zhu L, Park KS, Vogel J, Janietz S, Kim E, et al. Charge-Transfer Localization in Molecularly Doped Thiophene-Based Donor Polymers. The Journal of Physical Chemistry Letters. 2010; 1(13):2037-2041.

[15] Nonella M. Structures and Vibrational Spectra of p-Benzoquinone in Different Oxidation and Protonation States: A Density Functional Study. The Journal of Physical Chemistry B. 1997; 101(7):1235-1246.

[16] Xu Y, Hofmann OT, Schlesinger R, Winkler S, Frisch J, Niederhausen J, et al. Space-Charge Transfer in Hybrid Inorganic-Organic Systems. Physical Review Letters. 2013; 111(22):226802.

[17] M. Buchholz, P.G.Weidler, F. Bebensee, A. Nefedov, C.Wöll, Phys. Chem. Chem. Phys. 2014, 16:1672.

[18] W.N. Hansen, J. Opt. Soc. Am. 58 (1968) 380.

[19] W.N. Hansen, Symp. Faraday Soc. 4 (1970) 27.

[20] J.A. Mielczarski, R.H. Yoon, J. Phys. Chem. 93 (1989) 2034.

[21] M.C. Xu, Y.K. Gao, Y. Wang, C. Wöll, Phys. Chem. Chem. Phys. 12 (2010) 3649.

Chapter 8

Concluding Remarks

The research presented in this thesis contributes to the general understanding of the physics at semiconductor/organic interfaces. My work is motivated by the importance of such interfaces for organic electronic devices, because the performance and functionality of such devices is mainly governed by the hetero-interface between an inorganic semiconductor and organic molecules. The main goal of my dissertation is to gain a deeper insight into the charge transfer processes at these interfaces. Methodological aspects of DFT calculations in this context and their limitations when applied to semiconductor/organic interfaces are extensively studied. For accurately modeling the interface and the effects associated with charge transfer, new theoretical approaches are needed. The development of such approaches is an integral part of my research and part of this work. Also a comprehensive understanding of the surface structure of the substrate material is an important aspect to obtain reliable results of interfaces with organic molecules. The semiconducting material that is in the focus of this dissertation is ZnO, a material with a wide range of applications in optoelectronic and electronic devices. We used first principle methods and collaborated with experimentalists to investigate the surface structure of this transparent conducting oxide as well as its interface with organic acceptor molecules. Specifically the gained insight into charge transfer effects and the developed theoretical foundations to model such effects can be considered as a big progress in the field. In the following, the most relevant findings of this research are summarized.

Simulating charge transfer to the surface of doped semiconductors poses a difficult challenge using standard *ab inito* methods. The typically low concentration of dopants makes an explicit treatment computationally intractable and the spatial extent of the space charge region typically exceeds realistic supercell dimensions. However, considering the effects of the long-range, quasi-parabolic potential within the space charge region is essential to correctly model charge transfer. Specifically the amount of charge transfer is usually significantly limited by the build up of the electrostatic field associated with the long-ranged potential that results in the bending of the electronic bands. Therefore, before entering into the main question of this dissertation we needed to overcome this theoretical limitations and find a way to simulate the effect of the

space charge region in DFT calculations. This is achieved in the first step of my research. We refined the recently published Charge-Reservoir Electrostatic Sheet Technique[151] (CREST) and extend it in order to yield an energy correction for the band bending, while at the same time reducing the number of parameters required for the method. In **paper I** we presented this extended CREST formalism and, exemplarily, applied it to the particularly interesting case of O-terminated ZnO(000$\bar{1}$). By introducing a charge-sheet into the supercell we can mimic the electrostatic field within the space charge region and simulate its charge transfer limiting effect depending on the doping concentration of the material. In this approach the parabolic potential is approximated by a linear potential in the region below the slab. We make sure that the potential drop is equivalent to the actual emerging potential drop by a self-consistent scheme in which the properties of the charge-sheet are determined. We showed the capabilities of this extended CREST formalism by calculating the - to our knowledge - first doping-dependent surface phase diagram of the O-terminated ZnO(000$\bar{1}$) surface. Particular for ZnO, which is commonly employed in organic electronics, the surface composition is often not well known. For this material the number of theoretically proposed and experimentally observed surface reconstruction is particularly large. Recent work indicated that doping, that is often not systematically controlled, may be responsible for the observed diversity. From the calculated doping dependent surface phase diagrams, we found that the doping concentration has indeed a very notable impact on the relative phase stability, stabilizing hydrogen deficient phases at high doping concentrations. One of the main results of this work, the phase diagram for the defect free surface and the surface including oxygen vacancies are plotted in Fig. 8.1.
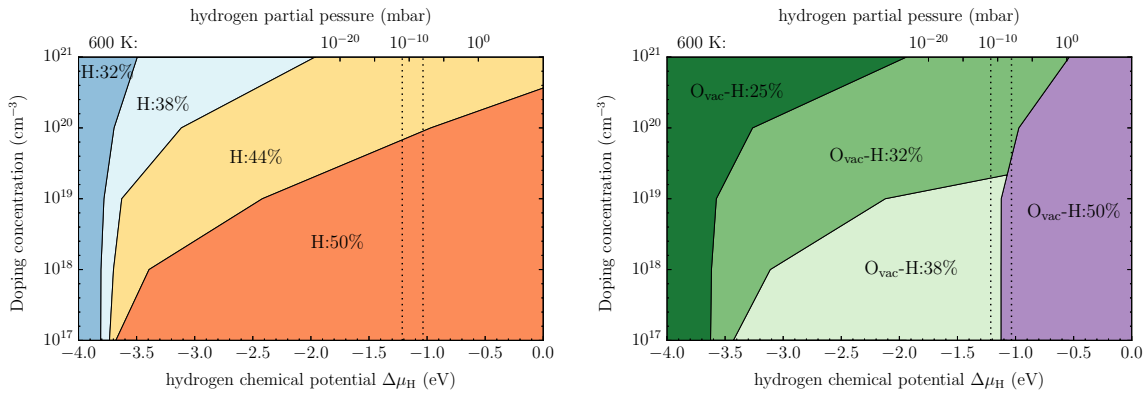
FIGURE 8.1: Doping dependence of the hydrogen coverage as a function of the hydrogen chemical potential μ_H. Colored regions represent the different surface structures with the corresponding coverage expressed as a percentage, *(left)* for the defect-free O-terminated ZnO(000$\bar{1}$) surface, and *(right)* for an oxygen vacancy concentration of 1/16 at the ZnO(000$\bar{1}$) surface.

Our results highlight that the doping concentration of transparent semiconducting oxides is an important material property that needs to be accounted for, experimentally as well as computationally. At the same time, it also provides a clear explanation for such a computational method that can be easily implemented into most quantum-mechanical codes. The extended CREST formalism can be applied to any semiconductor system where charge transfer occurs,

and is, therefore, also a valuable tool in simulating the charge transfer at semiconductor/organic interfaces and a big step forward in our research of such systems.

The charge transfer at semiconductor/organic interfaces and, therefore, also many device properties depend heavily on the exact structure of the substrate material. As described before the exact structures of polar ZnO surfaces are still not unambiguously resolved. In **paper II** we collaborated with experimentalists from the group of Norbert Koch and Frank Schreiber to contribute to this discussions by applying a novel approach to study surface structures: Using planar conjugated molecules as a probe for the surface. In this work we focused on the Zn-terminated ZnO(0001) surface. In the literature the stabilization of this surface by OH adlayers or by surface reconstructions is discussed. Over the course of this collaboration we found that an assignment of surface structures based on results from computed and experimentally obtained surface core-level shifts is not explicit enough. We therefore had to develop a new approach to identify the surface structure as it appears in experiments. We came up with the novel idea to use organic molecules as a probe to draw conclusions from their adsorption behavior to the surface. By comparing simulated adsorption heights of PTCDI molecules with values from XSW experiments, we were able to learn about the underlying surface structure. Three distinct surface models were tested (see Fig. 8.2), and the comparison yielded that only one qualified as a potential candidate: the surface structure without any OH-adlayer (Model 1). Additionally our results indicate that the PTCDI molecules adsorb in a deprotonated state on the surface.
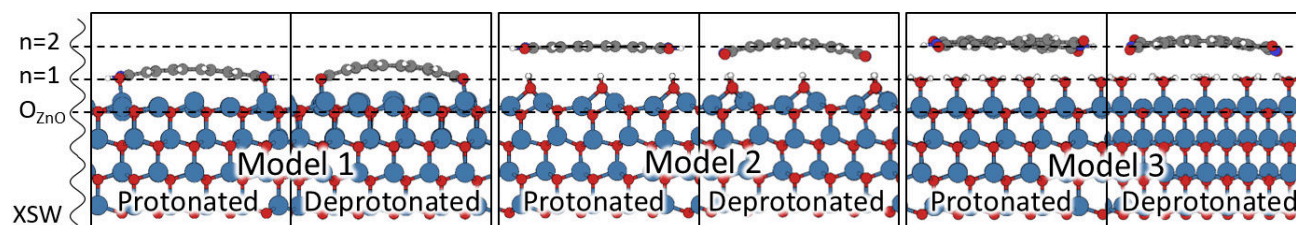
FIGURE 8.2: The six calculated geometries for three different ZnO(0001) surface models and two different chemical structures of PTCDI (protonated and deprotonated).

That means our comparison promoted the situation that organic molecule bind directly to the surface and are not kept away by any OH spacer-layers that are often proposed in the literature to appear at the ZnO(0001) surface. This dramatically reduces the number of possible surface structures and limits the search space for future studies of the precise structure. Furthermore, knowledge about the absence of adlayers is very relevant for modeling the adsorption behavior of organic molecules and therefore also for the charge transfer. Existing OH-adlayer would prevent a direct adsorption of molecules to the surface by acting as buffer layers. Although, following work specifically addressing the charge transfer are done for another ZnO surface, with the knowledge that such buffer layers are not present on Zn-terminated ZnO, the obtained results from later chapters can be applied to this surface as well.

In this dissertation the focus is not only on the amount of charge transfer from a semiconducting substrate to a molecular layer but primarily also on the localization of the transferred charge

within the molecular layer. Converging DFT calculations into solutions where the charge is localized on individual molecules can be troublesome, because the charge density is often initialized to be equal on all equivalent molecules. At my research stay at Duke University in the group of Volker Blum, we implemented an alternative initial electron density guess for FHI-aims based on extended Hückel theory, as it is used in many chemistry-focused DFT codes. The aim of this work was a speed up of our calculations of semiconductor/organic interfaces, by improving the initial guess of the charge density. The new initial guess proved to initialize the charge density better in terms of the charge localization for charge transfer system, but yielded no significant speed-up of the overall calculation. We learned that with optimized settings for the standard initialization, already an improvement of the convergence speed can be obtained. For solutions where charge is localized on individual molecules the initial moment of the atoms of the respective molecule should be manually set to the values of a charged molecule in the gas phase. The hitherto obtained findings pave the way for theoretically studying charge transfer processes at semiconductor/organic interfaces in a systematic manner.

A thorough understanding of charge transfer at semiconductor/organic is a prerequisite for advancing the field of hybrid inorganic/organic electronics. In **paper III** we studied the charge transfer mechanism at the interface between the prototypical strong electron acceptor molecule F4TCNQ and the mixed terminated $ZnO(10\bar{1}0)$ surface at the most fundamental level to resolve what exactly determines the charge transfer mechanism. Semiconductor/organic interface are particular interesting systems to study fundamental charge transfer effects, since the interaction between them can be readily tuned, e.g. via the substrate's free doping concentration. However, predicting the energy level alignment and the resultant charge transfer mechanism has proved challenging from a theoretical side. This is mainly attributed to the spurious tendency to over-delocalize charge for semilocal density functionals that is a result of the many-electron self-interaction error (MSIE). We found that from hybrid DFT calculations it is conceptually not possible to predict the occurrence of fractional or integer charge transfer for a specific system and with a MSIE-free functional calculations can be forced in either solution. Still, a lot of insight into the basic physical principles of charge transfer mechanisms can be gained from calculations of semiconductor/organic interfaces. Investigating the adsorption of the prototypical adsorbate F4TCNQ on ZnO(10-10), we made a finding that is quite counterintuitive: Although F4TCNQ is known to be a strong electron acceptor, at low doping concentrations the majority of the molecules are, in fact, positively charged. Triggered by this observation, we studied the underlying physics in more detail. In short, we find that the interaction between the organic adsorbate and the inorganic substrate proceeds through two different channels with different driving forces: Charge-donation, which is triggered by covalent interaction, and charge backdonation, which is driven by the difference in the electronegativity. While the former depends on the hybridization and affects all molecules at the interface equally (FCT), rendering the positive, the latter can be tuned via the doping concentration (i.e., the "metallicity") of the substrate and causes only a fraction of the molecules to become negatively charged (ICT). The amount of electrons transfered into the molecular layer thereby depends strongly on the substrates doping

concentration. At a charge carrier concentration of 1.9×10^{19} cm^{-3}, the ZnO substrate back-donates one electron per four F4TCNQ molecules. This exceeds the donated charge, leading to an overlayer that is overall negatively charged, as one would expect for the adsorption of a strong electron acceptor. The charge rearrangement for an undoped substrate and a substrate with a free charge carrier concentration of 1.9×10^{19} cm^{-3} is plotted in Fig.8.3. It shows that by introducing free charge carriers, the back-donated charge from the substrate localizes on individual molecules (here molecule 1), while the fractional positive charge transfer from the covalent interaction to all molecules within the molecular layer is not significantly influenced.
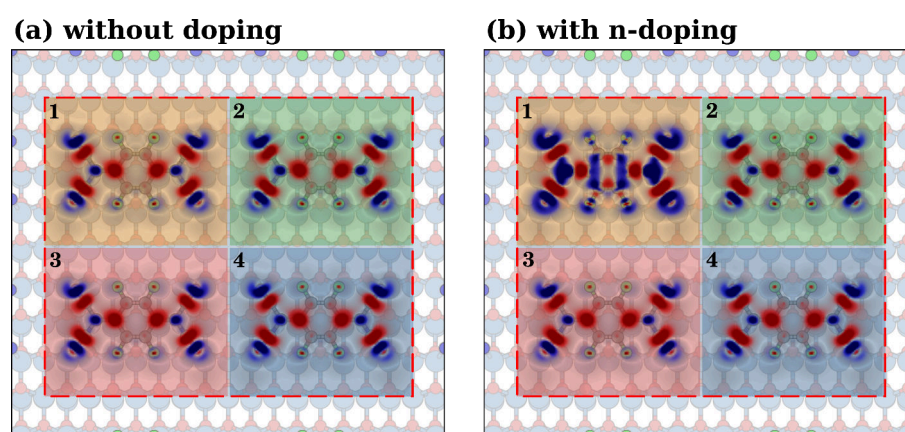
FIGURE 8.3: Line-averaged charge rearrangements within the surface supercell containing four F4TCNQ molecules, for **(a)** an undoped substrate and **(b)** a free charge carrier concentration of 1.9×10^{19} cm^{-3}. Blue areas indicate an increase in electron density, red areas a reduced electron density.

Thus, there seem to be two substrate-related properties that influence the charge-transfer mechanism: the propensity to hybridize with the adsorbate, and the availability of free charge-carriers. Although these properties are often correlated (i.e., metals have a larger charge-carrier concentration and tend to be more reactive than semiconductors), they are not causally related. We conclude from our findings that the charge transfer via the two channels act independently from each other and FCT and ICT can in principle occur simultaneously. This finding is general and can be readily transferred to other inorganic/organic interfaces. The nature and magnitude of charge-transfer is relevant for a large number of fields, including organic electronics, and we are therefore confident that our results are of high interest and yield a tremendous advancement for understanding charge transfer processes at interfaces.

Over the course of this work results also for O-terminated (2×1)-H ZnO were obtained. For this surface the hydrogen overlayer acts as a buffer such that the F4TCNQ molecules can not bind directly to the ZnO surface. Hence, no covalent bonds are formed and any positive charge transfer to a molecular monolayer is prevented. Charge transfer from substrate free charge carries into the LUMOs of the molecules occurs also for this surface in integer electron numbers and the number of negatively charge molecules is directly connected to the doping concentration of the ZnO.

Additionally to the finding presented in the paper a comprehensive investigation of the theoretical aspects of simulating charge transfer are illuminated in so far unpublished sections of this work. Methods how to determine an optimized hybrid functional to obtain a MSIE-free situation for interface systems are presented. These methods and the corresponding findings are more relevant for DFT calculations of interface systems from a technical point of view. They give an valuable insight of the impact of the MSIE for modeling inorganic/organic interfaces. We find that the required amount of exact exchange for a MSIE-free hybrid functional depends also on the doping concentration of the substrate material. With increasing doping concentration the screening from the substrate increases as well, reducing the required amount of exact exchange. In this work we not only discussed and clarified several methodological aspects of simulating charge transfer at semiconductor/organic interfaces, we primarily contributed to a better understanding of the mechanisms determining the charge transfer and the corresponding properties of hybrid interfaces.

So far we studied the charge transfer at an ideal, defect free $ZnO(10\bar{1}0)$ surface to learn about fundamental charge transfer mechanisms. For this defect free model system charge transfer to the LUMO of the F4TCNQ acceptor molecules stemmed from free charge carriers that are introduced by bulk doping. In reality surfaces are often not that ideal and charged surface states from surface defects may be an additional source of charge carriers. Such surface states can significantly reduce the band bending inside the inorganic semiconductor by pinning the Fermi level. This can have a huge impact on the functionality of an inorganic/organic semiconductor junction. Depending on the desired application, substantial surface band bending might be favored as it can promote the dissociation of excitons into mobile carriers at the interface. For applications where only the energy transfer is relevant, flat bands would be preferred at the interface. Therefore, also the source of the charge transfer is an important aspect, as it influences the amount of band bending. In **paper IV** we studied the charge transfer between the mixed-terminated $ZnO(10\bar{1}0)$ surface and the strong electron acceptor molecule F6TCNNQ, a molecule that is chemically related to the previously studied F4TCNQ. In collaboration with experimentalists from the group the Christof Wöll and Norbert Koch we identified the charge state of the molecules in the first monolayer on a nominally undoped substrate. Our experimental collaborators measured infrared vibrational spectra for mono- and multilayers of F6TCNNQ molecules on $ZnO(10\bar{1}0)$. The obtained spectra showed distinct shifts of certain vibrational bands between the two coverages. To explain these band shifts we performed a thorough theoretical analysis using density functional theory (DFT). We performed DFT simulations and vibrational analysis of the F6TCNNQ molecule in the gas phase, as well as adsorbed on the ZnO surface. The theoretical vibrational frequencies in the gas phase were evaluated for various charge states between a neutral molecule and a singly negatively charged molecule. This analysis gave a direct insight into the dependence of the vibrational frequencies on the charge state of the molecule. The calculation of theoretical vibrational frequencies for the interface system gave information on how the IR bands are influenced by the interaction of the molecule with the surface, i.e. the bonding of the molecule's cyano groups to surface Zn atoms. Hence,

our calculations revealed that two mechanisms govern the pronounced vibrational band shifts of the adsorbed molecule seen in the experiments: in addition to electron transfer into unoccupied molecular levels of the organic acceptor, also the bonding to the surface strongly affects the vibrational frequencies. Our approach to distinguish between these two effects allowed us to explain the observed IR band shifts for a molecular monolayer compared to multilayer spectra. With our contribution it was, therefore, possible to provide unambiguous evidence for electron transfer from the inorganic substrate to F6TCNNQ. The results indicate that charge transfer already occurs even without intentional doping of the substrate material. However, the intrinsic charge carrier concentration of bulk ZnO is not sufficient to explain the observed charge transfer to the molecules on the surface. We concluded that the charge transfer, therefore, mainly stems from surface defects and the LUMO of the molecules are pinned at the corresponding surface state level. In this collaboration we not only used vibrational spectroscopy to determine the charge state of molecules adsorbed on a ZnO substrate and from that were able to educe the origin of this charge transfer primarily from charged surfaces states; we also introduced an novel theoretical approach to determine the impact of both, LUMO charging and surface adsorption, on the vibrational modes of the molecule.

In summary, over the course of my dissertation, we performed quantum-mechanical computer simulations to study several aspects of semiconductor/organic interfaces. New insights into the surface structure of ZnO was gained, and a novel formalism to consider band bending effects at semiconductor interfaces was developed. By studying the charge transfer at the F4TCNQ/ZnO model system, we contributed to a better understanding of the fundamental mechanisms of charge transfer at hetero-interfaces between semiconductors and organic molecules. The approaches and the methodological aspects presented in this thesis are very relevant and helpful for future theoretical investigations of semiconductor/organic interfaces. The resultant findings imply a direct progress in understanding the important process of charge transfer, which is relevant for the whole field of hybrid inorganic/organic electronics.

Part III

Appendix

Appendix A

Potential Maps and Hubbard-U: PTCDA / NaCl / Ag(111)

A.1 Motivation

In this appendix to my dissertation, I summarize the results obtained from a side-project that was motivated by the work of Katherine A. Cochrane in the group of Prof. Sarah A. Burke at the University of British Columbia. K.A. Cochrane used Kelvin probe force microscopy (KPFM) to image the charge distribution within single molecules and molecular clusters of PTCDA, that were decoupled by a bilayer of NaCl from an Ag(111) substrate. Their first results were published in 2015 [152] and more findings were described in K.A. Cochrane's dissertation [153]. However, a theoretical confirmation of their results remained missing. My supervisor O.T. Hofmann was approached by Prof. Burke with the request of corroborating their findings with DFT calculations. This appendix should give a short overview of the current status of this project.

In our work we focus on two aspects of this system: The charge distribution within the proposed cluster geometries of a four-molecule PTCDA cluster, and the spatial resolved Hubbard-U parameter for a single molecule. For both questions it was necessary to use hybrid functionals, to correctly describe the charge transfer and also to get a correct relative energy level arrangement. All calculations for this system were performed with FHI-aims [101] using open boundary conditions. For the PTCDA molecule and the NaCl layers the default 'tight' settings were used. Test calculations including an Ag substrate were performed with the minimal basis set for Ag atoms, but are not presented here. As it will be explained in the corresponding parts we used the PBE functional as well as the hybrid PBEh* functional with 54% exact exchange (see below why we used this value). Long range dispersion forces were considered with the vdW-TS scheme [154] (Parameters for Na: $C_6 = 69.3$ / $\alpha = 13.6$ / $R_0 = 1.63$; Parameters for Cl: $C_6 = 23.7$ / $\alpha = 8.0$ / $R_0 = 3.0$). The geometry of the NaCl layers presented in this work were

build using lattice constants obtained from bulk calculations with the respective functional. Bulk calculations of the primitive NaCl bulk unit cell were performed with a $12 \times 12 \times 12$ k-grid. Lattice constants and band gap values for the used functionals are tabulated in Tab. A.1.

TABLE A.1: Measured and calculated lattice constant a and band gap values of bulk NaCl

a (Å)	Band gap (eV)	Reference
5.595	8.97	experiment[155]
5.391	5.68	pbe+vdW
5.427	10.14	pbeh*($\alpha = 0.53$)+vdW

A.2   Adsorption geometry for a single molecule on NaCl

We started with the search for the lowest energy local adsorption site for a single PTCDA molecule on a bilayer of NaCl. Calculations were done with the PBE functional. Our found adsorption geometry is depicted in Fig. A.1 and is equivalent to the geometry found by others for PTCDA on NaCl(100)[156,157].
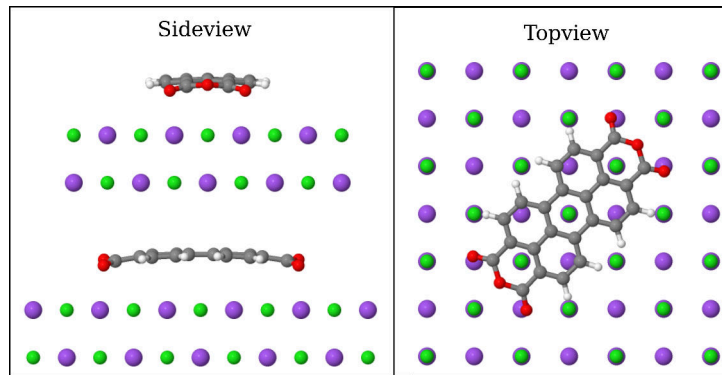
FIGURE A.1: Lowest energy local adsorption geometry for PTCDA on a bilayer NaCl (PBE calculation + vdW-TS)

A.3   Finding the Hubbard-U

In the experiments it is found that PTCDA on bilayer NaCl/Ag(111) is onefold negatively charged[153]. The Coulomb repulsion splits the partially occupied LUMO into two Hubbard states, i.e. a SOMO/SUMO pair. It is observed that an increased NaCl thickness results in an increased Hubbard gap and an overall upward shift of the energy levels. From DFT calculations the Hubbard-U can be extracted directly from the SOMO-SUMO splitting (see Fig. A.2). However, this is only valid if the energy levels do not change upon filling, i.e. for functionals that fulfill the straight-line energy condition. Therefore, expensive hybrid calculations are necessary with their exact-exchange chosen such that the straight-line condition is fulfilled.
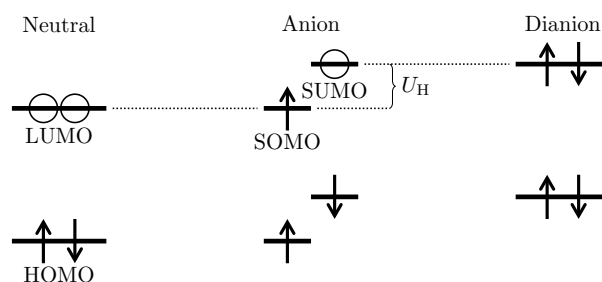
FIGURE A.2: Schematic energy level diagram of the HOMO and LUMO upon charging to illustrate the meaning of the Hubbard-U_H.

We determined the adequate PBEh* hybrid mixing parameter α to fulfill the straight-line condition for PTCDA in the gas phase as well as on a bilayer of NaCl. From the corresponding calculations we can directly extract the value of the Hubbard-U from the SUMO/SOMO energy difference at the straight-line α. The results of the calculations are put into graphs in Fig. A.3 and A.4, respectively. The presented energy values were all obtained from calculations from the fully relaxed geometry for the respective functional and charge state.
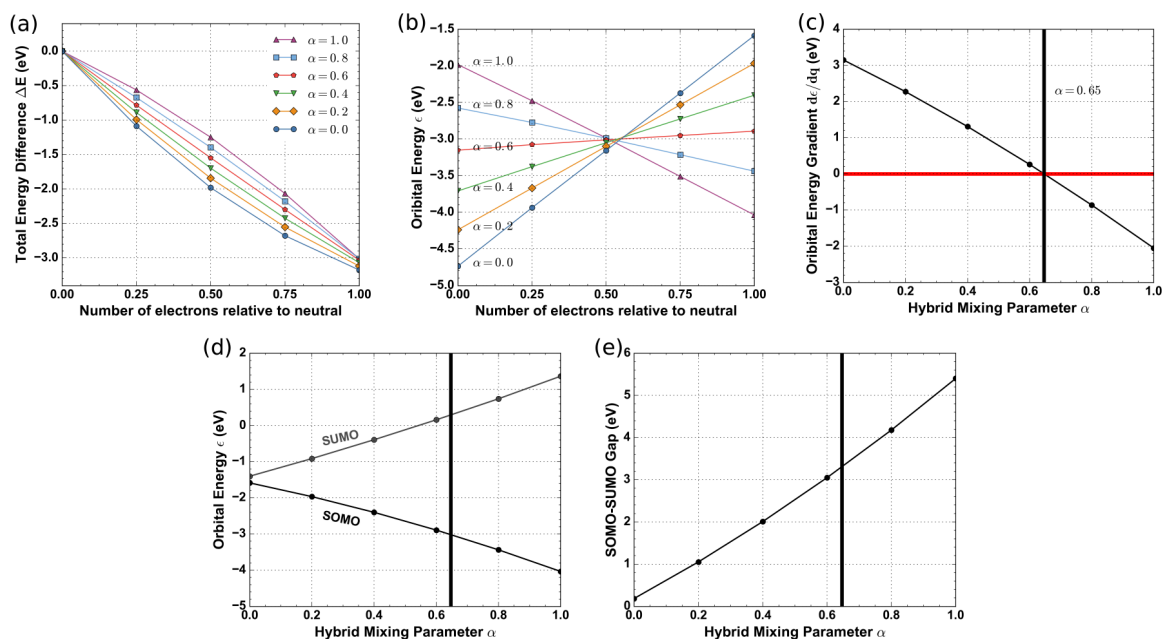
FIGURE A.3: Straight-line energy condition for PTCDA in the gas phase: *(a)* Total energy as a function of fractional LUMO occupation for various mixing parameters α; *(b)* Orbital energy evolution of the partially filled "SOMO". *(c)* Gradient of the orbital energy as a function of α. *(d)* Evolution of the SOMO and SUMO energies and *(e)* evolution of the SOMO-SUMO gap as α is increased. The black vertical line mark the position of the straight-line α.
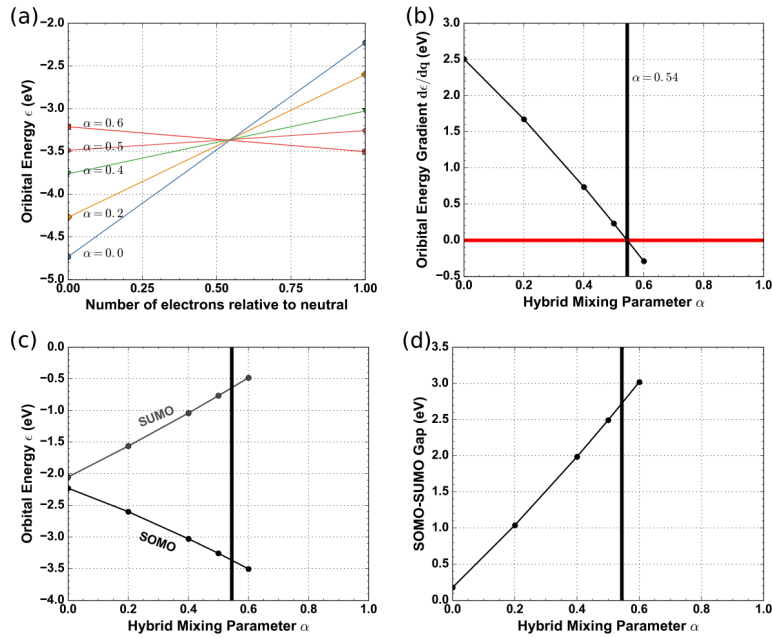
FIGURE A.4: Straight-line energy condition for PTCDA on a bilayer NaCl: *(a)* Total energy as a function of fractional LUMO occupation for various mixing parameters α; *(b)* Orbital energy evolution of the partially filled "SOMO". *(c)* Gradient of the orbital energy as a function of α. *(d)* Evolution of the SOMO and SUMO energies and *(e)* evolution of the SOMO-SUMO gap as α is increased. The black vertical line mark the position of the straight-line α.

We obtained a straight-line α for PTCDA in the gas phase of 0.65 and by considering the NaCl bilayer of 0.54. Equivalently to other substrates the required amount of exact exchange reduces because of screening effects. For the gas phase we found a Hubbard-U value of 3.3 eV. On a bilayer of NaCl we found a smaller value of 2.7 eV. Compared to the experiments these values are both to high (For PTCDA on a bilayer NaCl on Ag(111) 1.4 eV are reported). The reason is probably the missing Ag substrate and, therefore, the missing screening from the substrate in our calculations. Calculations including the Ag substrate would be the next step to adequately account for the screening effects arising from the Ag.

A.4   Plotting potential maps

We also tried to reproduce the KPFM images obtained in experiments of a single PTCDA molecule, to verify that indeed the assumed charge states are observed. In KPFM experiments, the local contact potential difference between the scanning probe tip and the surface is measured, a quantity that is closely related to the charge distribution on the surface[158,159,160]. Therefore the produced images are often assumed to resolve the spatial charge distribution.

We produced simulated potential maps in a similar way as in the work for Schuler et al.[161] and Mohn et al.[162]. For the system of a single PTCDA molecule we calculated the electrostatic potential (Hartree potential) in the vicinity of the molecule. Again calculations were done only

with a NaCl bilayer, omitting the Ag substrate. The Hartree potential is plotted at a distance of approx. 2.6 Å above the molecule. A comparison of experimentally obtained potential maps and our calculated potential maps are plotted in Fig. A.5.
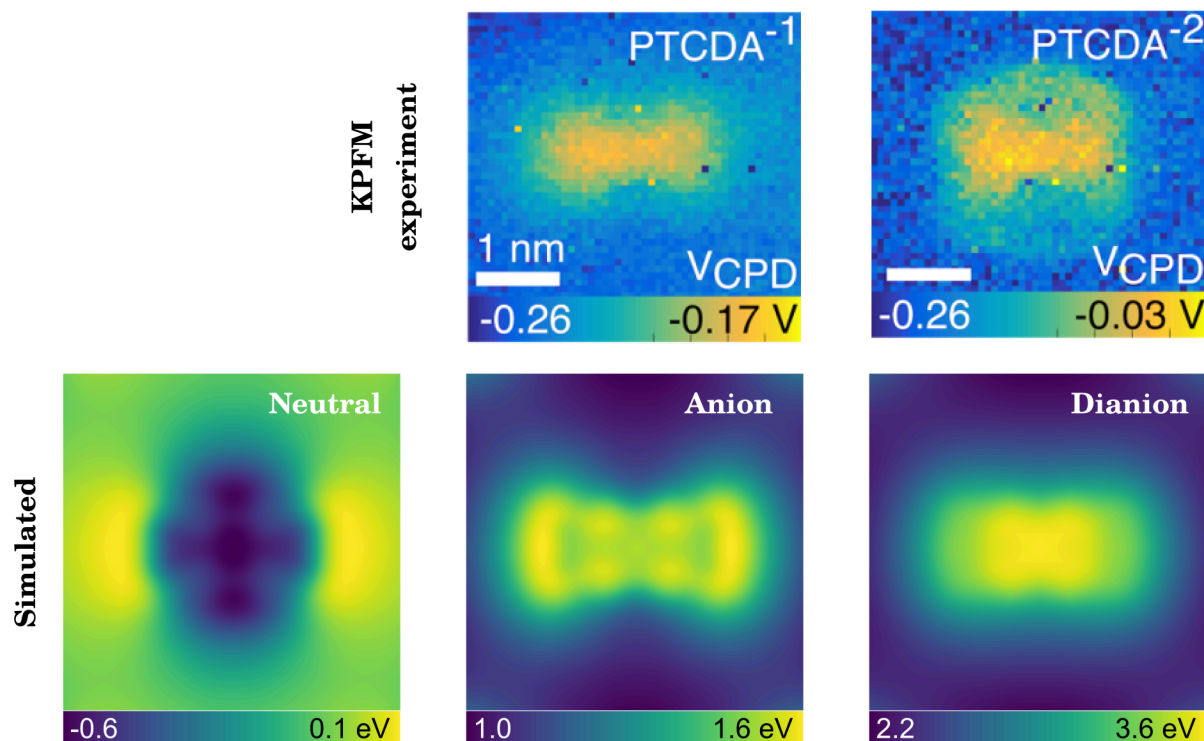
FIGURE A.5: In the first row the KPFM potential maps of a single PTCDA on NaCl on Ag(111) are shown for a onefold (anion) and twofold (dianion) charged molecule (modified from [153], the experimental potential map of a neutral molecule was not available). In the second line simulated potential maps (Hartree potential $\approx$ 2.6 Å above the molecule) are plotted for the neutral molecule as well as for the anion and dianion.

We found a reasonable but not perfect agreement of experimental and simulated potential maps for a PTCDA anion and dianion.

Experimentally also spatial maps of the Hubbard-U value were produced (However, I want to note that we are not entirely sure what a spatial varying U parameter means physically.). For the spatially resolved Hubbard-U they find lower values in the middle of two lobes. The lobed structure already appears in the "charging potential", i.e. in the change from a onefold charged molecule to a neutral molecule and from a onefold charged molecule to a twofold charged molecule. We also tried to reproduce such "charging potentials" by plotting the difference in the Hartree potential of a neutral molecule and an anion, and an anion and dianion. However we were not able to find such a lobed structure. More investigations into such "charging potentials" are necessary from the theory side to better understand the problem, here we only wanted to report the current status. A comparison between the KPFM charging maps and Hartree potential differences from our calculations are plotted in Fig. A.6.
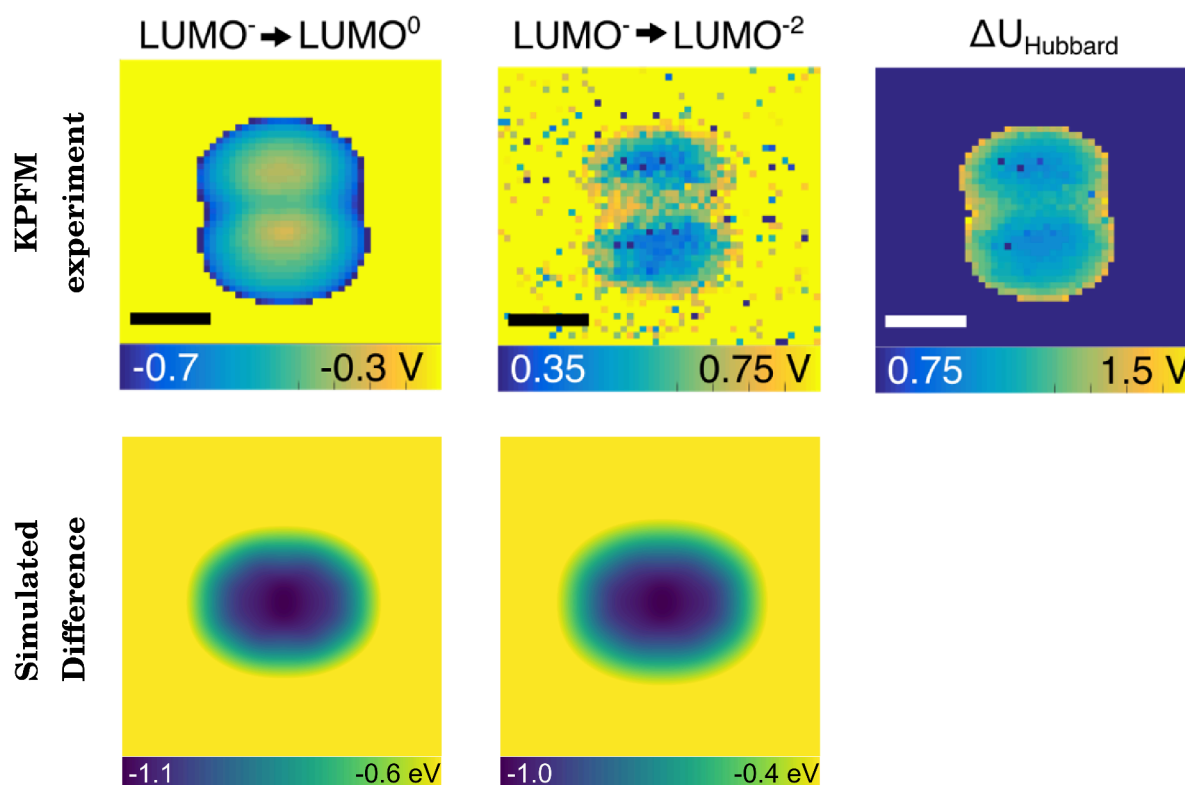
FIGURE A.6: In the first row the KPFM "charging potential maps" for the transition from an anion (LUMO$^-$) to a neutral molecule (LUMO^0), and from an anion (LUMO$^-$) to a dianion (LUMO^{-2}) are plotted. From the "charging potential" a spatial resolved Hubbard-U parameter is obtained (from [153]). In the second line the difference of simulated potential maps are plotted for "neutral molecule − anion", and "anion − dianion".

A.5 Four-molecule-cluster

For the cluster structures the progress of the research is limited to the cluster geometry so far. In experiment, two distinct cluster geometries for PTCDA on NaCl on Ag(111) are observed: "clover" and "diamond" [152]. Clover is fully symmetric with all four molecules being equivalent (C_4 symmetry; all four molecules experiencing the same chemical environment). Diamond has a C_2 symmetry containing two molecules with a close anhydride-anhydride interaction (See Fig. A.7).

The first step was to verify the geometry of the two 4-molecule-clusters and to check whether these are the arrangements we expect to see in experiments. We investigated a number of possible cluster geometries, however, we find the two cluster geometries observed in experiment are not the energetically most favorable ones in DFT. Using PBE and PBEh* calculations, we find two structures being more favorable, the "brick" and the "herringbone" structure. These first results are only for a NaCl bilayer without considering the Ag substrate and the NaCl structure was kept fixed during the relaxation. A top-view of the studied geometries and the respective energy difference to the lowest energy geometry of a 4-molecule-cluster calculated from PBE and PBEh* are shown in Fig. A.7.
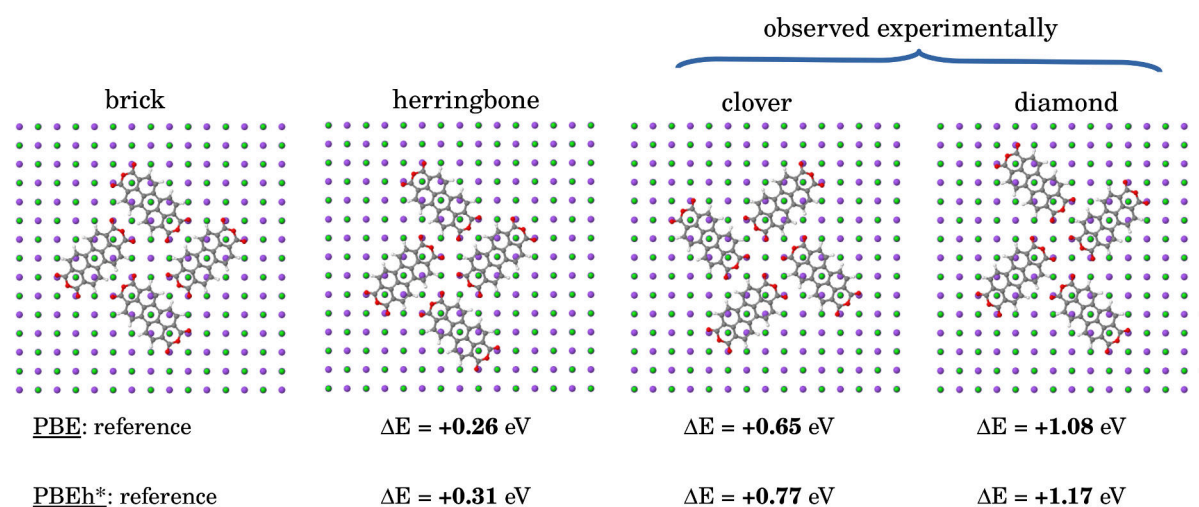
FIGURE A.7: The four theoretically found lowest energy geometries of a 4-molecule-PTCDA-cluster on a bilayer of NaCl.

It is quite surprising that from theory the experimentally observed structures could not be confirmed and the reason is not clear yet. For future investigations of this system, the Ag substrate should be included. Also the charge state might play a role. In our calculations neutral PTCDA molecules were assumed, however from experiment we know that charge transfer occurs. For the diamond structure it was found in KPFM images that more charge is located at the two molecules that are closer together. This is quite surprising since from Coulomb repulsion one would expect the molecules being furthest apart to hold more charge. An explanation would be the time-averaging nature of the experiment. In reality it might be that single electrons hop around within the cluster and they are simply more likely to sit on the molecules that are closer together. Since PBE is known to over-delocalize charge, in a next step we want to use hybrid functionals for charged clusters to be able to accurately describe the integer charge transfer situation. With hybrid calculations we expect to be able to estimate both, the energy barrier for electrons to hop between the molecules of a cluster, and the energetically preferred site for the electrons within the cluster. With knowing the probability of electrons being located on a specific molecule within the cluster we would be able to predict the time-averaged charge distribution observed in experiments.

Bibliography

[1] Hofmann, O. T., Rinke, P., Scheffler, M. & Heimel, G. Integer versus fractional charge transfer at metal (/insulator)/organic interfaces: Cu (/NaCl)/TCNE. *ACS nano* **9**, 5391–5404 (2015).

[2] Hollerer, M. *et al.* Charge transfer and orbital level alignment at inorganic/organic interfaces: The role of dielectric interlayers. *ACS nano* **11**, 6252–6260 (2017).

[3] Baldo, M. & Forrest, S. Interface-limited injection in amorphous organic semiconductors. *Physical Review B* **64**, 085201 (2001).

[4] Di, C.-a. *et al.* Effective modification of indium tin oxide for improved hole injection in organic light-emitting devices. *Applied physics letters* **89**, 033502 (2006).

[5] Koch, N. *et al.* Conjugated organic molecules on metal versus polymer electrodes: Demonstration of a key energy level alignment mechanism. *Applied Physics Letters* **82**, 70–72 (2003).

[6] Crispin, X. *et al.* Characterization of the interface dipole at organic/metal interfaces. *Journal of the American Chemical Society* **124**, 8131–8141 (2002).

[7] De Renzi, V. *et al.* Metal work-function changes induced by organic adsorbates: A combined experimental and theoretical study. *Physical review letters* **95**, 046804 (2005).

[8] Koch, N. *et al.* Adsorption-induced intramolecular dipole: Correlating molecular conformation and interface electronic structure. *Journal of the American Chemical Society* **130**, 7300–7304 (2008).

[9] Kahn, A., Koch, N. & Gao, W. Electronic structure and electrical properties of interfaces between metals and π-conjugated molecular films. *Journal of Polymer Science Part B: Polymer Physics* **41**, 2529–2548 (2003).

[10] Ishii, H., Sugiyama, K., Ito, E. & Seki, K. Energy level alignment and interfacial electronic structures at organic/metal and organic/organic interfaces. *Advanced materials* **11**, 605–625 (1999).

[11] Hoffmann, R. A chemical and theoretical way to look at bonding on surfaces. *Reviews of modern Physics* **60**, 601 (1988).

[12] Hoffmann, R. *Solids and surfaces: a chemist's view of bonding in extended structures* (Wiley-VCH, 1988).

[13] Hofmann, O. T., Atalla, V., Moll, N., Rinke, P. & Scheffler, M. Interface dipoles of organic molecules on Ag(111) in hybrid density-functional theory. *New Journal of Physics* **15**, 123028 (2013).

[14] Rau, U., Güttler, H. H. & Werner, J. H. The ideality of spatially inhomogeneous schottky contacts. *MRS Online Proceedings Library Archive* **260** (1992).

[15] Braun, S. & Salaneck, W. R. Fermi level pinning at interfaces with tetrafluorotetra-cyanoquinodimethane (F4-TCNQ): The role of integer charge transfer states. *Chemical physics letters* **438**, 259–262 (2007).

[16] Gruenewald, M. *et al.* Integer charge transfer and hybridization at an organic semiconductor/conductive oxide interface. *The Journal of Physical Chemistry C* **119**, 4865–4873 (2015).

[17] Duhm, S. *et al.* Weak charge transfer between an acceptor molecule and metal surfaces enabling organic/metal energy level tuning. *The Journal of Physical Chemistry B* **110**, 21069–21072 (2006).

[18] Romaner, L. *et al.* Impact of bidirectional charge transfer and molecular distortions on the electronic structure of a metal-organic interface. *Physical review letters* **99**, 256801 (2007).

[19] Heimel, G. *et al.* Charged and metallic molecular monolayers through surface-induced aromatic stabilization. *Nature chemistry* **5**, 187 (2013).

[20] Glowatzki, H. *et al.* "soft" metallic contact to isolated C_{60} molecules. *Nano letters* **8**, 3825–3829 (2008).

[21] Karzel, H. *et al.* Lattice dynamics and hyperfine interactions in ZnO and ZnSe at high external pressures. *Physical Review B* **53**, 11425 (1996).

[22] Reynolds, D. *et al.* Valence-band ordering in ZnO. *Physical Review B* **60**, 2340 (1999).

[23] Thomas, D. The exciton spectrum of zinc oxide. *Journal of Physics and Chemistry of Solids* **15**, 86–96 (1960).

[24] Alivov, Y. I. *et al.* Fabrication and characterization of n-ZnO/p-AlGaN heterojunction light-emitting diodes on 6H-SiC substrates. *Applied Physics Letters* **83**, 4719–4721 (2003).

[25] Ohta, H. *et al.* Current injection emission from a transparent p-n junction composed of p-$SrCu_2O_2$/n-ZnO. *Applied Physics Letters* **77**, 475–477 (2000).

[26] Ikram, M., Murray, R., Hussain, A., Ali, S. & Shah, S. I. Hybrid organic solar cells using both ZnO and PCBM as electron acceptor materials. *Materials Science and Engineering: B* **189**, 64–69 (2014).

[27] Schmidt-Mende, L. & MacManus-Driscoll, J. L. ZnO-nanostructures, defects, and devices. *Materials today* **10**, 40–48 (2007).

[28] Look, D. C. *et al.* Electrical properties of bulk ZnO. *Solid state communications* **105**, 399–401 (1998).

[29] Van de Walle, C. G. Hydrogen as a cause of doping in zinc oxide. *Physical review letters* **85**, 1012 (2000).

[30] Janotti, A. & Van de Walle, C. G. Native point defects in ZnO. *Physical Review B* **76**, 165202 (2007).

[31] Oba, F., Choi, M., Togo, A. & Tanaka, I. Point defects in ZnO: an approach from first principles. *Science and Technology of Advanced Materials* **12**, 034302 (2011).

[32] Hu, J. & Gordon, R. G. Textured aluminum-doped zinc oxide thin films from atmospheric pressure chemical-vapor deposition. *Journal of Applied Physics* **71**, 880–890 (1992).

[33] Ko, H. *et al.* Ga-doped ZnO films grown on gan templates by plasma-assisted molecular-beam epitaxy. *Applied Physics Letters* **77**, 3761–3763 (2000).

[34] Kalusniak, S., Sadofev, S., Schäfer, P. & Henneberger, F. Heavily n-type ZnO: A plasmonic material at telecommunication wavelengths. *physica status solidi (c)* **11**, 1357–1360 (2014).

[35] Morkoç, H. & Özgür, Ü. *Zinc oxide: fundamentals, materials and device technology* (John Wiley & Sons, 2008).

[36] Wöll, C. The chemistry and physics of zinc oxide surfaces. *Progress in Surface Science* **82**, 55–120 (2007).

[37] Mora-Fonz, D. *et al.* Why are polar surfaces of ZnO stable? *Chemistry of Materials* **29**, 5306–5320 (2017).

[38] Lauritsen, J. V. *et al.* Stabilization principles for polar surfaces of ZnO. *ACS nano* **5**, 5987–5994 (2011).

[39] Kresse, G., Dulub, O. & Diebold, U. Competing stabilization mechanism for the polar ZnO(0001)-zn surface. *Physical Review B* **68**, 245409 (2003).

[40] Du, M.-H., Zhang, S., Northrup, J. & Erwin, S. C. Stabilization mechanisms of polar surfaces: ZnO surfaces. *Physical Review B* **78**, 155424 (2008).

[41] Meyer, B. & Marx, D. Density-functional study of the structure and stability of ZnO surfaces. *Physical Review B* **67**, 035403 (2003).

[42] Meyer, B. *et al.* Partial dissociation of water leads to stable superstructures on the surface of zinc oxide. *Angewandte Chemie International Edition* **43**, 6641–6645 (2004).

[43] Sormann, H. Lecture notes in theoretische festkörperphysik, bandstrukturmethoden (2013). URL `https://itp.tugraz.at/LV/ewald/TFKP/`.

[44] Ostlund, N. S. & Szabo, A. *Modern Quantum Chemistry: Introduction to advanced electronic structure theory* (Dover Publications Inc New edition edn, 1996).

[45] Sakurai, J. J. & Commins, E. D. *Modern quantum mechanics, revised edition* (AAPT, 1995).

[46] Eschrig, H. *The fundamentals of density functional theory*, vol. 2 (Springer, 2003).

[47] Nogueira, F., Castro, A. & Marques, M. A. A tutorial on density functional theory. In *A Primer in Density Functional Theory*, 218–256 (Springer, 2003).

[48] Burke, K. & friends. The ABC of DFT. *Department of Chemistry, University of California* 40 (2007).

[49] Engel, E. & Dreizler, R. M. *Density functional theory* (Springer, 2013).

[50] Hohenberg, P. & Kohn, W. Inhomogeneous electron gas. *Phys. Rev.* **B136**, 864–871 (1964).

[51] Kohn, W. & Sham, L. Self-consistent equations including exchange and correlation effects. *Phys. Rev.* **A140**, 1133–1138 (1965).

[52] Ceperley, D. & Alder, B. Ground state of the electron gas by a stochastic method. *Phys. Rev. Lett.* **45**, 566–569 (1980).

[53] Perdew, J., Burke, K. & Ernzerhof, M. Generalized gradient approximation made simple. *Phys. Rev. Lett.* **77**, 3865–3868 (1996).

[54] Ernzerhof, M. & Scuseria, G. E. Assessment of the perdew–burke–ernzerhof exchange-correlation functional. *The Journal of chemical physics* **110**, 5029–5036 (1999).

[55] Lejaeghere, K., Van Speybroeck, V., Van Oost, G. & Cottenier, S. Error estimates for solid-state density-functional theory predictions: an overview by means of the ground-state elemental crystals. *Critical Reviews in Solid State and Materials Sciences* **39**, 1–24 (2014).

[56] Mori-Sánchez, P., Cohen, A. J. & Yang, W. Localization and delocalization errors in density functional theory and implications for band-gap prediction. *Physical review letters* **100**, 146401 (2008).

[57] Cohen, A. J., Mori-Sánchez, P. & Yang, W. Fractional charge perspective on the band gap in density-functional theory. *Physical Review B* **77**, 115123 (2008).

[58] Tozer, D. J. & De Proft, F. Computation of the hardness and the problem of negative electron affinities in density functional theory. *The Journal of Physical Chemistry A* **109**, 8923–8929 (2005).

[59] Teale, A. M., De Proft, F. & Tozer, D. J. Orbital energies and negative electron affinities from density functional theory: insight from the integer discontinuity. *The Journal of chemical physics* **129**, 044110 (2008).

[60] Peach, M. J., Teale, A. M., Helgaker, T. & Tozer, D. J. Fractional electron loss in approximate DFT and hartree-fock theory. *Journal of chemical theory and computation* **11**, 5262–5268 (2015).

[61] Zheng, X., Liu, M., Johnson, E. R., Contreras-García, J. & Yang, W. Delocalization error of density-functional approximations: A distinct manifestation in hydrogen molecular chains. *The Journal of chemical physics* **137**, 214106 (2012).

[62] Johnson, E. R., Otero-de-la Roza, A. & Dale, S. G. Extreme density-driven delocalization error for a model solvated-electron system. *The Journal of chemical physics* **139**, 184116 (2013).

[63] Bally, T. & Sastry, G. N. Incorrect dissociation behavior of radical ions in density functional calculations. *The Journal of Physical Chemistry A* **101**, 7923–7925 (1997).

[64] Ruzsinszky, A., Perdew, J. P., Csonka, G. I., Vydrov, O. A. & Scuseria, G. E. Spurious fractional charge on dissociated atoms: Pervasive and resilient self-interaction error of common density functionals. *The Journal of chemical physics* **125**, 194112 (2006).

[65] Mardirossian, N. & Head-Gordon, M. Thirty years of density functional theory in computational chemistry: an overview and extensive assessment of 200 density functionals. *Molecular Physics* **115**, 2315–2372 (2017).

[66] Rappoport, D., Crawford, N., Furche, F. & Burke, K. Which functional should i choose? *Computational Inorganic and Bioinorganic Chemistry* 594 (2008).

[67] Burke, K. Perspective on density functional theory. *The Journal of chemical physics* **136**, 150901 (2012).

[68] Perdew, J. P. *et al.* Restoring the density-gradient expansion for exchange in solids and surfaces. *Physical Review Letters* **100**, 136406 (2008).

[69] Zhang, Y. & Yang, W. Comment on "generalized gradient approximation made simple". *Physical Review Letters* **80**, 890 (1998).

[70] Perdew, J. P., Ernzerhof, M. & Burke, K. Rationale for mixing exact exchange with density functional approximations. *The Journal of chemical physics* **105**, 9982–9985 (1996).

[71] Heyd, J., Scuseria, G. E. & Ernzerhof, M. Hybrid functionals based on a screened coulomb potential. *The Journal of chemical physics* **118**, 8207–8215 (2003).

[72] Heyd, J., Scuseria, G. E. & Ernzerhof, M. Erratum: "hybrid functionals based on a screened coulomb potential" [J. Chem. Phys. 118, 8207 (2003)]. *The Journal of Chemical Physics* **124**, 219906 (2006).

[73] Becke, A. D. Density-functional thermochemistry. IV. a new dynamical correlation functional and implications for exact-exchange mixing. *The Journal of chemical physics* **104**, 1040–1046 (1996).

[74] Adamo, C. & Barone, V. Toward reliable density functional methods without adjustable parameters: The PBE0 model. *The Journal of chemical physics* **110**, 6158–6170 (1999).

[75] Jaramillo, J., Scuseria, G. E. & Ernzerhof, M. Local hybrid functionals. *The Journal of chemical physics* **118**, 1068–1073 (2003).

[76] Levy, M., Perdew, J. P. & Sahni, V. Exact differential equation for the density and ionization energy of a many-particle system. *Physical Review A* **30**, 2745 (1984).

[77] Almbladh, C.-O. & von Barth, U. Exact results for the charge and spin densities, exchange-correlation potentials, and density-functional eigenvalues. *Physical Review B* **31**, 3231 (1985).

[78] Vydrov, O. A. & Scuseria, G. E. Assessment of a long-range corrected hybrid functional. *The Journal of chemical physics* **125**, 234109 (2006).

[79] Janesko, B. G., Henderson, T. M. & Scuseria, G. E. Screened hybrid density functionals for solid-state chemistry and physics. *Physical Chemistry Chemical Physics* **11**, 443–454 (2009).

[80] Perdew, J. P. & Zunger, A. Self-interaction correction to density-functional approximations for many-electron systems. *Physical Review B* **23**, 5048 (1981).

[81] Pederson, M. R., Ruzsinszky, A. & Perdew, J. P. Communication: Self-interaction correction with unitary invariance in density functional theory (2014).

[82] Kümmel, S. & Kronik, L. Orbital-dependent density functionals: Theory and applications. *Rev. Mod. Phys.* **80**, 3–60 (2008).

[83] Filippetti, A. & Spaldin, N. A. Self-interaction-corrected pseudopotential scheme for magnetic and strongly-correlated systems. *Phys. Rev. B* **67**, 125109 (2003).

[84] Cococcioni, M. & de Gironcoli, S. Linear response approach to the calculation of the effective interaction parameters in the LDA + U method. *Phys. Rev. B* **71**, 035105 (2005).

[85] d'Avezac, M., Calandra, M. & Mauri, F. Density functional theory description of hole-trapping in Sio_2: A self-interaction-corrected approach. *Phys. Rev. B* **71**, 205210 (2005).

[86] Ruzsinszky, A., Perdew, J. P., Csonka, G. I., Vydrov, O. A. & Scuseria, G. E. Spurious fractional charge on dissociated atoms: Pervasive and resilient self-interaction error of common density functionals. *The Journal of Chemical Physics* **125**, 194112 (2006).

[87] Anisimov, V. I., Kozhevnikov, A. V., Korotin, M. A., Lukoyanov, A. V. & Khafizullin, D. A. Orbital density functional as a means to restore the discontinuities in the total-energy derivative and the exchange-correlation potential. *Journal of Physics: Condensed Matter* **19**, 106206 (2007).

[88] Stengel, M. & Spaldin, N. A. Self-interaction correction with Wannier functions. *Phys. Rev. B* **77**, 155106 (2008).

[89] Ruzsinszky, A., Perdew, J. P., Csonka, G. I., Vydrov, O. A. & Scuseria, G. E. Density functionals that are one-and two-are not always many-electron self-interaction-free, as shown for H^{2+}, He^{2+}, LiH^+, and Ne^{2+}. *The Journal of chemical physics* **126**, 104102 (2007).

[90] Sai, N., Barbara, P. F. & Leung, K. Hole localization in molecular crystals from hybrid density functional theory. *Physical review letters* **106**, 226403 (2011).

[91] Schmidt, T. & Kümmel, S. The influence of one-electron self-interaction on d-electrons. *Computation* **4**, 33 (2016).

[92] Perdew, J. P., Parr, R. G., Levy, M. & Balduz Jr, J. L. Density-functional theory for fractional particle number: derivative discontinuities of the energy. *Physical Review Letters* **49**, 1691 (1982).

[93] Mori-Sánchez, P., Cohen, A. J. & Yang, W. Many-electron self-interaction error in approximate density functionals. *The Journal of Chemical Physics* **125**, 201102 (2006).

[94] Stein, T., Autschbach, J., Govind, N., Kronik, L. & Baer, R. Curvature and frontier orbital energies in density functional theory. *The journal of physical chemistry letters* **3**, 3740–3744 (2012).

[95] Zhao, Q. & Kulik, H. J. Where does the density localize in the solid state? divergent behavior for hybrids and DFT+U. *Journal of chemical theory and computation* **14**, 670–683 (2018).

[96] Li, C., Zheng, X., Su, N. Q. & Yang, W. Localized orbital scaling correction for systematic elimination of delocalization error in density functional approximations. *National Science Review* **5**, 203–215 (2018).

[97] Henderson, T. M., Janesko, B. G. & Scuseria, G. E. Range separation and local hybridization in density functional theory. *The Journal of Physical Chemistry A* **112**, 12530–12542 (2008). PMID: 19006280.

[98] Dudarev, S., Botton, G., Savrasov, S., Humphreys, C. & Sutton, A. Electron-energy-loss spectra and the structural stability of nickel oxide: An LSDA+U study. *Physical Review B* **57**, 1505 (1998).

[99] Ivády, V. *et al.* Theoretical unification of hybrid-DFT and DFT+U methods for the treatment of localized orbitals. *Physical Review B* **90**, 035146 (2014).

[100] Verma, P. & Truhlar, D. G. Does DFT+U mimic hybrid density functionals? *Theoretical Chemistry Accounts* **135**, 182 (2016).

[101] Blum, V. *et al.* Ab initio molecular simulations with numeric atom-centered orbitals. *Computer Physics Communications* **180**, 2175–2196 (2009).

[102] Kaxiras, E., Bar-Yam, Y., Joannopoulos, J. D. & Pandey, K. Ab initio theory of polar semiconductor surfaces. I. methodology and the (22) reconstructions of gaas(111). *Physical Review B* **35**, 9625 (1987).

[103] Scheffler, M. Thermodynamic aspects of bulk and surface defects-first-principle calculations. In *Studies in Surface Science and Catalysis*, vol. 40, 115–122 (Elsevier, 1988).

[104] Qian, G.-X., Martin, R. M. & Chadi, D. First-principles study of the atomic reconstructions and energies of ga-and as-stabilized gaas(100) surfaces. *Physical Review B* **38**, 7649 (1988).

[105] Reuter, K., Stampf, C. & Scheffler, M. Ab initio atomistic thermodynamics and statistical mechanics of surface properties and functions. In *Handbook of materials modeling*, 149–194 (Springer, 2005).

[106] Liu, K.-Y., Liu, J. & Herbert, J. M. Accuracy of finite-difference harmonic frequencies in density functional theory. *Journal of computational chemistry* **38**, 1678–1684 (2017).

[107] Hanson-Heine, M. W., George, M. W. & Besley, N. A. Investigating the calculation of anharmonic vibrational frequencies using force fields derived from density functional theory. *The Journal of Physical Chemistry A* **116**, 4417–4425 (2012).

[108] Rauhut, G. & Pulay, P. Transferable scaling factors for density functional derived vibrational force fields. *The Journal of Physical Chemistry* **99**, 3093–3100 (1995).

[109] Scott, A. P. & Radom, L. Harmonic vibrational frequencies: an evaluation of Hartree-Fock, Møller-Plesset, quadratic configuration interaction, density functional theory, and semiempirical scale factors. *The Journal of Physical Chemistry* **100**, 16502–16513 (1996).

[110] Egelhoff Jr, W. Core-level binding-energy shifts at surfaces and in solids. *Surface Science Reports* **6**, 253–415 (1987).

[111] Koopmans, T. Über die zuordnung von wellenfunktionen und eigenwerten zu den einzelnen elektronen eines atoms. *Physica* **1**, 104–113 (1934).

[112] Janak, J. Proof that $\frac{\partial e}{\partial n_i} = \varepsilon$ in density-functional theory. *Physical Review B* **18**, 7165 (1978).

[113] Slater, J. C. *The self-consistent field for molecules and solids*, vol. 4 (McGraw-Hill, 1974).

[114] Göransson, C., Olovsson, W. & Abrikosov, I. A. Numerical investigation of the validity of the Slater-Janak transition-state model in metallic systems. *Physical Review B* **72**, 134203 (2005).

[115] Abrikosov, I., Olovsson, W. & Johansson, B. Valence-band hybridization and core level shifts in random Ag-Pd alloys. *Physical review letters* **87**, 176403 (2001).

[116] Johansson, B. & Mårtensson, N. Core-level binding-energy shifts for the metallic elements. *Physical Review B* **21**, 4427 (1980).

[117] Sinai, O. *et al.* Multiscale approach to the electronic structure of doped semiconductor surfaces. *Physical Review B* **91**, 075311 (2015).

[118] Moll, N., Xu, Y., Hofmann, O. T. & Rinke, P. Stabilization of semiconductor surfaces through bulk dopants. *New Journal of Physics* **15**, 083009 (2013).

[119] Oba, F., Togo, A., Tanaka, I., Paier, J. & Kresse, G. Defect energetics in ZnO: A hybrid Hartree-Fock density functional study. *Physical Review B* **77**, 245202 (2008).

[120] Yoshikawa, H. & Adachi, S. Optical constants of ZnO. *Japanese Journal of Applied Physics* **36**, 6237 (1997).

[121] Franco-Cañellas, A. *Impact of partial nitrogen and fluorine substitution on the interface properties of π-conjugated molecules adsorbed on inorganic substrates. A combined photoelectron-spectroscopy and X-ray-standing-waves study*. dissertation, Universität Tübingen (2018). URL `http://dx.doi.org/10.15496/publikation-24162`.

[122] Abedi, N. & Heimel, G. Correlating core-level shifts and structure of zinc-oxide surfaces. *physica status solidi (b)* **252**, 755–764 (2015).

[123] Foster, J. & Boys, S. Canonical configurational interaction procedure. *Reviews of Modern Physics* **32**, 300 (1960).

[124] Wannier, G. H. The structure of electronic excitation levels in insulating crystals. *Physical Review* **52**, 191 (1937).

[125] Wannier, G. H. Dynamics of band electrons in electric and magnetic fields. *Reviews of Modern Physics* **34**, 645 (1962).

[126] Marzari, N., Mostofi, A. A., Yates, J. R., Souza, I. & Vanderbilt, D. Maximally localized Wannier functions: Theory and applications. *Reviews of Modern Physics* **84**, 1419 (2012).

[127] Heimel, G., Romaner, L., Zojer, E. & Bredas, J.-L. The interface energetics of self-assembled monolayers on metals. *Accounts of Chemical Researchc* **41**, 721–729 (2008).

[128] Obersteiner, V., Egger, D. A., Heimel, G. & Zojer, E. Impact of collective electrostatic effects on charge transport through molecular monolayers. *The Journal of Physical Chemistry C* **118**, 22395–22401 (2014).

[129] Wruss, E., Zojer, E. & Hofmann, O. T. Distinguishing between charge-transfer mechanisms at organic/inorganic interfaces employing hybrid functionals. *The Journal of Physical Chemistry C* **122**, 14640–14653 (2018).

[130] Hoffmann, R. An extended Hückel theory. I. hydrocarbons. *The Journal of Chemical Physics* **39**, 1397–1412 (1963).

[131] Slater, J. C. Atomic shielding constants. *Physical Review* **36**, 57 (1930).

[132] Hinze, J. & Jaffe, H. H. Electronegativity. I. orbital electronegativity of neutral atoms. *Journal of the American Chemical Society* **84**, 540–546 (1962).

[133] Pople, J. A. & Segal, G. A. Approximate self-consistent molecular orbital theory. II. calculations with complete neglect of differential overlap. *The Journal of Chemical Physics* **43**, S136–S151 (1965).

[134] Alvarez, S. Tables of parameters for extended hückel calculations. *Universitat de Barcelona, Barcelona* (1989).

[135] Landrum, G. & Glassey, W. Yet another extended Hückel molecular orbital package (YAeHMOP). *Cornell University, Ithaca, NY* (2004).

[136] Basch, H., Viste, A. & Gray, H. B. Valence orbital ionization potentials from atomic spectral data. *Theoretica chimica acta* **3**, 458–464 (1965).

[137] Pyykkoe, P. & Lohr Jr, L. L. Relativistically parameterized extended hueckel calculations. 3. structure and bonding for some compounds of uranium and other heavy elements. *Inorganic Chemistry* **20**, 1950–1959 (1981).

[138] Fitzpatrick, N. J. & Murphy, G. H. Double zeta d radial wave functions for transition elements. *Inorganica chimica acta* **111**, 139–140 (1986).

[139] Pyykko, P. & Laaksonen, L. Relativistically parameterized extended hueckel calculations. 8. double-. zeta. parameters for the actinoids thorium, protactinium, uranium, neptunium, plutonium, and americium and an application on uranyl. *The Journal of Physical Chemistry* **88**, 4892–4895 (1984).

[140] Kim, K. & Jordan, K. Comparison of density functional and MP2 calculations on the water monomer and dimer. *The Journal of Physical Chemistry* **98**, 10089–10094 (1994).

[141] Wikimedia. Valence orbitals of oxygen atom and dioxygen molecule (diagram) (2015). URL `https://en.wikipedia.org/wiki/File:Valence_orbitals_of_oxygen_atom_and_dioxygen_molecule_(diagram).svg`.

[142] Ferraris, J., Cowan, D., Walatka, V. t. & Perlstein, J. Electron transfer in a new highly conducting donor-acceptor complex. *Journal of the American Chemical Society* **95**, 948–949 (1973).

[143] Avilov, I., Geskin, V. & Cornil, J. Quantum-chemical characterization of the origin of dipole formation at molecular organic/organic interfaces. *Advanced Functional Materials* **19**, 624–633 (2009).

[144] Marcus, R. A. On the theory of electrochemical and chemical electron transfer processes. *Canadian Journal of Chemistry* **37**, 155–163 (1959).

[145] Marcus, R. A. Electron transfer reactions in chemistry. theory and experiment. *Rev. Mod. Phys.* **65**, 599–610 (1993).

[146] Wu, Q. & Van Voorhis, T. Extracting electron transfer coupling elements from constrained density functional theory. *The Journal of Chemical Physics* **125**, 164105 (2006).

[147] Te Velde, G. *et al.* Chemistry with ADF. *Journal of Computational Chemistry* **22**, 931–967 (2001).

[148] Senthilkumar, K., Grozema, F. C., Bickelhaupt, F. M. & Siebbeles, L. D. A. Charge transport in columnar stacked triphenylenes: Effects of conformational fluctuations on charge transfer integrals and site energies. *The Journal of Chemical Physics* **119**, 9809–9817 (2003).

[149] Oberhofer, H. & Blumberger, J. Revisiting electronic couplings and incoherent hopping models for electron transport in crystalline C_{60} at ambient temperatures. *Physical Chemistry Chemical Physics* **14**, 13846–13852 (2012).

[150] Schober, C., Reuter, K. & Oberhofer, H. Critical analysis of fragment-orbital DFT schemes for the calculation of electronic coupling values. *The Journal of Chemical Physics* **144**, 054103 (2016).

[151] Sinai, O. *et al.* Multiscale approach to the electronic structure of doped semiconductor surfaces. *Phys. Rev. B* **91**, 075311 (2015).

[152] Cochrane, K., Schiffrin, A., Roussy, T., Capsoni, M. & Burke, S. Pronounced polarization-induced energy level shifts at boundaries of organic semiconductor nanostructures. *Nature communications* **6**, 8312 (2015).

[153] Cochrane, K. A. *Single Molecule Perspectives of Model Organic Semiconductors: Energy Level Mapping by High-Resolution Scanning Probe Microscopy.* dissertation, University

of British Columbia - Vancouver (2017). URL `https://open.library.ubc.ca/cIRcle/` `collections/ubctheses/24/items/1.0354979`.

[154] Tkatchenko, A. & Scheffler, M. Accurate molecular van der waals interactions from ground-state electron density and free-atom reference data. *Phys. Rev. Lett.* **102**, 073005 (2009).

[155] Roessler, D. & Walker, W. Electronic spectra of crystalline NaC and KCl. *Physical Review* **166**, 599 (1968).

[156] Le Moal, E., Müller, M., Bauer, O. & Sokolowski, M. Stable and metastable phases of PTCDA on epitaxial NaCl films on Ag(100). *Physical Review B* **82**, 045301 (2010).

[157] Aldahhak, H., Schmidt, W. & Rauls, E. Adsorption of PTCDA on NaCl(100) and KCl(100). *Surface Science* **617**, 242–248 (2013).

[158] Sommerhalter, C., Matthes, T. W., Glatzel, T., Jäger-Waldau, A. & Lux-Steiner, M. C. High-sensitivity quantitative kelvin probe microscopy by noncontact ultra-high-vacuum atomic force microscopy. *Applied Physics Letters* **75**, 286–288 (1999).

[159] Barth, C. & Henry, C. R. Surface double layer on (001) surfaces of alkali halide crystals: a scanning force microscopy study. *Physical review letters* **98**, 136804 (2007).

[160] Gross, L. *et al.* Measuring the charge state of an adatom with noncontact atomic force microscopy. *Science* **324**, 1428–1431 (2009).

[161] Schuler, B. *et al.* Contrast formation in Kelvin probe force microscopy of single π-conjugated molecules. *Nano letters* **14**, 3342–3346 (2014).

[162] Mohn, F., Gross, L., Moll, N. & Meyer, G. Imaging the charge distribution within a single molecule. *Nature nanotechnology* **7**, 227–231 (2012).

Abbreviations

CREST	Charge Reservoir Electrostatic Sheet Technique
DFT	Density Functional Theory
DOS	Density Of States
EA	Electron Affinity
F4TCNQ	7,7,8,8-tetracyano-2,3,5,6-tetrafluoroquinodimethane
F6TCNNQ	2,2'-(perfluoronaphthalene-2,6-diylidene)dimalononitrile
FCT	Fractional Charge Transfer
GGA	Generalized Gradient Approximation
HF	Hartree-Fock
HOMO	Highest Occupied Molecular Orbital
HSE	Heyd-Scuseria-Ernzerhof hybrid functional
IE	Ionization Energy
ICT	Integer Charge Transfer
IR	Infrared Radiation
KPFM	Kelvin Probe Force Microscopy
KS	Kohn-Sham
LDA	Local Density Approximation
LUMO	Lowest Unoccupied Molecular Orbital
MSIE	Many-electron Self-Interaction Error
PBE	Perdew-Burke-Ernzerhof functional
PTCDA	Perylenetetracarboxylic dianhydride
SCF	Self-Consistent Field
SI	Self Interaction
SIE	Self-Interaction Error
TCNQ	Tetracyanochinodimethan

VCA   **V**irtual **C**rystal **A**pproximation

vdW   **v**an **d**er **W**aals

xc   e**x**change-**c**orrelation

XSW   **X**-ray **S**tanding **W**ave